frontiers | Research Topics

Rapid detection of fungi, microbial, and viral pathogens based on emerging biosensing technology

Edited by
Han-Sheng Chuang, Haim Bau, Stuart Joseph Williams, Yu-Jui Fan,
Nan-Fu Chiu and Tzong-Rong Ger

Published in
Frontiers in Bioengineering and Biotechnology

ISSN 1664-8714
ISBN 978-2-83250-910-4
DOI 10.3389/978-2-83250-910-4

About Frontiers

Frontiers is more than just an open access publisher of scholarly articles: it is a pioneering approach to the world of academia, radically improving the way scholarly research is managed. The grand vision of Frontiers is a world where all people have an equal opportunity to seek, share and generate knowledge. Frontiers provides immediate and permanent online open access to all its publications, but this alone is not enough to realize our grand goals.

Frontiers journal series

The Frontiers journal series is a multi-tier and interdisciplinary set of open-access, online journals, promising a paradigm shift from the current review, selection and dissemination processes in academic publishing. All Frontiers journals are driven by researchers for researchers; therefore, they constitute a service to the scholarly community. At the same time, the *Frontiers journal series* operates on a revolutionary invention, the tiered publishing system, initially addressing specific communities of scholars, and gradually climbing up to broader public understanding, thus serving the interests of the lay society, too.

Dedication to quality

Each Frontiers article is a landmark of the highest quality, thanks to genuinely collaborative interactions between authors and review editors, who include some of the world's best academicians. Research must be certified by peers before entering a stream of knowledge that may eventually reach the public - and shape society; therefore, Frontiers only applies the most rigorous and unbiased reviews. Frontiers revolutionizes research publishing by freely delivering the most outstanding research, evaluated with no bias from both the academic and social point of view. By applying the most advanced information technologies, Frontiers is catapulting scholarly publishing into a new generation.

What are Frontiers Research Topics?

Frontiers Research Topics are very popular trademarks of the *Frontiers journals series*: they are collections of at least ten articles, all centered on a particular subject. With their unique mix of varied contributions from Original Research to Review Articles, Frontiers Research Topics unify the most influential researchers, the latest key findings and historical advances in a hot research area.

Find out more on how to host your own Frontiers Research Topic or contribute to one as an author by contacting the Frontiers editorial office: frontiersin.org/about/contact

Rapid detection of fungi, microbial, and viral pathogens based on emerging biosensing technology

Topic editors
Han-Sheng Chuang — National Cheng Kung University, Taiwan
Haim Bau — University of Pennsylvania, United States
Stuart Joseph Williams — University of Louisville, United States
Yu-Jui Fan — Taipei Medical University, Taiwan
Nan-Fu Chiu — National Taiwan Normal University, Taiwan
Tzong-Rong Ger — Chung Yuan Christian University, Taiwan

Citation
Chuang, H.-S., Bau, H., Williams, S. J., Fan, Y.-J., Chiu, N.-F., Ger, T.-R., eds. (2022). *Rapid detection of fungi, microbial, and viral pathogens based on emerging biosensing technology*. Lausanne: Frontiers Media SA.
doi: 10.3389/978-2-83250-910-4

Table of contents

frontiers | Frontiers in Bioengineering and Biotechnology

TYPE Editorial
PUBLISHED 17 November 2022
DOI 10.3389/fbioe.2022.1067322

Editorial: Rapid detection of fungi, microbial, and viral pathogens based on emerging biosensing technology

Han-Sheng Chuang[1,2]*, Yu-Jui Fan[3], Tzong-Rong Ger[4], Nan-Fu Chiu[5], Stuart J. Williams[6] and Haim H. Bau[7]

[1]Department of Biomedical Engineering, National Cheng Kung University, Tainan, Taiwan, [2]Medical Device Innovation Center, National Cheng Kung University, Tainan, Taiwan, [3]School of Biomedical Engineering, Taipei Medical University, Taipei, Taiwan, [4]Department of Biomedical Engineering, Chung Yuan Christian University, Taoyuan, Taiwan, [5]Laboratory of Nano-Photonics and Biosensors, Institute of Electro-Optical Engineering, National Taiwan Normal University, Taipei, Taiwan, [6]Department of Mechanical Engineering, University of Louisville, Louisville, KY, United States, [7]Department of Mechanical Engineering and Applied Mechanics, School of Engineering and Applied Science, University of Pennsylvania, Philadelphia, PA, United States

OPEN ACCESS

EDITED BY
Guozhen Liu,
The Chinese University of Hong Kong,
China

REVIEWED BY
Guosong Lai,
Hubei Normal University, China

*CORRESPONDENCE
Han-Sheng Chuang,
oswaldchuang@mail.ncku.edu.tw

SPECIALTY SECTION
This article was submitted to Biosensors and Biomolecular Electronics, a section of the journal Frontiers in Bioengineering and Biotechnology

RECEIVED 11 October 2022
ACCEPTED 04 November 2022
PUBLISHED 17 November 2022

CITATION
Chuang H-S, Fan Y-J, Ger T-R, Chiu N-F, Williams SJ and Bau HH (2022), Editorial: Rapid detection of fungi, microbial, and viral pathogens based on emerging biosensing technology.
Front. Bioeng. Biotechnol. 10:1067322.
doi: 10.3389/fbioe.2022.1067322

KEYWORDS

biosensing technology, pathogen, fungi, bacteria, viruses

Editorial on the Research Topic
Rapid Detection of Fungi, Microbial, and Viral Pathogens Based on Emerging Biosensing Technology

Fungi, microbial, and viral pathogens have been constantly posing serious threats to human society over the past centuries. Notorious examples in history that claimed millions of innocent lives, like the Plague of Justinian in 541 AD, the Black Death in 1347, the Italian Plague in 1629–1631, the Great Plague of London during the 16th and 17th centuries, the Spanish Flu in 1918, and recent COVID-19 pandemic that started in 2019, all resulted from either bacterium or virus outbreaks. However, the adverse situation had never been overturned until the second industrial resolution in the late 19th century and early 20th century that brought up immense science advances. The rapidly progressive technology, for the first, imparted humans some powerful weapons to win the unconventional war on the invisible battlefields. The comprehensive understanding of microbiology renders the science behind the microbes and leads researchers to decipher more traits about their weakness and strength. In the 1990s, the emerging microfabrication became the first cornerstone to bring the lab-on-a-chip style biosensing technology from theory to reality. The central concept is to seek early medical treatments by early diagnosis. Recently, numerous research efforts have been made in mechanical, optical, electrical, biochemical aspects, making the sensing technology more accurate, sensitive, specific, compact, cost-effective, and rapid than their past counterparts. Electrochemistry has been long adopted as a label-free means in most biochemical detections (CesewskiB and Johnson, 2020). Their simple integration with semiconductors promotes their high acceptance in variously electrical platforms. Surface enhanced Raman scattering (SERS) and surface plasmon resonance (SPR) are two advanced optical approaches that can easily achieve highly sensitive detection for trace pathogens (Kurochkin et al., 2020; Park et al., 2022a). However, their dependence on sophisticated analyzing instruments forms a barrier to layman users. Unlike most techniques, cellulose/paper-based lateral flow assays (LFA) need least external support, hence are cost-effective and can be carried out in resource-limited areas (Sohrabi et al., 2022). Unfortunately, the simplicity also limits the accuracy and sensitivity of the LFA on the other way. Notably, a novel biosensing technique taking advantage of the field effect transistors (FET) from the semiconductor industry, termed BioFET, has gradually drawn people's attention and emerged its potential in the demanding biosensing market. With the continual advancement of the current semiconductor technology, BioFET is believed to achieve unprecedented breakthroughs in all aspects in the future (Panahi et al., 2021). Among the techniques, many of them have been used to assist the detection of pathogens, yet, there still exist challenges that need to be addressed. Considering superbugs and variant viruses become more severe and hard to deal with nowadays, a majority of diagnostic approaches that rely on costly, labor-intensive, bulky, and expert-dependent facilities reflects the facts of low-efficiency, lack of flexibility, and inconvenience in our current medical systems. In this regard, decentralization of diagnosis (i.e., point-of-care testing, POCT) provides a promising solution to this deficiency. With POCT, people can manage their health in a more rapid, cost-effective, and user-friendly way.

After being raged by the COVID-19 pandemic for nearly 3 years, the world has realized the essence of rapid POCT tools in defending the health of our society. In response to the urgent needs and beyond, we edited this Research Topic to disclose the latest developments of various emerging biosensing technologies for rapid detection of pathogenic microbes. This Research Topic collected eight regular research articles and one review article, which cover broad focuses of microbes across *Candida auris*, *Staphylococcus aureus*, Hepatitis B virus, and more. Their research highlights are briefly summarized below to serve as an initial orientation for readers.

Among the accepted papers, five of them are associated with emerging bacteria-related diagnostic approaches. Chen et al., utilized cycling enzymatic amplification based on HRP and TMB to achieve rapid electrochemical microbial quantification and antimicrobial susceptibility (AST) profiling. Bacterial strains, including *Enterobacter cloacae*, *Escherichia coli*, *Klebsiella aerogenes*, and *Klebsiella pneumoniae*, were conducted in this study. Their findings concluded that 6 CFU/ml was the limit of detection (LoD) out of the 500-µl whole blood samples for their proposed method. For AST, they utilized dual-dilution kinetic curves and automatable molecular quantification of species-specific 16S rRNA through the use of an electrochemical sensor to assess microbiological responses to antibiotic exposure. In the final blinded clinical test, four urine samples were investigated at a concentration of 10^5 CFU/ml. All four results showed good agreements with the CLSI breakpoints. Eventually, they claimed the approach was able to identify all blood borne pathogens in 200–500 µl blood volume in less than 8 h while the total assay time for the uropathogen ID can be as short as 2 h due to high abundance in nature (>10^8 CFU/ml).

In another study, Zheng et al., reported a deliberate combination of silver nanoparticle (AgNP)-invertase complexes and the personal glucose meter (PGM) to detect the presence of bacteria. The principle is simply based on the competitive binding between PEI-AuNPs and other negatively charged species, which are invertase and bacteria in this case. The increased glucose concentration can be eventually measured by the PGM. By optimizing the operating conditions, they achieved a LoD of 7. 59×10^2 CFU/ml. With the same approach, *E. coli* and *S. aureus* both exhibited a good linear relationship between the PGM signal and the bacterial concentration from 10^2 to 10^7 CFU/ml. For AST, *E. coli* was treated with four antibiotics. All of them showed good inhibited results after 5-h incubation when the PGM signal was below 27.5 mg/dl. Despite the smart combination of AgNP-invertase complexes and the PGM, the approach appears not to be selective to bacterial strains.

In addition to bacteria, fungi-associated diseases are also commonly occurred in the human society and sometimes can be life-threatening if not been diagnosed in a timely fashion. To address this challenge, Lee et al., proposed a portable droplet magnetofluidic (DM) device along with a DM assay cartridge, termed POC.auris, to carry out the rapid duplex detection of *Candida auris* based on qPCR. Three major *C. auris* clade isolates that originate from South Asia, Africa, and South America were measured with the POC.auris. The measurement result was obtained within 30 min and a LoD of 300 CFU/ml was achieved. Despite the successful demonstration, the authors aimed to keep working on several improvements of the current system to make it a step closer to a clinic-ready product. The anticipated improvements are replacing the mock samples with real clinical ones, replacing the manual off-cartridge cell lysis and cartridge preparation with a simpler workflow, enhancing the sensitivity and turnaround time, adapting to different PCR assays, and reducing the operating cost.

Sharing similar interests in fungal infections with the previous group, Barbosa et al., developed a microfluidic chip combined with fluorescence *in situ* hybridization (FISH) to better monitor the urinary tract infection (UTI), caused by opportunistic pathogens such as *Candida albicans* or non-albicans *Candida species* (NACS). Instead of laborious, time- and reagent-consuming UTI diagnosis, the authors fabricated a microchannel to trap and separate target cells from suspension. A specific peptide nucleic acid (PNA) probe was used to identify the trapped cells and generate fluorescent signal. They believed that their proposed diagnostic method can be a solution herein and adapted to point-of-care detection. The final result showed that *C. tropicalis* detection (~10^5 cell/ml) in artificial urine was achieved in 6 h, which is faster than current urine culture method that takes 18–48 h. It should be noted that autofluorescence arising from biological matrices and inorganic debris may form a main challenge in FISH according to the authors' account.

In the collection of bacterial detection, a reviewer article authored by Chen et al., focuses on the up-to-date developments of aptamer-based biosensors for rapid and sensitive detection of *Staphylococcus aureus*. The authors emphasized timely, rapid and accurate detection of *S. aureus* is of particular significance in this paper. Unlike conventional immunoassays, aptamer is a specific oligonucleotide sequence that features high sensitivity, high specificity, and easy storage. Moreover, aptamers can efficiently and specifically attach to a wide range of targets, including small molecules, ions, peptides, proteins, viruses, bacteria and even cells. Benefit by aptamers, aptasensors have been rapidly emerging in recent years due to their fast, specific, low cost, low sample volume, automated, and portable advantages. To facilitate the introduction, sensors are divided in two categories—optical transduction and electrochemical transduction. The former aptasensors discussed are based on colorimetry, fluorescence, SERS, SPR, and chemiluminescence while the later aptasensors included are based on potentiometry, amperometry/voltammetry, impedance, and conductometry. In the end, some aptasensors in the point-of-care testing applications are discussed. While this review comprehensively explores the recent advances in aptasensors for *S. aureus* detection, some significant challenges regarding aptamers, such as tedious SELEX, biostability, interference effects from metal ions, anions, and antioxidants, reproducibility, and multiplexing detection, still need plenty of efforts to improve in order to achieve future practical use.

Unlike bacteria, viruses develop a different strategy to invade into human body and impair our health. Nucleic acid amplification has always been an effective measure to help clinicians diagnose the viral diseases in the early stage. Unfortunately, the conventional RT-PCR is obvious too tedious to provide handy and timely information. Therefore, Park et al., managed to develop one-step digital RT-PCR for viral RNA detection. Two viruses, tobacco mosaic virus and cucumber mosaic virus, were tested as model viral particles in this study. Instead of a bulky vial used in the conventional RT-PCR, a single unit comprising 20,000 chambers of sub-nanoliter volume was used to achieve multiple amplification reactions. As compared with the conventional RT-PCR, the proposed one-step digital RT-PCR mainly saved the processing time in virus lysis, reverse transcription, and cDNA purification. Finally, their analysis yielded 1,130.2 copies/μl using 10^{-2} μg/nl of viral particles in a 30 min.

Another study conducted by Waller et al., focused on developing a device to address the need for rapid, simple, scalable, and high-throughput multiplex diagnostics in non-laboratory settings. In this paper, the authors demonstrate a multiplex reverse-transcription loop-mediated isothermal amplification (RT-LAMP) coupled with a gold nanoparticle-based lateral flow immunoassay (LFIA) capable of detecting up to three unique SARS-CoV-2 viral gene targets (Orf1ab, Envelope, and Nucleocapsid) in 15 min for RT-LAMP plus 30 min for LFIA. A colorimetric change was used to confirm the presence of a positive sample. This approach was eventually tested with 30 positive and 30 negative clinical samples. Good agreements between the read-outs from the device and the standard were observed in all samples.

In the next paper, Li et al., built a flexible Terahertz (THz) metamaterial biosensor for ultra-sensitive detection of Hepatitis B viral DNA based on the metal-enhanced sandwich assay. THz spectroscopy is preferentially sensitive to the dynamic expressions of intermolecular modes and has proven to have potential to detect nucleic acids. With sandwich complexes comprising gold magnetic nanoparticle–rolling circle amplification–gold nanoparticles and a transparent and ultrathin PET substrate patterned with a planar array of asymmetric double-split rings, a larger magnitude of target DNA detection signal amplification was exhibited as compared to the traditional RCA-THz metamaterial biosensor method, which may be due to the gold-mediated nanoparticles' high refractive index. The final results confirmed that their THz biosensor achieved a LoD as low as 1.27 × 10^2 IU/ml of serum HBV DNA at concentrations in a range of 1.27 × 10^2–1.27 × 10^7 IU/ml.

At last, this Research Topic collects a paper that proposes a unique concentration device to enrich protein biomarkers for sensitive and rapid LFA detection. In this paper, Chen et al., successfully utilized osmotic pressure to concentrate specimens by up to 100-fold. The concentrated specimens were then collected and flown through commercial LFA rapid testing strips to examine the presence of target proteins. Two common biomarkers, chorionic gonadotropin hormone (hCG) and SARS-Cov-2 Nucleocaspid (N protein) were tested to evaluate the effects of their approach. With the osmotic concentration, the signal intensities of 0.02 μg/ml hCG and 0.04 ng/ml N protein were increased from 1.01 to 6.0 and 1.08 to 1.61, respectively. The authors believed their osmotic processor can achieve similar enrichment as the existing techniques.

Author contributions

All authors listed have made a substantial, direct, and intellectual contribution to the work and approved it for publication.

Funding

This work was supported by the National Science and Technology Council (NSTC) of Taiwan under the grant numbers: 111-2221-E-006-066 and 111-2811-E-006-016.

Acknowledgments

We deeply thank all the co-editors, authors, and reviewers who have contributed their precious time and efforts in this Research Topic.

Conflict of interest

The authors declare that the research was conducted in the absence of any commercial or financial relationships that could be construed as a potential conflict of interest.

Publisher's note

References

Barbosa, V. B., Rodrigues, C. F., Cerqueira, L., Miranda, J. M., and Azevedo, N. F. (2022). Microfluidics combined with fluorescence *in situ* hybridization (FISH) for Candida spp. detection. *Front. Bioeng. Biotechnol.* 10, 987669. doi:10.3389/fbioe.2022.987669

CesewskiB, E., and Johnson, N. (2020). Electrochemical biosensors for pathogen detection. *Biosens. Bioelectron.* 159, 112214. doi:10.1016/j.bios.2020.112214

Chen, J., Navarro, E., Nuñez, E., and Gau, V. (2021). Rapid electrochemical-based PCR-less microbial quantification and antimicrobial susceptibility profiling directly from blood and urine with unknown microbial load or species. *Front. Bioeng. Biotechnol.* 9, 744198. doi:10.3389/fbioe.2021.744198

Chen, S.-Y., Wu, A. Y., Lunde, R., and Lai, J. J. (2022). Osmotic processor for enabling sensitive and rapid biomarker detection via lateral flow assays. *Front. Bioeng. Biotechnol.* 10, 884271. doi:10.3389/fbioe.2022.884271

Chen, W., Lai, Q., Zhang, Y., and Liu, Z. (2022). Recent advances in aptasensors for rapid and sensitive detection of staphylococcus aureus. *Front. Bioeng. Biotechnol.* 10, 889431. doi:10.3389/fbioe.2022.889431

Kurochkin, I. N., Eremenko, A. V., Evtushenko, E. G., Nechaeva, N. L., Durmanov, N. N., Guliev, R. R., et al. (2020). SERS for bacteria, viruses, and protein biosensing. *Macro, Micro, Nano-Biosensors*, 75–94. doi:10.1007/978-3-030-55490-3_5

Lee, P.-W., Totten, M., Chen, L., Chen, F.-E., Trick, A. Y., Shah, K., et al. (2022). A portable droplet magnetofluidic device for point-of-care detection of multidrug-resistant Candida auris. *Front. Bioeng. Biotechnol.* 10, 826694. doi:10.3389/fbioe.2022.826694

Li, Y., Wang, X., Liu, Y., Jin, W., Tian, H., Xie, F., et al. (2022). Flexible Terahertz metamaterial biosensor for ultra-sensitive detection of Hepatitis B viral DNA based on the metal-enhanced sandwich assay. *Front. Bioeng. Biotechnol.* 10, 930800. doi:10.3389/fbioe.2022.930800

Panahi, A., Sadighbayan, D., Forouhi, S., and Ghafar-Zadeh, E. (2021). Recent advances of field-effect transistor technology for infectious diseases. *Biosens. (Basel).* 11, 103. doi:10.3390/bios11040103

Park, H., Jung, W., Jang, H., Namkoong, K., and Choi, K. Y. (2022). One-step RT-qPCR for viral RNA detection using digital analysis. *Front. Bioeng. Biotechnol.* 10, 837838. doi:10.3389/fbioe.2022.837838

Park, J. H., Cho, Y. W., and Kim, T. H. (2022). Recent advances in surface plasmon resonance sensors for sensitive optical detection of pathogens. *Biosens. (Basel).* 12, 180. doi:10.3390/bios12030180

Sohrabi, H., Majidi, M. R., Fakhraei, M., Jahanban-Esfahlan, A., Hejazi, M., Oroojalian, F., et al. (2022). Lateral flow assays (LFA) for detection of pathogenic bacteria: A small point-of-care platform for diagnosis of human infectious diseases. *Talanta* 243, 123330. doi:10.1016/j.talanta.2022.123330

Waller, L., Guo, Z., Tang, R., Zhang, Z., Wang, E., Yasuhara-Bell, J., et al. (2022). High sensitivity, rapid detection of virus in high traffic environments. *Front. Bioeng. Biotechnol.* 10, 877603. doi:10.3389/fbioe.2022.877603

Zheng, L., Shen, Y., Dong, W., Zheng, C., Zhou, R., and Lou, Y. L. (2021). Rapid detection and antimicrobial susceptibility testing of pathogens using AgNPs-invertase complexes and the personal glucose meter. *Front. Bioeng. Biotechnol.* 9, 795415. doi:10.3389/fbioe.2021.795415

frontiers
in Bioengineering and Biotechnology

ORIGINAL RESEARCH
published: 16 September 2021
doi: 10.3389/fbioe.2021.744198

Rapid Electrochemical-Based PCR-Less Microbial Quantification and Antimicrobial Susceptibility Profiling Directly From Blood and Urine With Unknown Microbial Load or Species

*Jade Chen, Eduardo Navarro, Eliseo Nuñez and Vincent Gau**

GeneFluidics, Irwindale, CA, United States

Novel molecular platforms are available for identifying (ID) the causative agents of microbial infections and generating antimicrobial susceptibility testing (AST) profiles, which can inform the suitable course of treatment. Many methods claim to perform AST in minutes or hours, often ignoring the need for time-consuming steps such as enrichment cultures and isolation of pure cultures. In clinical microbiology laboratories, an infectious microbial must first be cultured (overnight to days) and identified at the species level, followed by a subsequent AST with an additional turnaround time of 12–48 h due to the need for regrowth of the organism in the absence and presence of relevant antibiotics. Here, we present an electrochemical-based direct-from-specimen ID/AST method for reporting directly from unprocessed urine and blood in hours. In a limit of detection study of 0.5-ml whole blood samples for point-of-care and pediatric applications, 16.7% (4/24) of samples contrived at 2 CFU/ml and 100% (24/24) of samples contrived at 6 CFU/ml were reported positive in 6.5 h, indicating a limit of detection of 6 CFU/ml. In a separate direct-from-specimen AST study, the categorical susceptibility was reported correctly for blinded susceptible, intermediate, resistant, and polymicrobial contrived specimens in 4 h.

Keywords: direct-from-specimen, microbial quantification, electrochemical sensor, PCR-less molecular analysis, microbial responses, antimicrobial susceptibility testing, matrix interferant removal, cyclic enzymatic amplification

Edited by:
Han-Sheng Chuang,
National Cheng Kung University,
Taiwan

Reviewed by:
Ting-Yuan Tu,
National Cheng Kung University,
Taiwan
Huan Hu,
Zhejiang University, China

Correspondence:
Vincent Gau
vgau@genefluidics.com

Specialty section:
This article was submitted to Biosensors and Biomolecular Electronics, a section of the journal Frontiers in Bioengineering and Biotechnology

Received: *19 July 2021*
Accepted: *30 August 2021*
Published: *16 September 2021*

Citation:
Chen J, Navarro E, Nuñez E and Gau V (2021) Rapid Electrochemical-Based PCR-Less Microbial Quantification and Antimicrobial Susceptibility Profiling Directly From Blood and Urine With Unknown Microbial Load or Species. Front. Bioeng. Biotechnol. 9:744198. doi: 10.3389/fbioe.2021.744198

INTRODUCTION

Any time antibiotics are prescribed to patients suspected of harboring a severe bacterial infection, the stakes are high. They are either appropriately prescribed to prevent potentially severe infections, or inappropriately prescribed, which unnecessarily contributes to the risk of adverse effects, global antibiotic resistance, and more. There is an unmet need for rapid phenotypic diagnostics in clinical settings to assist in the prescribing of antibiotics for evidence-based definitive therapy (May et al., 2013; Timbrook et al., 2017). AST technologies help accelerate the initiation of targeted antimicrobial therapy for patients with infections by inferring the concentration of an antibiotic that would be required to inhibit multiplication of a microorganism *in vitro* with acceptable toxicity for patients. Although the AST platforms that are currently most used are robust and represent added value to the clinical diagnostic microbiology laboratory, their main shortcomings are suboptimal sensitivity and

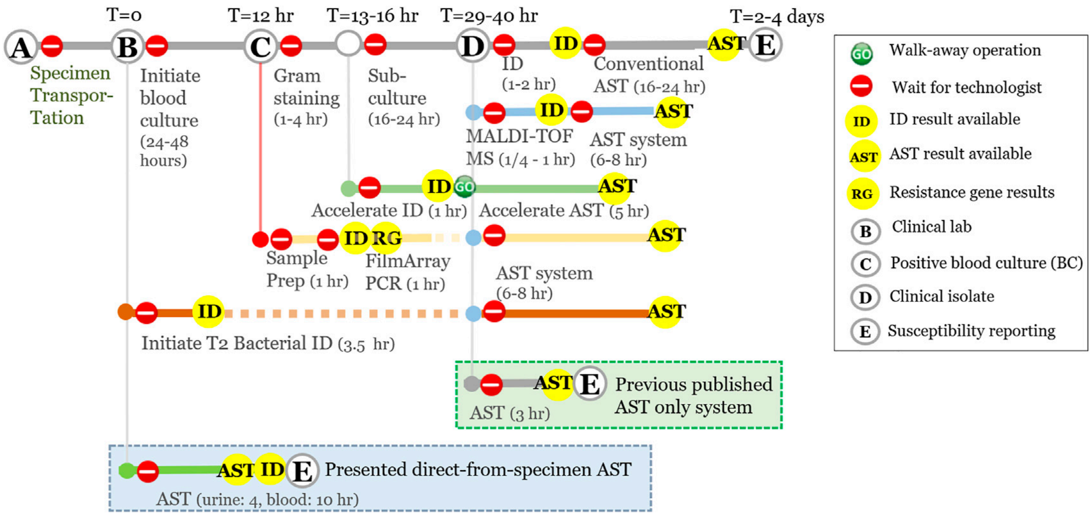

FIGURE 1 | Total turnaround time of proposed direct-from-specimen assays (blue box) compared to other methods used in the clinical microbiology laboratory.

specificity, a somewhat long time to result (TTR), and a lack of full automation, which may hinder the timely and accurate prescription of antibiotics (van Belkum et al., 2019). Owing to the lack of timely microbiological evidence, antibiotic therapy can only be prescribed empirically, rather than precisely upon specific target(s) (Jones and Puskarich, 2014; Han et al., 2020).

Being pivotal for the accurate management of patients with infectious diseases, identification has been significantly accelerated, miniaturized, and automated with bioMérieux VITEK2®, WalkAway MicroScan® (Siemens), or BD Phoenix® systems (**Figure 1**) (Anhalt and Fenselau, 1975; D'amato et al., 1981; Menozzi et al., 2006; Charretier et al., 2015; Welker, 2011). However, the selection of the right antibiotic treatment still requires time-consuming phenotypic AST according to FDA guidelines (at least 10 h following bacterial isolation), resulting in a delay of one to three days between the initiation of empirical antimicrobial therapy and the AST result (Van Belkum and Dunne, 2013). We previously published electrochemical-based microbiological response signatures that successfully distinguished resistant (R), intermediate (I), and susceptible (S) clinical isolates (not directly from specimen) using a laboratory automation system that demonstrated 98.5–100% AST categorical agreement with Clinical and Laboratory Standards Institute (CLSI) breakpoints and methodology in just 3.5 h (**Figure 1** green box) (Liu et al., 2020; Chen et al., 2021a).

However, in this study, we present a direct-AST method using electrochemical sensors without any purification or nucleic acid amplification that can start directly from unprocessed specimens and test multiple samples and/or specimen types simultaneously (**Figure 1** blue box). We acknowledge that most clinical microbiologists are not yet ready to accept the implementation of AST-only methods without pathogen ID, given the importance of establishing the identity of microbial species in the context of clinical decision making, as well as the potential challenges presented with performing AST directly from unprocessed clinical specimens. The first challenge derives from unprocessed polymicrobial clinical samples with multi-drug resistance. The organism with the higher bacterial load may dominate and prevent the other target(s) from being detected, or one target may be present below the limit of detection of the assay. The second challenge is the unknown microbial load of clinical specimens. According to the European Committee on Antimicrobial Susceptibility Testing and CLSI guidelines, identification of pathogens at the species level is currently an essential element in interpreting minimum inhibitory concentrations (MIC) of antibiotics for particular pathogens at a fixed inoculum concentration at 5×10^5 CFU/ml (Colony Forming Unit per milliliter). The unknown microbial load from unprocessed clinical specimens is a major limitation to report susceptibility essentially equivalent to the CLSI breakpoints using CLSI methods.

To facilitate targeted antimicrobial prescribing practices and to help reduce the global burden of antibiotic resistance, the presented testing method aims to address these challenges and demonstrate categorical susceptibility reporting (R, I, S) essentially equivalent to CLSI breakpoints and methodology using contrived specimens. This electrochemical-based direct-AST method is designed for a laboratory automation system. As illustrated in **Figure 2**, the general operating principle of the system will consist of loading urine and blood specimens collected in their respective tube types into the system, after which the system will perform the presented AST assay directly from these unprocessed specimens. The interfering matrix components of each specimen type are removed and replaced by culture media, followed by a short 2-h antibiotic exposure using dried antibiotic stripwells consisting of different antibiotic conditions and an electrochemical sensor assay to quantify the 16S ribosomal RNA (rRNA) present in each antibiotic condition after exposure. The use of 16S rRNA as an analyte has become a common practice in many applications, such as pathogen identification, and therefore, has led to the design of a wide variety of probe pairs that detect the many characterized 16S

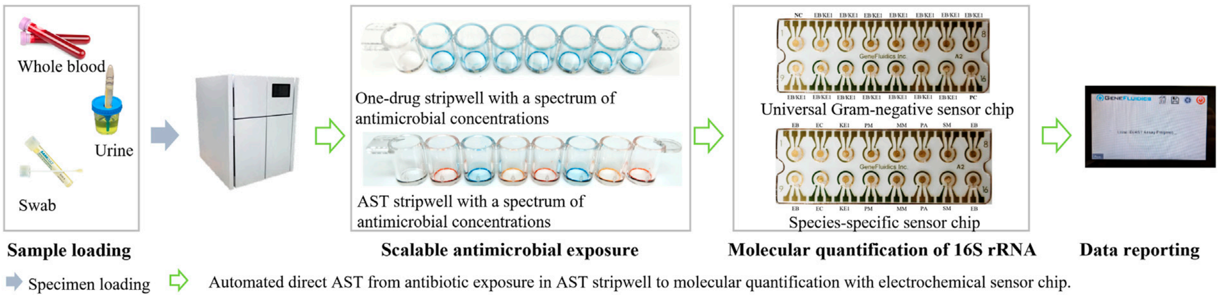

FIGURE 2 | Workflow of the presented direct-AST. The user loads specimens and consumables (stripwell and sensor chip), selects specimen type, and waits for susceptibility reporting (user intervention in blue arrows). The system is designed to automate scalable antimicrobial exposure and molecular quantification (green arrows) for AST reporting directly from whole blood or urine.

rRNA sequences of various bacterial strains (Soriano-Lerma et al., 2020). Oligonucleotide probes complementary to target 16S rRNA sequences have been used as a tool to identify bacteria at the species level and assist in differentiating between closely related bacterial species. Chakravorty et al. suggested that utilizing a small sequence of nucleotides carrying the most taxonomic information in combination with complementary oligonucleotide probes may increase assay sensitivity and applicability to archival specimens (Chakravorty et al., 2007). The presented method has the potential to bypass a lengthy TTR and provide antibiotic susceptibility profiles in hours without the need for specimen processing or ID results.

METHODS AND MATERIAL

Cyclic Enzymatic Amplification of Chronoamperometry Measurement

The principle of the presented electrochemical-based enzymatic amplification method for molecular quantification is to convert the concentration of the target analyte such as 16S rRNA into an electrical current (*Cycling Enzymatic Amplification Using HRP and TMB*) to allow the functionalized electrochemical sensor to precisely measure the electron flow proportional to the analyte concentration (*Molecular Quantification of 16S rRNA*). The presented electrochemical sensor is a compact analytical device that incorporates a self-assembled monolayer of species or group-specific oligonucleotides as the sensing element integrated within a physiochemical transducer surface.

Chronoamperometry involves stepping the bias potential at the working electrode from an initial potential to a final potential and holding that potential while the current is recorded at the electrode. These potentials are chosen to bracket the formal potential, E_0, of the analyte. At the initial potential, no significant current flows. Once the potential is stepped to the final potential, the analyte is consumed at the electrode surface via oxidation or reduction (depending on the direction of the step). This depletes the concentration of the analyte near the electrode. The current response is thus a rapid increase followed by a decay as the analyte is depleted and equilibrium is reached. The analysis of chronoamperometry or amperometry data is based on the Cottrell equation, which defines the current–time dependence for linear diffusion control. The final bias potential is determined such that the baseline current generated from electrolyte oxidation or reduction is minimized. This yields a better signal-to-noise ratio since the majority of background noise is from the electrolyte baseline. The Cottrell equation describes how the current, $i(t)$decays as a function of time, t

$$i(t) = nFAC\left(\frac{D}{\pi}\right)^{\frac{1}{2}} t^{-1/2} \qquad (1)$$

where n is the number of electrons appearing in half-reaction for the redox couple, F is Faraday's constant (96,485 C/mol), A is the electrode area (cm^2), C is the concentration of analyte (mole/L), D is the analyte's diffusion coefficient (cm^2/s), $\pi = 3.14159$, and t is the time the current was measured in amperes. The current decays as the reciprocal of the square root of time increases. This dependence on the square root of time reflects the fact that physical diffusion is responsible for the transport of the analyte to the electrode surface. The Cottrell plot is a straight-line graph plotted as $i(t)$ vs. $t^{-1/2}$ and can be used to determine concentration, the working electrode area, or an analyte's diffusion coefficient.

Cycling Enzymatic Amplification Using HRP and TMB

Horseradish peroxidase (HRP) is one of the most widely used enzymes for analytical purposes because its high kinetic rate maximizes enzymatic signal amplification. By converting HRP-catalyzed electron transfer to an amperometric signal, the electrochemical sensor described in this method can effectively measure the number of HRP molecules immobilized on the sensor surface. Therefore, the output current is proportional to the number of molecular targets in the sample. The generalized reaction of peroxidases is an irreversible ping-pong mechanism that can be described by three sequential steps (**Figure 3**):

Step 1. The H_2O_2 in the substrate solution will first oxidize HRP into Compound I ($Fe^{IV} = O^{-II}(porphyrin)^{+}$). HRP compound I is the oxidized form of HRP after losing two electrons. In other words, HRP will lose two electrons in the presence of H_2O_2 and will then be ready to react with TMB, the mediator.

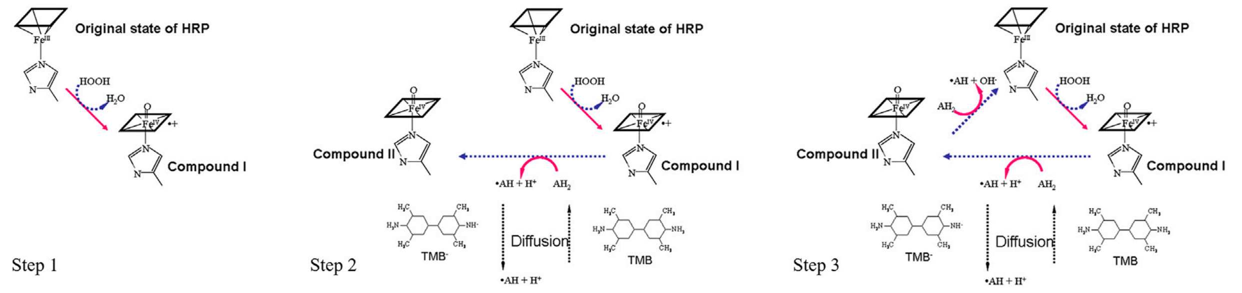

FIGURE 3 | Schematic representation of the HRP-TMB cycling enzymatic amplification.

$$Fe^{III}(porphyrin) + H_2O_2 \xrightarrow{k_1} Fe^{IV} = O^{-II}(porphyrin)^{\cdot +} + H_2O \tag{2}$$

Step 2. Oxidized HRP (Compound I) will oxidize the TMB (AH_2) in the substrate solution and turn oxidized HRP (Compound I) into Compound II ($Fe^{IV} = O^{-II}(porphyrin)H^{+}$). Concurrently, the oxidized TMB (AH) concentration will be increased and the amount will be proportional to the concentration of the analyte (16S rRNA) present. Neutral TMB is illustrated as AH_2 and oxidized TMB is illustrated as AH in the following schematics.

$$\begin{aligned} Fe^{IV} = O^{-II}(porphyrin)^{\cdot +} + AH_2 \xrightarrow{k_2} Fe^{IV} \\ = O^{-II}(porphyrin)H^{+} + AH^{\cdot} \end{aligned} \tag{3}$$

Step 3. Compound II ($Fe^{IV} = O^{-II}(porphyrin)H^{+}$) will also oxidize the TMB (AH_2) and return to the original state of HRP. This step will not only increase the concentration of oxidized TMB ($AH^{\cdot}$) but will also bring the HRP to its original state, making it ready to go back to Step 1 and react with H_2O_2 again. With sufficient TMB and H_2O_2, HRP can continuously be "recycled" and produce abundant oxidized TMB ($AH^{\cdot}$), which is the reactant to be measured by chronoamperometry.

$$\begin{aligned} Fe^{IV} = O^{-II}(porphyrin)H^{+} + AH_2 \xrightarrow{k_3} Fe^{III}(porphyrin) + AH^{\cdot} \\ + H_2O \end{aligned} \tag{4}$$

Molecular Quantification of 16S rRNA

Electrochemical detection of 16S rRNA was performed as previously described from thiolated capture probes immobilized on photolithographically prepared gold electrode arrays with modifications (Gau et al., 2001; Sun et al., 2005; Mach et al., 2011). The detection strategy of the electrochemical-based sensors was based on sandwich hybridization of capture and detector oligonucleotide probes with target 16S rRNA in the lysate. The sensor response was evaluated with a sandwich-type hybridization assay, using FITC as a tracer in the detector probe and anti-FITC-horseradish peroxidase (HRP) as the reporter molecule. 3,3′5,5′-tetramethylbenzidine (TMB)-H_2O_2 was the selected substrate for the electrochemical-based cycling enzymatic amplification measurement of the activity of the captured HRP reporter. The electrochemical sensor assay provided an amperometric readout of the concentration of rRNA present in a sample. Capture and detector probe pairs were designed to hybridize to species- and group-specific regions of the 16S rRNA molecule that are accessible to independent hybridization with oligonucleotide probes on each sensor (**Figure 4**). The analytical performance of the multiplex electrochemical biosensor was previously investigated to demonstrate comparable signal reporting between a species-specific probe, such as the *E. coli* (EC) probe pair, and a group-specific probe, such as the *Enterobacterales* (EB) probe pair, which was a previous version of the EB/KE1 pair (Gao et al., 2017). The EB/KE1 probe pair and sensor chip configuration illustrated in **Figure 4A** was used for all presented experiments.

Antibiotic Stripwells

Stripwells were prepared as previously described by drying antibiotics in DI water with 0.1% Tween onto EIA/RIA 8-well strips (Corning, Corning, NY) such that resuspension of these reagents with 100 μL of bacterial inoculum resulted in the final working concentrations for each antibiotic, or concentrations on or near the CLSI breakpoints of selected antibiotics (CLSI, 2009; Altobelli et al., 2017). The first well of each stripwell was left without antibiotic to be used as a growth control (GC). The dual-dilution antibiotic stripwell configurations used in this study are shown in **Figure 4**.

Blood and Urine Sample Collection

We used BD 367884 Vacutainer Lithium Heparin tubes and BD 364954 Vacutainer® Plus C&S Preservative tubes for blood and urine samples, respectively. These specimen collection tubes with the same physical dimensions were selected to allow our future lab automation system to accommodate multiple specimen types. Remnant blood and urine specimens used for preparing contrived samples were confirmed negatives. Specimens were collected under a Non-Human Subject Research determination without consent (45 CFR 46 exemption 4) under the approved New York-Presbyterian/Queens Institutional Review Board and joint master agreement.

Bacterial Strains

Strains tested in this study included clinically relevant organisms with MIC values on or near the susceptible and resistant breakpoints of each antibiotic. Specifically, these organisms

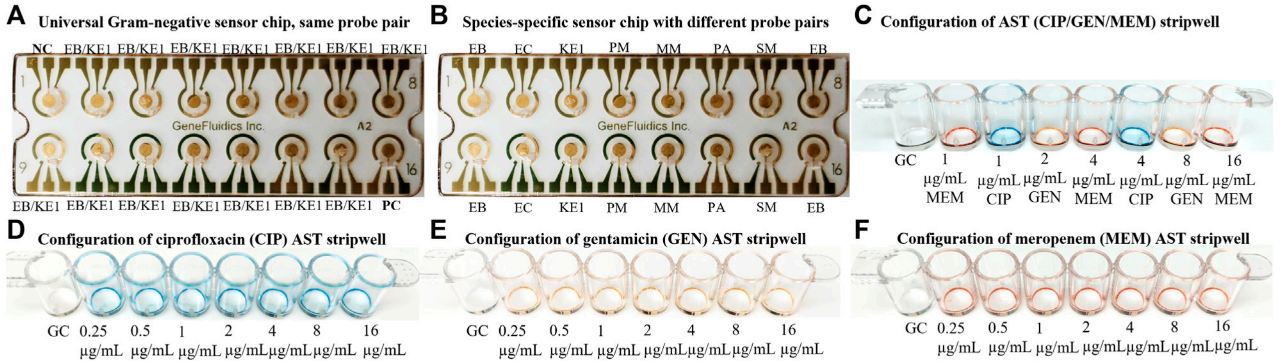

FIGURE 4 | (A) Sensor configuration of the same probe pair (EB/KE1 for most clinically relevant Gram-negative strains including *Enterobacterales* and *Pseudomonas aeruginosa*. EB capture probe: 5′-ACTTTATGAGGTCCGCTTGCTCT-3′, EB detector probe: 5′-CGCGAGGTCGCCTTCCTTTGTAT-3′, KE1 capture probe: 5′-GCACTTTATGAGGTCCGCTTGCTCT-3′, KE1 detector probe: 5′-CGCGAGGTCGCTTCTCTTTGTATGC-3′) for measurement of 16S rRNA from the same species with different conditions such as calibration curve and antimicrobial responses. **(B)** Sensor configuration of different probe pairs for detection of species-specific 16S rRNA of a polymicrobial sample. NC stands for Negative Control and PC stands for Positive Control. Additional probe pairs (EC, KE1, MM, PA, SM) can be added for a customized panel for *Escherichia coli*, *Pseudomonas aeruginosa*, *Serratia marcescens*, *Morganella morganii*, *Klebsiella pneumoniae*, *Klebsiella oxytoca*, *Enterobacter cloacae*, *Klebsiella aerogenes,* and *Citrobacter freundii* to quantify 16S rRNA content individually. **(C, D)** Example of two configurations of antibiotic stripwells to be used in this study. **(E, F)** Additional configurations of antibiotic stripwells.

included *Enterobacter cloacae, Escherichia coli, Klebsiella aerogenes, and Klebsiella pneumoniae.* Isolates used to prepare contrived samples were obtained from the CDC AR Bank and American Type Culture Collection (ATCC).

Whole Blood Direct Pathogen ID Assay

Two sets of 24 0.5-ml blood samples were contrived at 2 and 6 CFU/ml, after which 1.5 ml of RBC lysis buffer were added to each sample and incubated at room temperature for 9 min. Samples were then spun at 10,000 RPM for 5 min, and 1.8 ml of supernatant were removed and replaced with RBC lysis buffer. The samples were then incubated for 9 min at room temperature. Samples were spun again with the same conditions and 1.6 ml of supernatant were removed and replaced with cation-adjusted Mueller-Hinton II (MH) broth. After a 5-h viability culture at 37°C, samples were spun with the same conditions, and 1.85 ml of supernatant were removed, leaving a 150-μL pellet. To begin lysing, 90 μL of 1M NaOH were added to each sample, followed by a 5-min incubation at room temperature. Sixty microliters of 1M HCl were then added to each sample and 10 μL of lysate from each sample were added to their respective sensors on the sensor chips. All sensor chips were hybridized for 30 min at 43°C. After washing and drying each chip, 10 μL of HRP enzyme were added to all sensors, followed by a 5-min incubation at room temperature. Sensor chips were then washed and dried again, and 40 μL of TMB were added to each sensor. After a 30-s incubation at room temperature, an electrochemical reading of each sensor chip was performed.

Matrix Removal Protocol and Inoculum Preparation for Direct-AST

Urine samples of 4-ml starting volume were spun down to remove the majority of matrix components in the supernatant as previously described (Chen et al., 2021b). After the initial 15-min spin at 4,000 RPM, 3.5 ml of supernatant were removed, followed by the addition of 3.5 ml of MH broth to the remaining 0.5-ml pellet. Urine samples were then spun again with the same conditions after which 3 ml of supernatant were removed, leaving a 1-ml volume to make a 1X inoculum. Samples were then diluted by adding 3.2 ml of MH broth to 0.2 ml of the 1X sample to create a 0.06X inoculum.

AST From Clinical Isolates and Directly From Urine Specimens

The same AST assay was performed for clinical isolates and urine specimens with the exception of sample preparation and stripwell inoculation steps (Chen et al., 2021c). Clinical isolate suspensions were diluted to 7×10^6 CFU/ml and delivered to each well of their corresponding stripwells (100 μL per well). Urine samples were prepared with the matrix removal protocol described above. Following the matrix removal and inoculum preparation steps, the 1X and 0.06X inoculum were added to their respective wells in the antibiotic stripwell. Specifically, 100 μL of 1X were added to the first four wells and 100 μL of 0.06X were added to the last four wells. The AST assay was the same for both clinical isolates and urine samples from this point. Stripwells were incubated for 2 h at 37°C for antibiotic exposure, after which the lysing procedure began. Thirty-six microliters of 1M NaOH were added to each well, followed by a 5-min incubation at room temperature. Next, 24 μL of 1M HCl were added to each well, after which 15 μL of lysed sample, or lysate, from each well were delivered to their corresponding sensors on one sensor chip (two sensors per well). All sensor chips underwent hybridization for 30 min at 43°C. Sensor chips were then washed and dried, and 10 μL of enzyme were delivered to each sensor. Following a 5-min enzyme incubation at room temperature, sensor chips were washed

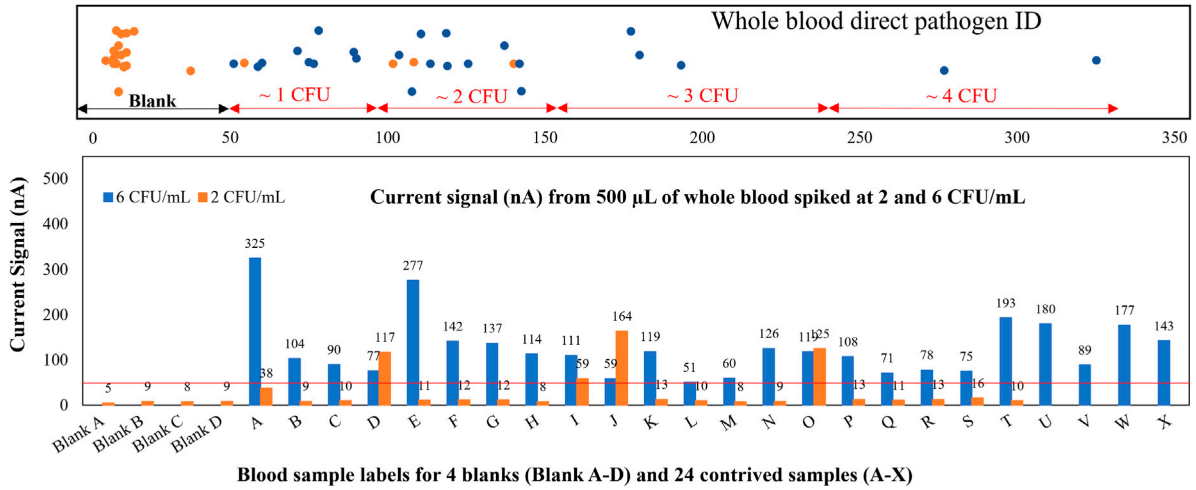

FIGURE 5 | Whole blood direct pathogen ID. Gram-negative samples spiked at 2 and 6 CFU/ml, assay results reflect the probability inherent in spiking a 0.5-ml whole blood sample at approximately 2 CFU/ml.

and dried again. Forty microliters of TMB were then added to each sensor, followed by an electrochemical reading of the sensor chip.

RESULTS

Limit of Detection of Direct Whole Blood ID

To demonstrate the ability to detect low-abundant pathogens (<10 CFU/ml for blood) directly from limited whole blood for point-of-care applications or neonatal patients without using polymerase chain reaction (PCR) amplification, we contrived 24 whole blood samples at 2 and 6 CFU/ml of *E. coli* and took only 500 µL of blood to test on our sensors. Statistically, a large percentage of these contrived 500-µL samples should contain no pathogen at all, while some samples have 1 and very few of them have 2. As shown in **Figure 5**, only 4 out of 24 samples contrived at 2 CFU/ml tested positive, 1 of which indicated ~1 CFU (sample I) and 3 of which indicated 2 CFU (samples D, J, O). These results agreed with our hypothesis. Signal ranges for each CFU count were confirmed with agar plating. Specifically, a duplicate set of all contrived samples were plated with 10 agar plates (100 µL per plate) and counted the following day. In a LoD verification experiment based on FDA guidelines, all 24 whole blood samples contrived at 6 CFU/ml tested positive. The spiked concentration was verified by plating 1 ml of the original sample on blood agar. The total assay time was 6.5 h, and the LoD was confirmed to be 6 CFU/ml with all positive signals well above the limit of blank with just 500 µL of whole blood. The electrochemical signal distribution for all samples contrived at 2 and 6 CFU/ml is shown at the top of **Figure 5**. The LoD can be further improved by taking larger blood volumes (2–8 ml) and/or utilizing a longer viability culture time as demonstrated previously (Chen et al., 2021d).

Transition From Categorical AST (S, I, and R), Minimum Inhibitory Concentration (MIC), to Direct-AST Reporting

Validation of microbiological responses to antibiotic exposure was performed with a panel of Gram-negative clinical isolates from the CDC AR bank and ATCC against ciprofloxacin, gentamicin, and meropenem as shown in **Figure 6**. Isolate suspensions were diluted to 7 × 10^6 CFU/ml and cultured in MH broth in antibiotic stripwells. The listed MIC for each antimicrobial in the table below each graph in **Figures 6A–D** was verified by CLSI microdilution or published by the CDC or ATCC, and the corresponding antimicrobial susceptibility category is in parentheticals. Electrochemical signals from each antimicrobial condition were normalized to that of the GC well, resulting in a GC ratio. Low GC ratios indicated inhibited microbial growth or a susceptible response to the antibiotic conditions. High GC ratios suggested uninhibited growth or resistance to antibiotics. Our electrochemical sensor assay demonstrated categorical agreement with the listed susceptibility for all four samples against ciprofloxacin and gentamicin. However, only 3 out of 4 samples exhibited categorical agreement, and 1 sample (**Figure 6B**) exhibited essential agreement (only one 2-fold dilution off) against meropenem.

The presented direct-AST protocol was evolved from a recently developed clinical specimen transportation method and molecular test based on the sequence-specific transcriptional responses of causative bacteria to antibiotic exposure directly from clinical urine specimens from NYPQ (Kung et al., 2021). The following content is from a previous publication of our stripwell protocol (Chen et al., 2021e). **Figure 7** and relevant content were included in the aforementioned publication as part of the method validation results: "To verify that our AST stripwells were functionalized with the desired antibiotic concentrations, we performed the

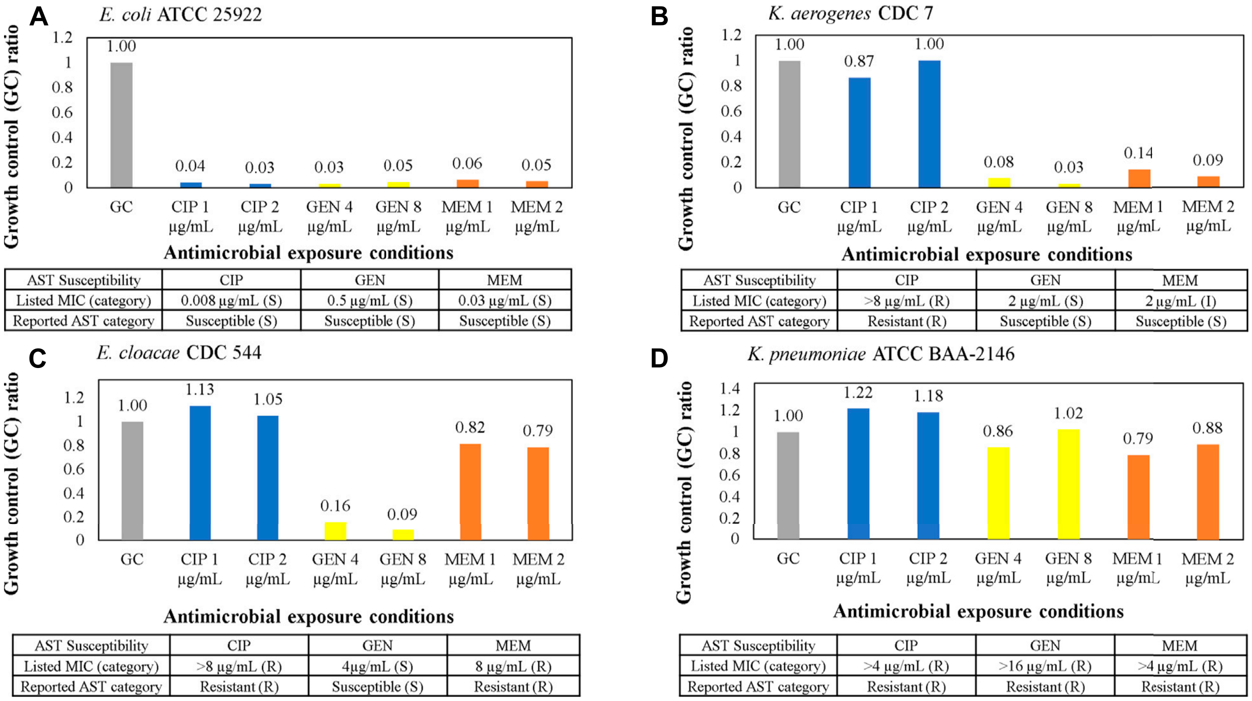

A

AST Susceptibility	CIP	GEN	MEM
Listed MIC (category)	0.008 µg/mL (S)	0.5 µg/mL (S)	0.03 µg/mL (S)
Reported AST category	Susceptible (S)	Susceptible (S)	Susceptible (S)

B

AST Susceptibility	CIP	GEN	MEM
Listed MIC (category)	>8 µg/mL (R)	2 µg/mL (S)	2 µg/mL (I)
Reported AST category	Resistant (R)	Susceptible (S)	Susceptible (S)

C

AST Susceptibility	CIP	GEN	MEM
Listed MIC (category)	>8 µg/mL (R)	4µg/mL (S)	8 µg/mL (R)
Reported AST category	Resistant (R)	Susceptible (S)	Resistant (R)

D

AST Susceptibility	CIP	GEN	MEM
Listed MIC (category)	>4 µg/mL (R)	>16 µg/mL (R)	>4 µg/mL (R)
Reported AST category	Resistant (R)	Resistant (R)	Resistant (R)

FIGURE 6 | (A–D) AST assay from clinical isolates using the AST stripwell in **Figure 4C**. Microbiological response from each condition for ciprofloxacin, gentamicin, and meropenem AST stripwells with antibiotic concentrations on or near breakpoints. The microbiological response is plotted as growth control (GC) ratios, or electrochemical signal levels in nano amperes normalized to that of the GC.

broth microdilution reference method as described in CLSI M07 (CLSI, 2009). Strains from the CDC AR Bank with different MICs for each antibiotic were suspended in Mueller-Hinton II broth and diluted to a concentration of 5 × 10^5 CFU/ml for testing. Stripwells were inoculated with bacterial samples (100 µL per well) and incubated for 16–20 h at 37°C. After this incubation period, the reference stripwells were visually checked for microbial growth inhibition. Wells with turbid inoculum indicated microbial growth, suggesting that the antibiotic condition for that particular well was ineffective against the bacteria. Wells with clear inoculum indicated microbial growth inhibition suggesting the antibiotic condition for that well was effective against the bacteria. The concentration of the first well to exhibit complete growth inhibition was compared to the strain's MIC as listed on the CDC AR Bank website. [**Figure** 7] below shows the microdilution results for AST and one-drug stripwells, as well as the results of an electrochemical biosensor assay quantifying 16S rRNA content of the inoculum in each well after the 3-h antimicrobial exposure."

After demonstrating in **Figure 7** that we can recover and detect clinically relevant microbial loads by varying the antibiotic exposure configuration, we designed the early version of our direct AST assay (Chen et al., 2021d). In this preceding version, we developed an algorithm for determining the MIC by identifying the maximum GC ratio reduction in 16S rRNA quantification over a spectrum of antimicrobial exposure conditions. Rather than using one stripwell as shown in **Figures 6**, **7**, we used two antibiotic stripwells inoculated with clinical specimens at the original concentration (1X) and at a 10-fold dilution (0.1X) to widen the spectrum of antimicrobial exposure conditions, thus, introducing the first dual-dilution configuration to be simplified in the presented study. Urine samples of various microbial loads ranging from 10^5 to 10^8 CFU/ml were tested with the earlier version of the direct-AST assay, which also included a matrix removal step and a 2-h antimicrobial exposure in MH broth (Chen et al., 2021c; Chen et al., 2021d). Similarly to the AST assay performed in **Figure 6**, the categorical susceptibility was determined by utilizing GC ratios in a microbiological response plot against a series of 2-fold dilutions of the antibiotic. The dual-dilution kinetics corresponded to the greatest change in slope of both 1X and 0.1X response curves. The first level of analysis was qualitative, whereby the maximum inhibitory antimicrobial condition derived from the maximum GC ratio reduction was compared to the corresponding antibiotic susceptibility results (R, I, S) from the clinical microbiology lab or CLSI reference methods. The electrochemical current reading of our potentiostat reader is set to saturate at 10,000 nA to maximize the resolution at lower current readings around the limit of detection, so the reading would be saturated if the starting microbial load were too high (>10^8 CFU/ml). This phenomenon was observed in the 10^7 and 10^8 CFU/ml samples. The reported inhibitory antimicrobial concentration or bug-to-drug ratio was adjusted down for every antibiotic concentration reported saturated at 10,000 nA and rounded up to the closest breakpoint,

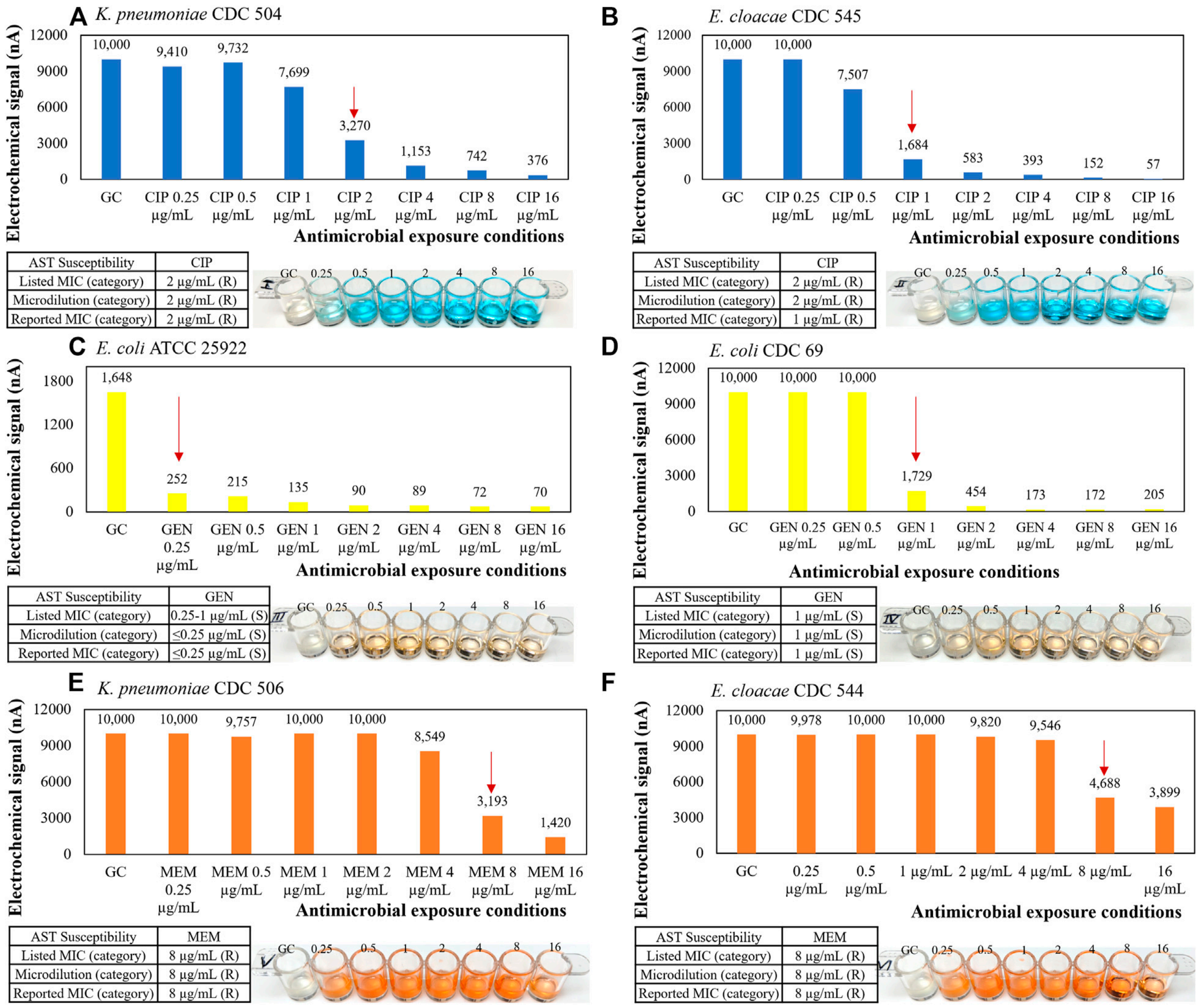

A

AST Susceptibility	CIP
Listed MIC (category)	2 µg/mL (R)
Microdilution (category)	2 µg/mL (R)
Reported MIC (category)	2 µg/mL (R)

B

AST Susceptibility	CIP
Listed MIC (category)	2 µg/mL (R)
Microdilution (category)	2 µg/mL (R)
Reported MIC (category)	1 µg/mL (R)

C

AST Susceptibility	GEN
Listed MIC (category)	0.25-1 µg/mL (S)
Microdilution (category)	≤0.25 µg/mL (S)
Reported MIC (category)	≤0.25 µg/mL (S)

D

AST Susceptibility	GEN
Listed MIC (category)	1 µg/mL (S)
Microdilution (category)	1 µg/mL (S)
Reported MIC (category)	1 µg/mL (S)

E

AST Susceptibility	MEM
Listed MIC (category)	8 µg/mL (R)
Microdilution (category)	8 µg/mL (R)
Reported MIC (category)	8 µg/mL (R)

F

AST Susceptibility	MEM
Listed MIC (category)	8 µg/mL (R)
Microdilution (category)	8 µg/mL (R)
Reported MIC (category)	8 µg/mL (R)

FIGURE 7 | Representative AST results with microbiological response plotted in electrochemical signal levels in nano amperes for **(A, B)** ciprofloxacin, **(C, D)** gentamicin, and **(E, F)** meropenem one-drug stripwells with 3-h antimicrobial exposure and corresponding CLSI microdilution result with 16–20-h antimicrobial exposure as a reference.

so the susceptibility reporting based on the inhibitory antimicrobial concentration of combined responses from both dilutions would be adjusted accordingly as described above.

A Dual-Dilution Response Curve Library for Direct-From-Specimen AST

The previous dual-dilution configuration was designed to expand the bug-to-drug ratio spectrum by using two one-drug stripwells (**Figure 4E**), one for 1X and one for 0.1X, to cover the clinically relevant microbial load range and CLSI R and S breakpoints defined at the reference inoculum concentration of 5 × 10^5 CFU/ml. In the new configuration shown in **Figure 8**, we changed the inoculum dilution from 0.1X to 0.06X to consolidate the antimicrobial spectrum tested and use only one stripwell rather than two. A set of 3 representative strains (R, I, S) for gentamicin was used to generate a preliminary abbreviated response curve library as shown in **Figure 8**. The dynamic microbial range was initially set to 3 orders of magnitude (10^5 to 10^8) CFU/ml for urine). With the gentamicin concentrations indicated in **Figure 8E** and the dual-dilution of the microbial load, the corresponding bug-to-drug ratio spectrum was 2.5 × 10^7 to 3.68 × 10^2 CFU/µg as shown in **Figure 8F**, covering both reference R and S breakpoints (bug-to-drug ratios at 3.125 × 10^4 and 1.25 × 10^5 CFU/µg) at the high and low ends of the microbial dynamic range. As detailed in **Figure 8F**, the bug-to-drug ratio in wells 6, 7, and 8 are similar to those in wells 2, 3, and 4 for the microbial load that is 10 times lower in order to observe microbiological trends with similar bug-to-drug ratios at different microbial loads; we designed the spectrum as such to widen the antibiotic coverage for any unknown microbial load within the target dynamic range. For example, when looking at the I strain with a gentamicin MIC of 8 µg/ml, the signal levels from wells 6, 7, and 8 of 10^7 CFU/ml (**Figure 8B**) were 1,317.59, 396.03, and

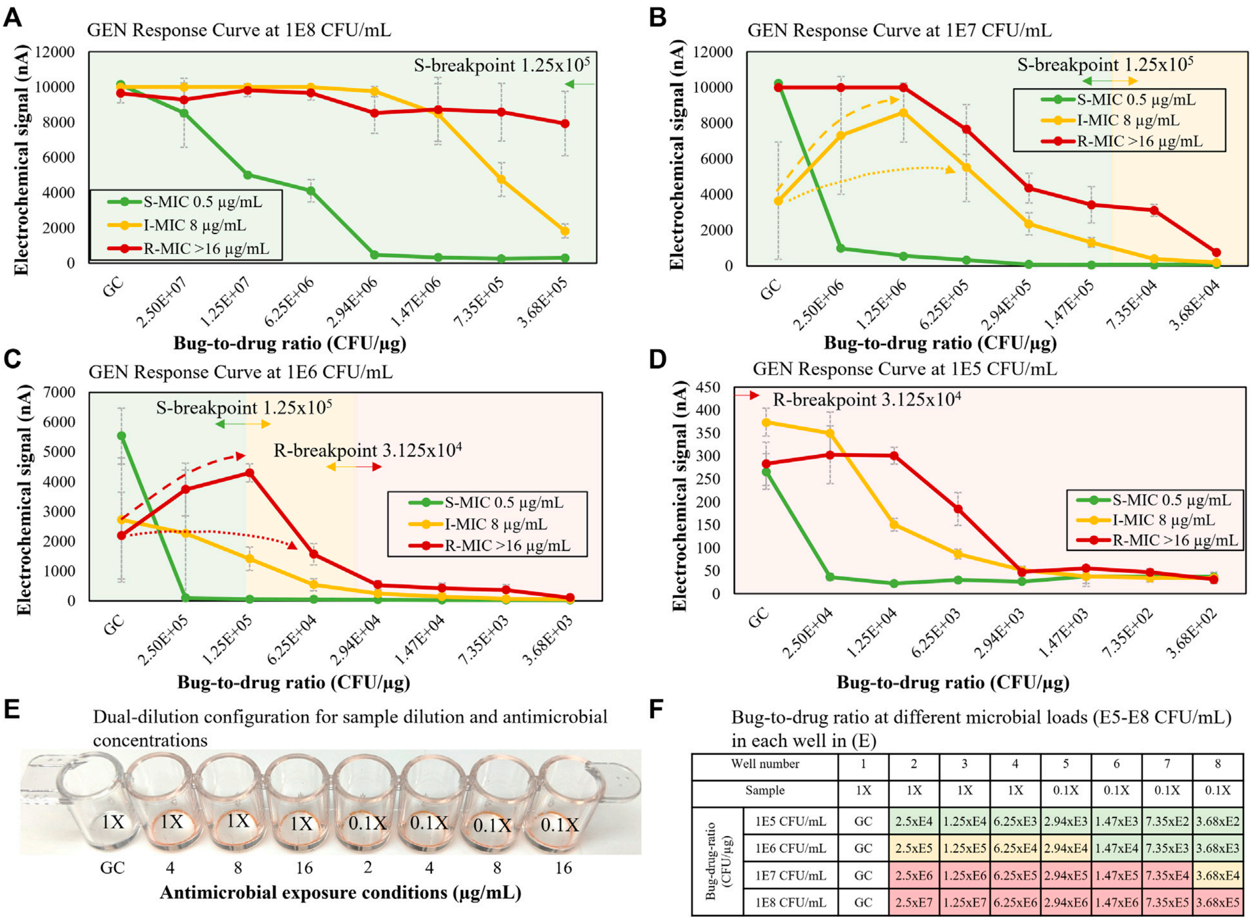

Well number		1	2	3	4	5	6	7	8
Sample		1X	1X	1X	1X	0.1X	0.1X	0.1X	0.1X
Bug-drug-ratio (CFU/µg)	1E5 CFU/mL	GC	2.5xE4	1.25xE4	6.25xE3	2.94xE3	1.47xE3	7.35xE2	3.68xE2
	1E6 CFU/mL	GC	2.5xE5	1.25xE5	6.25xE4	2.94xE4	1.47xE4	7.35xE3	3.68xE3
	1E7 CFU/mL	GC	2.5xE6	1.25xE6	6.25xE5	2.94xE5	1.47xE5	7.35xE4	3.68xE4
	1E8 CFU/mL	GC	2.5xE7	1.25xE7	6.25xE6	2.94xE6	1.47xE6	7.35xE5	3.68xE5

FIGURE 8 | (A–D) Gentamicin S, I, R response curves for microbial loads of 10^5–10^8 CFU/ml. **(E)** Stripwell configuration used for the dual-dilution microbial response curves shown in **(A–D)**. **(F)** Bug-to-drug ratios for different microbial loads from 10^5 to 10^8 CFU/ml with relation to S and R breakpoints. Green cells represent bug-to-drug ratios lower than an inoculum concentration of 5 × 10^5 CFU/ml with the S breakpoint antimicrobial concentration. Red cells represent bug-to-drug ratios higher than an inoculum concentration of 5 × 10^5 CFU/ml with the R breakpoint antimicrobial concentration. Yellow cells represent intermediate microbial responses between S and R breakpoints.

181.20 nA; those from wells 2, 3, and 4 of 10^6 CFU/ml (**Figure 8C**) were 2,995.91, 1415.58, and 541.08 nA. Signal levels from wells 2, 3, and 4 in **Figure 8C** were higher because the inoculum concentration (1X of 10^6 CFU/ml) was higher than that of **Figure 8B** (0.06X of 10^7 CFU/ml). If each well was normalized to the GC level, the resulting GC ratios would be 0.83, 0.39, and 0.15 for **Figure 8C** and 0.27, 0.08, and 0.04 for **Figure 8B**. Although the GC ratio drop was more apparent in wells 2, 3, and 4 in **Figure 8C**, a similar decreasing trend was observed in both **Figures 8B,C**. The larger GC ratio drop observed in **Figures 8B,C** was due to the inoculum concentration of 10^6 CFU/ml, which is closer to the load of 7 × 10^6 CFU/ml used in our previous AST assay from clinical isolates designed to match CLSI breakpoints. We observed a sudden increase in rRNA synthesis caused in part by antibiotic exposure in the R strain in **Figure 8B** and the I strain in **Figure 8C** (dashed arrows) as described by the literature (Starosta et al., 2014; Vargas-Blanco and Shell, 2020). For curves exhibiting this type of response, the current algorithm calibrated the response signature (dashed lines) to the dotted lines using the GC signal as illustrated in **Figures 8B,C**. **Figures 8A-D** were used as the signature library to interpretate susceptibility of blinded samples in the next portion of the study. Bacterial strain information and GC ratios for each condition in **Figure 8** may be found in **Supplementary Table S1**.

Contrived Blinded Samples

Negative urine samples were contrived by a different operator with 4 different microbial conditions (three monomicrobial S, I, and R strains and one polymicrobial with a different susceptibility profile), resulting in 4 blinded samples. The microbial response curves of the blinded samples using the dual-dilution configuration are shown in **Figure 9**. As shown below, we first estimated the microbial load of each blinded sample by comparing the GC signal level to set of previously generated calibration curves of configurable microbial quantification protocols with varying total assay times and LoDs for a range of 4 to 3 × 10^8 CFU/ml (Chen et al., 2021d). Their resulting curves were each matched to a set of signature curves. After determining the load, we identified consecutive inhibited or non-

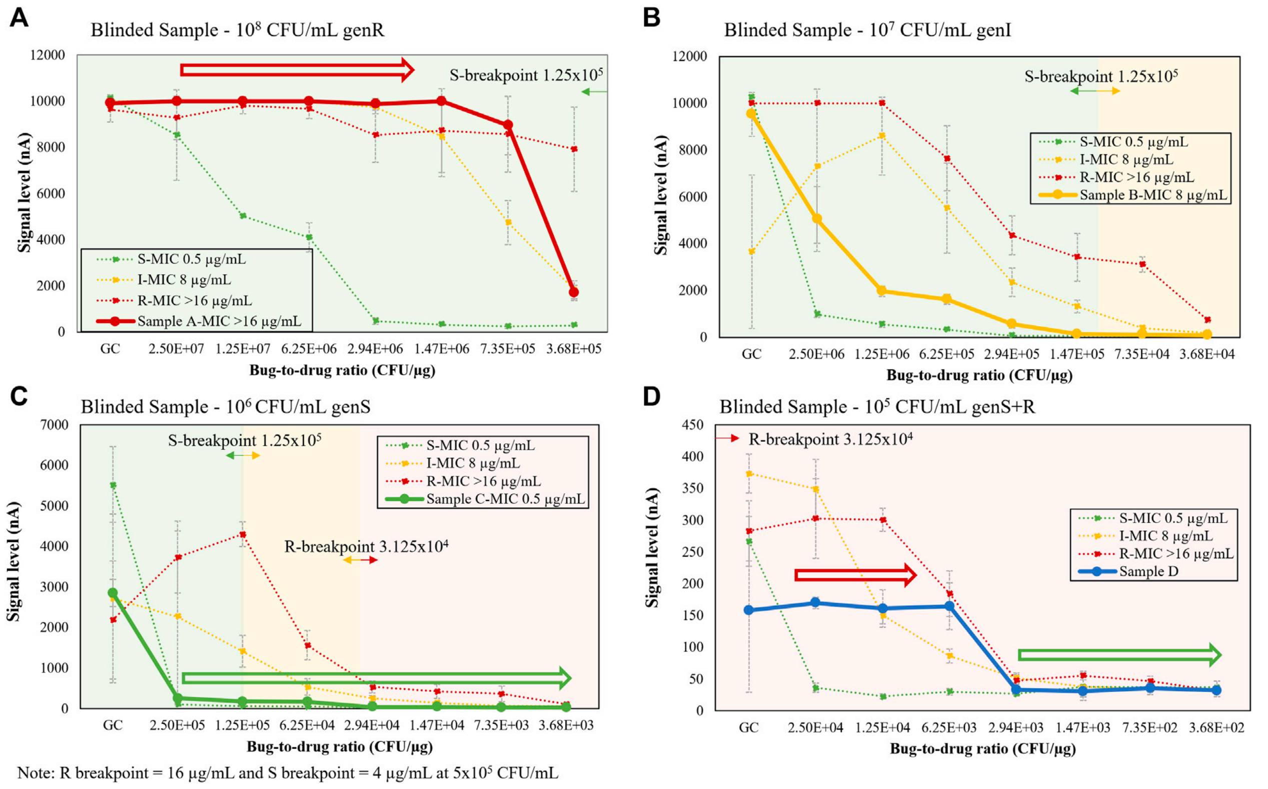

FIGURE 9 | (A–D) Single response curve for blinded samples (solid lines), including polymicrobial, S, I, and R strains, shown on top of 10^5-10^8 CFU/mL signature response library (dotted lines) from **Figure 8**. Each strain in the polymicrobial sample was contrived at 10^5 CFU/mL.

inhibited growth trends (hollow arrows), or lack thereof, and matched the result curve to the reference curve (dotted lines) sharing the most data points or trends. Based on this analysis, all 4 blinded samples were reported correctly. **Figures 9A,C** exhibited non-inhibited and inhibited growth, respectively, indicating S and R susceptibility. **Figure 9B** did not exhibit distinct inhibited or non-inhibited growth characteristics, and the curve pattern was between I and S reference curves, indicating an intermediate response. The polymicrobial sample in **Figure 9D** had both inhibited (green hollow arrow) and non-inhibited growth (red hollow arrow), indicating at least one S and one R population. Bacterial strain information and GC ratios for each condition in **Figure 9** may be found in **Supplementary Table S2**.

DISCUSSION

Developments in the field of rapid AST platforms have been slow over the past decade (Van Belkum and Dunne, 2013; van Belkum et al., 2019; Pulido et al., 2013), most likely due to suboptimal sensitivity and specificity and long time to result, as many clinical studies have shown that a delay in adequate antibiotic treatment for severe infections may increase mortality (Liu et al., 2017). Despite a certain level of automation achieved in recent decades, obtaining AST results in modern clinical laboratories still requires more than 10 h following bacterial isolation (Van Belkum and Dunne, 2013). As a result, one to 3 days of delay occur between the initiation of empirical antimicrobial therapy and the AST result. Therefore, a stand-alone AST method would be ideal to reduce the time to result. From a basic microbiological perspective, a stand-alone AST method needs to address the challenges of unknown pathogen identity and microbial load and be able to adapt to the fast-changing understanding of current antibiotic resistance mechanisms, the discovery of new mechanisms, epidemiological aspects, variation of the growth-associated lag time, and heterogeneity of resistance. The presented method aims to address these challenges by utilizing a biosensor to perform AST directly from unprocessed clinical specimens. Biosensors can be categorized by the reactant that they measure after the recognition event. Specifically, biosensor types include optical (light), bioluminescent (photons), thermal (heat), mass (resonance frequency changes), and electrochemical (electron transfer). While each of these types has inherent strengths and weaknesses, optical and electrochemical biosensors have become the most widely used. Although optical biosensors have been adopted throughout clinical diagnostics and life science research due to their speed and sensitivity, most still require the use of target amplification such that the signal is enhanced to a measurable level. Of these amplification methods, real-time PCR has emerged as the most widely adopted and is now considered the gold standard for the detection of nucleic acids from a variety of origins. Our method utilizes electrochemical biosensors due to their superior speed and selectivity at a low cost. Historically, however, electrochemical biosensors have lacked sufficient sensitivity for use beyond glucose monitoring and clinical chemistry analysis. Unlike previously reported electrochemical sensors that used graphite or carbon electrodes, a single layer of gold (Au) is used in this method for all three electrodes, i.e., working, auxiliary, and reference electrodes. Typically, Ag/AgCl or a saturated calomel electrode (SCE) is used as the reference electrode so that reversible oxidation/reduction occurs at a fixed potential at the reference electrode. In contrast, Au is used as the reference electrode in this method because its malleability and durability simplify fabrication and allow for extremely thin electrodes. In this particular application, where the reduction of a mediator is monitored, Au can be successfully used as the reference electrode because a low voltage difference is maintained for short periods of time. The Au/Au/Au electrode system is characterized by cycling enzymatic amplification and targets are measured by amperometry (Gau et al., 2005). The high turnover number of mediated HRP-TMB redox-cycling amplification replaces the need for nucleic acid amplification, and the antifouling properties of the casein coating on all electrodes enable direct-from-specimen detection with a baseline level that is less than 50 nA (Liao et al., 2007; Pan et al., 2010).

The major challenges of conventional electrochemical-based biosensors are lack of detection sensitivity and interference with matrix components from unprocessed specimens, therefore most electrochemical detection methods only report qualitative measurement of high abundant analytes, not quantification of extremely low abundant analytes ($<10^5$ CFU/ml for urine and <10 CFU/ml for blood) directly from specimens. However, in the presented study, we were able to detect as low as one single colony in 0.5 ml of whole blood (**Figure 5**) by removing matrix interferents at the start of the assay. Furthermore, we were able to perform categorical susceptibility and MIC reporting of clinical isolates in **Figures 6**, **7** by generating microbial response curves of electrochemical signal levels in nano amperes (nA) with an elaborated one-drug stripwell. With this method, we then established a dual-dilution signature for direct-from-urine AST and a library of response curves at different microbial loads in **Figure 8**. The feasibility of the direct-from-specimen AST with unknown microbial loads, susceptibility, or species was demonstrated with blinded contrived urine samples with S, I, and R susceptibility to gentamicin, as well as a polymicrobial sample consisting of microorganisms with different susceptibilities in **Figure 9**.

The LoD is the lowest concentration at which analyte can be detected 95% of the time (a 5% likelihood of a false negative). Alternatively stated, the LoD is the true value where the likelihood of a false negative measurement is 5%. The much smaller blood volume (200–500 μL) required for point-of-care or pediatric applications introduces a new dilemma of a compromised LoD. Even with the successful identification of just 1 bacterium in 500 μL of whole blood, the best LoD is 6 CFU/ml, which seems to be inferior to the 1 CFU/ml LoD criteria for adult sepsis with a 10-ml blood sample. In the preliminary evaluation of detecting whole blood contrived at 2 CFU/ml, only 4 out of 24 (16.7%) 0.5-ml samples were reported positive above the limit of blank (LoB) of 50 nA from the electrochemical current quantification. While most 2 CFU/ml samples were reported negative, the signal levels of the positive samples suggested one sample each harbored 1 or 2 colonies. One goal of this study was to achieve the best clinical sensitivity and specificity to identify all blood borne pathogens in 200–500 μL blood volume in less than 8 h. Uropathogens usually appear in high abundance ($>10^8$ CFU/ml), so the total assay time for direct-from-urine pathogen ID can be as short as 2 h (data not shown).

The removal of interfering matrix components in blood or urine and a comparison of microbial responses from different drug-to-bug ratios can enable antimicrobial susceptibility reporting in hours directly from unprocessed specimens instead of days from clinical isolates as demonstrated in **Figures 8**, **9**. The presented direct-AST reports Resistant (R), Intermediate (I), and Susceptible (S) results correlated to CLSI breakpoints and MICs determined by CLSI methodology used in traditional AST. In **Figures 8**, **9**, we established a library of microbiological signatures from a range of microbial loads with an electrochemical-based molecular analysis platform and demonstrated robust performance when validated in three representative susceptibility categories covering R, I, and S. The detection method described utilizes dual-dilution kinetic curves and automatable molecular quantification of species-specific 16S rRNA through the use of an electrochemical sensor to assess microbiological responses to antibiotic exposure.

Limitations and Future Plan–We have demonstrated the feasibility of a direct-ID/AST assay, which we plan to further optimize and validate. The presented study included a select group of antibiotics, species, and susceptibilities; therefore, we will expand the antibiotic panel, target species, and polymicrobial conditions. We will also test different contrived concentrations of representative pathogens to match the microbial loads and polymicrobial combinations in adult blood and urine for evaluating microbial recovery rate. Additionally, we tested only Gram-negative bacteria due to the lack of an important outer membrane layer in Gram-positive bacteria that is present in Gram-negative bacteria, making Gram-positive organisms less resistant to most antibiotics than Gram-negative ones (Breijyeh et al., 2020). Therefore, we plan to scale up the species-specific probe pairs for both Gram-positive and Gram-negative bacteria to cover clinically relevant organisms and antibiotic selections for each infection site and increase the clinical utility and commercial value. Finally, the presented method is intended to be automated to reduce the workload and hands-on time for ID and AST. Once automated, a future study with a much larger sample size of prospectively collected specimens in a clinical trial is needed to cover the most common causative pathogens in blood and urine specimens found in clinical settings.

DATA AVAILABILITY STATEMENT

The original contributions presented in the study are included in the article/**Supplementary Material**, further inquiries can be directed to the corresponding author.

AUTHOR CONTRIBUTIONS

JC, ENa, and ENu were responsible for generating all data presented in figures. JC and VG were responsible for drafting and editing the article for submission.

FUNDING

VG received funding from the following institutions to support the research reported in the described study: National Institute of Allergy and Infectious Diseases, Award Number: RO1AI117059; Eunice Kennedy Shriver National Institute of Child Health and Human Development, Award Number: R44HD084033. As a non-academic, commercial company, the employer and funder provided support in the form of salaries for authors, but did not have any additional role in the study design, data collection and analysis, decision to publish, or preparation of the article.

SUPPLEMENTARY MATERIAL

The Supplementary Material for this article can be found online at: https://www.frontiersin.org/articles/10.3389/fbioe.2021.744198/full#supplementary-material

REFERENCES

Altobelli, E., Mohan, R., Mach, K. E., Sin, M. L. Y., Anikst, V., Buscarini, M., et al. (2017). Integrated Biosensor Assay for Rapid Uropathogen Identification and Phenotypic Antimicrobial Susceptibility Testing. *Eur. Urol. Focus* 3 (2-3), 293–299. doi:10.1016/j.euf.2015.12.010

Anhalt, J. P., and Fenselau, C. (1975). Identification of Bacteria Using Mass Spectrometry. *Anal. Chem.* 47, 219–225. doi:10.1021/ac60352a007

Breijyeh, Z., Jubeh, B., and Karaman, R. (2020). Resistance of Gram-Negative Bacteria to Current Antibacterial Agents and Approaches to Resolve it. *Molecules* 25 (6), 1340. doi:10.3390/molecules25061340

Chakravorty, S., Helb, D., Burday, M., Connell, N., and Alland, D. (2007). A Detailed Analysis of 16S Ribosomal RNA Gene Segments for the Diagnosis of Pathogenic Bacteria. *J. Microbiol. Methods* 69 (2), 330–339. doi:10.1016/j.mimet.2007.02.005

Charretier, Y., Dauwalder, O., Franceschi, C., Degout-Charmette, E., Zambardi, G., Cecchini, T., et al. (2015). Rapid Bacterial Identification, Resistance, Virulence and Type Profiling Using Selected Reaction Monitoring Mass Spectrometry. *Sci. Rep.* 5, 13944. doi:10.1038/srep13944

Chen, J., San, S. S. S., Kung, A., Tomasek, M., Liu, D., Rodgers, W., et al. (2021). Direct-from-specimen Microbial Growth Inhibition Spectrums under Antibiotic Exposure and Comparison to Conventional Antimicrobial Susceptibility Testing (Accessed July 14, 2021). doi:10.1101/2021.02.12.430910

Chen, J., Tomasek, M., Cruz, A., Faron, M. L., Liu, D., Rodgers, W. H., et al. (2021). Feasibility and Potential Significance of Rapid *In Vitro* Qualitative Phenotypic Antimicrobial Susceptibility Testing of Gram-Negative Bacilli with the ProMax System. *PLoS One* 16 (3), e0249203. doi:10.1371/journal.pone.0249203

Chen, J., Tomasek, M., and Gau, V. (2021). Categorizing Microbial Growth Inhibition through Quantification of 16S rRNA Growth Marker with Stripwells Covering a Spectrum of Antimicrobial Conditions. *MethodsX* 8, 101453. doi:10.1016/j.mex.2021.101453

Chen, J., Tomasek, M., Nuñez, E., and Gau, V. (2021). Method for Concentrating Viable Microorganisms for Microbial Load Determination and Eliminating Uncertainty from Matrix Effects from Urine and Whole Blood. *MethodsX* 8, 101451. doi:10.1016/j.mex.2021.101451

Chen, J., Tomasek, M., Nuñez, E., and Gau, V. (2021). Phenotypic Microbial Response to Antimicrobial Exposure Conditions with a Molecular Analysis Quantification of Species-specific 16S rRNA Content. *MethodsX* 8, 101468. doi:10.1016/j.mex.2021.101468

CLSI (2009). *Methods for Dilution Antimicrobial Susceptibility Tests for Bacteria that Grow Aerobically; Approved Standard—Eighth Edition. CLSI Document M07-A8.* Wayne, PA: Clinical Laboratory Standards Institute.

D'amato, R. F., Holmes, B., Bottone, E. J., and Tilton, R. C. (1981). The Systems Approach to Diagnostic Microbiology. *CRC Crit. Rev. Microbiol.* 9, 1–44. doi:10.3109/10408418109104485

Gao, J., Jeffries, L., Mach, K. E., Craft, D. W., Thomas, N. J., Gau, V., et al. (2017). A Multiplex Electrochemical Biosensor for Bloodstream Infection Diagnosis. *SLAS TECHNOLOGY: Translating Life Sci. Innovation* 22 (4), 466–474. doi:10.1177/2211068216651232

Gau, J. J., Lan, E. H., Dunn, B., Ho, C. M., and Woo, J. C. (2001). A MEMS Based Amperometric Detector for *E. coli* Bacteria Using Self-Assembled Monolayers. *Biosens. Bioelectron.* 16 (9-12), 745–755. doi:10.1016/s0956-5663(01)00216-0

Gau, V., Ma, S.-C., Wang, H., Tsukuda, J., Kibler, J., and Haake, D. A. (2005). Electrochemical Molecular Analysis without Nucleic Acid Amplification. *Methods* 37 (1), 73–83. doi:10.1016/j.ymeth.2005.05.008

Han, Y.-Y., Lin, Y.-C., Cheng, W.-C., Lin, Y.-T., Teng, L.-J., Wang, J.-K., et al. (2020). Rapid Antibiotic Susceptibility Testing of Bacteria from Patient's Blood via Assaying Bacterial Metabolic Response with Surface-Enhanced Raman Spectroscopy. *Sci. Rep.* 10 (1), 12538. doi:10.1038/s41598-020-68855-w

Jones, A. E., and Puskarich, M. A. (2014). The Surviving Sepsis Campaign Guidelines 2012: Update for Emergency Physicians. *Ann. Emerg. Med.* 63 (1), 35–47. doi:10.1016/j.annemergmed.2013.08.004

Kung, A., Chen, J., Tomasek, M., Liu, D., Rodgers, W., and Gau, V. (2021). Transportation Protocols for Accurate Assessment of Microbial burden Classification Using Molecular Methods. *Sci. Rep.* 11, 16069. doi:10.1038/s41598-021-95619-x

Liao, J. C., Mastali, M., Li, Y., Gau, V., Suchard, M. A., Babbitt, J., et al. (2007). Development of an Advanced Electrochemical DNA Biosensor for Bacterial Pathogen Detection. *J. Mol. Diagn.* 9 (2), 158–168. doi:10.2353/jmoldx.2007.060052

Liu, D., Gau, V., Tomasek, M., Chen, J., Singh, V., Memmer, M., et al. (2020). Evaluation of an Automated rRNA Quantitation System for Rapid AST in Clinical Lab diagnosticsAssociation for Molecular Pathology 2020 Annual Meeting Abstracts. *J. Mol. Diagn.* 22 (11 Suppl. l), S28. doi:10.1016/S1525-1578(20)20513-410.1016/s1525-1578(20)30513-4

Liu, V. X., Fielding-Singh, V., Greene, J. D., Baker, J. M., Iwashyna, T. J., Bhattacharya, J., et al. (2017). The Timing of Early Antibiotics and Hospital Mortality in Sepsis. *Am. J. Respir. Crit. Care Med.* 196, 856–863. doi:10.1164/rccm.201609-1848OC

Mach, K. E., Mohan, R., Baron, E. J., Shih, M.-C., Gau, V., Wong, P. K., et al. (2011). A Biosensor Platform for Rapid Antimicrobial Susceptibility Testing Directly from Clinical Samples. *J. Urol.* 185 (1), 148–153. doi:10.1016/j.juro.2010.09.022

May, L., Cosgrove, S., L'Archeveque, M., Talan, D. A., Payne, P., Jordan, J., et al. (2013). A Call to Action for Antimicrobial Stewardship in the Emergency Department: Approaches and Strategies. *Ann. Emerg. Med.* 62 (1), 69–77. doi:10.1016/j.annemergmed.2012.09.002

Menozzi, M. G., Eigner, U., Covan, S., Rossi, S., Somenzi, P., Dettori, G., et al. (2006). Two-center Collaborative Evaluation of Performance of the BD phoenix Automated Microbiology System for Identification and Antimicrobial Susceptibility Testing of Gram-Negative Bacteria. *J. Clin. Microbiol.* 44, 4085–4094. doi:10.1128/JCM.00614-06

Pan, Y., Sonn, G. A., Sin, M. L. Y., Mach, K. E., Shih, M.-C., Gau, V., et al. (2010). Electrochemical Immunosensor Detection of Urinary Lactoferrin in Clinical Samples for Urinary Tract Infection Diagnosis. *Biosens. Bioelectron.* 26 (2), 649–654. doi:10.1016/j.bios.2010.07.002

Pulido, M. R., García-Quintanilla, M., Martín-Peña, R., Cisneros, J. M., and McConnell, M. J. (2013). Progress on the Development of Rapid Methods for Antimicrobial Susceptibility Testing. *J. Antimicrob. Chemother.* 68, 2710–2717. doi:10.1093/jac/dkt253

Soriano-Lerma, A., Pérez-Carrasco, V., Sánchez-Marañón, M., Ortiz-González, M., Sánchez-Martín, V., Gijón, J., et al. (2020). Influence of 16S rRNA Target Region on the Outcome of Microbiome Studies in Soil and Saliva Samples. *Sci. Rep.* 10 (1), 13637. doi:10.1038/s41598-020-70141-8

Starosta, A. L., Lassak, J., Jung, K., and Wilson, D. N. (2014). The Bacterial Translation Stress Response. *FEMS Microbiol. Rev.* 38 (6), 1172–1201. doi:10.1111/1574-6976.12083

Sun, C.-P., Liao, J. C., Zhang, Y.-H., Gau, V., Mastali, M., Babbitt, J. T., et al. (2005). Rapid, Species-specific Detection of Uropathogen 16S rDNA and rRNA at Ambient Temperature by Dot-Blot Hybridization and an Electrochemical Sensor Array. *Mol. Genet. Metab.* 84 (1), 90–99. doi:10.1016/j.ymgme.2004.11.006

Timbrook, T. T., Caffrey, A. R., Ovalle, A., Beganovic, M., Curioso, W., Gaitanis, M., et al. (2017). Assessments of Opportunities to Improve Antibiotic Prescribing in an Emergency Department: A Period Prevalence Survey. *Infect. Dis. Ther.* 6, 497–505. doi:10.1007/s40121-017-0175-9

van Belkum, A., Bachmann, T. T., Bachmann, T. T., Lüdke, G., Lisby, J. G., Kahlmeter, G., et al. (2019). Developmental Roadmap for Antimicrobial Susceptibility Testing Systems. *Nat. Rev. Microbiol.* 17, 51–62. doi:10.1038/s41579-018-0098-9

Van Belkum, A., and Dunne, W. M., Jr. (2013). Next-generation Antimicrobial Susceptibility Testing. *J. Clin. Microbiol.* 51, 2018–2024. doi:10.1128/JCM.00313-13

Vargas-Blanco, D. A., and Shell, S. S. (2020). Regulation of mRNA Stability during Bacterial Stress Responses. *Front. Microbiol.* 11, 2111. doi:10.3389/fmicb.2020.02111

Welker, M. (2011). Proteomics for Routine Identification of Microorganisms. *Proteomics* 11, 3143–3153. doi:10.1002/pmic.201100049

Conflict of Interest: As authors of this study (JC, ENa, ENu, VG), we declare that we are employed by GeneFluidics, a nonacademic, commercial company.

frontiers
in Bioengineering and Biotechnology

ORIGINAL RESEARCH
published: 18 January 2022
doi: 10.3389/fbioe.2021.795415

Rapid Detection and Antimicrobial Susceptibility Testing of Pathogens Using AgNPs-Invertase Complexes and the Personal Glucose Meter

*Laibao Zheng**[†], *Yunqiu Shen*[†], *Wenjia Dong, Chaochuan Zheng, Ruolan Zhou and Yong-Liang Lou**

Wenzhou Key Laboratory of Sanitary Microbiology, Key Laboratory of Laboratory Medicine, Ministry of Education, School of Laboratory Medicine and Life Science, Wenzhou Medical University, Wenzhou, China

Edited by:
Yu-Jui Fan,
Taipei Medical University, Taiwan

Reviewed by:
Ponmurugan Karuppiah,
King Saud University, Saudi Arabia
Chia-Che Wu,
National Chung Hsing University, Taiwan
Zhao Chao,
Jilin University, China

***Correspondence:**
Yong-Liang Lou
lyl@wmu.edu.cn
Laibao Zheng
zhenglaibao@wmu.edu.cn

[†] *These authors have contributed equally to this work and share first authorship*

Specialty section:
This article was submitted to Biosensors and Biomolecular Electronics, a section of the journal Frontiers in Bioengineering and Biotechnology

Received: *15 October 2021*
Accepted: *16 December 2021*
Published: *18 January 2022*

Citation:
Zheng L, Shen Y, Dong W, Zheng C, Zhou R and Lou Y-L (2022) Rapid Detection and Antimicrobial Susceptibility Testing of Pathogens Using AgNPs-Invertase Complexes and the Personal Glucose Meter. Front. Bioeng. Biotechnol. 9:795415. doi: 10.3389/fbioe.2021.795415

Rapid detection of pathogens and assessment of antimicrobial susceptibility is of great importance for public health, especially in resource-limiting regions. Herein, we developed a rapid, portable, and universal detection method for bacteria using AgNPs-invertase complexes and the personal glucose meter (PGM). In the presence of bacteria, the invertase could be released from AgNPs-invertase complexes where its enzyme activity of invertase was inhibited. Then, the enzyme activity of invertase was restored and could convert sucrose into glucose measured by a commercially PGM. There was a good linear relationship between PGM signal and concentration of *E. coli* or *S. aureus* as the bacteria model with high sensitivity. And our proposed biosensor was proved to be a rapid and reliable method for antimicrobial susceptibility testing within 4 h with consistent results of Minimum Inhibitory Concentrations (MICs) testing, providing a portable and convenient method to treat infected patients with correct antibiotics and reduce the production of antibiotic-resistant bacteria, especially for resource-limiting settings.

Keywords: nanoparticle-enzyme complexes, personal glucose meter, pathogen detection, antimicrobial susceptibility testing, rapid detection

INTRODUCTION

Rapid detection of pathogens and assessment of antimicrobial susceptibility is of great importance for the treatment of infectious diseases, especially in resource-limiting regions. The well-established pathogen detection and antimicrobial susceptibility testing (AST) methods, including culture-based methods, PCR, and mass spectrometry, are classical and useful. However, long detection periods, the need for expensive instruments, and professional operation limit their application in point-of-care testing. Moreover, the lack of point-of-care testing methods for pathogens will lead to the outbreak and spread of infectious diseases (Váradi et al., 2017; Xiao et al., 2021). Therefore, rapid and sensitive detection and AST method for pathogens are still in urgent need.

Thanks to the development of nanotechnology, various colorimetric, fluorescent, and electrochemical biosensors have been developed for rapid and sensitive detection of pathogenic bacteria using functionalized nanomaterials, such as gold/silver nanoparticles (Bi et al., 2020), carbon dots (Zheng et al., 2019a), gold/silver nanoclusters (Zheng et al., 2018; Zheng et al., 2019b; Chen et al., 2021), and magnetic nanoparticles (Wang et al., 2020b). These nanomaterials usually recognize and bind to the surface of bacteria cells through recognition elements, including antibodies (Bu et al., 2020; Wang T. et al., 2020), aptamer (Hua et al., 2018; Wang et al., 2020a), antimicrobial peptides (Pranantyo et al., 2019), and positively charged ligands (Berry et al., 2005). Unlike specific recognition elements (e.g., antibody, aptamer), positively charged ligands bind to bacteria non-specifically through electrostatic interaction, providing a versatile detection method for a wide range of bacterial strains (Phillips et al., 2008; Li et al., 2017; Wang et al., 2019). The positive-charged nanoparticles conjugated with enzymes proved to be a useful tool for bacteria detection. Cationic nanoparticles could bind to anionic enzyme through electrostatic interactions resulting in the inhibition of the enzymatic activity. While negative or neutral charged nanoparticles showed no inhibition effect towards the enzyme (Miranda et al., 2011). The surface of bacteria was negatively charged due to phosphate and carboxyl groups and could easily bind to positive-charged surfaces (Phillips et al., 2008; Ahmed et al., 2014). In the presence of bacteria, Cationic nanoparticles could bind to bacteria forming nanoparticle-bacteria conjugates and enzymes would be released from nanoparticle-enzyme complexes, resulting in the recovery of the enzymatic activity. Up to date, a few colorimetric and smell-based rapid bacteria detection methods based on nanoparticle-enzyme (e.g., β-galactosidase (β-Gal) (Miranda et al., 2011; Thiramanas and Laocharoensuk, 2016), lipase (Duncan et al., 2017), and urease (Singh et al., 2019) complexes have been reported. However, these methods are rather qualitative, and the quantitative assay is still requiring advanced instruments such as UV-vis spectrometry.

Recently, personal glucose meters (PGMs), the successful point-of-care diagnostic tools for blood glucose measurement in the medical diagnostic field for decades, are devoted to being repurposed for quantitative detection of a variety of analytical targets other than blood glucose due to they are portable, inexpensive, and quantitative. Since Lu's group first reported the portable detection of other analytical targets using PGMs, the rapid and quantitative detection of DNA (Xiang and Lu, 2011; Xiang and Lu, 2012), metal ions (Xiang and Lu, 2013; Qiu et al., 2016), and bacteria (Wang et al., 2015; Wan et al., 2016; Yang et al., 2021) using PGMs have been achieved by researchers. The glucose-generating enzyme or glucose combined with recognition elements binds to targets to generate a glucose signal, which is measured using PGMs. Antibody or aptamer as the recognition element-based sandwich biosensor were usually used for bacteria detection in PGM based method. A portable and quantitative immunochromatographic assay was reported for *E. coli* O157:H7 detection with a PGM(Huang et al., 2018). PGM-based method using aptamer as recognition and hybridization chain reaction as signal amplification strategy was developed for portable detection of *S. aureus* (Yang et al., 2021).

Herein, we developed a rapid, portable, and quantitative detection method for bacteria using AgNPs-invertase complexes and PGMs. In the AgNPs-invertase complex system, the enzyme activity of invertase was inhibited by AgNPs electrostatically bound to the invertase. However, the invertase was released and restored its enzyme activity in the presence of bacteria. Then, the active invertase could convert sucrose into glucose measured by a commercially PGM, allowing the one-pot quantitative detection of bacteria without multiple washing and rinsing steps. Our proposed biosensor provides a portable and universal method for bacteria detection. And the proof-of-concept experiments were conducted by measuring the concentration of *E. coli* after being treated with antibiotics.

MATERIALS AND METHODS

Regents and Materials

Invertase from baker's yeast (*S. cerevisiae*) was purchased from Sigma–Aldrich (St. Louis, MO, United States). Sodium citrate, tannic acid, silver nitrate, polyethyleneimine (M.w. = 1800), sucrose, MES, and other chemicals were of analytical reagent grade from Aladdin Reagent Co. Ltd (Shanghai, China). The glucose level was measured using a commercial PGM (Omnitest plus, B. Braun, Melsungen, Germany). Ultrapure water (18.2 MΩ cm) was used throughout the experiments.

Synthesis of PEI-AgNPs

The positive charged PEI-AgNPs were prepared according to the previously reported method (Singh et al., 2019). Tannic acid-capped anionic AgNPs were first synthesized by mixing tannic acid (5 mM) and sodium citrate (0.025 mM) into 50 ml water boiled along with vigorous stirring. Then 25 mM silver nitrate was added into the solution with a further reaction for 20 min. The as-prepared tannic acid-capped AgNPs were then washed twice by centrifugation at 10,000 rpm for 40 min at 4°C and adjusted OD_{400} = 1.0. To prepare PEI-AgNPs, 1 ml tannic acid capped anionic AgNPs was added into 1 ml 0.03 mg/ml PEI solution with vigorous stirring for 60 min at room temperature. The PEI-AgNPs were washed twice by centrifugation at 10,000 rpm for 40 min and adjusted to OD_{400} = 1.0 and stored at 4°C for further use.

Preparation of Bacteria

Escherichia coli (*E. coli*) and *Staphylococcus aureus* (*S. aureus*) used in our experiments were cultured in Luria–Bertani (LB) liquid media at 37°C overnight. Then the bacteria suspension was rinsed three times by centrifugation at 4,000 rpm for 5 min and diluted to the desired concentration ranging from 10 to 1.00×10^9 cfu/ml in MES buffer or tap water. The bacteria concentrations were determined using the plate counting method.

Procedures for Bacteria Detection

AgNPs-invertase complexes were formed by mixing invertase solution (0.8 μg/ml, 30 μL) and the as-prepared PEI-AgNPs (3 μL) for 10 min. Then, 117 μL bacteria of different concentrations or MES buffer were added and incubated for 15 min at room temperature. After adding the sucrose solution (0.5 M, 50 μL), the solution was allowed to react for 20 min at 55°C, followed by measured using the PGM.

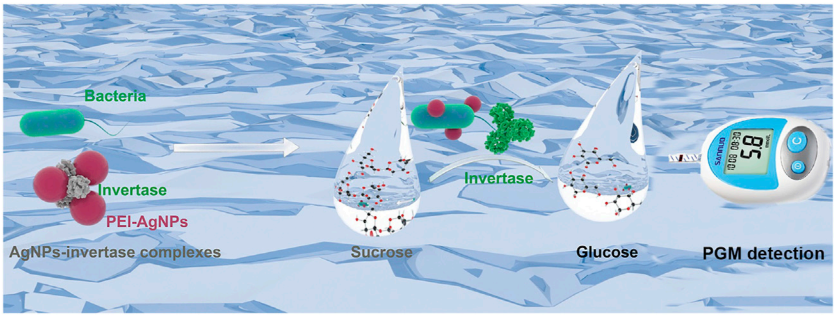

FIGURE 1 | Schematic illustration of the simple, portable, and quantitative detection method for bacteria using AgNPs-invertase complexes and PGMs.

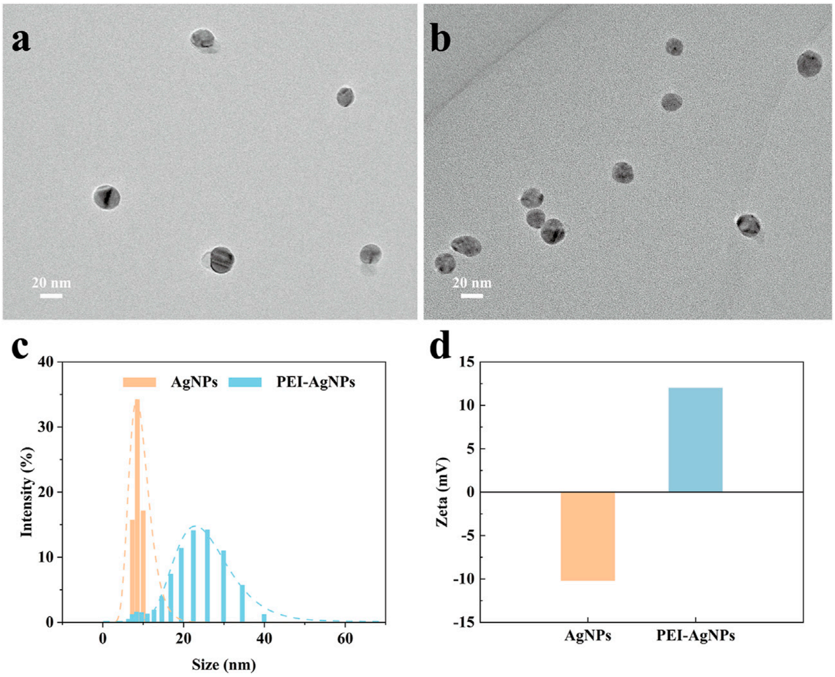

FIGURE 2 | Characterization of unmodified AgNPs and PEI-AgNPs. TEM image of unmodified AgNPs **(A)** and PEI-AgNPs **(B)**. DLS analysis **(C)** and Zeta potential **(D)** of unmodified AgNPs and PEI-AgNPs.

AST of Bacteria

The AST of *E. coli* towards four antibiotics (colistin, spectinomycin, streptomycin, tetracycline) were confirmed using Minimum Inhibitory Concentrations (MICs) testing according to Clinical and Laboratory Standard Institute (Cockerill et al., 2012). Briefly, the suspensions of *E. coli* at a concentration of 0.5 McFarland were diluted 1,000 times with Mueller Hinton Broth and then treated with different concentrations of antibiotics from 0 to 64 μg/ml. For the traditional method, the MIC values are determined by the lowest concentration of antibiotics without visible growth after incubation for 18–24 h at 37°C. Using our proposed method, the bacteria suspension incubated for 5 h was measured to evaluate the antimicrobial susceptibility of *E. coli*.

RESULTS

Detection Principle

The detection principle of our designed potable and sensitive biosensor for bacteria detection using nanoparticle-enzyme complexes and the PGM is schematically illustrated in **Figure 1**. The biosensor combines three main components: 1) invertase, an anionic enzyme, to provide signal amplification and convert sucrose into glucose measured by PGMs; 2) sucrose, a catalytic substrate of invertase; 3) PEI-AgNPs, a cationic nanoparticle, which could recognize bacteria and reversibly bind to invertase, inhibiting the catalytic activity. The catalytic activity of invertase is inhibited without denaturation by forming AgNPs-invertase complexes through electrostatic interaction.

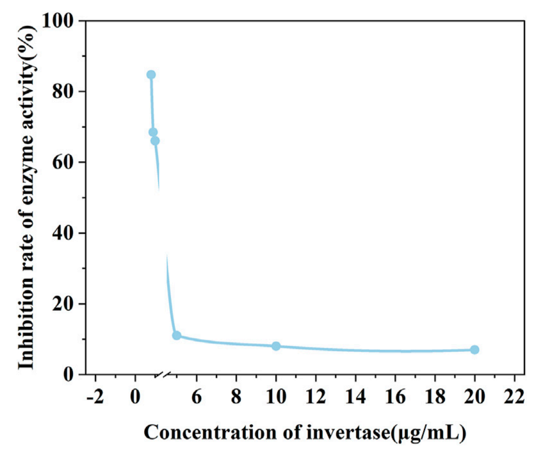

FIGURE 3 | The enzyme activity of AgNPs-invertase complexes with different concentrations of invertase.

However, in the presence of bacteria, the cationic AgNPs competitively bind to the anionic surface of bacteria to displace the invertase with the recovery of enzyme activity. The active invertase converts sucrose into glucose, which could be measured by a commercially PGM. Thus, the concentration of bacteria could be quantified using a PGM.

Feasibility Study

Before the feasibility study of our biosensor, PEI-AgNPs were well synthesized according to the previously reported research (Singh et al., 2019). As shown in **Figure 2**, TEM images of unmodified AgNPs (**Figure 2A**) and PEI-AgNPs (**Figure 2B**) were well dispersed with similar sizes. However, after modification with PEI, the obtained PEI-AgNPs showed a larger radius of hydration than unmodified AgNPs according to the DLS analysis (**Figure 2C**). And as shown in **Figure 2D**, the Zeta potential changed from −10.2 mV (unmodified AgNPs) to +12 mV (PEI-AgNPs). The results indicated the successful synthesis of positive charged PEI-AgNPs and the synthesis condition was optimized by changing the concentration of PEI (**Supplementary Figure S1**). And the DLS and zeta potential change of PEI-AgNPs and AgNPs-invertase complexes indicate the success of AgNPs-invertase complexes (**Supplementary Figure S2**). Next, we optimized the concentration of invertase to form AgNPs-invertase complexes to inhibit the enzyme activity. When the concentration of AgNPs was fixed, the inhibition rate of enzyme activity deserves to decrease with the concentration of invertase increasing. As shown in **Figure 3**, the inhibition rate reaches the highest when the concentration of invertase is 0.8 μg/ml. Theoretically, the inhibition rate should continue to increase as the concentration of invertase is below 0.8 μg/ml. However, the glucose concentration could not be detected by the PGM when the concentration of invertase is less than 0.8 μg/ml within 20 min. Thus, 0.8 μg/ml of invertase was used to form AgNPs-invertase complexes for the biosensor.

To prove the feasibility of the biosensor, the glucose signal generated under different conditions was measured using a PGM. As shown in **Figure 4**, the PGM signal of the optimized AgNPs-invertase complexes is significantly lower than that of free invertase, proving the inhibition of enzyme activity by PEI-AgNPs. And the PGM signal is recovered when *E. coli* (10^7 cfu/ml), as a model of bacteria, was added into the AgNPs-invertase complexes. Obviously, no signal was detected using AgNPs and *E. coli* alone, indicating that the AgNPs and bacteria could not catalyze the hydrolysis of sucrose into glucose. Thus, the PGM signal generated from the mixture of AgNPs-invertase complexes and *E. coli* should be attributed to the activity recovery of the invertase displaced by bacteria from AgNPs-invertase complexes. Therefore, the above results successfully demonstrated the feasibility of the proposed strategy for bacteria detection using nanoparticle-enzyme complexes and the PGM.

Optimization of Assay Conditions

To determine the optimal assay conditions of the proposed detection method, three assay parameters including the reaction time of bacteria combined with AgNPs-invertase complexes, the temperature, and pH for the catalytic activity of invertase, were investigated, since the assay performance is mostly dependent on the catalyst activity of invertase displaced by bacteria from AgNPs-invertase complexes. As the reaction time of bacteria combined with AgNPs-invertase complexes increases, the invertase released into the solution from AgNPs-invertase complexes rises, inducing that the PGM signal increases gradually and reaches a plateau after about 15 min as shown in **Figure 5A**. Since the catalytic activity and stability of invertase are greatly influenced by temperature and pH, the temperature and pH of the solution were investigated indicating the optimal temperature and pH should be 55°C and 5.0 (**Figures 5B,C**). Thus, the reaction time of 15 min for bacteria combined with AgNPs-invertase complexes, the temperature of 55°C, and pH at 5.0 was used as the optimal assay conditions for the bacteria detection procedure.

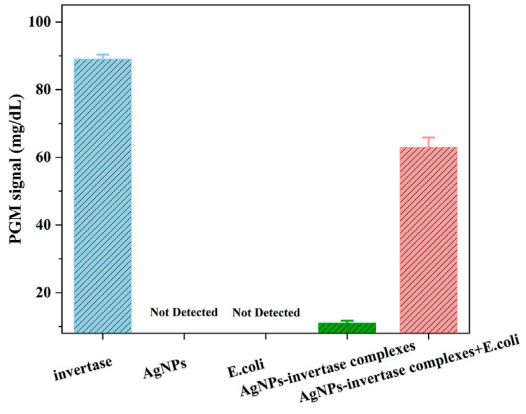

FIGURE 4 | PGM signals under different conditions: invertase, AgNPs, *E. coli*, AgNPs-invertase complexes, and AgNPs-invertase complexes + *E. coli*.

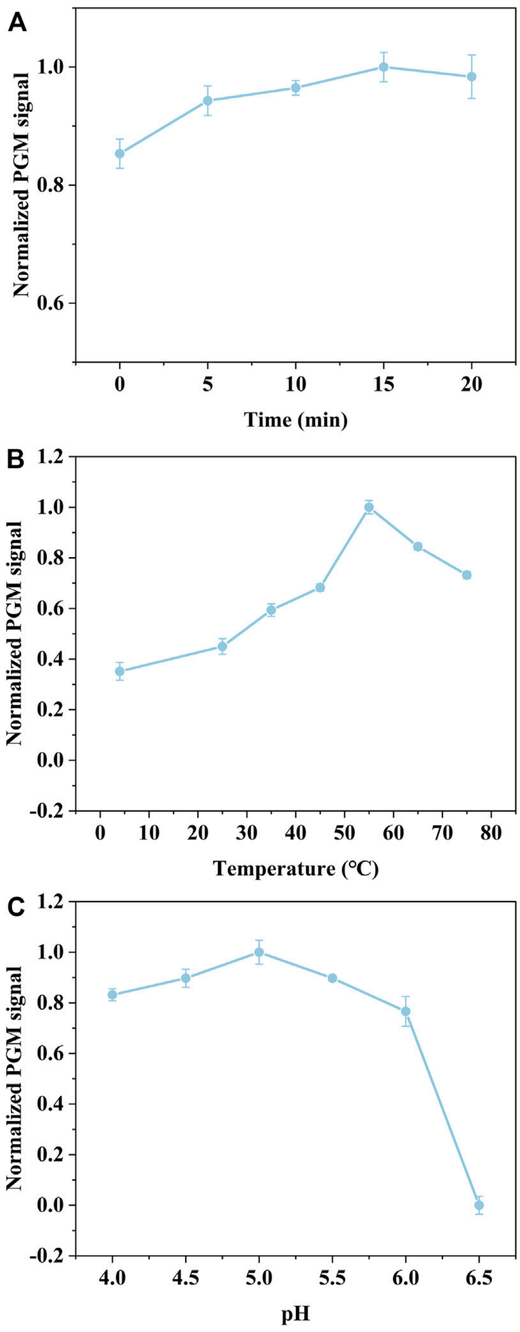

FIGURE 5 | Effect of the reaction time of bacteria combined with AgNPs-invertase complexes **(A)**. Effect of temperature **(B)** and pH **(C)** for the catalytic activity of invertase.

Detection Performances

Under the optimal assay conditions, we established a universal bacteria detection method using nanoparticle-enzyme complexes and the PGM without multiple washing and rinsing steps. To evaluate the detection performance of our proposed method, *E. coli* and *S. aureus* were selected as the model of Gram-negative bacteria and Gram-positive bacteria. After 15 min of the reaction of bacteria and the AgNPs-invertase complexes, sucrose, the catalytic substrate, was added followed by the measurement of the glucose signal using a PGM. The detection procedure is simple and portable without multiple washing and rinsing steps. There was a good linear relationship between PGM signal and concentration of *E. coli* (from 1.00×10^2 cfu/ml to 1.00×10^7 cfu/ml) or *S. aureus* (from 1.00×10^3 cfu/ml to 1.00×10^7 cfu/ml) (**Figure 6**). And the limit of detection (3σ/S) of *E. coli* and *S. aureus* are 3 cfu/ml and 7.59×10^2 cfu/ml respectively. The difference in detection sensitivity between *E. coli* and *S. aureus* may be attributed to the variety of sizes and structures of bacteria surfaces.

Real Sample Detection

To further evaluate the possibility of our proposed detection method of bacteria in real samples, the recovery test was studied by detecting the *E. coli* and *S. aureus* spiked with different concentrations in tap water. As shown in **Table 1**, the proposed method shows satisfactory recovery values ranging from 93.93 to 106.45%, with RSD values all below 2.52%, indicating the possibility of the nanoparticle-enzyme complexes and the PGM-based bacteria detection method for practical applications. However, there are many different species of bacteria in real sample, which may limit its application for detection of specific bacteria.

AST of Bacteria

To investigate the possibility of our proposed method for rapid AST, *E. coli* was chosen as a target and treated with four antibiotics (colistin, spectinomycin, streptomycin, tetracycline). After incubation with different concentrations of antibiotics for 5 h, the concentration of *E. coli* was measured with our proposed method. As shown in **Figure 7**, the PGM signal decreased with the increase of the concentration of four antibiotics. When the PGM signal is below 27.5 mg/dl, the corresponding concentration of the antibiotic is consistent with the results of MIC testing (**Table 2**). However, conventional MIC testing needs 18–24 h, which results in irrational empiric therapy and the development of bacterial drug resistance. Our proposed biosensor was demonstrated to be a rapid and reliable method for AST.

DISCUSSION

Antibiotic resistance is becoming one of the major challenges for global health (D'Costa et al., 2011; Yelin and Kishony, 2018). The number of people who died from infections with antibiotic-resistant pathogens will surpass cancer in 2050 if no effective measures are taken to reduce misuse and abuse of antibiotics (O'Neil, 2014). Thus, there is an urgent need for rapid bacteria detection and AST of pathogens to treat infected patients with correct antibiotics and reduce the production of antibiotic-resistant bacteria. Current culture-based AST methods usually take at least 1–2 days to get a reliable readout, which makes it difficult to choose suitable treatment in the early, often critical, stages of infection (Syal et al., 2017). As a consequence, the physician often prescribes broad-spectrum antibiotics, which increased the risk of bacterial resistance (Baltekin et al., 2017).

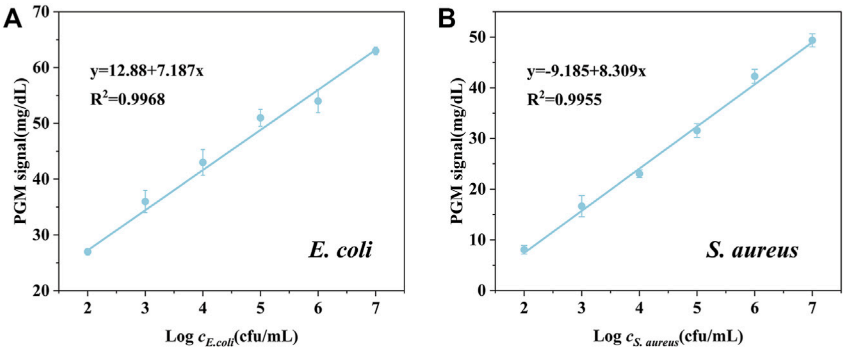

FIGURE 6 | PGM signal against the different concentrations of E. coli **(A)** and S. aureus **(B)**.

TABLE 1 | Recovery tests of *E. coli* and *S. aureus* in tap water (n = 3).

	Bacteria spiked (cfu/ml)	Bacateria found (cfu/ml)	RSD (%)	Recovery (%)
E. coli	1×10^3	0.95×10^3	0.58	94.73
	1×10^4	1.04×10^4	1.53	104.00
	1×10^5	1.06×10^5	1.15	106.45
S. aureus	1×10^3	1.13×10^3	2.52	113.33
	1×10^4	0.95×10^4	1.15	95.00
	1×10^5	0.94×10^5	1.53	93.93

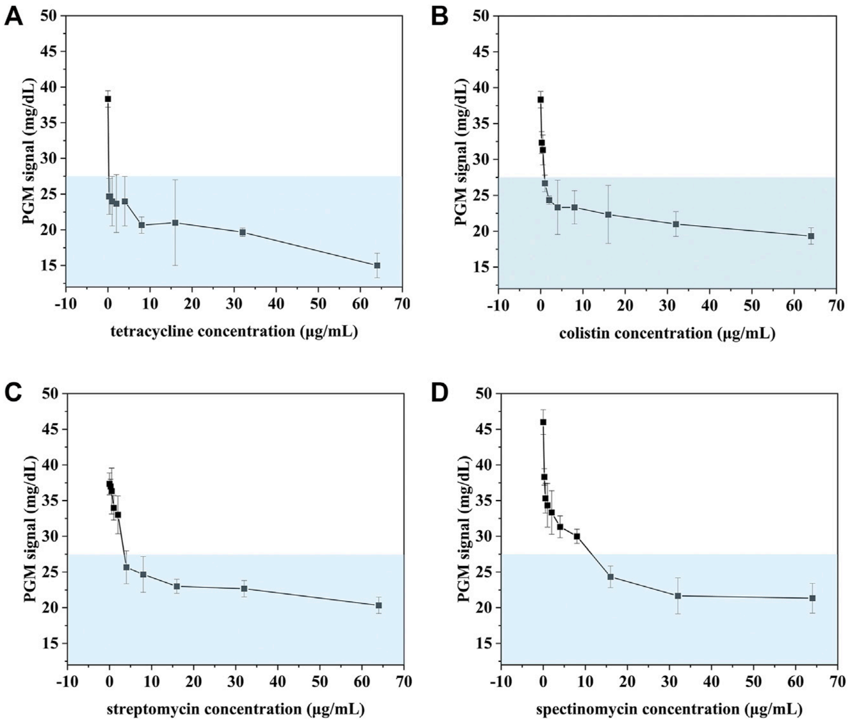

FIGURE 7 | AST of *E. coli* treated with tetracycline **(A)**, colistin **(B)**, streptomycin **(C)**, spectinomycin **(D)** detected using our proposed method.

TABLE 2 | The result of AST of *E. coli* with our proposed method and MIC.

Antibiotics	Tetracycline	Streptomycin	Colistin	Spectinomycin
Testing results (μg ml^{-1})	<0.25	4	2	>16
MIC (μg ml^{-1})	<0.25	2–4	2–4	>16

To reduce the time of AST, emerging rapid AST technologies have been developed based on fast phenotypic responses to antibiotics using flow cytometry (Gauthier et al., 2002), Roman (Yang et al., 2019), and mass spectrometry (Yi et al., 2019), or genotypes of bacteria using real-time PCR or whole-genome sequencing (Behera et al., 2019). However, the requirement of expensive instruments and experienced operators limits their application, especially in resource-limited areas. Recently, various biosensors using antibodies (Li et al., 2014) and aptamers (Jo et al., 2018) have been developed for rapid AST by monitoring bacterial growth, which is economical, convenient, and rapid. The use of antibodies and aptamers provided high selectivity, but also complexity for different pathogens through changing corresponding antibodies and aptamers. Thus, a universal bacteria detection platform is needed for the development of a rapid and easy-to-use AST method in medically underserved areas.

Herein, we proposed a universal bacteria detection method for a wide range of bacterial strains based on AgNPs-invertase complexes and PGMs using the electrostatic interactions between AgNPs and bacterial surface, unlike specific recognition elements (e.g., antibody, aptamer). The enzyme-nanoparticle complex-based bacteria colorimetric detection method was first reported by (Miranda et al., 2011) using β-Gal-AuNPs conjugate. The enzyme activity of β-Gal was inhibited by forming β-Gal-AuNPs complexes through strong electrostatic interactions. The presence of bacteria would release β-Gal from β-Gal-AuNPs complexes through competing reactions, resulting in the recovery of the enzymatic activity to catalyze CPRG into a red product. The enzyme activity of lipase and urease could be inhibited by forming lipase-AuNPs (Duncan et al., 2017) and urease-AgNPs complexes (Singh et al., 2019) through strong electrostatic interactions using positively charged nanoparticles and be released by bacteria. However, these methods are rather qualitative, or advanced instruments-required.

Recently, PGM-based biosensors were proved to be a useful tool for universal targets detection with advantages of portability, low cost, simple operation, and ease of getting. Therefore, we developed a novel AgNPs-invertase based biosensor with a PGM for bacteria detection. The invertase released from AgNPs-invertase complexes by bacteria through competing reaction could convert sucrose into glucose, measured using a PGM. Under the optimal assay conditions, there was a good linear relationship between the PGM signal and the concentration of bacteria. Furthermore, our proposed biosensor was proved to be a rapid and reliable method for AST within 4 h with consistent results of MIC testing. The rapid and non-specific detection method provides the opportunity as a universal AST method for various bacteria by monitoring the bacteria concentration treated with antibiotics. And the use of PGMs makes it a portable and convenient method to treat infected patients with correct antibiotics and reduce the production of antibiotic-resistant bacteria, especially for resource-limiting settings.

In summary, the proposed AgNPs-invertase complexes and PGMs based bacteria detection method was proved to be a rapid, portable, and universal detection method with high sensitivity and satisfied recoveries. However, the proposed method could respond to different bacteria without high selectivity which may limit its application for specific bacteria detection in real samples. The use of antibody-coated cationic nanoparticles may resolve the problem (Singh et al., 2019). Surprisingly, the result of four antibiotics towards *E. coli* are consistent with the results of MIC testing, indicating our proposed biosensor to be a rapid and reliable method for AST. Moreover, the nanoparticle-enzyme complexes-based biosensor using other surface-functionalized nanoparticles, enzymes, and portable devices could develop novel point-of-care testing methods and broaden the application towards a variety of analytes.

DATA AVAILABILITY STATEMENT

The original contributions presented in the study are included in the article/Supplementary Material, further inquiries can be directed to the corresponding authors.

AUTHOR CONTRIBUTIONS

Conceptualization, LZ; methodology, validation, and investigation, YS, WD, CZ, RZ; writing-original draft preparation, YS and WD; writing-review and editing, CZ and LZ; visualization, LZ; supervision, LZ and Y-LL. All authors have read and agreed to the published version of the manuscript.

FUNDING

This work was supported by the Zhejiang Provincial Natural Science Foundation of China under Grant No. LQ21H200008, the Science and Technology Bureau of Wenzhou under Grant No. Y2020108, National Major Infectious Disease Prevention Projects under Grant No. 2018ZX10201001-009, and The Key Discipline of Zhejiang Province in Medical Technology (First Class, Category A).

SUPPLEMENTARY MATERIAL

The Supplementary Material for this article can be found online at: https://www.frontiersin.org/articles/10.3389/fbioe.2021.795415/full#supplementary-material

REFERENCES

Ahmed, A., Rushworth, J. V., Hirst, N. A., and Millner, P. A. (2014). Biosensors for Whole-Cell Bacterial Detection. *Clin. Microbiol. Rev.* 27, 631–646. doi:10.1128/CMR.00120-13

Baltekin, Ö., Boucharin, A., Tano, E., Andersson, D. I., and Elf, J. (2017). Antibiotic Susceptibility Testing in Less Than 30 Min Using Direct Single-Cell Imaging. *Proc. Natl. Acad. Sci. USA* 114, 9170–9175. doi:10.1073/pnas.1708558114

Behera, B., Anil Vishnu, G. K., Chatterjee, S., Sitaramgupta V, V. S. N., Sreekumar, N., Nagabhushan, A., et al. (2019). Emerging Technologies for Antibiotic Susceptibility Testing. *Biosens. Bioelectron.* 142, 111552. doi:10.1016/j.bios.2019.111552

Berry, V., Gole, A., Kundu, S., Murphy, C. J., and Saraf, R. F. (2005). Deposition of CTAB-Terminated Nanorods on Bacteria to Form Highly Conducting Hybrid Systems. *J. Am. Chem. Soc.* 127, 17600–17601. doi:10.1021/ja056428l

Bi, L., Wang, X., Cao, X., Liu, L., Bai, C., Zheng, Q., et al. (2020). SERS-active Au@Ag Core-Shell Nanorod (Au@AgNR) Tags for Ultrasensitive Bacteria Detection and Antibiotic-Susceptibility Testing. *Talanta* 220, 121397. doi:10.1016/j.talanta.2020.121397

Bu, T., Yao, X., Huang, L., Dou, L., Zhao, B., Yang, B., et al. (2020). Dual Recognition Strategy and Magnetic Enrichment Based Lateral Flow Assay toward Salmonella Enteritidis Detection. *Talanta* 206, 120204. doi:10.1016/j.talanta.2019.120204

Chen, Q., Gao, R., and Jia, L. (2021). Enhancement of the Peroxidase-like Activity of Aptamers Modified Gold Nanoclusters by Bacteria for Colorimetric Detection of. *Talanta* 221, 121476. doi:10.1016/j.talanta.2020.121476

Cockerill, F. R., Wikler, M. A., Alder, J., Dudley, M. N., Eliopoulos, G. M., Ferraro, M. J., et al. (2012). *Methods for Dilution Antimicrobial Susceptibility Tests for Bacteria that Grow Aerobically*. Wayne, NJ: Clinical and Laboratory Standards Institute.

D'Costa, V. M., King, C. E., Kalan, L., Morar, M., Sung, W. W. L., Schwarz, C., et al. (2011). Antibiotic Resistance Is Ancient. *Nature* 477, 457–461. doi:10.1038/nature10388

Duncan, B., Le, N. D. B., Alexander, C., Gupta, A., Yesilbag Tonga, G., Yazdani, M., et al. (2017). Sensing by Smell: Nanoparticle-Enzyme Sensors for Rapid and Sensitive Detection of Bacteria with Olfactory Output. *ACS Nano* 11, 5339–5343. doi:10.1021/acsnano.7b00822

Gauthier, C., St-Pierre, Y., and Villemur, R. (2002). Rapid Antimicrobial Susceptibility Testing of Urinary Tract Isolates and Samples by Flow Cytometry. *J. Med. Microbiol.* 51, 192–200. doi:10.1099/0022-1317-51-3-192

Hua, R., Hao, N., Lu, J., Qian, J., Liu, Q., Li, H., et al. (2018). A Sensitive Potentiometric Resolved Ratiometric Photoelectrochemical Aptasensor for Escherichia coli Detection Fabricated with Non-metallic Nanomaterials. *Biosens. Bioelectron.* 106, 57–63. doi:10.1016/j.bios.2018.01.053

Huang, H., Zhao, G., and Dou, W. (2018). Portable and Quantitative point-of-care Monitoring of Escherichia coli O157:H7 Using a Personal Glucose Meter Based on Immunochromatographic Assay. *Biosens. Bioelectron.* 107, 266–271. doi:10.1016/j.bios.2018.02.027

Jo, N., Kim, B., Lee, S.-M., Oh, J., Park, I. H., Jin Lim, K., et al. (2018). Aptamer-functionalized Capacitance Sensors for Real-Time Monitoring of Bacterial Growth and Antibiotic Susceptibility. *Biosens. Bioelectron.* 102, 164–170. doi:10.1016/j.bios.2017.11.010

Li, B., Li, X., Dong, Y., Wang, B., Li, D., Shi, Y., et al. (2017). Colorimetric Sensor Array Based on Gold Nanoparticles with Diverse Surface Charges for Microorganisms Identification. *Anal. Chem.* 89, 10639–10643. doi:10.1021/acs.analchem.7b02594

Li, S., Cui, H., Yuan, Q., Wu, J., Wadhwa, A., Eda, S., et al. (2014). AC Electrokinetics-Enhanced Capacitive Immunosensor for point-of-care Serodiagnosis of Infectious Diseases. *Biosens. Bioelectron.* 51, 437–443. doi:10.1016/j.bios.2013.08.016

Miranda, O. R., Li, X., Garcia-Gonzalez, L., Zhu, Z.-J., Yan, B., Bunz, U. H. F., et al. (2011). Colorimetric Bacteria Sensing Using a Supramolecular Enzyme-Nanoparticle Biosensor. *J. Am. Chem. Soc.* 133, 9650–9653. doi:10.1021/ja2021729

O'Neil, J. (2014). *Review on Antibiotic Resisitance. Antimicrobial Resistance : Tackling a Crisis for the Health and Wealth of Nations*. London, United Kingdom: UK government. Available at: https://amr-review.org/sites/default/files/AMR Review Paper - Tackling a crisis for the health and wealth of nations_1.pdf.

Phillips, R. L., Miranda, O. R., You, C.-C., Rotello, V. M., and Bunz, U. H. F. (2008). Rapid and Efficient Identification of Bacteria Using Gold-Nanoparticle-Poly(para-Phenyleneethynylene) Constructs. *Angew. Chem. Int. Ed.* 47, 2590–2594. doi:10.1002/anie.200703369

Pranantyo, D., Liu, P., Zhong, W., Kang, E.-T., and Chan-Park, M. B. (2019). Antimicrobial Peptide-Reduced Gold Nanoclusters with Charge-Reversal Moieties for Bacterial Targeting and Imaging. *Biomacromolecules* 20, 2922–2933. doi:10.1021/acs.biomac.9b00392

Qiu, Z., Shu, J., Jin, G., Xu, M., Wei, Q., Chen, G., et al. (2016). Invertase-labeling Gold-Dendrimer for *In Situ* Amplified Detection Mercury(II) with Glucometer Readout and Thymine-Hg 2+ -thymine Coordination Chemistry. *Biosens. Bioelectron.* 77, 681–686. doi:10.1016/j.bios.2015.10.044

Singh, P., Kakkar, S., Bharti, B., Kumar, R., and Bhalla, V. (2019). Rapid and Sensitive Colorimetric Detection of Pathogens Based on Silver-Urease Interactions. *Chem. Commun.* 55, 4765–4768. doi:10.1039/C9CC00225A

Syal, K., Mo, M., Yu, H., Iriya, R., Jing, W., Guodong, S., et al. (2017). Current and Emerging Techniques for Antibiotic Susceptibility Tests. *Theranostics* 7, 1795–1805. doi:10.7150/thno.19217

Thiramanas, R., and Laocharoensuk, R. (2016). Competitive Binding of Polyethyleneimine-Coated Gold Nanoparticles to Enzymes and Bacteria: a Key Mechanism for Low-Level Colorimetric Detection of Gram-Positive and Gram-Negative Bacteria. *Microchim. Acta* 183, 389–396. doi:10.1007/s00604-015-1657-7

Váradi, L., Luo, J. L., Hibbs, D. E., Perry, J. D., Anderson, R. J., Orenga, S., et al. (2017). Methods for the Detection and Identification of Pathogenic Bacteria: Past, Present, and Future. *Chem. Soc. Rev.* 46, 4818–4832. doi:10.1039/C6CS00693K

Wan, Y., Qi, P., Zeng, Y., Sun, Y., and Zhang, D. (2016). Invertase-mediated System for Simple and Rapid Detection of Pathogen. *Sensors Actuators B: Chem.* 233, 454–458. doi:10.1016/j.snb.2016.04.098

Wang, L., Huo, X., Qi, W., Xia, Z., Li, Y., and Lin, J. (2020a). Rapid and Sensitive Detection of Salmonella Typhimurium Using Nickel Nanowire Bridge for Electrochemical Impedance Amplification. *Talanta* 211, 120715. doi:10.1016/j.talanta.2020.120715

Wang, L., Huo, X., Zheng, L., Cai, G., Wang, Y., Liu, N., et al. (2020b). An Ultrasensitive Biosensor for Colorimetric Detection of Salmonella in Large-Volume Sample Using Magnetic Grid Separation and Platinum Loaded Zeolitic Imidazolate Framework-8 Nanocatalysts. *Biosens. Bioelectron.* 150, 111862. doi:10.1016/j.bios.2019.111862

Wang, T., Lin, H., Wu, Y., Guo, Z., Hao, T., Hu, Y., et al. (2020c). Fast Scan Voltammetry-Derived Ultrasensitive Faraday Cage-type Electrochemical Immunoassay for Large-Size Targets. *Biosens. Bioelectron.* 163, 112277. doi:10.1016/j.bios.2020.112277

Wang, Z., Chen, Z., Gao, N., Ren, J., and Qu, X. (2015). Transmutation of Personal Glucose Meters into Portable and Highly Sensitive Microbial Pathogen Detection Platform. *Small* 11, 4970–4975. doi:10.1002/smll.201500944

Wang, Z., Yao, X., Wang, R., Ji, Y., Yue, T., Sun, J., et al. (2019). Label-free Strip Sensor Based on Surface Positively Charged Nitrogen-Rich Carbon Nanoparticles for Rapid Detection of Salmonella Enteritidis. *Biosens. Bioelectron.* 132, 360–367. doi:10.1016/j.bios.2019.02.061

Xiang, Y., and Lu, Y. (2013). An Invasive DNA Approach toward a General Method for Portable Quantification of Metal Ions Using a Personal Glucose Meter. *Chem. Commun.* 49, 585–587. doi:10.1039/c2cc37156a

Xiang, Y., and Lu, Y. (2012). Using Commercially Available Personal Glucose Meters for Portable Quantification of DNA. *Anal. Chem.* 84, 1975–1980. doi:10.1021/ac203014s

Xiang, Y., and Lu, Y. (2011). Using Personal Glucose Meters and Functional DNA Sensors to Quantify a Variety of Analytical Targets. *Nat. Chem* 3, 697–703. doi:10.1038/nchem.1092

Xiao, X., Lin, Z., Huang, X., Lu, J., Zhou, Y., Zheng, L., et al. (2021). Rapid and Sensitive Detection of Vibrio Vulnificus Using CRISPR/Cas12a Combined with a Recombinase-Aided Amplification Assay. *Front. Microbiol.* 12, 767315. doi:10.3389/fmicb.2021.767315

Yang, K., Li, H.-Z., Zhu, X., Su, J.-Q., Ren, B., Zhu, Y.-G., et al. (2019). Rapid Antibiotic Susceptibility Testing of Pathogenic Bacteria Using Heavy-Water-

Labeled Single-Cell Raman Spectroscopy in Clinical Samples. *Anal. Chem.* 91, 6296–6303. doi:10.1021/acs.analchem.9b01064

Yang, Y., Wu, T., Xu, L.-P., and Zhang, X. (2021). Portable Detection of Staphylococcus aureus Using Personal Glucose Meter Based on Hybridization Chain Reaction Strategy. *Talanta* 226, 122132. doi:10.1016/j.talanta.2021.122132

Yelin, I., and Kishony, R. (2018). Antibiotic Resistance. *Cell* 172, 1136. doi:10.1016/j.cell.2018.02.018

Yi, J., Wang, X., Dai, Y., Qiao, L., and Liu, B. (2019). Plasmonic Colloidosome-Based Multifunctional Platform for Bacterial Identification and Antimicrobial Resistance Detection. *Anal. Chem.* 91, 14220–14225. doi:10.1021/acs.analchem.9b04038

Zheng, L., Qi, P., and Zhang, D. (2018). DNA-templated Fluorescent Silver Nanoclusters for Sensitive Detection of Pathogenic Bacteria Based on MNP-DNAzyme-AChE Complex. *Sensors Actuators B: Chem.* 276, 42–47. doi:10.1016/j.snb.2018.08.078

Zheng, L., Qi, P., and Zhang, D. (2019a). Identification of Bacteria by a Fluorescence Sensor Array Based on Three Kinds of Receptors Functionalized Carbon Dots. *Sensors Actuators B: Chem.* 286, 206–213. doi:10.1016/j.snb.2019.01.147

Zheng, L., Ye, X., Qi, P., Zhang, D., and Sun, Y. (2019b). Fluorometric Detection of Sulfate-Reducing Bacteria via the Aggregation-Induced Emission of glutathione-Gold(I) Complexes. *Microchim. Acta* 186, 382. doi:10.1007/s00604-019-3427-4

Conflict of Interest: The authors declare that the research was conducted in the absence of any commercial or financial relationships that could be construed as a potential conflict of interest.

frontiers
in Bioengineering and Biotechnology

ORIGINAL RESEARCH
published: 07 March 2022
doi: 10.3389/fbioe.2022.837838

One-Step RT-qPCR for Viral RNA Detection Using Digital Analysis

Hyuna Park[1]†, Wonjong Jung[2]†, Hyeongseok Jang[2], Kak Namkoong[2]* and Kwon-Young Choi[1]*

[1]Department of Environmental Engineering, College of Engineering, Ajou University, Suwon-si, South Korea, [2]Device Research Center, Advanced Sensor Lab, Samsung Advanced Institute of Technology, Samsung Electronics Co.Ltd., Suwon-si, South Korea

Edited by:
Nan-Fu Chiu,
National Taiwan Normal University, Taiwan

Reviewed by:
Aayushi Shukla,
Swedish University of Agricultural Sciences, Sweden
Xingan Hao,
Northwest Agriculture and Forest University, China
Daoyang Sun,
Northwest A and F University, China

***Correspondence:**
Kak Namkoong
kak.namkoong@samsung.com
Kwon-Young Choi
kychoi@ajou.ac.kr

†These authors have contributed equally to this work

Specialty section:
This article was submitted to Biosensors and Biomolecular Electronics,
a section of the journal Frontiers in Bioengineering and Biotechnology

Received: *17 December 2021*
Accepted: *24 January 2022*
Published: *07 March 2022*

Citation:
Park H, Jung W, Jang H, Namkoong K and Choi K-Y (2022) One-Step RT-qPCR for Viral RNA Detection Using Digital Analysis.
Front. Bioeng. Biotechnol. 10:837838.
doi: 10.3389/fbioe.2022.837838

The rapid detection of viruses is becoming increasingly important to prevent widespread infections. However, virus detection *via* reverse transcription-quantitative polymerase chain reaction (RT-qPCR) is time-consuming, as it involves independent nucleic acid extraction and complementary DNA synthesis. This process limits the potential for rapid diagnosis and mass analysis, which are necessary to curtail viral spread. In this study, a simple and rapid thermolysis method was developed to circumvent the need for extraction and purification of viral RNA. The developed protocol was applied to one-chip digital PCR (OCdPCR), which allowed thermolysis, RT, and digital PCR in a single unit comprising 20,000 chambers of sub-nanoliter volume. Two viruses such as tobacco mosaic virus and cucumber mosaic virus were tested as model viral particles. First, the temperature, exposure time, and template concentration were optimized against tobacco mosaic viral particles, and the most efficient conditions were identified as 85°C, 5 min, and 0.01 µg/nL with a cycle threshold of approximately 33. Finally, the OCdPCR analysis yielded 1,130.2 copies/µL using 10^{-2} µg/nL of viral particles in a 30 min thermolysis-RT reaction at 70°C. This novel protocol shows promise as a quick, accurate, and precise method for large-scale viral analysis in the future.

Keywords: thermolysis, RT-qPCR, virus detection, one-chip digital PCR, multiplex detection

1 INTRODUCTION

The global spread of the coronavirus disease since late 2019 has resulted in the infection of over 190 million people worldwide, with more than 4.09 million fatalities, as of 22 July 2021 (World Health Organization, https://www.who.int). At several points during the pandemic, the number of infected individuals has rapidly increased due to small-scale infections and mutated viruses. Although recent trends have shown signs that the severity of the current pandemic is declining, there are growing concerns regarding similar situations in the future.

Along with the development of vaccines and treatments against virus, the diagnosis of viral infections using high-speed and accurate ribonucleic acid (RNA) detection assays is paramount, as various studies have reported (Brown et al., 2021; Garg and Garg, 2021; Howe et al., 2021; Ibrahimi et al., 2021; Luethy and Johnson, 2021; Van Rijn and Boonstra, 2021; Yuan et al., 2021). For example, an integrated microfluidic system with reverse transcription-polymerase chain reaction (RT-PCR) has been developed for the rapid detection of influenza A viruses (Shen et al., 2019). In addition, several assays and sensors for detection of pathogens such as virus have been developed, including quantitative RT-PCR (RT-qPCR) using loop-mediated isothermal amplification, magnetic bead-based RNA extraction for rapid large-scale testing, and electrode-based electrochemical immunosensing (Klein et al., 2020; Nagura-Ikeda et al., 2020; Fabiani et al., 2021; Taki et al., 2021). A fundamental limitation of the current diagnostic analysis methods of viral pathogens, however, is the reliance on two consecutive enzyme reactions: reverse transcription (RT), followed by polymerase chain reaction (PCR). This requires labor-intensive laboratory-based protocols to isolate viral RNAs and amplify deoxyribonucleic acid (DNA). At the laboratory level, it is difficult to achieve desirable accuracy and precision in viral RNA detection and diagnosis due to time and resource limitations. However, in a pandemic situation, allocation of necessary resources is prioritized, allowing for large-scale development of diagnostic methods.

Although RT-PCR is an accurate method for detecting viruses, certain disadvantages do exist (Van Rijn and Boonstra, 2021). The essential steps of isolating RNA from a viral sample and synthesizing complementary DNA (cDNA) through an RT reaction, then amplifying this cDNA using PCR, are routinely conducted manually (Garg and Garg, 2021; Voon et al., 2021; Yuan et al., 2021). In general, a total reaction time of at least 4 h is required to isolate viral RNA from biological samples, synthesize cDNA, and perform PCR according to the manufacturer protocols (Arevalo-Rodriguez et al., 2020; Ibrahimi et al., 2021). Moreover, conventional RT-qPCR analyses rely on 96- or 384-well plates, limiting high-throughput sample analysis in the case of mass infection. This can cause a shortage of commercial kits make and virus detection and diagnosis difficult. Additionally, the RT and PCR reactions differ in terms of optimum reaction conditions and constituents, such as solution pH, temperature, and concentration, and the buffer used. Although nucleic acid extraction and isolation kits are commercially available, they are expensive and time-consuming. For example, commercial viral RNA isolation kits require a lysis step involving chemical treatment, followed by a concentration step using an elution buffer (Li et al., 2015). This protocol limits large-scale sample analysis and rapid diagnosis (Tang et al., 2013; Abdallah et al., 2020; Ulloa et al., 2020). Additionally, the lysis buffers provided in commercial kits contain reagents such as RNase inhibitors for membrane lysis and RNA stabilization (Tosh et al., 1997; Li et al., 2015; Zucha et al., 2020). As RNA is relatively unstable during heating and hydrolysis, certain conditions can result in sample degradation by RNase, reducing the concentration of the RNA template and producing low amplification results (Campos et al., 2021; Rattanachaisit et al., 2021; Schoenmaker et al., 2021).

Due to the rapid spread of viral pathogens, precise, large-scale detection with few false positives and a high true negative rate is an important factor in diagnostic performance. Moreover, determining the precise concentration of viral RNA is the most critical factor in diagnosis, and depends on the absolute number of RNA copies in the initial analytical volume. This is challenging and limits the application of conventional RT-qPCR analysis. Therefore, a sensitive PCR technique that can analyze viral RNA with precise and repeatable outputs is required (De Boer et al., 2011). Recent digital PCR (dPCR) technology enables the precise analysis of nucleic acids, and are capable of absolute quantification of viral load regardless of the availability of reference RNA (Basu, 2017; Cristiano et al., 2021; Karon et al., 2021; Martin et al., 2021; Rattanachaisit et al., 2021; Yi Han Tan et al., 2021). dPCR can provide not only unparalleled precision by splitting the sample into tens of thousands of partitions and analyzing these each using microfluidic technology, but also low-level viral RNA detection even in the presence of inhibitors, by offering nanoscale reaction environments suitable for one-step thermolysis RT-qPCR. dPCR works by splitting a DNA or cDNA sample into several separate, parallel PCR reactions. After PCR analysis, the negative fraction can be used to generate an absolute number of target molecules in a sample, without standards or endogenous controls. Of course, the price of digital PCR equipment and consumable chips should be considered, but basically, RNA isolation and purification steps can be omitted, enabling analysis in a shorter time when RT and PCR reactions are performed in one pot. There is no need to rely on reference materials or standards, and it has the advantages of high resistance to inhibitors and excellent analysis ability for complex mixtures (Basu, 2017; Yi Han Tan et al., 2021).

A potential means to overcome common diagnostic limitations is to directly use a viral particle as an RT reaction template, bypassing the RNA isolation step. Additional treatment is necessary because the isolation of viral RNA templates for cDNA synthesis requires disruption of the viral membrane. This study presents a protocol to obtain viral RNA using simple thermolysis, in which viral RNA was directly utilized as an RT reaction template. Tobacco mosaic virus (TMV) and cucumber mosaic virus (CMV) were used as model virus particles (Knight, 1955; Du et al., 2013). Furthermore, a one-step direct RT-qPCR method was developed to detect viruses within a single PCR tube without the need for separate chemical treatment or purification. This protocol was applied to a one-chip digital PCR, which showed high accuracy and precision. As biological risks such as COVID-19 and other pathogens continue to be reported, it is necessary to prepare rapid identification protocols. This study provides an important reference for the development of rapid, precise, and high-throughput analysis methods for viral detection.

2 MATERIALS AND METHODS

2.1 Virus Information

The tobacco mosaic virus (*Tobamovirus,* Accession No. PV-000806) was isolated from *Petunia hybrida* (Niehl et al., 2014), and cucumber mosaic virus (*Cucumovirus,* Accession No. PV-000302) was isolated from *Nicotina tabacum* (NCBI:txid4097) (Alonso-Prados et al., 1998). Viral particles were provided by the Plant Virus GenBank, Seoul, South Korea.

2.2 Preparation of Leaf Samples for Pre-Treatment

Viral particles were added to a sterilized 0.01 M potassium phosphate buffer (pH 7.0) and mixed thoroughly immediately prior to use without centrifugation in order to include debris in the assay sample. Powdered viral RNA samples were used as templates for chemical purification or thermal treatment. The concentration of infected leaves was expressed in μg/nL, using the weight of dried leaves in μg/volume of phosphate buffer in nL.

2.3 Pre-Treatment of Viral Particles for RT and RT-PCR

The Viral Gene-spin™ Viral DNA/RNA Extraction Kit (Promega, Madison, Wisconsin, United States) was supplied by Intron Biotechnology, South Korea. RNA was extracted according to manufacturer instructions. For thermolysis, ground leaves were placed in a heat block with varying temperature from 50 to 95°C for an appropriate time between 5 and 10 min.

2.4 Synthesis of cDNA

cDNA was synthesized from purified viral RNA or RNA in a heat-degraded leaf sample using two different commercial kits at room temperature. At 50°C, The TOPscript cDNA synthesis kit (Enzynomics Daejeon, South Korea) was used, while the RocketScript™ Reverse transcriptase (Bioneer, Daejeon, South Korea) was used at 70°C. Synthesis procedures were carried out according to manufacturer protocols.

2.5 PCR Conditions and Detection of TMV and CMV

Target genes for each of the two viruses were amplified using TOPReal™ qCPR 2x premix (Enzynomics) and the StepOnePlus Real-Time PCR System (Thermo Fisher Scientific, Waltham, MA, United States). Specific primer pairs were used to amplify TMV and CMV: 5′-CGACATCAGCCGATGCAGC-3′ and 5′-ACCGTTTTC GAACCGAGACT-3′ were used for the forward, and 5′-ACCGTT TTCGAACCGAGACT-3′ and 5′-TACTGATAAACCAGTACC GGTGA-3′ for the backward, respectively. Reverse transcriptase was mixed with the PCR premix and used in RT-PCR, and the temperature for RT was added to the front end of the PCR thermal cycle. For the one-step direct method, ground leaves were placed into the RT-PCR solution and the reaction was carried out for a total of 40 cycles. The PCR protocol was as follows: 10 s at 95°C for denaturation, 15 s at 60°C for annealing, and 30 s at 72°C for extension. The temperature for the combined thermolysis and RT reaction was 50°C.

2.6 Preparation for One-Chip Digital RT-PCR

CMV particles were added to a premix containing reverse transcriptase, primers, and a probe with master mix containing DNA polymerase, dNTP, buffer (Tris-HCl, KCl, $MgCl_2$, pH8.5), etc. The reverse transcriptase and master mix used were RocketScript™ reverse transcriptase, RNase H minus (Bioneer), and QuantStudio™ 3D Digital PCR Master Mix v2 (Thermo Fisher Scientific), respectively. The prepared reaction solution containing CMV particles was injected into a loading blade, loaded onto a digital PCR chip (QuantStudio™ 3D Digital PCR 20 K Chip Kit v2, Thermo Fisher Scientific) comprising sub-nanoliter-sized chambers using a QuantStudio™ 3D Digital PCR Chip Loader (Thermo Fisher Scientific) and sealed.

2.7 Digital RT-PCR Conditions and Detection of CMV

For digital RT-PCR, The temperature for thermolysis and RT were conducted at 70°C. PCR steps included 40 cycles of 15 s at 96°C, 30 s at 56°C, and 30 s at 72°C. After the reaction, the fluorescence intensity of each sub-nL-sized chamber in a chip was measured using a QuantStudio™ 3D Digital PCR instrument (Thermo Fisher Scientific) and statistically analyzed based on Poisson distribution.

TABLE 1 | C_T values at various viral template concentrations. The template was prepared using commercial extraction kit. All data were averaged and deviated (*n* ≥ 3).

Template concentration (μg/nL)	C_T value
0	Not detected
0.01	29.42 ± 0.05
0.025	29.80 ± 0.22
0.05	33.44 ± 0.20
0.075	33.65 ± 0.30
0.1	35.75 ± 0.21

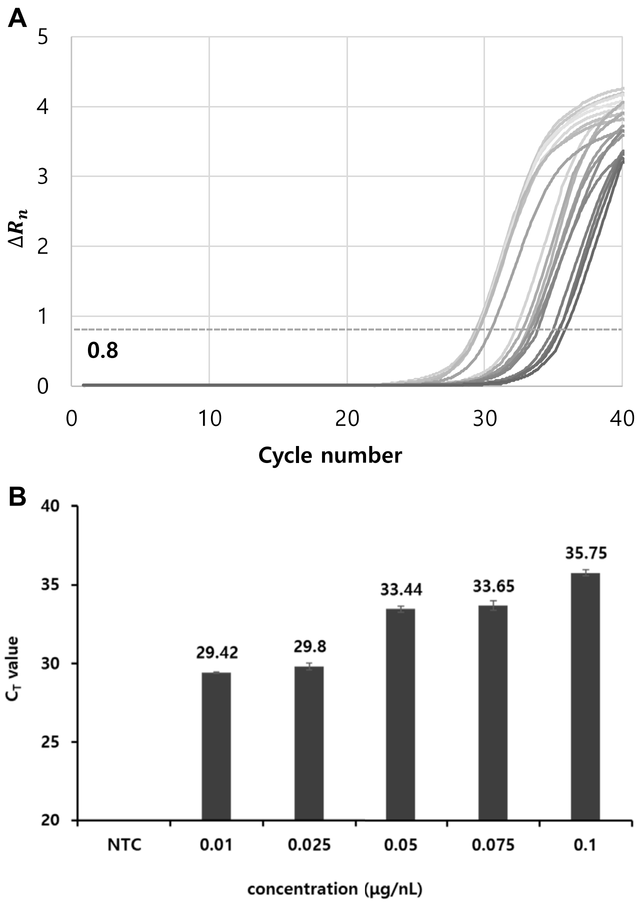

FIGURE 1 | Determination of C_T values depending on various TMV template concentration. **(A)** RT-PCR curves with C_T numbers. ΔR_n threshold was set as 0.8. **(B)** Determination of C_T values at template TMV particle concentrations of 0.1 to 0.01 μg/nL. Viral RNA was extracted using a commercial RNA extraction kit, followed by conventional separate RT and PCR reactions. All data were averaged and deviated (bars = S.D., *n* ≥ 3).

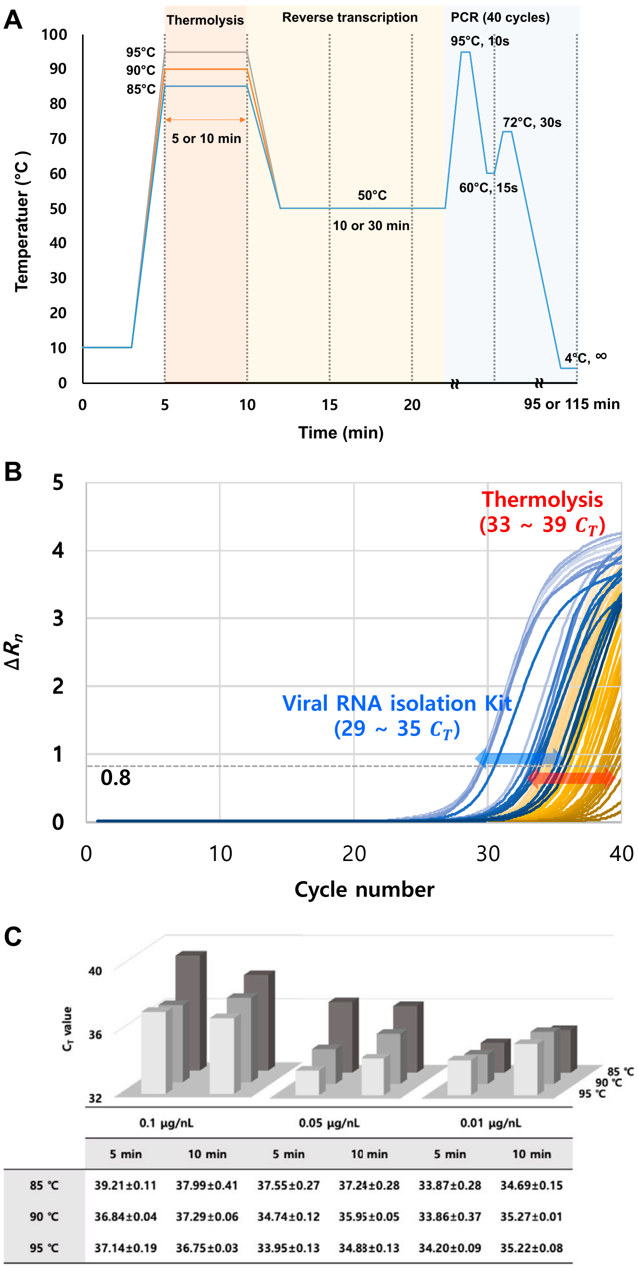

	0.1 μg/nL		0.05 μg/nL		0.01 μg/nL	
	5 min	10 min	5 min	10 min	5 min	10 min
85 ℃	39.21±0.11	37.99±0.41	37.55±0.27	37.24±0.28	33.87±0.28	34.69±0.15
90 ℃	36.84±0.04	37.29±0.06	34.74±0.12	35.95±0.05	33.86±0.37	35.27±0.01
95 ℃	37.14±0.19	36.75±0.03	33.95±0.13	34.83±0.13	34.20±0.09	35.22±0.08

FIGURE 2 | Determination of C_T values by varying TMV template concentration and thermolysis conditions. **(A)** Thermolysis-based RT-qPCR protocol optimization by varying thermolysis temperature and time. **(B)** RT-qPCR curve comparison between different RNA isolation methods (RNA isolation kit and thermolysis isolation). C_T values were obtained with the ΔR_n threshold set as 0.8. **(C)** Summary of obtained C_T results under different thermolysis conditions. C_T values were obtained by thermolysis-based RNA isolation, followed by conventional separate RT and PCR reactions. All data were averaged and deviated (*n* ≥ 3).

3 RESULTS AND DISCUSSION

3.1 Evaluation of TMV Detection Through RT and PCR

TMV was used as a model system to verify thermolysis-based RNA isolation and RT-qPCR. The efficiency of RNA isolation using the commercial kit protocol and thermolysis method were evaluated and compared. Following the extraction of TMV viral RNA using a nucleic acid extraction kit, RT and PCR reactions were carried out according to the manufacturer's protocol provided by a commercial kit. First, the dependence of the RT-qPCR results on the RNA template concentration was investigated by varying the RNA concentration. As such, the optimal concentration for RT-qPCR was determined (**Table 1**). The cycle threshold (C_T), determined when the ΔR_n threshold was set at 0.8, tended to

TABLE 2 | Determination of limit of detection concentration by varying the tobacco mosaic virus template concentration. All data were averaged and deviated ($n \geq 3$).

Template concentration (μg/nL)	C_T value
0	Not detected
10^{-2}	26.57 ± 0.47
10^{-5}	30.19 ± 0.24
10^{-10}	33.55 ± 0.35
10^{-20}	33.91 ± 0.02
10^{-30}	32.86 ± 0.07

increase as the template RNA concentration increased. This is probably because a purified template by RNA extraction kit was used for RT-qPCR reaction whereas various inhibiting chemicals could be generated at a high template concentration when crude viral particle samples are used. In general, the C_T ranged from 29 to 35 at RNA concentrations of 0.01–0.1 μg/nL (**Figure 1A**). An amplification curve was not observed in the negative control without an RNA template and was not infected with the virus, and the lowest RNA concentration that yielded a meaningful C_T (29) with RT-qPCR was 0.01 μg/nL (**Figure 1B**).

3.2 Temperature Dependency of Thermolysis and C_T Values

Three different variations in temperature, exposure time, and RNA template concentration were tested for thermolysis before RT-qPCR. This was carried out to verify the performance of the thermolysis method at three different temperatures (at 85, 90, and 95°C), two exposure times (for 5 and 10 min), and three different crude viral particle concentrations in the sample (0.01, 0.05, 0.1 μg/nL). Then, qPCR was evaluated by analyzing C_T values

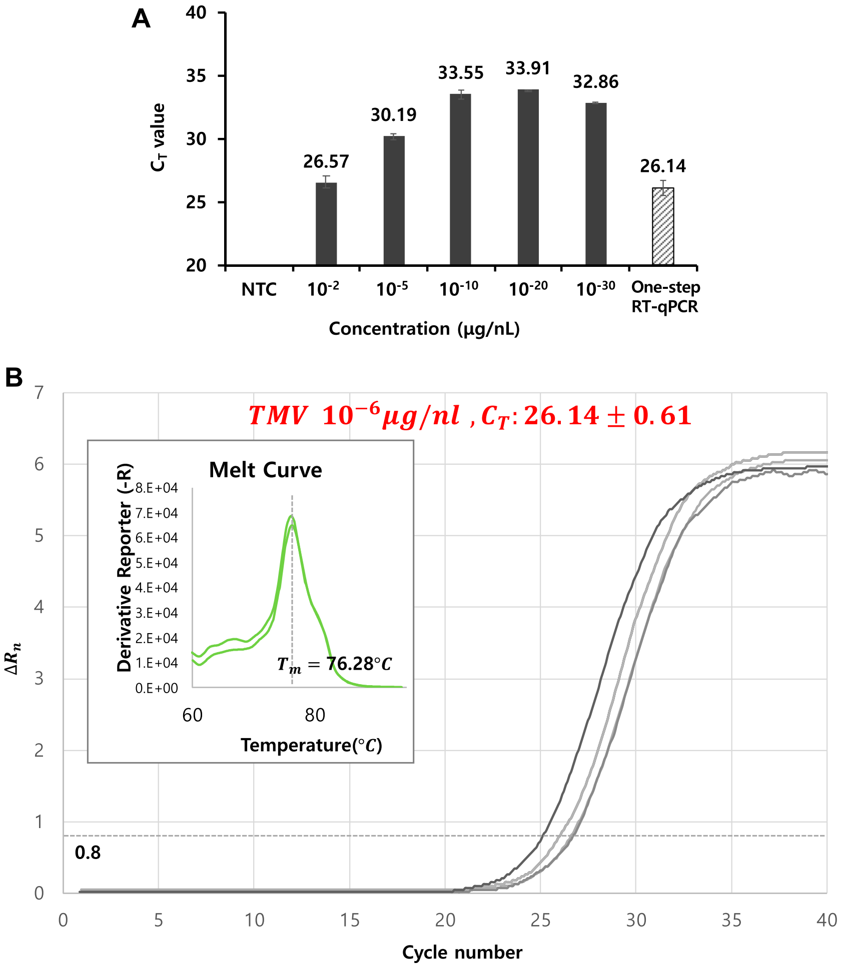

FIGURE 3 | (A) Determination of the lowest concentration for viral particle detection using optimized thermolysis conditions at 85°C for 5 min. A specifically designed primer set (see **section 2.5** PCR conditions and detection of TMV and CMV) was used for cDNA synthesis, and both RT and PCR reactions were conducted by a one-step process in a single tube. Each C_T value was determined against a series of viral particle concentrations of 10^{-2}, 10^{-5}, 10^{-10}, 10^{-20}, and 10^{-30} μg/nL (black bar). **(B)** RT-qPCR curves from one-step thermolysis. A viral concentration of 10^{-6} μg/nL was used as a template, and the PCR cycle was programmed by adding two steps: thermolysis for 5 min at 85°C and an RT reaction for 60 min at 50°C prior to the PCR amplification cycles. The obtained C_T value was included as slashed bar in **Figure 3A** for a comparison. All data were averaged and deviated (bars = S.D., $n \geq 3$).

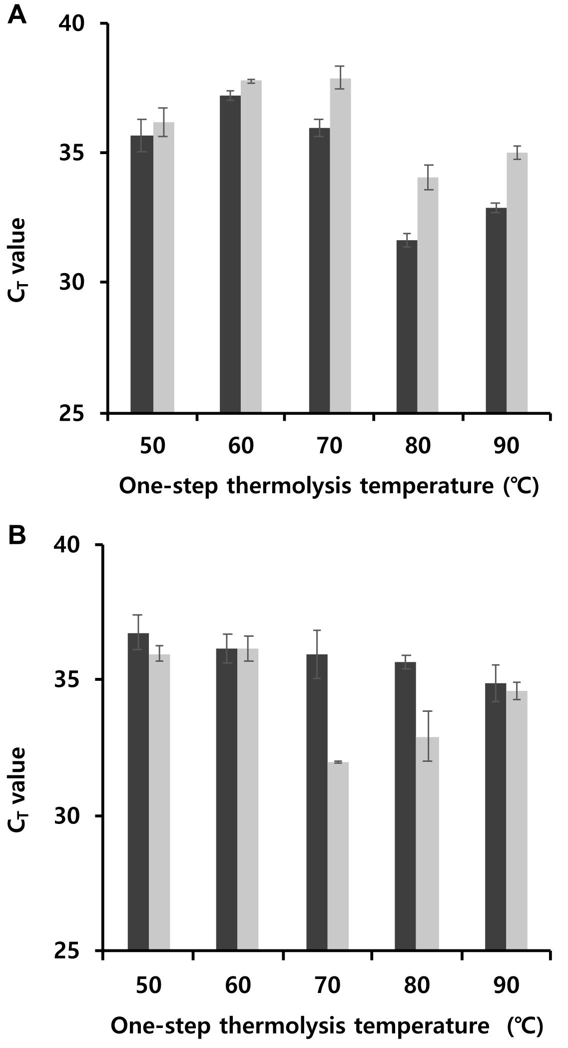

FIGURE 4 | Determination of C_T values to reduce total operational time by reducing the difference between the thermolysis and RT temperatures at a viral particle concentration of 10^{-6} μg/nL. **(A)** TMV and **(B)** CMV (Black bar: 5 min, grey bar: 10 min). The thermolysis temperature varied from 50 to 90°C for five or 10 min, followed by RT reaction at same temperature. All data were averaged and deviated (bars = S.D., *n* ≥ 3).

TABLE 3 | Results of one-step detection of tobacco mosaic virus (TMV) and cucumber mosaic virus (CMV) in one tube. All data were averaged and deviated (*n* ≥ 3).

Viral targets	Thermolysis + reverse transcription time[a]	C_T values
TMV	5 min	30.49 ± 0.06
	10 min	32.68 ± 0.11
CMV	5 min	not determined
	10 min	32.42 ± 0.32

[a] *Temperature for thermolysis and reverse transcription reaction: 60°C.*

in cycles (**Figure 2A**). Following thermal treatment under 18 different sets of conditions, the crude mixture was directly used as the RT reaction template without a purification step, and the C_T was monitored (**Supplementary Figures S1–S3**). In addition, melting point analysis graphs with no shoulder peak observed were added to the supplementary data (**Supplementary Figure S4**).

Initially, it was clear that the TMV particles could be detected with RT-qPCR after either thermolysis or commercial RNA isolation. However, slight changes in the C_T value depending on thermolysis conditions were observed (**Figure 2B**). Overall, lower C_T values were observed at higher temperatures. This trend was most apparent when the viral concentration was 0.05 μg/nL. The C_T differences between 85 and 95°C were highest, around 2.4 to 3.6, whereas temperature did not greatly affect the C_T values, with differences of 0.4 and 2.1 at viral particle concentrations of 0.01 and 0.1 μg/nL, respectively. In particular, the temperature dependency on C_T values were the weakest at a viral particle concentration of 0.01 μg/nL (**Figure 2C**).

3.3 Effect of RNA Template Concentration on Thermolysis and C_T Values

In general, C_T values of 33–35 were observed at a viral concentration of 0.01 μg/nL. However, it was increased up to 37 to 39 at 0.1 μg/nL. Interestingly, the average C_T values at different thermolysis temperatures and times were lowest at a viral concentration of 0.01 μg/nL. The C_T value increased with viral particle concentration. For example, C_T value reached a peak of 39 at 0.1 μg/nL with 5 min thermolysis, and reached 37 with 10 min thermolysis. This might be due to the increase in impurities generated from the host during lysis, including tissues, DNA, and viral debris, because the dried viral sample was directly used for thermolysis. These impurities may have acted as inhibitors in the RT-qPCR reaction, thereby resulting in increased C_T values. In addition, concentration and temperature had a complex effect on the C_T values, as described previously. For example, when the viral particle concentration was as low as 0.01 μg/nL, a dramatic change by the thermolysis temperature was not observed at all.

3.4 Exposure Time Dependency on Thermolysis and C_T Values

At a viral particle concentration of 0.01 μg/nL, the lowest C_T values were obtained at an exposure time of 5 min for all temperatures. As a result of the instability of isolated RNA, long exposure times and high temperatures are likely to degrade RNA templates, leading to higher C_T values. With an increase in the temperature and exposure time, there was also an increased release of viral debris into the reaction. Therefore, a clear general tendency of the C_T-thermolysis relationship was not observed (see the results at 90 and 95°C). There was no significant difference between the C_T values at exposure times of 5 and 10 min. For example, at a viral concentration of 0.05 μg/nL, the C_T difference was less

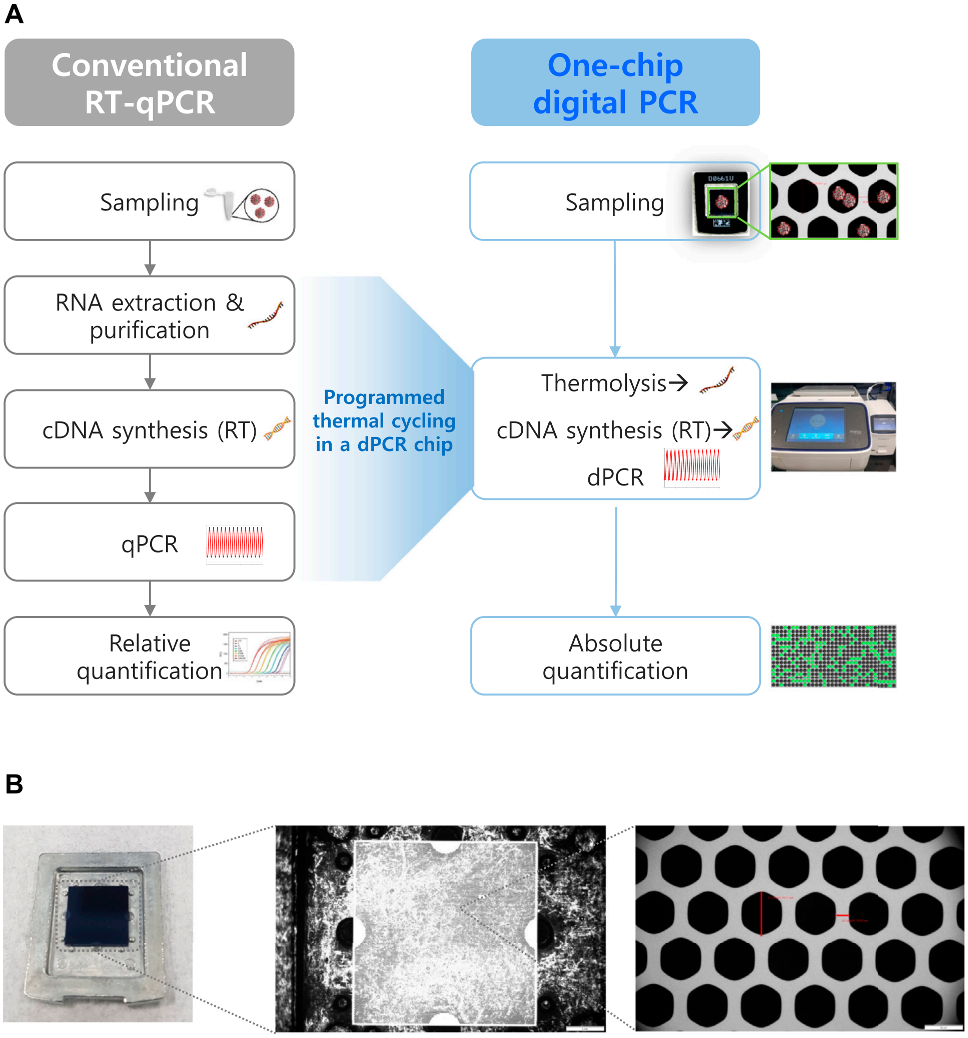

FIGURE 5 | Digital PCR analytical protocols and CMV detection results with chip images and fluorescence intensity distribution. **(A)** Overall digital PCR analysis scheme compared to conventional RT-qPCR analysis. **(B)** Photograph of the QuantStudio 3D digital PCR chip (10 × 10 × 0.3 mm^3) with 20,000 nanoscale through-hole PCR wells, and optical microscope image of through-hole PCR wells. The diagonal length of through-hole is about 60 μm and the width of sidewall is about 18 μm. **(C)** Digital PCR chip analysis images. CMV concentrations of 0, 10^{-2}, and 10^{-3} μg/nL. Fluorescence intensity distribution at each CMV template concentration. For RNA isolation, a commercial RNA extraction kit was used, and RT reactions were conducted at 70°C for 60 min. **(D)** One-chip digital PCR results of CMV detection with dPCR chip analysis images. Simultaneous thermolysis and RT reactions were conducted at 70°C for either 30 min or 5 min, and CMV concentration were set at either 10^{-2} μg/nL or 10^{-4} μg/nL.

than 1.0 at all temperatures. This was observed at all the viral concentrations and temperatures.

3.5 Determination of Viral RNA Detection Limit

The lowest concentration for viral particle detection using thermolysis was determined under the optimal thermolysis condition: 85°C for 5 min. A specifically designed primer set described in the experimental section was used for cDNA synthesis, and both RT and PCR reactions were conducted in a single tube by a one-step process. Each C_T value was determined against a series of viral particle concentrations of 10^{-2}, 10^{-5}, 10^{-10}, 10^{-20}, and 10^{-30} μg/nL, resulting in C_T values between 26 and 33 (**Table 2**). For the 10^{-10} μg/nL sample, the C_T value reached 33.55, which was an increase of four cycles compared to the value from the RNA extraction kit-based RT-qPCR. A similar range of C_T values was maintained up to the 10^{-30} μg/nL diluted sample. These results suggested that the limit of detection under thermolysis conditions was approximately 10^{-5} and 10^{-10} (**Figure 3A**).

3.6 Feasibility of One-Step Thermolysis RT-qPCR

Next, the feasibility of combining thermolysis and RT-qPCR in a single tube using a programmed PCR cycle was investigated against TMV. A mixture solution containing viral particles, constituents of the RT reaction, constituents of the qPCR

C

Thermolysis & RT (min)	Template (μg/nL)	Chip image	Fluorescence intensity distribution	Copies/μL
RNA extraction Kit & 70°C for 60 min	None	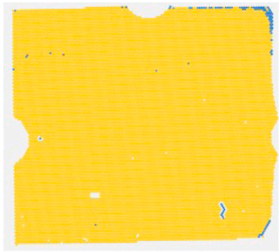	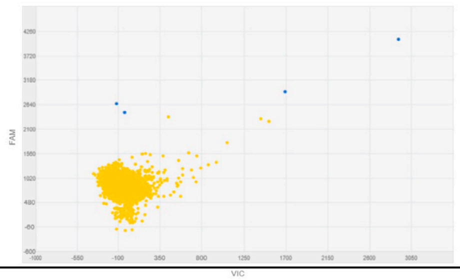	<1
	10^{-2}	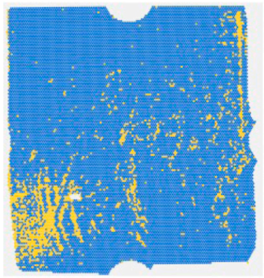	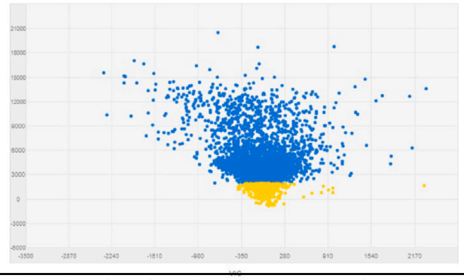	Saturated
	10^{-3}	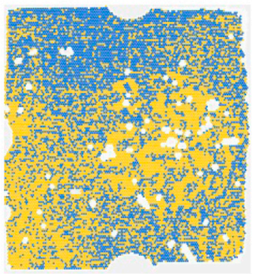	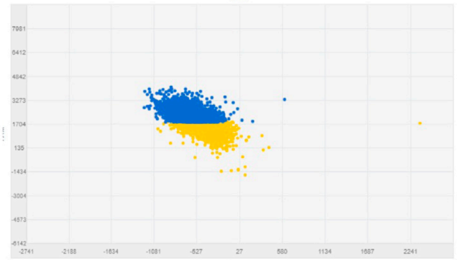	869.8

FIGURE 5 | (Continued).

reaction, and specific primers was prepared and reacted in a PCR thermocycler. The PCR cycle was programmed by adding two steps of thermolysis for 5 min at 85°C and an RT reaction for 60 min at 50°C prior to the PCR amplification cycles. When a 10^{-6} μg/nL viral particle concentration was used as the template, cDNA was successfully synthesized by RT and amplified by qPCR, with a C_T value of 26.14 ± 0.61 (**Figure 3B**). Also, the amplified DNA products were again separated by gel electrophoresis analysis and verified to confirm the correct amplification.

3.7 Optimization of One-Step Thermolysis RT-qPCR

The operational process for one-step thermolysis RT-qPCR was optimized by reducing the total operation time. In this case, CMV was tested to apply the one-step protocol to other viral particles. The most time-consuming step in the developed protocol was the RT reaction, which was set to 80 min. The initial step of 5 min exposure time for thermolysis at 85°C included additional time, required to lower the temperature to the optimum RT temperature of 50°C, and needed to maintain this temperature for 30 min or more. The first attempt to reduce the total operation time was carried out by reducing the difference between the thermolysis and RT temperatures with the viral particle concentration fixed at 10^{-6} μg/nL. The thermolysis temperature was optimized by varying the temperature from 50 to 90°C for five or 10 min, followed by RT reaction at same temperature. One-step thermolysis in programmed PCR against TMV was most effective at 80°C for 5 min, while the optimal condition against CMV was found to be 70°C for 10 min (**Figures 4A,B**). However, no significant difference of three cycles or more was observed at any thermal treatment time for either virus, indicating feasibility of the thermolysis protocol at lower temperatures.

Then, the feasibility of synchronizing thermolysis and RT at 60°C was verified by programming a continuous isothermal reaction in a thermocycler, thereby reducing the total exposure time up to 5 and 10 min. Interestingly, when the

D

Thermolysis + RT (min)	Template (µg/nL)	Chip image	Fluorescence intensity distribution	Copies/µL
30	10^{-2}	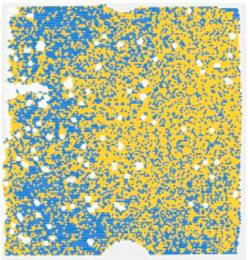	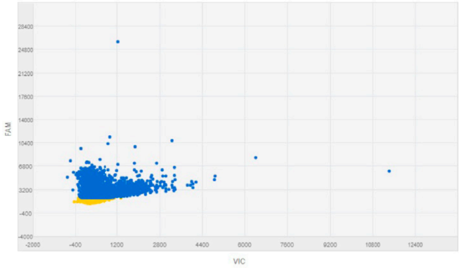	1130.2
	10^{-4}	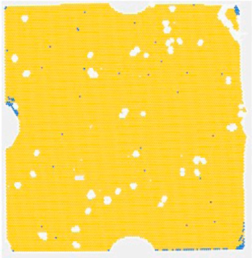		4.394
5	10^{-2}	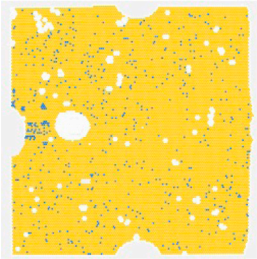	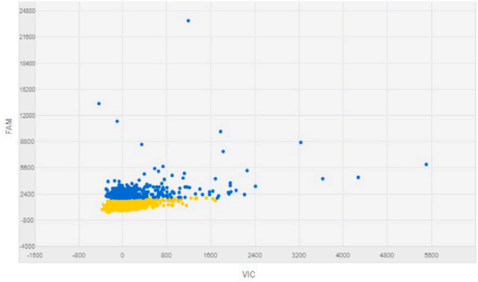	56.3
	10^{-4}	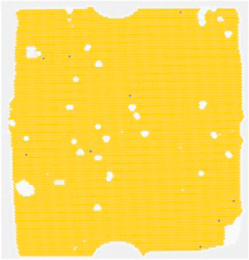	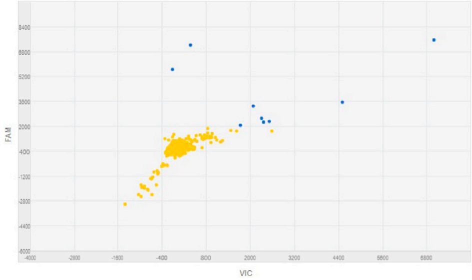	< 1

FIGURE 5 | (Continued).

total time of thermolysis and RT reaction was 10 min against either TMV or CMV particles, the C_T was less than 33 (**Table 3**). This suggested that not only was thermolysis successful at 60°C, but also that the RT reaction was effective even under 10 min, although a slight C_T increase of 4–five cycles was observed compared to values at 85°C thermolysis (**Figure 3B**). Moreover, TMV was detected with C_T value of 30.49 ± 0.06 at a total reaction time of 5 min. These findings confirmed that continuous one-step thermolysis, RT, and PCR could be performed in a single PCR tube using a single thermocycler.

3.8 dPCR-Based Viral Particle Detection

Viral particle analysis was performed using dPCR to verify whether the one-step analysis protocol obtained from RT-qPCR analysis was appropriate for dPCR assay. A ThermoFisher QuantStudio 3D digital PCR system was used, in which the DNA concentration of a sample could be quantified with a dPCR chip containing 20,000 chambers of less than 1 nL (**Figure 5A**). The application of a thermolysis-based protocol in sub-nanoliter-sized partitioned chambers has a great advantage in that partitioning has both concentration and purification effects, minimizing inhibition

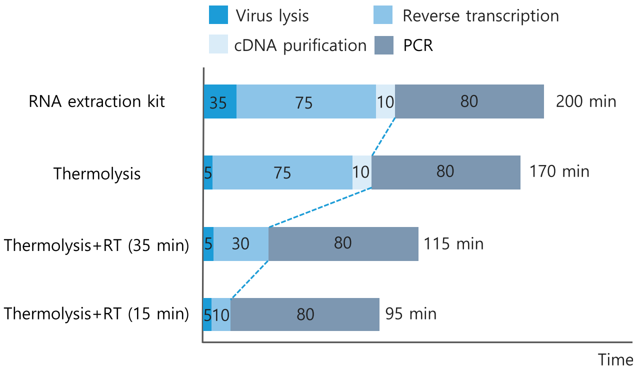

FIGURE 6 | Summary of the developed thermolysis-based one-step qPCR protocol and comparison of operation time. Numbers in each bar indicate each operational time in min. Details of operational time and C_T values are listed in **Table 4**.

by lysis debris and RT reaction components. Considering the size of a single dPCR chamber (approximately 60 μm in diameter and 300 μm in height, **Figure 5B**), the sphere-shaped CMV particles with 20 nm diameter would be more appropriate for positioning in a dPCR chamber than the rod-shaped TMV particles with 300 nm length and 10 nm width. Therefore, CMV particles were used as model viral particles for the dPCR analysis.

The cDNA synthesized by RT reaction (70°C, 60 min) from CMV particles using an RNA extraction kit was used as a qPCR template for comparison, and the results showed a C_T value of 35.47 ± 0.33. This corresponded to the observed negative control values. In the dPCR system, a negative control without viral particles resulted in an output of less than 1 copy/μL. Analysis with viral concentrations of 10^{-2} and 10^{-3} μg/nL resulted in a saturated and 869.8/μL concentration output, respectively (**Figure 5C**). The concentration of RNA copies from the 10^{-2} μg/nL sample was interpreted as saturated because the number of positive chambers was too large to be quantified using Poisson statistics. It was predicted that the viral particle concentration in 10^{-3} μg/nL yielded approximately 8.7×10^2 copies RNA/μg viral particles based on the amplification output value of 869.8 copies/μL in the dPCR analysis.

3.9 One-Chip Digital PCR Based on Thermolysis Protocol

It was confirmed that the detection of viral was feasible with meaningful output through dPCR. Based on previous results, the one-step RT-qPCR protocol was applied to dPCR analysis to verify the one-chip digital PCR protocol. Although the optimal conditions of 85°C thermolysis for 5 min were secured as one-step assay conditions in RT-qPCR assay, thermolysis in the one-chip dPCR system was performed at 70°C to maintain activation of the reverse transcriptase, which was more critical in one-chip dPCR assay. Therefore, a continuous thermolysis-RT reaction cycle for either 30 or 5 min was introduced prior to the PCR cycle, and the concentration output results were compared at 10^{-2} μg/nL and 10^{-4} μg/nL viral particle templates, respectively.

At a viral particle concentration of 10^{-2} μg/nL, output values of 1,130.2 and 56.3 copies/μL were calculated for 30 and 5 min thermolysis-RT reactions, respectively (**Figure 5D**). This suggested that longer thermolysis-RT reaction time led to higher efficiency of RNA separation and cDNA conversion from the viral particles, resulting in a higher output. Meanwhile, output values of 4.4 and less than 1 copies/μL concentration were obtained at 30 and 5 min thermolysis-RT reactions at 10^{-4} μg/nL concentration, respectively. This suggested that the limit of detection for the 5 min reaction time was 10^{-4} μg/nL. However, no cDNA amplification was obtained in any of these four reaction conditions when the same one-chip dPCR conditions were applied to RT-qPCR

TABLE 4 | Summary of the developed thermolysis-based qPCR protocol and comparison of operation time and C_T values. All data were averaged and deviated ($n \geq 3$).

Protocol	RNA extraction	Reverse transcription	cDNA purification	PCR	Total time (min)	C_T value (cycles)
RNA extraction kit	35 (Extraction kit)	75	10	80	200	29.42 ± 0.05
Thermolysis	5 (thermolysis)	75	10	80	170	33.87 ± 0.29
Thermolysis + RT-PCR (35 min)	5 (thermolysis)	30	—	80	115	21.95 ± 0.44[a]
Thermolysis + RT-PCR (15 min)	5 (thermolysis)	10	—	80	95	20.72 ± 0.69[a]

[a]*C_T, values were determined at thresholds of 0.4 due to lowered intensity.*

TABLE 5 | One-chip analysis results for cucumber mosaic virus particle detection. Chip image and fluorescence intensity distribution are shown in **Figure 6**.

Protocol	Thermolysis (min)	Reverse transcription (min)	Template (μg/nL)	Concentration (copies/μL)
RNA extraction kit	35	60	0	<1.0
	35	60	10^{-2}	Saturated
	35	60	10^{-3}	869.8
One-chip assay	Thermolysis	30	10^{-2}	1,130.2
		5	10^{-2}	56.3
		30	10^{-4}	4.4
		5	10^{-4}	<1.0

analysis, suggesting that it would be impossible to detect the viral particles with qPCR under conditions that were suitable for one-chip dPCR conditions. In conclusion, the results that 10^2 to 10^3 copies RNA/μg ranges of viral particles, which were calculated by multiplying the viral particle concentration with the output copies/μL, could be detectable even in a 5 min reaction, which supports the hypothesis that the one-chip dPCR protocol can efficiently detect viral particles quantitatively.

4 CONCLUSION

This study developed a thermolysis-based RT-qPCR protocol to overcome the laborious and time-consuming process of conventional RT-PCR reactions by circumventing RNA isolation and purification steps. TMV and CMV were tested as model viruses using this protocol, and were directly detected. Of all thermolysis conditions, the lowest C_T value was obtained at 85°C thermolysis for 5 min with 0.01 μg/nL of viral particles. Compared to the C_T values obtained using a commercial RNA extraction kit, the TMV concentrations of 0.1, 0.05, 0.1 μg/nL produced C_T differences of 1.0–3.5, 0.5–4.1, and 4.4–5.9, respectively. Under all thermolysis conditions, the C_T values were approximately 33–39, which was about four cycles higher than those resulting from a commercial RNA extraction kit (**Figure 2B**). It was demonstrated that viral particles could be detected with distinct thresholds through RT-qPCR using the thermolysis method.

The protocol focused on a simple and rapid virus detection method. By optimizing thermolysis conditions, such as temperature, exposure time, and template concentrations, an effective RT-qPCR protocol was developed, achieving a significant decrease in the total operational time compared to conventional methods (**Figure 6**). The continuous one-step thermolysis of viral particles and an RT reaction at 60°C for 5 min followed by PCR reactions within a single tube were successful in detecting viral particles within 95 min of total operational time. A total of 105 min in operational time could be saved compared to that of commercial kit-based RNA isolation and quantitative RT-qPCR methods (**Table 4**). Additionally, there was considerable improvement in the C_T value, which was 20.72 ± 0.69, although the threshold was set to a value of 0.4, as the one-step RT-qPCR resulted in a relatively low amplification intensity compared to those of previously optimized protocols.

The developed method presents opportunities to be further refined, decreasing the total time to less than 1 h. The only protocol that was not optimized or engineered in this study was that of PCR cycling, which was set as a 10-10-35 s process with 40 cycles. cDNA amplification through PCR therefore occupied most of the viral RNA detection time, considering the shorted RNA extraction and cDNA synthesis step. There is ample scope for shortening the viral RNA detection time by shortening the PCR cycle. For this purpose, future optimization studies are needed. For example, the design of an optimal oligonucleotide primer set for amplification and the selection of the ideal amplification region and length could shorten the overall process. In addition, optimization of PCR cycle time and reaction conditions suitable for one-step and dPCR systems is required.

The developed protocol was applied to one-step dPCR, which allowed the detection of 1,130.2 RNA copies/μL using 10^{-2} μg/nL of viral particles with a 30 min thermolysis-RT reaction at 70°C (**Table 5**). The protocol developed by optimizing RT-qPCR analysis was verified and applied to dPCR analysis. Not only did the dPCR technique provide a much higher precision and accuracy in quantifying nucleic acids than that of the qPCR, but it also allowed for suitable reaction conditions in a one-chip assay. Considering the physical shape of the dPCR chip, one of the benefits of this system is the increase in concentration and purification effect by partitioning (Basu, 2017). In addition, silicon-based dPCR has a much higher heat transfer and thermal controllability in sub-nanoliter-sized chambers, resulting in faster thermal changes during PCR cycles. Because the PCR reaction depends on thermal changes during the amplification cycle, most of the operational time relies on thermal ramping steps rather than each reaction, so efficient thermal changes speed up the process. For the conventional PCR reaction, components such as dNTPs, polymerase, oligomers, and other reagents were mixed in a 10–20 μL reaction volume. However, this could be dispersed into less than 1 nL of reaction volume under dPCR conditions, providing much less possibility of interference by reaction elements. This effective concentration and purification by partitioning was optimal in continuous RT and PCR reactions in a single dPCR chamber because fewer interfering and inhibiting elements in different reaction systems could be effectively partitioned in a single dPCR chamber, resulting in higher RNA and cDNA yields and amplification.

Also, the precision in dPCR was well known to be limited by the Poisson statistics of which the total number of template molecules in the analyzed sample. This means that the lower prevision could be obtained as the volume of the viral particle increases in a limited reaction volume. When applied to RT-qPCR, the size of the virus is not a big problem because there are few spatial restrictions, but when applied to digital PCR, the size of the virus is also one of the important variables. However, the chip volume can be controllable depending on the size of analyzing viral particles. The sensitivity of virus detection due to the volume effect may be affected, but since the size of the digital PCR chamber is approximately 60 μm, it is possible to sufficiently detect viruses corresponding to 20–100 nm size. This was confirmed through digital PCR analysis results for TMV corresponding to 18 nm × 300 nm, which showed analysis results at a level similar to that of CMV at 20 nm. To efficiently detect viral RNA, it is important to develop analysis protocols simultaneously. This indicates the necessity of studying reverse transcriptase and DNA polymerase enzymes, which are critical factors in cDNA synthesis and amplification. In addition, most commercial enzymes and supplementary element concentrations are not suitable for the chamber size of the dPCR system, and will require optimization for efficient viral RNA detection and diagnosis. Currently, RT-qPCR probes, such as Progema company's GoTaq® Probe qPCR and RT-qPCR system or myPOLS company's Volcano3G® RT-PCR master mix, operate in a single step. In addition, commercial kits that can accurately detect viral particles with a high speed as the goal of this study are emerging due to the development of hot-start polymerase enzymes that optimize the different reaction conditions of RT and PCR such as temperature, buffer, and pH.

Various techniques have been developed for detecting viral RNA. For these technological developments, analyzing equipment, detection protocols and data analysis should proceed together. The precision and accuracy of viral RNA diagnosis are important along with the speed of the method. In particular, the qPCR technologies verified in this study can be utilized as a technology that enables mankind to cope with and overcome pandemic situations by pathogens in the future.

DATA AVAILABILITY STATEMENT

The original contributions presented in the study are included in the article/**Supplementary Material**, further inquiries can be directed to the corresponding authors.

AUTHOR CONTRIBUTIONS

The manuscript was written with the contribution of all authors. HP designed and performed the optimization experiments and digital PCR analysis. WJ, HJ, KN, and K-YC conceptualized the thermolysis RT-qPCR protocol development and dPCR analysis, supervised the project, and analyzed the data to finalize the manuscript. All the authors approved the final version of the manuscript.

FUNDING

This study was supported by a research grant from the Samsung Advanced Institute of Technology.

SUPPLEMENTARY MATERIAL

The Supplementary Material for this article can be found online at: https://www.frontiersin.org/articles/10.3389/fbioe.2022.837838/full#supplementary-material

REFERENCES

Abdallah, N. M. A., Zaki, A. M., and Abdel-Salam, S. A. (2020). Stability of MERS-CoV RNA on Spin Columns of RNA Extraction Kit at Room Temperature. *Diagn. Microbiol. Infect. Dis.* 98, 115182. doi:10.1016/j.diagmicrobio.2020.115182

Alonso-Prados, J. L., Aranda, M. A., Malpica, J. M., García-Arenal, F., and Fraile, A. (1998). Satellite RNA of Cucumber Mosaic Cucumovirus Spreads Epidemically in Natural Populations of its Helper Virus. *Phytopathology* 88, 520–524. doi:10.1094/phyto.1998.88.6.520

Arevalo-Rodriguez, I., Buitrago-Garcia, D., Simancas-Racines, D., Zambrano-Achig, P., Del Campo, R., Ciapponi, A., et al. (2020). False-negative Results of Initial RT-PCR Assays for COVID-19: A Systematic Review. *PLoS One* 15, e0242958. doi:10.1371/journal.pone.0242958

Basu, A. S. (2017). Digital Assays Part I: Partitioning Statistics and Digital PCR. *SLAS TECHNOLOGY: Translating Life Sci. Innovation* 22, 369–386. doi:10.1177/2472630317705680

Brown, J. R., O'Sullivan, D. M., Shah, D., Atkinson, L., Pereira, R. P. A., Whale, A. S., et al. (2021). Comparison of SARS-CoV-2 N Gene Real-Time RT-PCR Targets and Commercially Available Mastermixes. *J. Virol. Methods* 295, 114215. doi:10.1016/j.jviromet.2021.114215

Campos, K. R., Sacchi, C. T., Gonçalves, C. R., Pagnoca, É. V. R. G., Dias, A. D. S., Fukasawa, L. O., et al. (2021). COVID-19 Laboratory Diagnosis: Comparative Analysis of Different RNA Extraction Methods for SARS-CoV-2 Detection by Two Amplification Protocols. *Rev. Inst. Med. Trop. Sao Paulo* 63, e52. doi:10.1590/S1678-9946202163052

Cristiano, D., Peruzy, M. F., Aponte, M., Mancusi, A., Proroga, Y. T. R., Capuano, F., et al. (2021). Comparison of Droplet Digital PCR vs Real-Time PCR for Yersinia Enterocolitica Detection in Vegetables. *Int. J. Food Microbiol.* 354, 109321. doi:10.1016/j.ijfoodmicro.2021.109321

De Boer, M. E., Berg, S., Timmermans, M. J., Den Dunnen, J. T., Van Straalen, N. M., Ellers, J., et al. (2011). High Throughput Nano-Liter RT-qPCR to Classify Soil Contamination Using a Soil Arthropod. *BMC Mol. Biol* 12, 11. doi:10.1186/1471-2199-12-11

Du, L., Xiang, J. L., Fan, J. L., Li, X., and Luo, L. (2013). Detection of Tobacco Mosaic Virus (TMV) in Rehmannia Glutinosa F. Hueichingensis by IC-RT-PCR. *Zhongguo Zhong Yao Za Zhi* 38, 2092–2095.

Fabiani, L., Saroglia, M., Galatà, G., De Santis, R., Fillo, S., Luca, V., et al. (2021). Magnetic Beads Combined with Carbon Black-Based Screen-Printed Electrodes for COVID-19: A Reliable and Miniaturized Electrochemical Immunosensor for SARS-CoV-2 Detection in Saliva. *Biosens. Bioelectron.* 171, 112686. doi:10.1016/j.bios.2020.112686

Garg, J., and Garg, A. (2021). Evaluation of SARS CoV-2 RT-PCR in a Multiple Sample Pool. *Indian J. Med. Res.* 153, 699–700. doi:10.4103/ijmr.ijmr_4282_20

Howe, K., Hale, M., and Reynolds, G. E. (2021). SARS-CoV-2 RT-PCR Test Results across Symptomatic COVID-19 Cases in Auckland, New Zealand, February-June 2020. *Commun. Dis. Intell.* 1, 45. doi:10.33321/cdi.2021.45.32

Ibrahimi, N., Delaunay-Moisan, A., Hill, C., Le Teuff, G., Rupprecht, J.-F., Thuret, J.-Y., et al. (2021). Screening for SARS-CoV-2 by RT-PCR: Saliva or Nasopharyngeal Swab? Rapid Review and Meta-Analysis. *PLoS One* 16, e0253007. doi:10.1371/journal.pone.0253007

Karon, B. S., Donato, L., Bridgeman, A. R., Blommel, J. H., Kipp, B., Maus, A., et al. (2021). Analytical Sensitivity and Specificity of Four point of Care Rapid Antigen Diagnostic Tests for SARS-CoV-2 Using Real-Time Quantitative PCR, Quantitative Droplet Digital PCR, and a Mass Spectrometric Antigen Assay as Comparator Methods. *Clin. Chem.* 67 (11), 1545–1553. doi:10.1093/clinchem/hvab138

Klein, S., Muller, T. G., Khalid, D., Sonntag-Buck, V., Heuser, A. M., Glass, B., et al. (2020). SARS-CoV-2 RNA Extraction Using Magnetic Beads for Rapid Large-Scale Testing by RT-qPCR and RT-LAMP. *Viruses* 12, 863. doi:10.3390/v12080863

Knight, C. A. (1955). Are Cucumber Viruses 3 and 4 Strains of Tobacco Mosaic Virus? *Virology* 1, 261–267. doi:10.1016/0042-6822(55)90023-4

Li, X., Mauro, M., and Williams, Z. (2015). Comparison of Plasma Extracellular RNA Isolation Kits Reveals Kit-dependent Biases. *Biotechniques* 59, 13–17. doi:10.2144/000114306

Luethy, P. M., and Johnson, J. K. (2021). Comparison of Three Sample-To-Answer RT-PCR Testing Platforms for the Detection of SARS-CoV-2 RNA in Positive Nasopharyngeal and Nasal Swabs. *J. Appl. Lab. Med.* 6, 1635–1639. doi:10.1093/jalm/jfab066

Martin, A., Storto, A., Le Hingrat, Q., Collin, G., André, B., Mallory, A., et al. (2021). High-sensitivity SARS-CoV-2 Group Testing by Digital PCR Among Symptomatic Patients in Hospital Settings. *J. Clin. Virol.* 141, 104895. doi:10.1016/j.jcv.2021.104895

Nagura-Ikeda, M., Imai, K., Tabata, S., Miyoshi, K., Murahara, N., Mizuno, T., et al. (2020). Clinical Evaluation of Self-Collected Saliva by Quantitative Reverse Transcription-PCR (RT-qPCR), Direct RT-qPCR, Reverse Transcription-Loop-Mediated Isothermal Amplification, and a Rapid Antigen Test to Diagnose COVID-19. *J. Clin. Microbiol.* 58, e01438–20. doi:10.1128/JCM.01438-20

Niehl, A., Pasquier, A., Ferriol, I., Mély, Y., and Heinlein, M. (2014). Comparison of the Oilseed Rape Mosaic Virus and Tobacco Mosaic Virus Movement Proteins (MP) Reveals Common and Dissimilar MP Functions for Tobamovirus Spread. *Virology* 456-457, 43–54. doi:10.1016/j.virol.2014.03.007

Rattanachaisit, P., Suksawatamnuay, S., Sriphoosanaphan, S., Thanapirom, K., Thaimai, P., Siripon, N., et al. (2021). Stability of Hepatitis B Virus Pregenomic RNA in Plasma Specimens under Various Temperatures and Storage Conditions. *PeerJ* 9, e11207. doi:10.7717/peerj.11207

Schoenmaker, L., Witzigmann, D., Kulkarni, J. A., Verbeke, R., Kersten, G., Jiskoot, W., et al. (2021). mRNA-Lipid Nanoparticle COVID-19 Vaccines: Structure and Stability. *Int. J. Pharmaceutics* 601, 120586. doi:10.1016/j.ijpharm.2021.120586

Shen, K.-M., Sabbavarapu, N. M., Fu, C.-Y., Jan, J.-T., Wang, J.-R., Hung, S.-C., et al. (2019). An Integrated Microfluidic System for Rapid Detection and Multiple Subtyping of Influenza A Viruses by Using Glycan-Coated Magnetic Beads and RT-PCR. *Lab. Chip* 19, 1277–1286. doi:10.1039/c8lc01369a

Taki, K., Yokota, I., Fukumoto, T., Iwasaki, S., Fujisawa, S., Takahashi, M., et al. (2021). SARS-CoV-2 Detection by Fluorescence Loop-Mediated Isothermal Amplification with and without RNA Extraction. *J. Infect. Chemother.* 27, 410–412. doi:10.1016/j.jiac.2020.10.029

Tang, Y.-W., Lowery, K. S., Valsamakis, A., Schaefer, V. C., Chappell, J. D., White-Abell, J., et al. (2013). Clinical Accuracy of a PLEX-ID Flu Device for Simultaneous Detection and Identification of Influenza Viruses A and B. *J. Clin. Microbiol.* 51, 40–45. doi:10.1128/jcm.01978-12

Tosh, C., Hemadri, D., Sanyal, A., Pattnaik, B., and Venkataramanan, R. (1997). One-tube and One-Buffer System of RT-PCR Amplification of 1D Gene of Foot-And-Mouth Disease Virus Field Isolates. *Acta Virol.* 41, 153–155.

Ulloa, S., Bravo, C., Parra, B., Ramirez, E., Acevedo, A., Fasce, R., et al. (2020). A Simple Method for SARS-CoV-2 Detection by rRT-PCR without the Use of a Commercial RNA Extraction Kit. *J. Virol. Methods* 285, 113960. doi:10.1016/j.jviromet.2020.113960

Van Rijn, P. A., and Boonstra, J. (2021). Critical Parameters of Real Time Reverse Transcription Polymerase Chain Reaction (RT-PCR) Diagnostics: Sensitivity and Specificity for Bluetongue Virus. *J. Virol. Methods* 295, 114211. doi:10.1016/j.jviromet.2021.114211

Voon, K., Johari, N. A., Lim, K. L., Wong, S. T., Khaw, L. T., Wong, S. F., et al. (2021). COVID-19 Sample Pooling: From RNA Extraction to Quantitative Real-Time RT-PCR. *Bio Protoc.* 11, e4005. doi:10.21769/BioProtoc.4005

Yi Han Tan, S., Yi Milton Kwek, S., Low, H., and Ling Joy Pang, Y. (2021). Absolute Quantification of SARS-CoV-2 with Clarity Plus Digital PCR. *Methods* S1046-2023 (21), 00184–00185. doi:10.1016/j.ymeth.2021.07.005

Yuan, F., Fu, J., Liu, X., Bai, J., and Peddireddi, L. (2021). Development of a Quantitative Real Time RT-PCR Assay for Sensitive and Rapid Detection of Emerging Atypical Porcine Pestivirus Associated with Congenital Tremor in Pigs. *J. Virol. Methods* 296, 114220. doi:10.1016/j.jviromet.2021.114220

Zucha, D., Androvic, P., Kubista, M., and Valihrach, L. (2020). Performance Comparison of Reverse Transcriptases for Single-Cell Studies. *Clin. Chem.* 66, 217–228. doi:10.1373/clinchem.2019.307835

Conflict of Interest: WJ, HJ, and KN were employed by Samsung Electronics Co.Ltd.

The remaining authors declare that the research was conducted in the absence of any commercial or financial relationships that could be construed as a potential conflict of interest.

frontiers
in Bioengineering and Biotechnology

ORIGINAL RESEARCH
published: 24 March 2022
doi: 10.3389/fbioe.2022.877603

High Sensitivity, Rapid Detection of Virus in High Traffic Environments

Lauren Waller[1†], Zhilin Guo[2†], Rui Tang[3], Zunming Zhang[3], Edward Wang[2], Jarred Yasuhara-Bell[4], Louise Laurent[5] and Yu-Hwa Lo[3]*

[1]Department of Bioengineering, University of California, San Diego, San Diego, CA, United States, [2]Department of Mechanical and Aerospace Engineering, University of California, San Diego, San Diego, CA, United States, [3]Department of Electrical and Computer Engineering, University of California, San Diego, San Diego, CA, United States, [4]Independent Consultant, San Diego, CA, United States, [5]Department of Obstetrics and Gynecology and Reproductive Sciences, University of California, San Diego, San Diego, CA, United States

Edited by:
Run Zhang,
The University of Queensland,
Australia

Reviewed by:
Chaolong Liu,
Qingdao University, China
Liu Jianping,
Southern Medical University, China
Wenzhu Zhang,
Dalian University of Technology, China

***Correspondence:**
Yu-Hwa Lo
ylo@ucsd.edu

†These authors have contributed equally to this work and share first authorship

Specialty section:
This article was submitted to Biosensors and Biomolecular Electronics,
a section of the journal Frontiers in Bioengineering and Biotechnology

Received: 16 February 2022
Accepted: 11 March 2022
Published: 24 March 2022

Citation:
Waller L, Guo Z, Tang R, Zhang Z, Wang E, Yasuhara-Bell J, Laurent L and Lo Y-H (2022) High Sensitivity, Rapid Detection of Virus in High Traffic Environments.
Front. Bioeng. Biotechnol. 10:877603.
doi: 10.3389/fbioe.2022.877603

The global pandemic caused by the SARS-CoV-2 virus has underscored the need for rapid, simple, scalable, and high-throughput multiplex diagnostics in non-laboratory settings. Here we demonstrate a multiplex reverse-transcription loop-mediated isothermal amplification (RT-LAMP) coupled with a gold nanoparticle-based lateral flow immunoassay (LFIA) capable of detecting up to three unique viral gene targets in 15 min. RT-LAMP primers associated with three separate gene targets from the SARS-CoV-2 virus (Orf1ab, Envelope, and Nucleocapsid) were added to a one-pot mix. A colorimetric change from red to yellow occurs in the presence of a positive sample. Positive samples are run through a LFIA to achieve specificity on a multiplex three-test line paper assay. Positive results are indicated by a characteristic crimson line. The device is almost fully automated and is deployable in any community setting with a power source.

Keywords: COVID19, SARS-cov-2, lateral flow assay, RT-LAMP, rapid diagnostics, point of care diagnostics, multiplexed loop mediated isothermal amplification

INTRODUCTION

In late December 2019, a major outbreak of a novel coronavirus of zoonotic origin broke out in Wuhan, Hubei province, China (Wang et al., 2020). The rampant global spread of COVID-19 has shocked and forever changed the world, with 271,376,643 confirmed cases and 5,324,969 deaths globally as of 16 December 2021 (World Health Organisation, 2021) [“WHO Coronavirus (COVID-19) Dashboard” 2021].

Socioeconomic expansion and increased travel in this modern age have become associated with a rise in the emergence of novel viruses, with notable examples including the 2003 severe acute respiratory syndrome coronavirus (SARS) outbreak, the 2009 swine flu pandemic, the 2012 Middle East respiratory syndrome coronavirus outbreak (MERS), the 2013-2016 Ebola epidemic, and the 2015 Zika virus epidemic (Baker et al., 2021). With modern transportation capable of moving a person with a contagious illness to nearly any location in the world in under 24 h, the potential for highly contagious new outbreaks poses an incredible global health risk.

Novel respiratory pathogens such as SARS-CoV-2 have an established precedent of elevated transmissibility *via* high-traffic hubs of national or international travel such as airports, train stations, and cruise terminals (Pavia 2007) (Luo et al., 2021). Fueled by its high reproduction number, asymptomatic carriers, superspreading events, increasing socio economic globalization, and an immunologically naive population, COVID-19 has wreaked havoc across the world (Hu et al., 2020).

More than ever before, rapid diagnostic tests have become a fundamental component of outbreak mitigation, with crucial roles ranging from initial detection and quarantining procedures to population-level monitoring (Oeschger et al., 2021). Although a number of diagnostic technologies exist, RT-qPCR is commonly considered the gold standard and is consequently the most widely adopted diagnostic method in test centers and hospitals. The technique consists of three steps: collection of nasopharyngeal or oropharyngeal swabs from patients; total RNA extraction or isolation; and specific detection of target viral genome sequences *via* RT-qPCR. In RT-qPCR, the viral RNA is transcribed into cDNA by reverse transcriptase. The cDNA is the template for qPCR. Amplification products are quantified by the addition of a fluorescent label during replication. As the reaction proceeds, the fluorescence signal is directly proportional to DNA concentration and the linear correlation can be used to determine the amount of template at the start of the reaction (Kralik and Ricchi 2017). The inclusion of reverse transcription for the diagnosis of RNA viruses provides the necessary sensitivity and specificity for widespread use in a laboratory setting.

However, RT-qPCR is not sufficient for use in many high-traffic community settings for a number of reasons. This technique includes several sample handling steps; therefore, the sample-to-result procedure in a clinical diagnostic laboratory can take about 3–24 h or more, depending on the test center (Dao Thi et al., 2020). RT-qPCR also requires specialized lab equipment such as thermocyclers and fluorometers, and skilled operational personnel. These requirements are not easily implementable in community settings without significant equipment, training, and staffing costs, especially in underdeveloped and remote areas.

Isothermal amplification techniques are a popular solution for bringing diagnostic testing to non-laboratory environments due to its impressive sensitivity and ability to be performed with minimal resources (Sahoo et al., 2016). While a large number of isothermal amplification methods exist, loop-mediated isothermal amplification (LAMP) is amongst the most popular. LAMP enables nucleic acid amplification in 10–40 min using 4 to 6 primers and a polymerase with chain displacing ability at a constant temperature of around 65°C. In the case of reverse transcription LAMP (RT-LAMP), the process is initiated by reverse transcription from the backward inner primer (BIP) by binding onto the 3’ end. Concurrently, a new cDNA strand is created by binding of the B3 primer to the template aided by a strand displacing DNA polymerase. Loops at the 3’ end are created as the single stranded copy binds to itself. Then, the forward inner primer (FIP) binds to the 5’ end and aided by DNA polymerase, synthesizes a complementary strand. The F3 primer with DNA polymerase binds to the complementary strand and generates a new double stranded DNA while displacing the previous single strand. The amplification products are an amalgamation of target RNA and primers. The single stranded DNA forms dumbbell-like structures as the ends fold and bind to themselves. Exponential amplification of the dumbbell-like structure is then initiated. The addition of loop primers greatly speeds up the reaction (Huang et al., 2020) (Mautner et al., 2020) (Thompson and Lei, 2020).

The detection of target amplification products in RT-LAMP assays is frequently colorimetric. One common method is to use a pH indicator (e.g., phenol red) and execute the reaction in a weakly buffered environment. The lowering of the pH as the reaction proceeds results in a visible color change from red to yellow (Dao Thi et al., 2020). With pre-mixed reverse transcription and colorimetric LAMP reagents widely available (e.g., WarmStart Colorimetric LAMP 2X Master Mix, New England Biolabs, MA, United States), RT-LAMP is an appealing technique for deployment in high-traffic community settings. The colorimetric detection can be accelerated by adding chemicals (e.g., guanidine hydrochloride) and primers associated with additional target gene segments from the same virus. In the same spirit, primers for multiple diseases can be multiplexed to yield a single positive or negative in a one-pot mixture.

To achieve specificity of specific disease targets within this one-pot mixture, RT-LAMP can be coupled with a lateral flow immunoassay (LFIA). LFIAs offer an enticing solution to point-of-care diagnostics due to their low cost, high specificity, and simplicity of use (Koczula and Gallotta 2016) (Zhu et al., 2020) (Chen et al., 2021) (Zhang et al., 2021). Lateral flow assays are a paper-based platform that allows a sample to be placed on a test device and results to be displayed in about 10 min. The device usually consists of a sample pad, a conjugate pad, a nitrocellulose membrane, and an absorbent pad. The sample is mixed with running buffers and placed onto the sample pad. The conjugate pad usually contains reporter particles such as functionalized gold nanoparticles. If a positive sample is present, the reporter particles will bind to the analyte. Striped lines of antibody on the nitrocellulose membrane capture the analyte, and a control line captures extraneous reporter particles to validate the test. Positive results for an analyte will appear as a red line.

Here we present a high-throughput, rapid diagnostic machine that can be employed in almost any high-traffic public setting for the rapid detection of up to three gene targets, and the method can be readily extended to more targets from different organisms. The system uses RT-LAMP to isothermally amplify target sequences and provide a rapid yes or no diagnostic response based on the colorimetric change from red to yellow. Then, the RT-LAMP product is run through a lateral flow immunoassay to provide specificity. Here we use three gene targets of SARS-CoV-2 (Orf1ab, N, and E); however, the diagnostic ability can be more broadly applied by substituting the appropriate primers for other viral gene targets.

MATERIALS AND METHODS

Automated System Architecture

A customized machine is utilized to automate all steps beyond the loading of patient samples. The machine leverages an existing pipetting robot (OT2-Pipettes, Opentrons, Long Island City, NY, United States) for precision liquid transfer. Customized 96-well plate holders and cassette holders driven by stepper motors are used to convey 96-well plates and LFIA cassettes into and out from the machine. Position sensors are installed to ensure precision and repeatability. A customized heating unit is

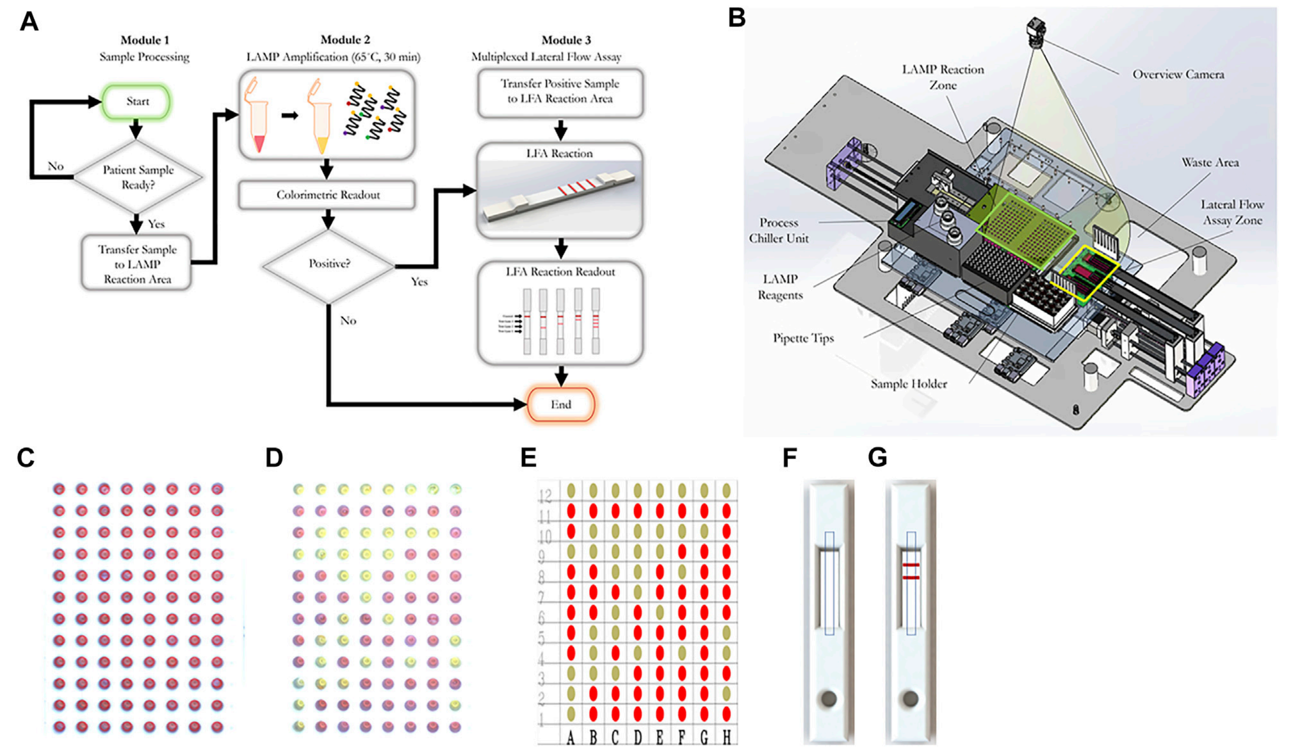

FIGURE 1 | The workflow of our RT-LAMP-LFIA prototype system and the schematic of our automatic system. **(A)** Workflow schematic from initial patient sample placement to end. Samples undergo a colorimetric loop-mediated isothermal amplification reaction. Samples that are positive (as indicated by a colorimetric change from red to yellow) are transferred to a multiplexed lateral flow assay test strip, which can differentiate from up to three target sequences. **(B)** Machine schematic **(C)** Example 96-well plate image captured by the overview camera before RT-LAMP reaction. The red circle represents the region of interest (ROI) of each well. The decision matrix is determined by the color change within the red circles **(D)** Example 96-well plate image captured by the overview camera after RT-LAMP reaction. **(E)** Final decision matrix for RT-LAMP reaction readout **(F)** Example rendering of LFIA cassette image captured by the overview camera before LFIA. Dashed rectangles represent ROIs of the LFIA cassettes. **(G)** Example rendering of LFIA cassette image captured by the overview camera after LFIA.

installed under the 96-well plate to enable LAMP reaction heating. The colorimetric reaction readouts are detected using an overview camera (Flea3 USB3, Model: FL3-U3-13E4C-C, Teledyne FLIR LLC). A process chiller unit (Temperature Module, Opentrons) is adopted for liquid storage (e.g., LAMP reagents).

The machine is controlled by a desktop computer and a two-level user interface. The first level user interface opens to the system developers, which includes the system installation and calibration access. After initial installation and calibration, the second level user interface is opened to system operators for information loading and result display. Given the simplicity of the graphical user interface (GUI), system operators can be trained in minutes.

System Automation and Overarching Workflow

Nasopharyngeal swabs are collected from patients using a nasal swab and stored in iSwab Microbiome-EL (Extraction-Less) buffer (MAWI DNA Technologies, Hayward, CA, United States). Collected patient samples are loaded into the sample holder by a human operator (**Figure 1B**). All reagents are stored on top of the process chiller unit. Upon initialization, 96-well plates and cassettes filled with LFIA are conveyed into the LAMP reaction zone and the lateral flow assay zone, respectively.

TABLE 1 | Concentrations of each oligonucleotide in the 10× primer mix.

Primer	10× Concentration (stock)	1 (µM) X Concentration (final)
F (µM)IP	16	1.6
BIP	16	1.6
F3	2	0.2
B3	2	0.2
LF	8	0.8
LB	8	0.8

TABLE 2 | Concentrations of each reagent in the RT-LAMP assay.

Reagents	Volume (µl)
WarmStart Colorimetric LAMP 2X Master Mix	10
LAMP Primer Mix (10X)	2
Guanidine Hydrochloride	2
Nasopharyngeal Swab Sample	2
dH$_2$O	4
Total Volume	20

TABLE 3 | Primer sequences against Nucleocapsid (N-2), Envelope (E-2), and Orf1a-1 genes of the SARS-CoV-2 virus.

Gene target	Primer	Name	Tag	Sequence
N2	FIP	N2 FIP	5'-FITC	TGCGGCCAATGTTTGTAATCAGCCAAGGAAATTTTGGGGAC
	BIP	N2 BIP	—	CGCATTGGCATGGAAGTCACTTTGATGGCACCTGTGTAG
	F3	N2 F3	—	AACACAAGCTTTCGGCAG
	B3	N2 B3	—	GAAATTTGGATCTTTGTCATCC
	LF	N2 LF	—	TTCCTTGTCTGATTAGTTC
	LB	N2 LB	5'-Biotin	ACCTTCGGGAACGTGGTT
Orf1a	FIP	Orf1a FIP	5'-DigN	GAGGGACAAGGACACCAAGTGTATGGTTGAGCTGGTAGCAGA
	BIP	Orf1a BIP	—	CCAGTGGCTTACCGCAAGGTTTTAGATCGGCGCCGTAAC
	F3	Orf1a F3	—	CTGCACCTCATGGTCATGTT
	B3	Orf1a B3	—	AGCTCGTCGCCTAAGTCAA
	LF	Orf1a LF	—	CCGTACTGAATGCCTTCGAGT
	LB	Orf1a LB	5'-Biotin	TTCGTAAGAACGGTAATAAAGGAGC
E2	FIP	E2 FIP	—	ACCTGTCTCTTCCGAAACGAATTTGTAAGCACAAGCTGATG
	BIP	E2 BIP	—	CTAGCCATCCTTACTGCGCTACTCACGTTAACAATATTGCA
	F3	E2 F3	—	CCGACGACGACTACTAGC
	B3	E2 B3	—	AGAGTAAACGTAAAAAGAAGGTT
	LF	E2 LF	5'-TexRed	TCGATTGTGTGCGTACTGC
	LB	E2 LB	5'-Biotin	TGAGTACATAAGTTCGTAC

TABLE 4 | Sequences of N, E, and Orf1ab gene blocks.

Gene blocks	Sequence
N gene (229 nt)	AACACAAGCTTTCGGCAGACGTGGTCCAGAACAAACCCAAGGAAATTTTGGGGACCAGGAACTAATCAGACAAGGAACTGATTACAAACATTGGCCGCAAATTGCACAATTTGCCCCCAGCGCTTCAGCGTTCTTCGGAATGTCGCGCATTGGCATGGAAGTCACACCTTCGGGAACGTGGTTGACCTACACAGGTGCCATCAAATTGGATGACAAAGATCCAAATTTC
E gene (234 nt)	CCGACGACGACTACTAGCGTGCCTTTGTAAGCACAAGCTGATGAGTACGAACTTATGTACTCATTCGTTTCGGAAGAGACAGGTACGTTAATAGTTAATAGCGTACTTCTTTTTCTTGCTTTCGTGGTATTCTTGCTAGTTACACTAGCCATCCTTACTGCGCTTCGATTGTGTGCGTACTGCTGCAATATTGTTAACGTGAGTCTTGTAAAACCTTCTTTTTACGTTTACTCT
Orf1ab gene (289 nt)	TCCAGATGAGGATGAAGAAGAAGGTGATTGTGAAGAAGAAGAGTTTGAGCCATCAACTCAATATGAGTATGGTACTGAAGATGATTACCAAGGTAAACCTTTGGAATTTGGTGCCACTTCTGCTGCTCTTCAACCTGAAGAAGAGCAAGAAGAAGATTGGTTAGATGATGATAGTCAACAAACTGTTGGTCAACAAGACGGCAGTGAGGACAATCAGACAACTACTATTCAAACAATTGTTGAGGTTCAACCTCAATTAGAGATGGAACTTACACCAGTTGTTCAGACT

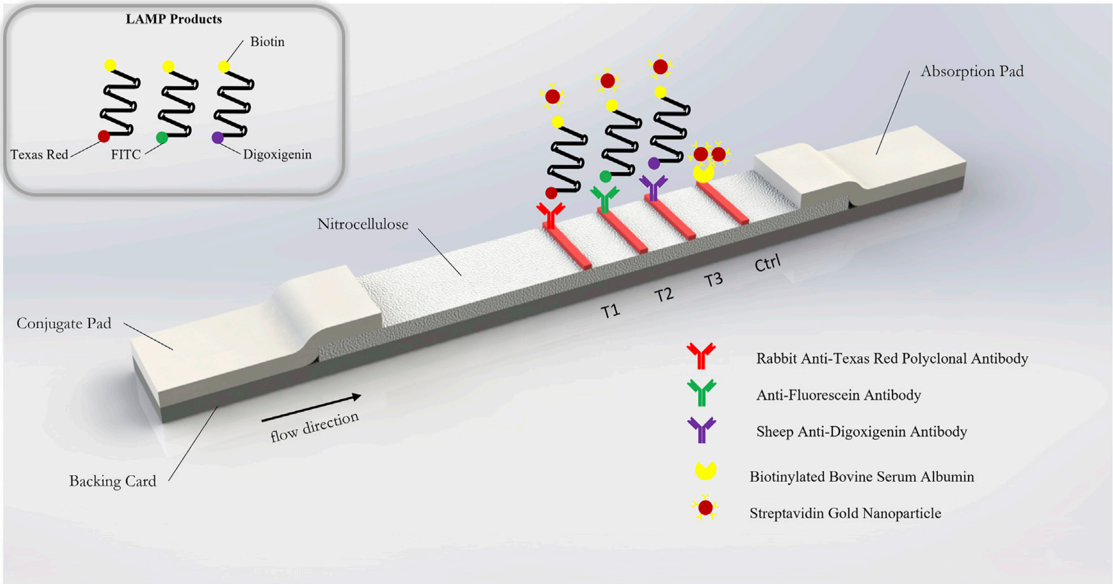

FIGURE 2 | Schematic of gold nanoparticle based lateral flow immunosorbent assay for the detection of SARS-CoV-2 Orf1a, N2, and E2 target genes.

After the system operator enters the sample information (e.g., number of samples, sample identification numbers), the machine first loads the pre-mixed LAMP reaction concoction (**Table 1**, **Table 2**) into a new 96-well plate. Next, the machine pipettes 2 µl of each patient sample into a single well in the 96-well plate. Pipette tips are changed after each sample to prevent cross-contamination of samples. Once all samples are loaded, the heating unit under the LAMP reaction zone heats the plate up to 65°C. A system timer starts once it reaches 65°C. After a preset reaction time (15–30 min), the RT-LAMP reaction is complete and positive samples are clearly identifiable by a colorimetric change from red to yellow. The colorimetric change is detected and quantitatively measured by the overview camera (Flea3 USB3, Model: FL3-U3-13E4C-C, Teledyne FLIR LLC), and the process is complete for samples that meet the threshold for a negative result. For samples that meet the criteria for a positive result, 3 µl of the LAMP product is mixed with 40 µl of running buffer (1 × PBS, pH 7.4 with 2% Tween 20) and deposited onto a lateral flow immunoassay. A system timer begins, and the result is detected and quantified after a predetermined amount of time. On the lateral flow immunoassay, positive results for each specific viral gene target will appear as a characteristic crimson line. A fourth crimson line acts as a control line and serves to validate the test. The positive readings which stand for the presence of COVID-19 RT-LAMP products are visible after 5 to 10 min using the LFIA. The colorimetric change of the LFIA is detected using the overview camera and then quantitatively measured on the computer. The final result for each sample is displayed on the user interface and a Portable Document Format (PDF) file including the sample information and detection results will be automatically stored in the local disk (or on the cloud if internet access is enabled). The system automatically displays a warning window on the user interface for 96-well plates and cassettes replenishment when needed (e.g., all the wells have been used).

Quantification of the RT-LAMP Reaction and LFIA Readout

For the RT-LAMP reaction readout, after loading the new 96-well plates, the system first identifies the region of interest (ROI) of all wells. The RT-LAMP colorimetric readout is determined based on the color change within the ROI of each well. Two images are captured, one prior to the RT-LAMP reaction and one after the RT-LAMP reaction. YUV color space is used to compare the difference between two images. Wells that exceed the threshold are considered positive samples. **Figures 1B,C,D**, show an example image captured before and after the RT-LAMP reaction, respectively. The RT-LAMP reaction detection result is shown in **Figure 1E**.

For the LFIA readout, after loading the LFIA cassettes, the system will first identify the ROI of each LFIA cassette. The LFIA colorimetric readout is determined by the appearance or lack thereof of a crimson line within the ROI. Two images are captured, one prior to the LFIA reaction and one after the LFIA reaction. For each image, mean intensity along the width direction is obtained, which compresses the ROIs into two decision lines. YUV color space is used to compare the color difference between two lines. The final LFIA readout is obtained from the peak detection result from the YUV color space difference. **Figures 1D,F,G**, show an example rendered image captured before and after the LFIA reaction, respectively.

TABLE 5 | Cq values obtained from RT-QPCR for clinical nasopharyngeal specimens.

Sample no	Test result	Cq value
1-30	Negative	Undetectable
31	Positive	27.514
32	Positive	33.405
33	Positive	25.0205
34	Positive	27.708
35	Positive	28.526
36	Positive	32.840
37	Positive	27.422
38	Positive	32.859
39	Positive	30.810
40	Positive	29.406
41	Positive	27.204
42	Positive	32.703
43	Positive	35.175
44	Positive	25.782
45	Positive	21.299
46	Positive	34.516
47	Positive	26.791
48	Positive	31.589
49	Positive	27.127
50	Positive	25.745
51	Positive	26.304
52	Positive	26.203
53	Positive	31.114
54	Positive	34.482
55	Positive	33.929
56	Positive	28.251
57	Positive	34.532
58	Positive	35.496
59	Positive	33.400
60	Positive	31.301

RT-LAMP Primer Design and Viral Targets Information

RT-LAMP primers against Nucleocapsid (N-2), Envelope (E-2), and ORFla-1 genes (**Table 3**) were designed according to previously published specifications (Zhang et al., 2020) and were synthesized by Integrated DNA Technologies (IDT, San Diego, CA, United States). The sequence of primers and concentrations of each oligonucleotide in the 10x primer mix are shown in **Tables 1**, **2**. The 10× primer mix was prepared by dissolving the oligonucleotides in nuclease-free water. It was stored at −20°C before use.

The RT-LAMP primer sets corresponding to the N-2, E-2, and ORF1a-1 genes were each designed to incorporate a unique tag onto each amplified RT-LAMP product. Texas Red was labeled on the 5’ end of the E-2 LF primer, FITC was labeled on the 5’ end of the N-2 FIP primer, and Digoxigenin was labeled on the 5’ end of the ORF1a-1 FIP primers. Biotin was labeled on the 5’ end of the LB primers for all three genes. Accordingly, Anti-Texas Red, Anti-Fluorescein, and Anti-Digoxigenin antibodies were striped onto the nitrocellulose membrane of the LFIA as

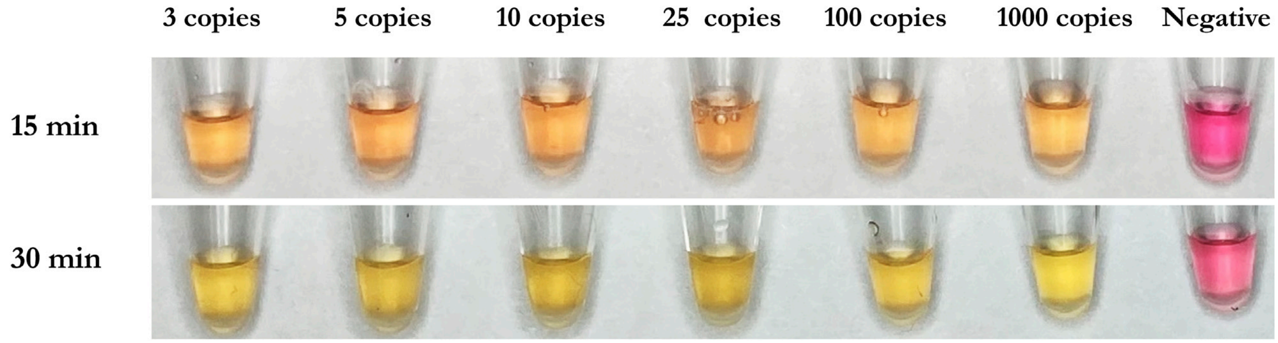

FIGURE 3 | Demonstrative colorimetric loop-mediated isothermal reaction using primers as listed in **Table 1**. Viral RNA from SARS-CoV-2 (ATCC) were spiked in the amounts of 0, 3, 5, 10, 25, 100, and 1,000 RNA copies per microwell and reactions were imaged after 15 and 30 min, respectively.

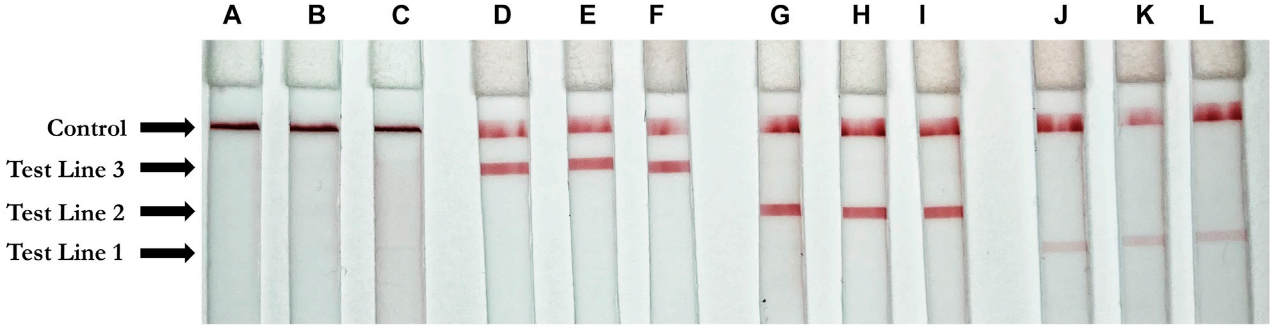

FIGURE 4 | Positive test results for three unique gene blocks (subsections of SARS-CoV-2 viral genome). Test Line 1 (Texas Red Antibody, 1 mg/ml, Cat. #A-6399, ThermoFisher Scientific, Waltham, MA, United States); Test line 2 (Fluorescein antibody, 1 mg/ml, Cat. #ab19491, Abcam, Cambridge, United Kingdom); Test Line 3 (Digoxigenin antibody, 2.5 mg/ml, Cat. #3210-0488, Bio-Rad, Hercules, CA, United States); Control line (biotinylated bovine serum albumin, 3 mg/ml, Cat. #B-2007-10, Vector Labs, Burlingame, CA, United States) **(A–C)** Negative control. **(D–F)** Orf1a gene block (1 ng/µl) **(G–I)** N gene block (1 ng/µl) **(J–L)** E gene block (1 ng/µl).

test lines, while the biotin-BSA was used as the control line. Leveraging the natural affinity of streptavidin to biotin, which is one of the strongest non-covalent interactions in nature, streptavidin gold nanoparticles (Streptavidin, 40 nm 10 OD Colloidal Gold, Attogene, TX, United States) served as the reporter particle. Therefore, the RT-LAMP products for each gene only bind to one test line, enabling the detection of up to three distinct viral gene target detections on a single LFIA. Because in this instance all three gene targets were from RNA from the same virus and thus competition between templates can occur, gene blocks (sub-sequences of the entire SARS-CoV-2 RNA template) are used to validate the test. In the clinical and contrived viral tests, competition between primer sets can obscure some gene sequences on the LFIA; however, the RT-LAMP colorimetric change from red to yellow will be unaffected.

The SARS-CoV-2 RNA (VR-3280SD) was purchased from the American Type Culture Collection (ATCC, Manassas, Virginia, United States). The COVID-19 RNA was diluted as necessary by nuclease-free water. The Nucleocapsid (N), Envelope (E), and ORF1ab gene blocks were synthesized by Integrated DNA Technologies (IDT, IA, United States), with sequences shown in **Table 4**.

Lateral Flow Immunoassay

The lateral flow immunoassay (LFIA) (**Figure 2**) was comprised of a conjugate pad (GFCP203000 Glass Fiber Conjugate Pad Sheets, Millipore Sigma, St. Louis, MO, United States), a nitrocellulose membrane (Whatman FF120HP, Cytiva Life Sciences, Marlborough, MA, United States), an absorbent pad (Blotting Paper, Grade 222, Ahlstrom-Munksjö, Helsinki, Finland), and a backing card (DCN Diagnostics, Carlsbad, CA, United States). The dimensions of the conjugate pad were 2 cm × 30 cm; the dimensions of the nitrocellulose membrane were 2.5 cm × 30 cm; the dimensions of the absorbent pad were 2 cm × 30 cm); and the dimensions of the backing card were 6 cm × 30 cm. The conjugate pad was soaked in a blocking solution (1% bovine serum albumin + 0.05% Tween 20 + 0.2% sucrose, diluted in PBS) on a shaker at low speed for 10 min and the conjugate pads were dried on a drying rack overnight. Anti-texas red antibody (anti-TexR, 1 mg/ml, Cat. #A-6399, ThermoFisher Scientific, Waltham, MA, United States), rabbit anti-fluorescein antibody (anti-FITC, 1 mg/ml, Cat. # ab19491, Abcam, Cambridge, United Kingdom), sheep anti-digoxigenin antibody (anti-DigN, 2.5 mg/ml, Cat. #3210-0488, Bio-Rad, Hercules, CA, United States) and biotinylated bovine serum

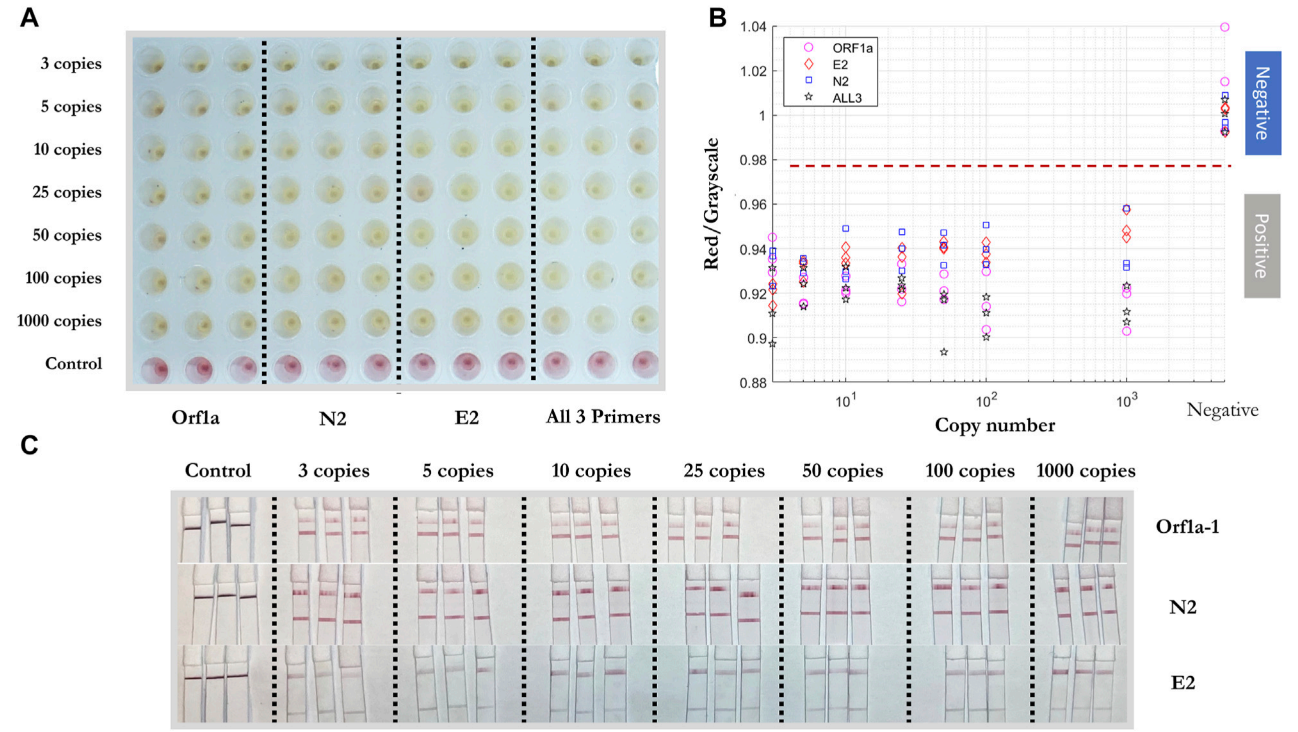

FIGURE 5 | Sensitivity test of colorimetric RT-LAMP reaction and LFIA of artificial SARS-CoV-2 RNA template. **(A)** Positive/negative RT-LAMP products with ORF1a-1, N-2, E-2, and all three primer sets after the reaction, taken by overview camera. **(B)** Red/grayscale value vs. RNA copy numbers of both positive and negative samples. **(C)** LFIA read-outs for RT-LAMP products amplified for ORF1ab, N, and E gene blocks.

albumin (biotin-BSA, 3 mg/ml, Cat. #B-2007-10, Vector Labs, Burlingame, CA, United States) were stripped at the detection regions on the nitrocellulose using a lateral flow reagent dispenser (Claremont Biosolutions, Upland, CA, United States) at test line 1 (TL1), test line 2 (TL2), test line 3 (TL3) and control line (Ctrl), respectively, with each line separated by 5 mm. The membranes were then assembled together and the assembled LFIA were cut into 4-mm dipsticks. Then, 3 µl of streptavidin gold nanoparticles (Streptavidin, 40 nm 10 OD Colloidal Gold, Attogene, TX, United States) were immobilized at one end of the conjugate pad for each strip and dried in a vacuum. The dipsticks were packaged in a plastic cassette (DCNDx, Carlsbad, CA, United States) and stored in a 4°C fridge in a heat-sealed foil packet with a silica gel desiccant until use. The LFIAs were tested 3 months later and found to still be viable.

Quantification of the RT-LAMP Reaction and LFIA Readout

The colorimetric change of the RT-LAMP reaction is quantitatively measured by the overview camera (Flea3 USB3, Model: FL3-U3-13E4C-C, Teledyne FLIR LLC). The prototype algorithm identifies the region of interest (ROI) of all RT-LAMP wells in the 96-well plate. The grayscale and red values of each well are evaluated inside the ROI. In each batch, at least three negative samples are present to serve as negative controls. The average value of the red/grayscale value of these negative controls are used to normalize the red/grayscale value for every well. Intuitively, a larger red/grayscale value means that the sample is more red, corresponding to a negative result of colorimetric RT-LAMP. A smaller red/grayscale value means that the sample is less red–and thus a colorimetric change from red to yellow has occurred. Accordingly, our algorithm assigns a cutoff value of > 0.98 for negative samples and < 0.98 for positive samples. Independently, the same algorithm was employed using the built-in tools of ImageJ for quantification for the experiments denoted in the Results section.

Clinical Sample Handling and RT-qPCR

Clinical samples were obtained from the UCSD COVID-19 Research Biobank (University of California, San Diego, CA, United States). Nasopharyngeal swabs from patients both positive and negative for the SARS-CoV-2 virus were collected in iSwab Microbiome-EL (Extraction-Less) buffer. Collected samples were aliquoted into freezer tubes in a BSL2 + hood and were stored at −80°C prior to use. RT-qPCR was performed on all samples. Cq values are noted in **Table 5**.

RESULTS

Time-To-Result Test

WarmStart Colorimetric LAMP 2X Master Mix and guanidine hydrochloride solution (New England Biolabs, Ipswich, MA,

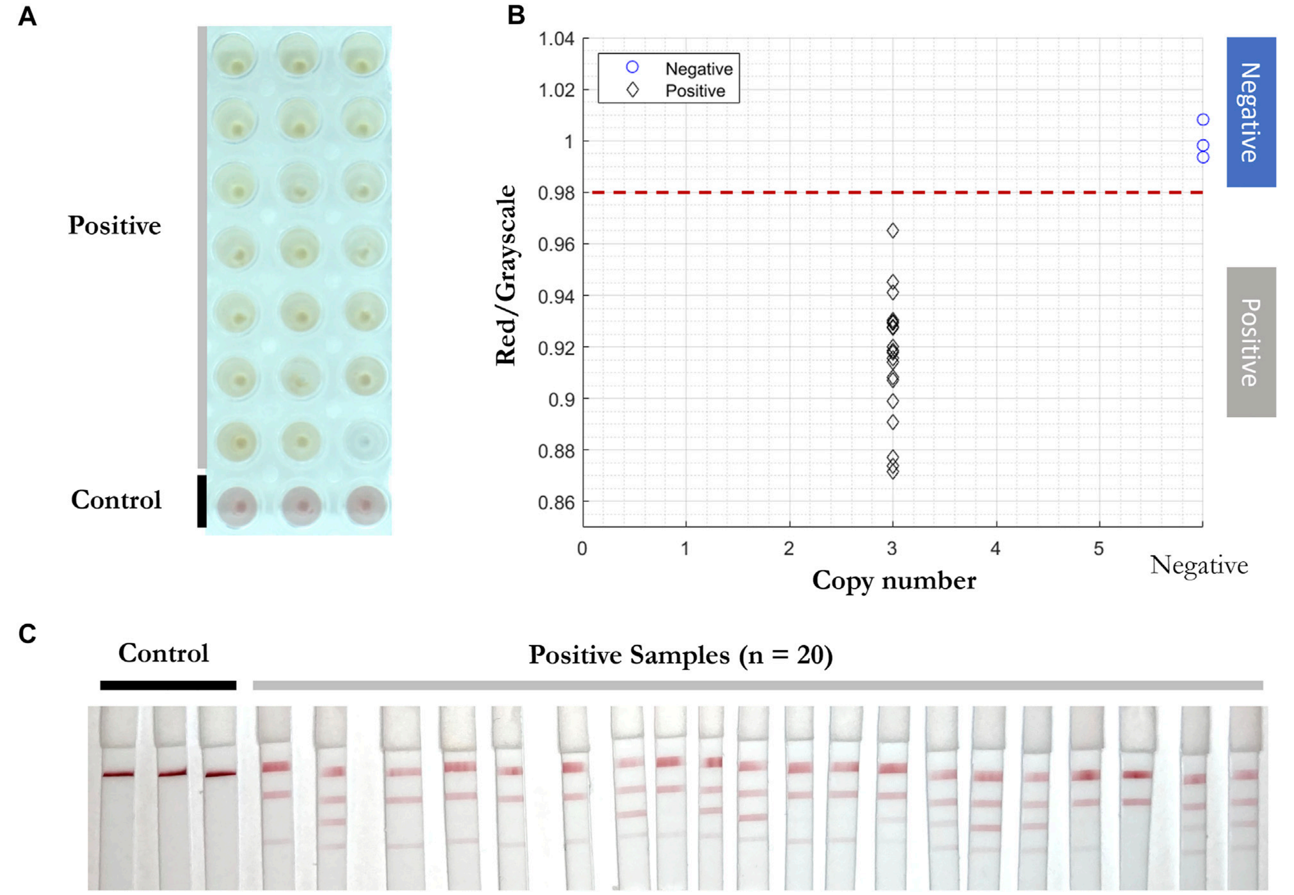

FIGURE 6 | Reproducibility test of RT-LAMP-LFIA prototype system at the lower limit of detection. **(A)** RT-LAMP products from 3 initial template copies (*n* = 20) and negative control samples (*n* = 3) after the reaction, taken by overview camera. **(B)** Red/grayscale vs. copy numbers of both positive and negative samples. **(C)** LFIA read-outs for RT-LAMP products amplified for all three genes.

United States) were used to detect the SARS-CoV-2 RNA template. The RNA template was diluted by nuclease-free water into samples with 3, 5, 10, 25, 50, 100, and 1,000 genome copies/ well. The three custom RT-LAMP primers against Nucleocapsid (N-2), Envelope (E-2), and ORFla-1 genes (**Table 3**) were mixed together. The colorimetric RT-LAMP reaction was conducted at 65°C and imaged after 15 and 30 min. The test demonstrated a sensitivity of 3 copies/ well of SARS-CoV-2 RNA template after 15 min, as observed by the red to yellow color change, while the negative sample stayed red after the reaction (**Figure 3**). The 30 min time point was chosen for subsequent experiments to allow ample time for the reaction to proceed to completion.

Multiplexed Gene Detection by Colorimetric RT-LAMP and LFIA

Using each single gene block (N, E, and Orf1ab), RT-LAMP reactions were carried out in triplicate with all three primers present. Following the reaction, 3 µl of LAMP product was applied to the sample region of the LFIA with 40 µl of running buffer. As expected, only one positive line relative to the corresponding amplified RT-LAMP product was observed on each strip, confirming that in the presence of a single non-competing RNA template (gene block), the three mixed primer sets from Orf1a, E-2, and N-2 genes will produce a single positive result on the LFIA corresponding to their appropriate tag (Digoxigenin, Texas Red, or Fluorescein). The weaker signal for E2 is attributed to natural variation in antibody efficacy but is still clearly visible. The no template control showed no result at any test line. Accumulation of streptavidin AuNPs at the control line was observed in all cases. Results are depicted in **Figure 4**.

Sensitivity of Colorimetric RT-LAMP and LFIA

To test the sensitivity of the colorimetric RT-LAMP reaction of the SARS-CoV-2 RNA template, N-2, E-2, and ORF1a-1 primer sets were added individually and together in colorimetric RT-LAMP master mix solutions with 3, 5, 10, 25, 50, 100, and 1,000 RNA copies per well (**Figure 5**). All conditions were tested in triplicate. All positive samples turned yellow within 30 mins, while negative samples remained red. The results were quantified using red/ grayscale values measured by ImageJ. Positive samples amplified

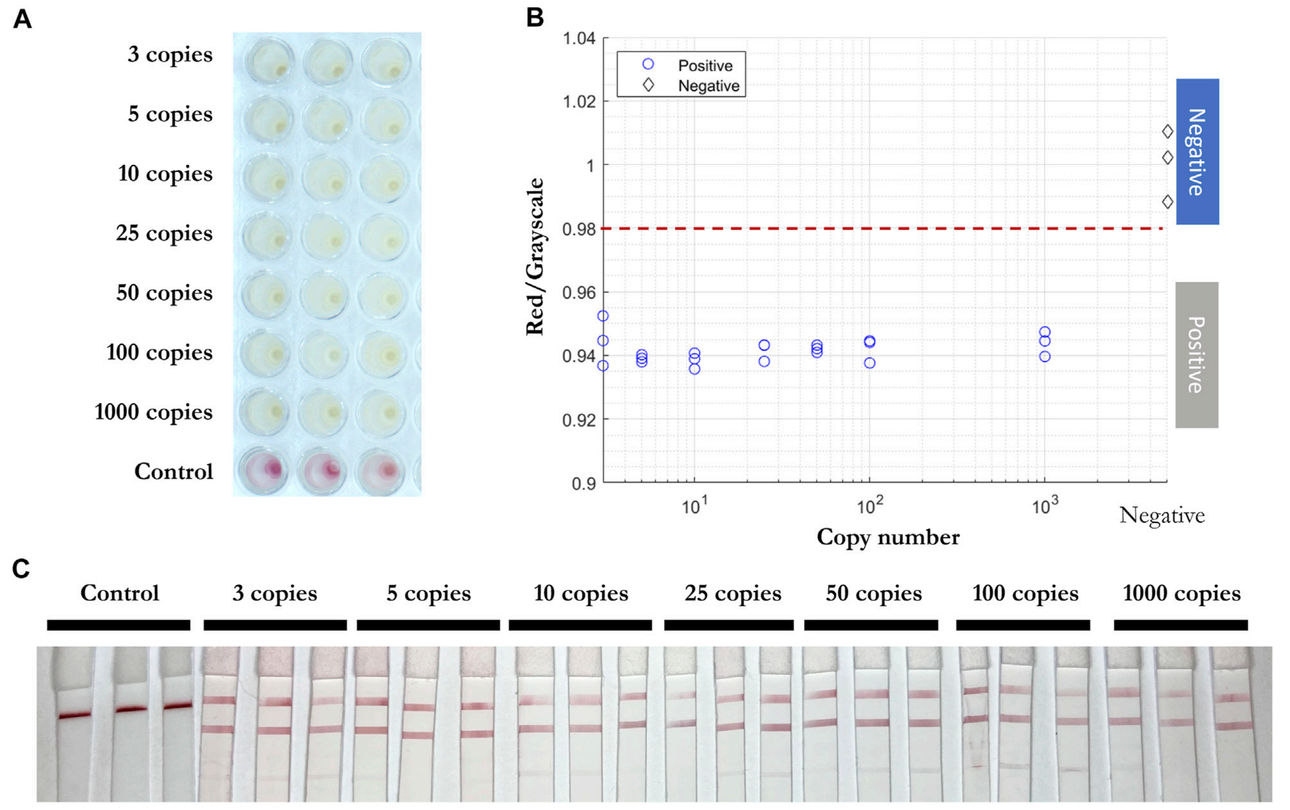

FIGURE 7 | Direct RT-LAMP-LFIA testing of inactivated viral particles without prior RNA purification or extraction. **(A)** RT-LAMP products for inactivated viral particles (3, 5, 10, 25, 50, 100, and 1,000 copies) and negative control samples with three sets of primers, taken by overview camera. **(B)** Red/grayscale vs. copy numbers of both positive and negative samples. **(C)** LFIA read-outs for RT-LAMP products amplified for all three genes.

by primer sets alone or together were distributed between 0.9 and 0.96. For negative samples, these values were around 1. For RT-LAMP products amplified by one set of primers, 3 µl of each amplification product was run on the LFIA. As expected, only one positive line relative to the appropriate amplified gene was observed on each strip for all positive samples.

To test the reproducibility of the RT-LAMP-LFIA prototype system at the lower limit of detection, all three primers were added into the RT-LAMP master mix with 3 copies of SARS-CoV-2 RNA template for twenty replicates, with triplicates of negative controls. The experiment was carried out at 65°C for 30 min. A red to yellow color change was observed by the prototype camera from above. The red/grayscale values measured by ImageJ distributed below 0.98 for positive samples, while the values for negative control samples were around 1 (**Figure 6**).

As expected, 5 to 10 min after adding the RT-LAMP products and running buffer onto each conjugate pad of the LFIA, different positive readings were shown. In the presence of a single RNA target and three sets of primers, competition for a limited amount of template strands means that some reactions can overtake others. As a self-limiting reaction, the process stops when a certain amount of products form or the reaction reaches certain (acid) pH values. Therefore, the amount of N-2, E-2, and ORF1a-1 primer sets' amplified products can vary and show different positive read-outs on the LFIA (**Figure 6C**).

Validation of RT-LAMP and LFIA for Inactivated Whole Viral Particles

RT-qPCR (Smyrlaki et al., 2020) (Wee et al., 2020) and RT-LAMP assays (Lamb et al., 2020) (Rabe and Cepko 2020) are compatible with direct testing of nasopharyngeal and oropharyngeal swab specimens without an RNA purification or extraction step. To test the efficiency of RT-LAMP and LFIA, inactivated viral particles (ATCC, VR-1986HK) diluted into 3, 5, 10, 25, 50, 100, and 1,000 copies were added in the RT-LAMP master mix with the three gene primer sets (**Figure 7**). After 30 min at 65°C, a red to yellow color change was captured in wells with the inactivated viral particles by the prototype system camera. The red/grayscale value as measured by ImageJ for positive samples was distributed at around 0.94, while all the negative samples had red/grayscale values above 0.98. Next, 3 µl of each amplification product was mixed with 40 µl of running buffer before being deposited on the conjugate pad of a LFIA strip. Positive read-outs were mainly observed for ORF1a-1 gene amplified products (**Figure 7C**) as a result of primers competing during the self-limiting RT-LAMP reaction.

Next, inactivated viral particles were spiked into unique negative patient swab samples preserved in iSwab Microbiome-EL (Extraction-Less) buffer to mimic patient-to-patient variation of conditions in amounts of 3, 5, 10, 25, 50, 100, and 1,000 copies per reaction. All samples were red prior to the RT-LAMP reaction,

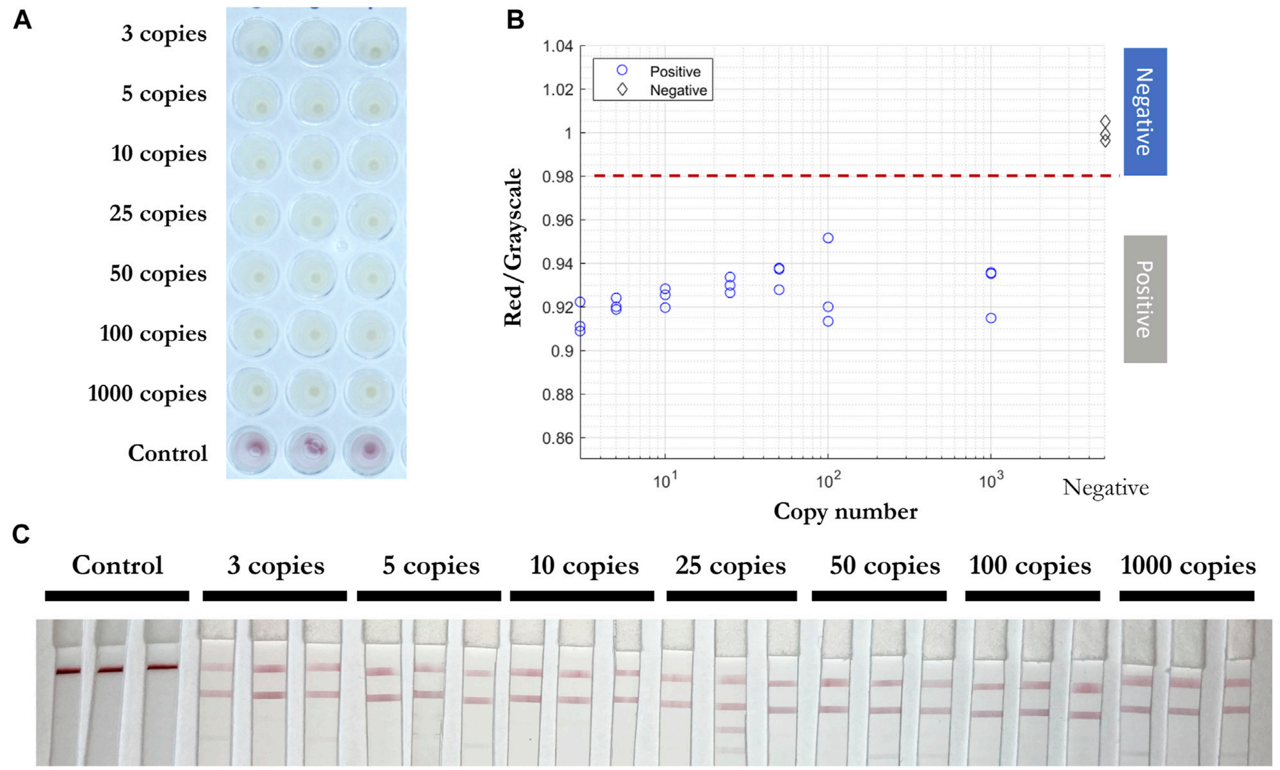

FIGURE 8 | Direct RT-LAMP-LFIA testing of spiked inactivated viral particles in nasopharyngeal swab specimens without a prior RNA purification or extraction. **(A)** RT-LAMP products for inactivated viral particles spiked in nasopharyngeal swab specimens (3, 5, 10, 25, 50, 100, and 1,000 copies) and negative control samples with three sets of primers, taken by overview camera. **(B)** Red/grayscale vs. copy numbers of both positive and negative samples. **(C)** LFIA read-outs for RT-LAMP products amplified for all three genes.

and positive samples were yellow after 30 min at 65°C. The red/grayscale values of positive samples were consistently below 0.96, while the negative samples were distributed around 1 (**Figure 8**). Due to primers competing during the self-limiting RT-LAMP reaction, positive read-outs on the LFIA were mainly observed for ORF1a-1 gene amplified products (**Figure 8C**).

Validation of RT-LAMP and LFIA For Clinical Samples

2 μl of solution from 30 positive and 30 negative clinical samples (**Table 5**) were added into RT-LAMP master mix with all three primer sets present. The positive samples turned yellow within 30 min at 65°C and had red/grayscale values between 0.9 and 0.94. The negative samples remained red with red/grayscale values above 0.98 as quantified by ImageJ (**Figure 9**). For positive samples, read-outs were observed for all samples on at least one test line on the LFIA (**Figure 9C**).

DISCUSSION

In this paper, we presented a semi-automated RT-LAMP-LFIA prototype system and evaluated its capability to test nasopharyngeal swab samples from patients without a prior RNA purification or extraction step. The system is almost fully automated and does not require trained personnel or specialized laboratory equipment such as thermocyclers. The simple design and automated sample-to-answer workflow indicate that our system is suitable for implementation in high-traffic community settings such as airports or event centers for rapid and easy to use point-of-care diagnostics.

We tested RT-LAMP primer sets for N, E, and ORF1ab genes of the SARS-CoV-2 virus and validated their results on the LFIA. Multiplexing of colorimetric RT-LAMP reactions in a single pot for the SARS-CoV-2 gene targets accelerated the reaction to yield results within 15 min. Moreover, the multiplexed read-out of up to 3 genes on a single LFIA can further distinguish multiple viral public health threats on the same platform - for example, SARS-CoV-2, Ebola, and yellow fever.

The main advantages of the RT-LAMP-LFIA method–its simplicity, low cost, high sensitivity, and high specificity–makes it ideal for use as a high-throughput diagnostic device in non-laboratory settings. To apply the method and system to detect multiple viruses or their variants, one can extend the primer set and divide the sample into a few LAMP reaction pots, each containing a chosen set of gene targets for specific organisms. Thus the overall technique and system reported here are scalable to protect the public from future outbreak and epidemic.

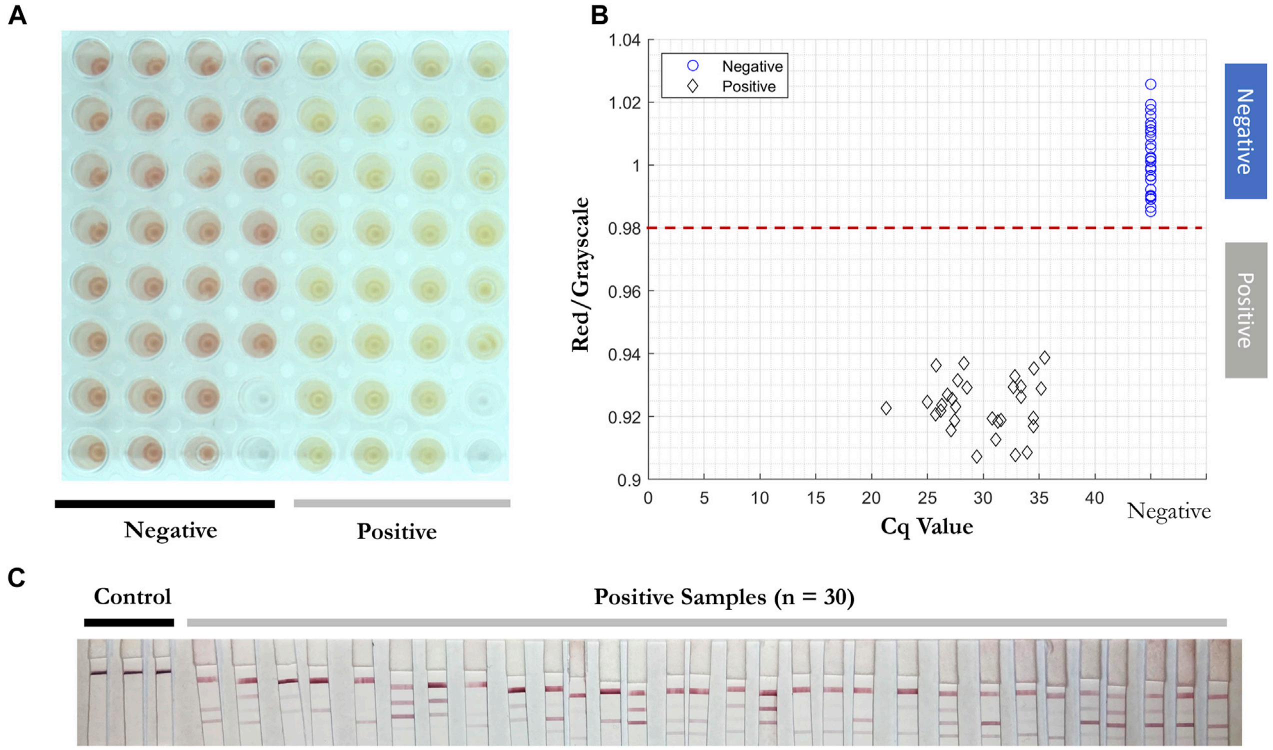

FIGURE 9 | Direct RT-LAMP-LFIA testing of 30 positive and 30 negative clinical nasopharyngeal swab specimens without a prior RNA purification or extraction. **(A)** RT-LAMP products for 30 positive and 30 negative clinical samples amplified with three sets of primers, taken by overview camera. **(B)** Red/grayscale vs. copy numbers of both positive and negative samples. **(C)** LFIA read-outs for RT-LAMP products amplified for all three genes.

DATA AVAILABILITY STATEMENT

The original contributions presented in the study are included in the article/**Supplementary Material**, further inquiries can be directed to the corresponding author.

AUTHOR CONTRIBUTIONS

LW and ZG have contributed equally to this work and share first authorship.

FUNDING

This research is based upon work supported in part by the Office of the Director of National Intelligence (ODNI), Intelligence Advanced Research Projects Activity (IARPA), *via* 2020-20090400002. The views and conclusions contained herein are those of the authors and should not be interpreted as necessarily representing the official policies, either expressed or implied, of ODNI, IARPA, or the United States Government. The United States Government is authorized to reproduce and distribute reprints for governmental purposes notwithstanding any copyright annotation therein. This work was performed, in part, at the San Diego Nanotechnology Infrastructure (SDNI) of UCSD, a member of the National Nanotechnology Coordinated Infrastructure (NNCI), which is supported by the National Science Foundation (Grant No. ECCS-1542148).

SUPPLEMENTARY MATERIAL

The Supplementary Material for this article can be found online at: https://www.frontiersin.org/articles/10.3389/fbioe.2022.877603/full#supplementary-material

REFERENCES

Baker, R. E., Mahmud, A. S., Miller, I. F., Rajeev, M., Rasambainarivo, F., Rice, B. L., et al. (2021). Infectious Disease in an Era of Global Change. *Nat. Rev. Microbiol* 20, 193–205. doi:10.1038/s41579-021-00639-z

Chen, X., Wang, S., Tan, Y., Huang, J., Yang, X., and Li, S. (2021). Nanoparticle-Based Lateral Flow Biosensors Integrated with Loop-Mediated Isothermal Amplification for the Rapid and Visual Diagnosis of Hepatitis B Virus in Clinical Application. *Front. Bioeng. Biotechnol.* 9, 731415. doi:10.3389/fbioe.2021.731415

Dao Thi, V. L., Herbst, K., Boerner, K., Meurer, M., Kremer, L. P., Kirrmaier, D., et al. (2020). A Colorimetric RT-LAMP Assay and LAMP-Sequencing for

Detecting SARS-CoV-2 RNA in Clinical Samples. *Sci. Transl. Med.* 12, 556. doi:10.1126/scitranslmed.abc7075

Hu, B., Guo, H., Zhou, P., and Shi, Z.-L. (2020). Characteristics of SARS-CoV-2 and COVID-19. *Nat. Rev. Microbiol.* 19, 141–154. doi:10.1038/s41579-020-00459-7

Huang, W. E., Lim, B., Hsu, C. C., Xiong, D., Wu, W., Yu, Y., et al. (2020). RT-LAMP for Rapid Diagnosis of Coronavirus SARS-CoV-2. *Microb. Biotechnol.* 13 (4), 950–961. doi:10.1111/1751-7915.13586

Koczula, K. M., and Gallotta, A. (2016). Lateral Flow Assays. *Lateral Flow Assays" 60* 60 (1), 111–120. doi:10.1042/EBC20150012

Kralik, P., and Ricchi, M. (2017). A Basic Guide to Real Time PCR in Microbial Diagnostics: Definitions, Parameters, and Everything. *Front. Microbiol.* 8. doi:10.3389/fmicb.2017.00108

Lamb, L. E., Bartolone, S. N., Ward, E., and Chancellor, M. B. (2020). Rapid Detection of Novel Coronavirus/Severe Acute Respiratory Syndrome Coronavirus 2 (SARS-CoV-2) by Reverse Transcription-Loop-Mediated Isothermal Amplification. *PLoS ONE* 15, e0234682. doi:10.1371/journal.pone.0234682

Luo, Z., Wang, W., Ding, Y., Xie, J., Lu, J., Xue, W., et al. (2021). Epidemiological Characteristics of Infectious Diseases Among Travelers between China and Foreign Countries before and during the Early Stage of the COVID-19 Pandemic. *Front. Public Health* 9. doi:10.3389/fpubh.2021.739828

Mautner, L., Baillie, C.-K., Herold, H. M., Volkwein, W., Guertler, P., Eberle, U., et al. (2020). Rapid point-of-care Detection of SARS-CoV-2 Using Reverse Transcription Loop-Mediated Isothermal Amplification (RT-LAMP). *Virol. J.* 17 (160). doi:10.1186/s12985-020-01435-6

Oeschger, T. M., McCloskey, D. S., Buchmann, R. M., Choubal, A. M., Boza, J. M., Mehta, S., et al. (2021). Early Warning Diagnostics for Emerging Infectious Diseases in Developing into Late-Stage Pandemics. *Acc. Chem. Res.* 54 (19), 3656–3666. doi:10.1021/acs.accounts.1c00383

Pavia, A. T. (2007). Germs on a Plane: Aircraft, International Travel, and the Global Spread of Disease. *J. Infect. Dis.* 195 (5), 621–622. doi:10.1086/511439

Rabe, B. A., and Cepko, C. (2020). SARS-CoV-2 Detection Using Isothermal Amplification and a Rapid, Inexpensive Protocol for Sample Inactivation and Purification. *Proc. Natl. Acad. Sci. U.S.A.* 117, 24450–24458. doi:10.1073/pnas.2011221117

Sahoo, P. R., Sethy, K., Mohapatra, S., and Panda, D. (2016). Loop Mediated Isothermal Amplification: An Innovative Gene Amplification Technique for Animal Diseases. *Vet. World* 9, 465–469. doi:10.14202/vetworld.2016.465-469

Smyrlaki, I., Ekman, M., Lentini, A., Rufino de Sousa, N., Papanicolaou, N., Vondracek, M., et al. (2020). Massive and Rapid COVID-19 Testing Is Feasible by Extraction-free SARS-CoV-2 RT-PCR. *Nat. Commun.* 11. doi:10.1038/s41467-020-18611-5

Thompson, D., and Lei, Y. (2020). Mini Review: Recent Progress in RT-LAMP Enabled COVID-19 Detection. *Sensors Actuators Rep.* 2, 100017. doi:10.1016/j.snr.2020.100017

Wang, C., Horby, P. W., Hayden, F. G., and Gao, G. F. (2020). A Novel Coronavirus Outbreak of Global Health Concern. *The Lancet* 395 (10223), 470–473. doi:10.1016/S0140-6736(20)30185-9

Wee, S. K., Sivalingam, S. P., and Yap, E. P. H. (2020). Rapid Direct Nucleic Acid Amplification Test without RNA Extraction for SARS-CoV-2 Using a Portable PCR Thermocycler. *Genes* 11 (6), 664. doi:10.3390/genes11060664

World Health Organization (2021). WHO Coronavirus (COVID-19) Dashboard. Available at: https://covid19.who.int/.

Zhang, C., Zheng, T., Wang, H., Chen, W., Huang, X., Liang, J., et al. (2021). Rapid One-Pot Detection of SARS-CoV-2 Based on a Lateral Flow Assay in Clinical Samples. *Anal. Chem.* 93 (7), 3325–3330. doi:10.1021/acs.analchem.0c05059

Zhang, Y., Odiwuor, N., Xiong, J., Sun, L., Nyaruaba, R. O., Wei, H., et al. (2020). Rapid Molecular Detection of SARS-CoV-2 (COVID-19) Virus RNA Using Colorimetric LAMP. *Medrxiv*. doi:10.1101/2020.02.26.20028373

Zhu, X., Wang, X., Han, L., Chen, T., Wang, L., Li, H., et al. (2020). Multiplex Reverse Transcription Loop-Mediated Isothermal Amplification Combined with Nanoparticle-Based Lateral Flow Biosensor for the Diagnosis of COVID-19. *Biosens. Bioelectron.* 166, 112437. doi:10.1016/j.bios.2020.112437

Conflict of Interest: The authors declare that the research was conducted in the absence of any commercial or financial relationships that could be construed as a potential conflict of interest.

frontiers
in Bioengineering and Biotechnology

ORIGINAL RESEARCH
published: 24 March 2022
doi: 10.3389/fbioe.2022.826694

A Portable Droplet Magnetofluidic Device for Point-of-Care Detection of Multidrug-Resistant *Candida auris*

Pei-Wei Lee[1], Marissa Totten[2], Liben Chen[1], Fan-En Chen[3], Alexander Y. Trick[3], Kushagra Shah[3], Hoan Thanh Ngo[1], Mei Jin[3], Kuangwen Hsieh[1]*, Sean X. Zhang[2]* and Tza-Huei Wang[1,3,4]*

[1]Department of Mechanical Engineering, Johns Hopkins University, Baltimore, MD, United States, [2]Division of Microbiology, Department of Pathology, Johns Hopkins School of Medicine, Baltimore, MD, United States, [3]Department of Biomedical Engineering, Johns Hopkins University, Baltimore, MD, United States, [4]Institute of NanoBioTechnology, Johns Hopkins University, Baltimore, MD, United States

Candida auris is an emerging multidrug-resistant fungal pathogen that can cause severe and deadly infections. To date, *C. auris* has spurred outbreaks in healthcare settings in thirty-three countries across five continents. To control and potentially prevent its spread, there is an urgent need for point-of-care (POC) diagnostics that can rapidly screen patients, close patient contacts, and surveil environmental sources. Droplet magnetofluidics (DM), which leverages nucleic acid-binding magnetic beads for realizing POC-amenable nucleic acid detection platforms, offers a promising solution. Herein, we report the first DM device—coined POC.auris—for POC detection of *C. auris*. As part of POC.auris, we have incorporated a handheld cell lysis module that lyses *C. auris* cells with 2 min hands-on time. Subsequently, within the palm-sized and automated DM device, *C. auris* and control DNA are magnetically extracted and purified by a motorized magnetic arm and finally amplified *via* a duplex real-time quantitative PCR assay by a miniaturized rapid PCR module and a miniaturized fluorescence detector—all in ≤30 min. For demonstration, we use POC.auris to detect *C. auris* isolates from 3 major clades, with no cross reactivity against other *Candida* species and a limit of detection of ~300 colony forming units per mL. Taken together, POC.auris presents a potentially useful tool for combating *C. auris*.

Keywords: droplet magnetofluidics, point-of-care diagnostics, sample preparation, lysis, miniaturized rapid PCR, *Candida auris*, multidrug resistance, fungal pathogen

Edited by:
*Han-Sheng Chuang,
National Cheng Kung University,
Taiwan*

Reviewed by:
*Milena Kordalewska,
Hackensack Meridian Health,
United States
Michael Mauk,
University of Pennsylvania,
United States*

****Correspondence:***
*Kuangwen Hsieh
khsieh4@jhu.edu
Sean X. Zhang
szhang28@jhmi.edu
Tza-Huei Wang
thwang@jhu.edu*

Specialty section:
*This article was submitted to
Biosensors and Biomolecular
Electronics,
a section of the journal
Frontiers in Bioengineering and
Biotechnology*

Received: *01 December 2021*
Accepted: *01 March 2022*
Published: *24 March 2022*

Citation:
*Lee P-W, Totten M, Chen L, Chen F-E, Trick AY, Shah K, Ngo HT, Jin M, Hsieh K, Zhang SX and Wang T-H (2022) A Portable Droplet Magnetofluidic Device for Point-of-Care Detection of Multidrug-Resistant Candida auris.
Front. Bioeng. Biotechnol. 10:826694.
doi: 10.3389/fbioe.2022.826694*

INTRODUCTION

Multidrug-resistant microorganisms present an ongoing global healthcare crisis. Among them, *Candida auris* is an emerging nosocomial fungal pathogen (Meis and Chowdhary, 2018; Vallabhaneni et al., 2019) that is resistant to antifungal drugs and can cause severe infections. Indeed, over 40% of *C. auris* isolates are resistant to 2 or more antifungal drug classes (Chowdhary et al., 2018; Kordalewska et al., 2018; Tsay et al., 2018; Hou et al., 2019; Park et al., 2019), while severe healthcare-associated invasive infections caused by *C. auris* may reach a mortality rate up to 60% in patients with underlying comorbidities (Schelenz et al., 2016; Eyre et al., 2018; Meis and Chowdhary, 2018; Armstrong et al., 2019). Importantly, *C. auris* acquisition appears most likely due to exogenous exposure with the healthcare environment being the major reservoir (Welsh et al., 2017; Sexton et al., 2018; Armstrong et al., 2019). *C. auris* can remain viable on medical devices, instrument, equipment, furniture, and beddings for up to 14 days at hospital settings (Welsh et al., 2017). *C. auris* may also colonize in patients without causing clinical symptoms for up to 3 months (Eyre et al., 2018; Bradley, 2019). The long viability in the hospital environment and persistent colonization in patients facilitate transmission and spread of the organism in healthcare settings, as evidenced by several nosocomial outbreaks in the United States and reported infections in thirty-three countries across five continents (Schelenz et al., 2016; Vallabhaneni et al., 2017; Adams et al., 2018; Eyre et al., 2018; Jeffery-Smith et al., 2018; Armstrong et al., 2019). Currently, control and prevention of the spread of *C. auris* requires monitoring patients, screening close patient contacts, and surveilling environmental sources for the organism (Adams et al., 2018; Eyre et al., 2018; Ku et al., 2018; Tsay et al., 2018). Effectiveness of this practice critically depends on reliable, rapid, cost-effective, and ideally, point-of-care (POC) identification of *C. auris*. Unfortunately, despite advances in laboratory-based methods that can identify *C. auris* (e.g., MALDI-TOF mass spectrometry (Mizusawa et al., 2017) and benchtop PCR (Kordalewska et al., 2017; Arastehfar et al., 2018; Leach et al., 2018; Sexton et al., 2018; Ahmad et al., 2019; Hou et al., 2019; Jainlabdin et al., 2019; Kordalewska et al., 2019; Leach et al., 2019; Lima et al., 2019)), an urgent but unmet need for POC identification of *C. auris* still remains.

Droplet magnetofluidics (DM), in recent years, has emerged as a promising technology for detecting pathogenic nucleic acids at POC (Zhang et al., 2011; Chiou et al., 2013; Zhang and Wang, 2013; Shin et al., 2014; Shin and Wang, 2014; Shin et al., 2017; Shin et al., 2018; Chen F.-E. et al., 2021; Chen L. et al., 2021; Trick Alexander et al., 2021). DM uses magnetic beads to capture nucleic acids and transport them (with the assistance of external magnets) between discrete droplets of reagents and achieve extraction, purification, and amplification of nucleic acids. Such use of magnetic beads facilitates automation and obviates fluidic control components such as pumps and valves for manipulating reagents, which significantly increases the amenability of DM-based devices toward POC use. More recently, small thermoplastic cartridges and fully integrated yet portable devices have been developed to perform DM-based pathogen detection (Shin et al., 2018; Chen F.-E. et al., 2021; Chen L. et al., 2021; Trick Alexander et al., 2021). In addition to automating DM-based nucleic acid extraction and purification, the extruded wells in the cartridges and the miniaturized thermocycling units and fluorescence detectors in the integrated devices facilitate ultrafast real-time quantitative PCR and enable rapid detection. It is, therefore, a promising opportunity to leverage the advent of DM technology toward developing POC detection of *C. auris*.

We are, thus, motivated to develop such a portable DM device for POC detection of *C. auris*—conveniently named POC.auris. As part of POC.auris, we incorporate a handheld cell lysis method that rapidly and effectively lyses *C. auris* cells. *C. auris* DNA in the lysate is extracted, purified, and amplified in full automation within the DM assay cartridge and the DM device. A duplex real-time quantitative PCR (qPCR) assay that specifically detects *C. auris* and an internal assay control plasmid is implemented in POC.auris. Importantly, when performed in the DM assay cartridge and the portable DM device, the duplex qPCR assay is miniaturized and as a result accelerated to ~26 min. For demonstration, we use POC.auris to detect *C. auris* isolates from 3 major clades that originate from South Asia, Africa, and South America, with no cross reactivity against multiple non-*C. auris Candida* species and a limit of detection (LOD) of 300 colony-forming units (CFU)/mL.

MATERIALS AND METHODS

Candida Species, Storage, Subculture, and Handling

All *Candida* species tested in this work were isolates from either the United States Center for Disease Control and Prevention or the Johns Hopkins Hospital Microbiology Laboratory (**Supplementary Table S1**). *Candida auris* (*C. auris*) AR0382 (a strain belonging to the South Asia clade), AR0384 (a strain belonging to the Africa clade), AR0385 (a strain belonging to the South America clade), and AR0388 (a strain belonging to the South Asia clade) were obtained from the United States Center for Disease Control and Prevention. *C. auris* Pt3 (i.e., Patient #3) was a clinical isolate (originating from India, which belongs to the South Asia clade) obtained from the Johns Hopkins Hospital Microbiology Laboratory. Other *Candida* species, including *C. albicans*, *C. duobushaemulonii*, *C. glabrata*, *C. haemulonii*, *C. krusei*, *C. parapsilosis*, and *C. tropicalis* were also clinical isolates from the Johns Hopkins Hospital Microbiology Laboratory and were identified to the species level *via* in-house MALDI-TOF mass spectrometry (MALDI Biotyper®, Bruker, Billerica, MA).

All isolates were kept at −80°C in Microbank™ 2D vials that are filled with beads and specially formulated cryopreservative. For subculture, a single bead was removed from Microbank™ 2D vial, plated on Sabouraud Dextrose Agar (SDA; pH 5.6), incubated at 30°C for 24—72 h, and observed periodically throughout incubation. If only a few isolates were observed after 72 h, then an isolate from the SDA plate was plated onto a new SDA plate and grown under the same conditions. For making cell suspensions and dilutions, colonies were scraped and suspended in phosphate-buffered saline (PBS). The cell suspension was measured *via* optical density at wavelength 600 nm (i.e., OD600) to estimate its concentration, where OD600 = 0.1 was approximated as 3×10^6 CFU/ml (Bravo Ruiz et al., 2019; Lima et al., 2019; Srivastava and Ahmad, 2020). All *Candida* species were handled within biosafety cabinets and with appropriate personal protective equipment in accordance with the biosafety level 2 (BSL-2) guideline.

Benchtop Extraction and Purification of Genomic DNA From *Candida* Species

Genomic DNA from all *Candida* cell suspensions were extracted and purified using Quick-DNA Fungal/Bacterial Miniprep Kit (Zymo Research, Irvine, CA), which is based on bead beating and spin column purification. Briefly, a pea sized amount of *Candida* cells was directly added to 750 µL BashingBead™ Buffer and lysed in a ZR BashingBead™ Lysis Tube (0.1 and 0.5 mm), on a vortexer fitted with a bead-beating adapter at maximum speed for 10 min, and finally spun down. The supernatant was subsequently filtered through a Zymo-Spin™ III-F Filter *via* centrifugation. The filtrate was mixed with the Genomic Lysis Buffer (without beta-mercaptoethanol) and transferred to a Zymo-Spin™ IICR Column, where binding, washing, and elution of DNA were performed. The elution volume was 100 µL for all samples. Finally, the DNA concentrations for all samples were quantified using a Qubit fluorometer (Invitrogen, Waltham, MA).

Preparation of Control DNA Plasmid

Two versions of the control DNA plasmid, both of which contain a fragment of the bicoid gene (GenBank Accession Number: NT_033777.3, Position: 6755842—6759466), were used in this work. One version of the plasmid was acquired from Addgene (Plasmid # 34340; Watertown, MA) as *E. coli* in an agar stab culture. This plasmid is named Addgene plasmid hereafter. Addgene plasmid-containing *E. coli* colonies were selected by plating the agar stab culture on agar plates containing kanamycin (50 mg/ml) and incubating at 37°C overnight. Subsequently, Addgene plasmid from plasmid-containing *E. coli* colonies were purified from *E. coli* using ZymoPure II Plasmid Maxiprep kit (Zymo Research, Irvine, CA) according to the manufacturer's specifications, with the exception of the *E. coli* colonies that were directly suspended in the ZymoPURE P1 solution to begin the purification process. Unused plasmid-containing *E. coli* colonies from the kanamycin-containing agar plates were transferred to Microbank™ 2D vials and stored at −80°C. Once extracted, Addgene plasmid was aliquoted into microcentrifuge tubes and stored at −20°C. The other version of the plasmid was obtained as a gBlock from Integrated DNA Technologies (IDT; Coralville, IA). This plasmid is named IDT plasmid hereafter. The IDT plasmid was resuspended in UltraPure™ DNase/RNase-free distilled water (Thermo Fisher Scientific, Waltham, MA) at 100 µM concentration, aliquoted into 0.5 ml DNA Lo-Bind tubes (Eppendorf, Germany), and stored at −20°C.

Benchtop Droplet Magnetofluidic-Compatible Rapid Duplex qPCR

The rapid duplex qPCR assay employed in this work was adopted and slightly modified from a previously reported assay (Leach et al., 2018) that had been adopted by the United States Center for Disease Control and Prevention. The duplex qPCR assay targets both *C. auris* and an assay control. The *C. auris* PCR primers and FAM-labeled TaqMan probe (**Table 1**; purchased from IDT) target a region within ITS2 gene that is specific to *C. auris*. The assay control PCR primers and TYE-labeled Taqman probe (**Table 1**; purchased from IDT) target a region within the bicoid gene (GenBank Accession Number: NT_033777.3, Position: 6755842—6759466). Lyophilized PCR primers and TaqMan probes were reconstituted in nuclease-free water (Promega, Madison, WI) at 100 µM. Reconstituted oligonucleotides were stored at −20°C. Promega GoTaq Probe qPCR Master Mix (Promega, Madison, WI) was used for all PCR reactions throughout this work. Unless otherwise specified, a typical benchtop rapid duplex qPCR assay (20 µL) included 1× PCR mix, 500 nM of *C. auris* forward and reverse primer each, 100 nM of *C. auris* probe, 100 nM of bicoid forward and reverse primer each, 100 nM of bicoid probe, 1 mg/ml BSA (New England BioLabs, Ipswich, MA), 0.05% Tween 20 (Millipore-Sigma, St. Louis, MO), 2 µL bicoid plasmid (1 pg for IDT plasmid or 10 pg for Addgene plasmid), and 1 µL genomic DNA from *Candida* species (various amount for each reaction, either bench top extracted and purified or magnetically purified and eluted into the PCR mix). All PCR assays sans bicoid plasmid and genomic DNA from *Candida* species were prepared inside a PCR hood (AirClean Systems, Creedmoor, NC). Bicoid plasmid and genomic DNA from *Candida* species were added inside a separate biosafety cabinet (The Baker Company, Sanford, ME) to minimize contamination. All benchtop PCR reactions were performed in a Bio-Rad CFX96 Touch Real-Time PCR Detection System (Bio-Rad, Hercules, CA). Unless otherwise specified, a typical benchtop PCR reaction began with a 95°C hot start for 2 min, followed by 40 cycles of 95°C for 3 s and 60°C for 15 s, during which the fluorescence signals were measured every cycle. The fluorescence signals measured by the Bio-Rad CFX96 system were baseline subtracted *via* the built-in curve fit function in the CFX Manager Software and the PCR cycles of quantification (C_q) were determined by the built-in single threshold algorithm in the CFX Manager Software.

TABLE 1 | Primer and probe sequences for detecting the *C. auris* ITS2 region and control plasmid containing the bicoid gene.

Name	Sequence (5′—3′)
C_AUR_ITS2_F	CAGACGTGAATCATCGAATCT
C_AUR_ITS2_R	TTTCGTGCAAGCTGTAATTT
C_AUR_ITS2_P	/6-FAM/AATCTTCGC/ZEN/GGTGGCGTTGCATTCA/IABkFQ/
BICOID_F	CAGCTTGCAGACTCTTAG
BICOID_R	GAATGACTCGCTGTAGTG
BICOID_P	/TYE665/AACGCTTTGACTCCGTCACCCA/IAbRQSp/

Manual magnetic-based DNA purification was added to complete the development of benchtop droplet magnetofluidic-compatible rapid duplex qPCR assay. ChargeSwitch™ gDNA Plant Kit (CS18000, Thermo Fisher Scientific, Waltham, MA), which can isolate genomic DNA from fungal samples, was used in this work. 1 µL *C. auris* genomic DNA, 1 µL control DNA plasmid and 1 µL of 3.6 µg/ml human genomic DNA (Promega, Madison, WI) were added to 97 µL 1× PBS (Thermo Fisher Scientific, Waltham, MA) to make the 100 µL sample. The magnetic bead buffer in this work was made by mixing 4 µL of ChargeSwitch magnetic particles (25 mg/ml in 1 mM sodium acetate, pH 4.5), 10 µL Binding Buffer from ChargeSwitch™ gDNA Plant Kit and 8 µL 10% Tween 20. The 100 µL sample was pipette mixed with the 22 µL magnetic bead buffer in a 1.5 ml microcentrifuge tube. The mixture was kept at room temperature for 1 min to allow binding between magnetic beads and *C. auris* DNA and control DNA plasmid. The tube was placed onto a DynaMag™-2 Magnet (Thermo Fisher Scientific, Waltham, MA) until a visible pellet of magnetic beads was formed on the tube wall before the supernatant was removed *via* pipetting. Forty nine µL wash buffer from ChargeSwitch™ gDNA Plant Kit with 1 µL 10% Tween 20 was subsequently added into the tube to wash the magnetic beads. The tube was briefly centrifuged and again placed onto the DynaMag™-2 Magnet to pellet the magnetic beads and remove the supernatant. Next, 10 µL rapid duplex qPCR mix was added to the pelleted magnetic beads in the tube. The tube was briefly centrifuged , kept at 80°C for 2 min to elute DNA into the PCR mix, and again placed onto the DynaMag™-2 Magnet to pellet and separate the magnetic beads from the PCR mix. The PCR mix (along with eluted DNA) was pipette transferred into a PCR tube (0.2 ml 8-Tube PCR Strips, Bio-Rad, Hercules, CA) before commencing PCR in the Bio-Rad CFX96 Touch Real-Time PCR Detection System.

Droplet Magnetofluidic Assay Cartridge Fabrication

The design and fabrication of the DM assay cartridge, in which the POC.auris assay was performed, were based on our previous works (Chen F.-E. et al., 2021; Chen L. et al., 2021; Trick Alexander et al., 2021). Briefly, the assay cartridge, which measures approximately 4 cm (L) × 1 cm (W) × 1 cm (H) and houses a sample well, a wash buffer well, and a PCR mix well, was fabricated from inexpensive plastic components (material cost per assay cartridge = USD $0.31, **Supplementary Table S2**) *via* laser-cutting and thermoforming. The assay cartridge was composed of 3 layers: a top cap layer for establishing a sample injection opening while enclosing the rest of the assay cartridge, a center spacer layer for joining the layers, and a bottom well layer for holding the assay reagents. The cap layer of each assay cartridge was laser-cut by a CO_2 laser-cutter from a polymethylmethacrylate (PMMA) sheet laminated with a polytetrafluoroethylene (PTFE) tape (McMaster-Carr, Elmhurst, IL, USA). Except for the inlet opening that was laser-cut into the cap layer, the rest of cap layer fit atop the spacer layer to enclose the assay cartridge. The spacer layer was laser-cut by the CO_2 laser-cutter from a PMMA sheet laminated with pressure-adhesive tape (PSA, 9472LE adhesive transfer tape, 3M, USA) on both sides. The well layer was thermoformed from 0.2-mm-thick polypropylene sheet (AKAHA) over three-dimensional (3D)-printed molds (Form 2, Formlabs, Somerville, MA, USA) designed in Solidworks 2017 computer-aided design (CAD) software (Dassault Systèmes, Vélizy-Villacoublay, France) using a commercial dental vacuum forming instrument (Meta Dental Corp, Glendale, NY) to produce extruded wells. Upon fabrication of these individual layers, the spacer layer and the well layer were first assembled *via* PSA into an open assay cartridge. Both the cap layer and the open assay cartridge were kept separately at room temperature until full assembly for experimentation.

Droplet Magnetofluidic Device Design and Construction

The design and assembly of the integrated portable DM device for automating POC.auris were based on our previous works (Chen L. et al., 2021; Trick Alexander et al., 2021). Briefly, the device was composed of a motorized magnetic arm, a miniature thermocycling module, a fluorescence detector (Fluo Sens Integrated, Qiagen), and a microcontroller (Arduino Uno R3) with a motorshield (Arduino Motor Shield Rev3) and a custom printed circuit board shield. The motorized magnetic arm was a 3D-printed (Formlabs Form 2) shaft with a pair of permanent neodymium magnets that were actuated by a rotational servo motor (HS–485HB Hitec RCD, Poway, CA, USA) and a linear servo motor (PQ12-R Actuonix, Victoria, BC, Canada). The bi-axial movement of the motorized magnetic arm pulled the beads in and out of each well, as well as across different wells of the DM cartridge, thereby achieving magnetic transfer within the cartridge. The miniature thermocycling module is the assembly of an aluminum heat block, a thermoelectric cooler, a heat sink, and a miniature fan. The fluorescence detector, which can detect both green fluorescence (excitation wavelength at 470 nm and emission wavelength at 520 nm) and red fluorescence (excitation wavelength at 625 nm and emission wavelength at 680 nm), was positioned and aligned to the PCR well of the cartridge at a predetermined distance. The microcontroller controlled the other 3 components—the movement of the motorized magnetic arm, the temperatures of the miniature thermocycling module (with electrical current supplied by the motorshield), and the timing for acquiring fluorescence signals by the fluorescence detector. The motorized magnetic arm, the fluorescence detector, and the microcontroller were affixed within the main housing of the device, whereas the miniature thermocycling module was affixed on the detachable faceplate, both of which were 3D-printed (Formlabs Form 2, black resin). The parts were embedded with permanent neodymium magnets, such that they could be aligned and magnetically clasped for attachment. The material cost of the DM device used in this work—a one-time cost—is USD $3539.41, nearly 90% of which is attributed to the fluorescence detector (**Supplementary Table S3**).

Handheld Lysis of *C. auris*

In this work, handheld lysis of *C. auris* was achieved by using a commercial OmniLyse device (Claremont BioSolutions, Upland, CA), which performs micro-motor-based bead-beating mechanical lysis. Importantly, all handheld lysis of *C. auris* was performed within a biosafety cabinet and with appropriate personal protective equipments in accordance with the BSL-2 guideline. For performing lysis, the single-use lysis module was first connected to a single-use 5 ml syringe and attached to the reusable Bat-Pac™ battery pack *via* their electrical connectors. Immediately before loading a cell suspension into the lysis module, it was pre-washed by passing 500 µL1× PBS back and forth through it five times while it was switched on. After pre-washing, the module was emptied and switched off. *C. auris* cells (and other *Candida* species cells) were suspended in either 1×

PBS or ESwab® medium (Copan Diagnostics, Murrieta, CA) to a final volume of 500 µL in a 1.5 ml microcentrifuge tube (DNA Lo-Bind, Eppendorf, Germany). For one cycle of lysis, the cell suspension was drawn through the powered-on lysis module into the syringe and infused through the powered-on lysis module into the microcentrifuge tube in ~5—10 s. Unless otherwise specified, ten cycles were performed, which could be accomplished in <2 min. After lysis, the lysate was entirely infused into the microcentrifuge tube and subsequently pipette loaded into the sample well of the droplet magnetofluidic assay cartridge to initiate POC.auris. The used lysis module and the used syringe were discarded. Of note, each lysis module costs USD $11.25, which currently represents the most expensive component of the POC.auris assay (**Supplementary Table S4**).

POC.auris Assay

Prior to performing POC.auris assays, assay cartridges with pre-loaded reagents were prepared. Specifically, 49 µL wash buffer supplemented with 1 µL 10% Tween 20 and 20 µL PCR mix were loaded into the wash buffer well and the PCR well of an open cartridge, respectively. The cap layer was then capped onto the open cartridge *via* PSA before 450 µL silicone oil (50 cSt, Millipore-Sigma, USA) was injected through the sample injection opening to overlay both the wash buffer and the PCR mix. This immiscible silicone oil layer served both as a medium for transporting the magnetic beads in the cartridge and as a separator that prevented the mixing of assay reagents between the wells. The cartridge was either used immediately or placed on ice with the sample injection opening seal with tape (Scotch Magic Tape, 3M, USA) until use. Of note, these reagents added USD $0.98 per cartridge to the cost of each POC.auris assay (**Supplementary Table S4**).

For performing POC.auris, a 100-µL sample (e.g., *C. auris* lysate in either 1× PBS or ESwab® medium along with 1 µL control DNA plasmid and 1 µL human genomic DNA for simulating background DNA that may be present in a swab sample) was pipette mixed with 22 µL magnetic bead buffer and then loaded into the sample well of the assay cartridge. After sample loading, the cartridge was tape-sealed (Scotch Magic Tape, 3M, USA) and mounted onto the faceplate of the DM device with the PCR mix well of the assay cartridge seated in the aluminum heat block, whose inner surface was coated with a thermally conductive paste (Arctic Silver 5, Visalia, California, USA) for ensuring consistent thermal contact throughout PCR. The faceplate was then magnetically clasped onto the main housing of the device, such that the sample well was positioned between the pair of permanent magnets of the motorized magnetic arm.

POC.auris began with a ~3-min automated sample preparation process, during which the magnetic beads and bound DNA were concentrated from the sample well, transferred to the wash buffer well for wash, and finally transferred to the PCR mix well. Once the magnetic beads and bound DNA arrived in the PCR mix well, the thermocycling module began thermocycling with concurrent real-time fluorescence detection. PCR began with a 95°C hot start for 2 min followed by 45 cycles of 106°C for 1 s and 65°C for 15 s. The fluorescence detector measured the fluorescence signal emitted from the PCR mix at well every cycle at the annealing and extension step.

Analytical Sensitivity and Analytical Specificity of POC.auris

C. auris AR0382 was used to assess the analytical sensitivity of POC.auris. Here, *C. auris* AR0382 cell suspension was initially adjusted to OD600 = 0.1 (~3 × 10^6 CFU/ml (Bravo Ruiz et al., 2019; Lima et al., 2019; Srivastava and Ahmad, 2020)) and then serially diluted in PBS to final concentrations of 3×10^5, 3×10^4, 3×10^3, and 3 × 10^2 CFU/ml. One hundred µL of each cell dilution was used as the sample. Each sample was subjected to 10 cycles of lysis by an OmniLyse device. All 100 µL of lysate was mixed with 22 µL magnetic bead buffer, 1 µL control DNA plasmid, and 1 µL of 3.6 µg/ml human genomic and subsequently, loaded into the sample well of the DM assay cartridge to initiate POC.auris. For evaluating the analytical specificity of POC.auris, we tested all 3 strains of *C. auris* along with *C. albicans*, *C. glabrata*, *C. parapsilosis*, and *C. tropicalis*. All *Candida* species cell suspensions were initially adjusted to OD600 = 0.1 (~3 × 10^6 CFU/ml (Bravo Ruiz et al., 2019; Lima et al., 2019; Srivastava and Ahmad, 2020)) and then diluted in PBS to final concentrations of 10^3 CFU/ml. One hundred µL of each cell dilution was used as the sample. Each sample was subjected to 10 cycles of lysis by an OmniLyse device. All 100 µL of lysate was mixed with 22 µL magnetic bead buffer, 1 µL control DNA plasmid and 1 µL of 3.6 µg/ml human genomic DNA and subsequently loaded into the sample well of the DM assay cartridge to initiate POC.auris.

Data Analysis and Presentation

Data were analyzed *via* Microsoft Excel 365 and plotted in Origin 2018. The fluorescence signals and C_q values measured by the Bio-Rad CFX96 system (**Supplementary Figures S3–S7, S9**) were first exported to Excel and subsequently plotted in Origin. For POC.auris, the FAM and TYE fluorescence signals measured by the fluorescence detector in the droplet magnetofluidic device (**Supplementary Figures S8, S10–S13**) were first exported to Excel. In Excel, both FAM and TYE fluorescence signals of the first PCR cycle were subtracted from FAM and TYE fluorescence signals of each PCR cycle. The subtracted FAM and TYE fluorescence signals were subsequently plotted in Origin. POC.auris C_q values were directly calculated by the linear regression algorithm that was built-in companion software of DM device. For evaluating the analytical sensitivity of POC.auris, the mean and standard deviation of C_q values from >3 technical replicates were calculated in Excel and subsequently were plotted in Origin, where the data were presented as mean ± 1SD.

RESULTS

Overview of POC.auris

POC.auris provides a rapid, streamlined, and POC-amenable diagnostic testing solution for *C. auris* with the aid of DM (**Figure 1**). The assay begins with lysis of *C. auris* cells *via* a handheld bead-beating-based lysis module that can effectively

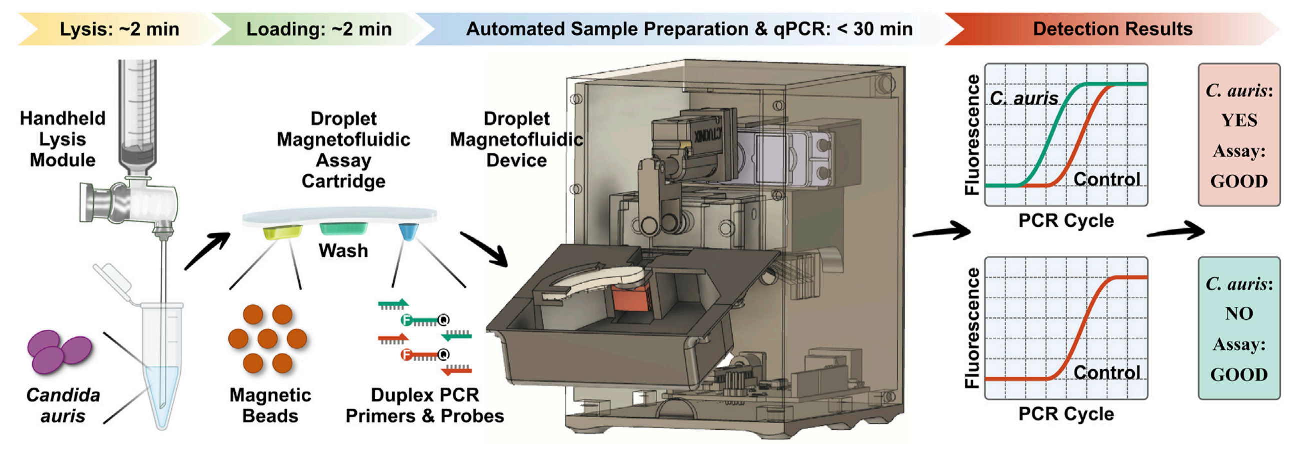

FIGURE 1 | Overview of POC.auris—a rapid, streamlined, and POC-amenable diagnostic testing solution for *C. auris* with the aid of droplet magnetofluidic (DM) technology. POC.auris begins with handheld bead-beating-based lysis of *C. auris* cells that can lyse *C. auris* cells with ~2 min hands-on time. The lysate, a magnetic bead buffer, and an internal control DNA plasmid are loaded into the sample well of the DM assay cartridge, where DNA is captured by the magnetic beads. The assay cartridge also contains a wash buffer well for purifying DNA and a PCR mixture well, which holds PCR primers and fluorophore (F)- and quencher (Q)-labeled TaqMan probes for amplifying and detecting *C. auris* and the internal control. After the ~2 min loading step, the assay cartridge is inserted in the DM device to initiate the assay in full automation. Within the device, DNA is magnetically transported to the wash buffer and to the PCR mixture, where DNA is amplified and detected *via* rapid duplex real-time quantitative PCR (qPCR). The resulting PCR curves for *C. auris* (green) and the internal control (red), which can be acquired in <30 min, indicate the presence or absence of *C. auris* and the reliability of the assay.

lyse *C. auris* cells with ~2 min hands-on time. The lysate is loaded along with a magnetic bead buffer and an internal control DNA plasmid into the sample well of the DM assay cartridge, where DNA is captured by the magnetic beads. The assay cartridge also houses a wash buffer for DNA purification and a PCR mixture that contains primers and TaqMan probes for amplification and detection of *C. auris* and the internal control. After the ~2 min loading step, the assay cartridge is inserted in the DM device, and the device is prompted to initiate the automated assay by first magnetically transporting the magnetic bead pellet and the captured DNA from the sample well to the wash buffer and then to the PCR mixture. Once DNA arrives in the PCR mixture well, the device commences duplex qPCR with concurrent dual-color fluorescence detection after every PCR cycle. Importantly, as the DM device employs a miniaturized thermocycling module, the duplex qPCR assay is significantly accelerated, and the turnaround time for the entire automated assay is shortened to <30 min. Finally, the resulting PCR curves for *C. auris* and the internal control indicate the presence or absence of *C. auris* and the reliability of the assay.

POC.auris employs our previously reported disposable thermoplastic DM assay cartridge (**Supplementary Figure S1**) and the integrated portable DM device (**Supplementary Figure S2**) (Chen F.-E. et al., 2021; Chen L. et al., 2021; Trick Alexander et al., 2021). The assay cartridge has a compact footprint (similar to a USB drive) and is fabricated *via* simple assembly of low-cost plastic materials. The assay cartridge has 3 independent wells for holding the mixture of sample and magnetic bead buffer ($pH = 5$), a wash buffer ($pH = 7$), and the PCR mix, which are further separated by an immiscible oil that prevents evaporation and mixing of these aqueous reagents. After sample loading, each disposable assay cartridge is tape-sealed and mounted in the portable DM device. The device houses a motorized magnetic arm, a miniature thermocycling module, a compact dual-color fluorescence detector, and a microcontroller for automating these components. The motorized magnetic arm, which is equipped with a pair of permanent magnets located at the opposing ends of the assay cartridge, moves bi-axially to concentrate, and sequentially transport the magnetic beads from the sample well to the wash buffer well and then to the PCR reaction mix well. Upon the arrival of the magnetic beads and DNA, the thermocycling module begins to thermocycle the PCR reaction mix well while the fluorescence detector measures the fluorescence emitted from PCR in real time.

Development of Benchtop Droplet Magnetofluidic-Compatible Rapid Duplex qPCR

We first developed a benchtop rapid duplex qPCR assay that is compatible with DM. To do so, we employed US CDC-adopted primers and probes that target the ITS2 region of *C. auris* and an internal control plasmid (Leach et al., 2018), and verified their compatibility with rapid PCR and DM in a step-by-step process. In these initial developments, we used benchtop extracted and purified DNA from 3 clinically isolated *C. auris* that originate from 2 major clades (South Asia and Africa) and a control DNA plasmid containing the bicoid gene. We tested 1 ng, 10 pg, and 100 fg purified *C. auris* genomic DNA (corresponding to ~70000, ~700, and ~7 copies) and 10 pg control DNA plasmid. We first verified that both *C. auris* DNA and bicoid plasmid DNA could be detected using one of our DM-compatible PCR mixes (Promega GoTaq Probe qPCR Master Mix) under its fast cycling protocol with 95°C hot start for 2 min and 40 cycles of

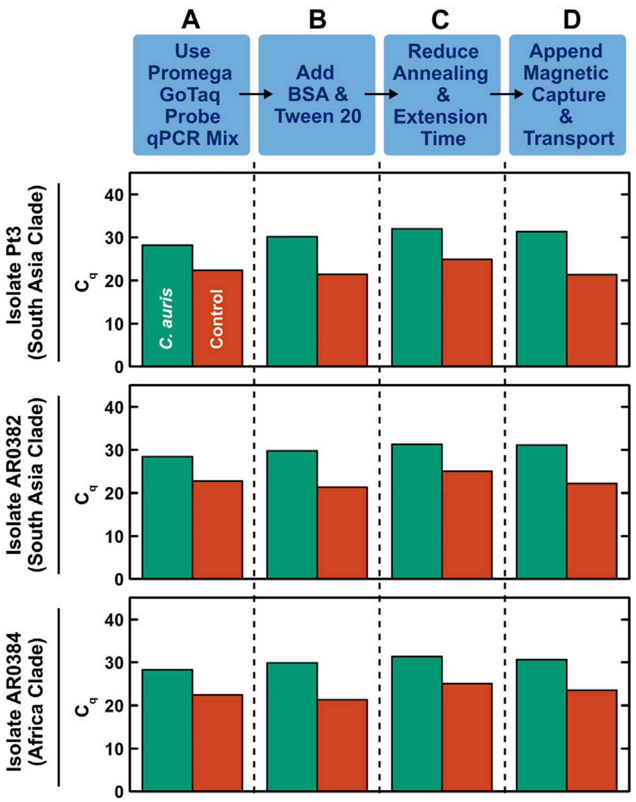

FIGURE 2 | Development of benchtop droplet magnetofluidic-compatible rapid duplex qPCR. The step-by-step development process shown here employs benchtop extracted and purified DNA (100 fg) from 3 strains of *C. auris* that originate from 2 major clades (South Asia and Africa) and a control DNA plasmid containing the bicoid gene (10 pg) as the inputs. **(A)** Using Promega GoTaq Probe qPCR Master Mix, which is compatible with droplet magnetofluidics, under its fast cycling protocol (95°C hot start for 2 min and 40 cycles of 95°C for 3 s and 60°C for 30 s), both *C. auris* DNA and control DNA plasmid directly spiked into the PCR mix can be detected, as indicated by clear cycle of quantification (C_q) values in both the FAM channel associated with the *C. auris* probe (green) and the TYE channel associated with the bicoid probe (red). The C_q values are comparable among the 3 strains of *C. auris*. **(B)** Addition of BSA and Tween 20—standard additives for PCR in droplet magnetofluidic assays—causes negligible differences to the PCR assay. **(C)** Accelerating the PCR assay by reducing the annealing and extension step at 60°C from 30 to 15 s only slightly delays the C_q values. **(D)** Appending manual magnetic capture and transport of both *C. auris* DNA and control DNA plasmid upstream to the accelerated rapid duplex qPCR assay still result in successful detection of both targets. This assay can be readily adapted into the droplet magnetofluidic cartridge and device.

95°C for 3 s and 60°C for 30 s, as indicated by robust PCR curves (**Supplementary Figure S3**) and clear cycle of quantification (C_q) values in both the FAM channel associated with the *C. auris* probe and the TYE channel associated with the bicoid probe (**Figure 2A**, green and red, respectively). We subsequently ensured the addition of BSA and Tween 20—standard PCR additives in our magnetofluidic assays—causes negligible differences to the PCR assay (**Figure 2B** and **Supplementary Figure S4**). We further accelerated the benchtop PCR by reducing the annealing and extension step at 60°C from 30 to 15 s, which still retained comparable amplification efficiency (**Figure 2C** and **Supplementary Figure S5**). We next verified the specificity of the *C. auris* primers by testing against 7 other *Candida* species (**Suppplementary Figure S6**). Notably, the primers successfully discriminated against *C. haemulonii* and *C. duobushaemulonii*, which are genetically close to *C. auris*. Finally, to simulate clinical swab eluates, we added human genomic DNA as background DNA to the sample before appending manual magnetic bead-based DNA capture upstream to rapid duplex qPCR. Even with the added background of human genomic DNA, we successfully detected 100 fg *C. auris* DNA and 10 pg control DNA (**Figure 2D**). In the absence of *C. auris* DNA, we still detected the control DNA plasmid, which effectively illustrates its control function (**Supplementary Figure S7**). Importantly, the C_q values for the samples with magnetically extracted DNA were comparable to those for the samples with directly spiked DNA (**Supplementary Figure S7**), which suggests sufficient recovery of DNA in our assay. These results establish our benchtop DM-compatible rapid duplex qPCR assay for detecting *C. auris* with assay control.

Development of POC.auris With Handheld Cell Lysis

Taking a step-by-step approach for establishing POC.auris, we first adapted the benchtop rapid duplex qPCR within the DM assay cartridge and the portable DM device. Here, we directly spiked benchtop which was extracted and purified *C. auris* DNA and the internal control DNA plasmid in the PCR well of the assay cartridge and performed PCR using the miniature thermocycling module and the fluorescence detector in the DM device. We adopted the elevated denaturation temperature (106°C) and the short denaturation time per PCR cycle (1 s) used in the DM device from our earlier works (Chen L. et al., 2021; Trick Alexander et al., 2021); this denaturation condition was previously verified to support PCR without causing visible evaporation of the PCR mix. Combined with 15 s annealing and extension time per PCR cycle, the duplex qPCR assay with 45 cycles could be completed in ~26 min in the DM. We subsequently fine-tuned the annealing and extension temperature in the DM device to ensure robust duplex qPCR even with rapid thermocycling (**Supplementary Figure S8**). We found that using 65°C for annealing and extension, duplex qPCR in our assay cartridge and device could robustly detect 100 fg purified DNA from the 3 strains of *C. auris* and 1 pg control plasmid DNA, as indicated by clear PCR curves in both the FAM and TYE channels (**Figure 3A**). Of note, during the development of POC.auris, we switched the provider for the control DNA plasmid and found that 1 pg was sufficient for providing control in the absence of *C. auris* DNA (**Figure 3A**).

We subsequently appended magnetic bead-based capture and transport of DNA prior to PCR. Specifically, we loaded benchtop extracted and purified *C. auris* DNA, the internal control DNA plasmid, and human genomic DNA (as background DNA for simulating clinical swab elutes) along with magnetic bead buffer into the sample well of each assay cartridge and allowed binding between DNA and magnetic beads. We then immediately installed the assay cartridge in the DM device and initiated its

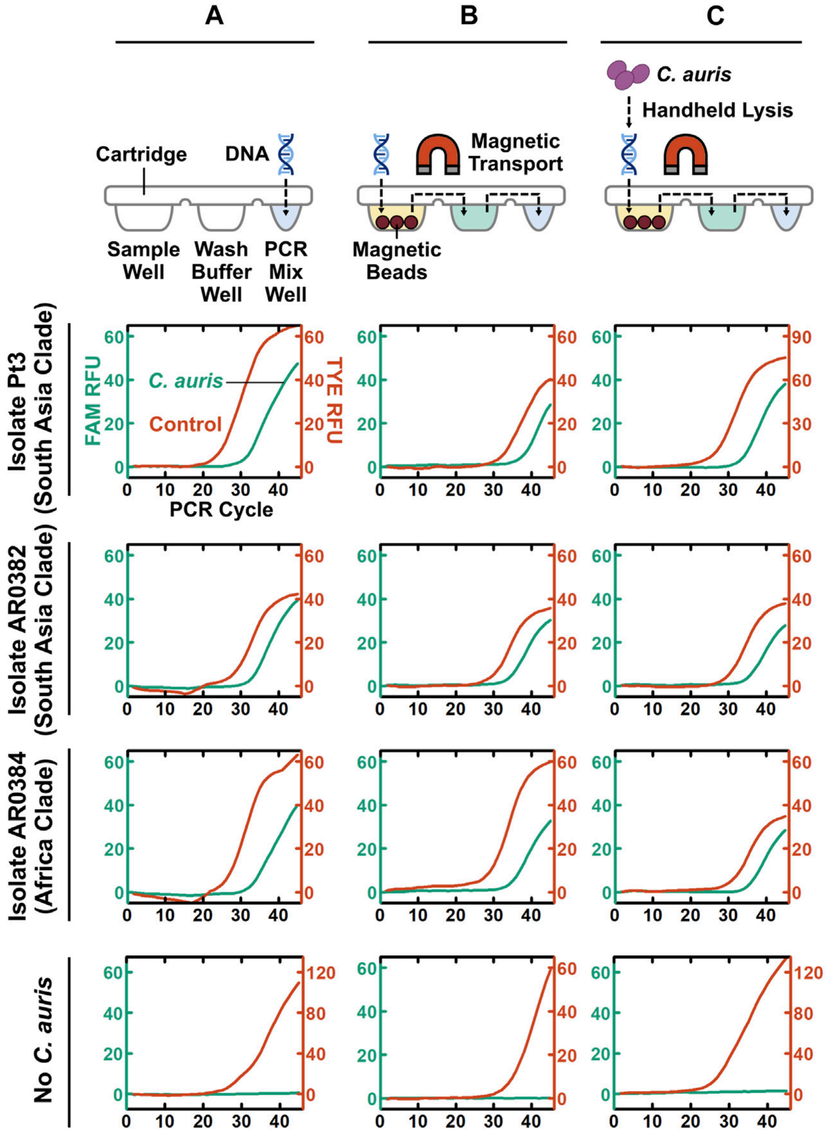

FIGURE 3 | Step-by-step development of POC.auris. **(A)** Benchtop purified *C. auris* DNA from 2 major clades (100 fg) and the control DNA plasmid (1 pg), as well as the no-*C. auris* DNA control, are directly spiked into the PCR mix well of assay cartridges, which are then mounted in the DM device to perform rapid duplex qPCR. Robust *C. auris* curves (green) and control DNA plasmid curves (red) indicate successful duplex qPCR performed by the miniature thermocycling module and the fluorescence detector in the DM device. **(B)** Benchtop purified *C. auris* DNA from 2 major clades (100 fg) and the control DNA plasmid (1 pg), as well as the no-*C. auris* DNA control, are first loaded into the sample well of DM assay cartridges. Subsequently, within the DM device, both *C. auris* DNA and control DNA plasmid are captured by magnetic beads, transported through the wash buffer well to the PCR mix well, eluted directly in PCR mix, and amplified and detection *via* rapid duplex qPCR—all in full automation. Robust *C. auris* PCR curves (green) and control DNA plasmid PCR curves (red) demonstrate successful DNA extraction, transport, and elution within the assay cartridges and the device. **(C)** A simple, fast, and handheld method for lysing *C. auris* cells is incorporated to complete the development of POC.auris. This lysis method uses a single-use microbead-beating module that is battery-powered to mechanically lyse *C. auris* cells. *C. auris* cells from 2 major clades at 3×10^3 CFU/ml serve as samples and are subjected to full POC.auris—including handheld cell lysis, automated magnetic-based DNA extraction and transport, and rapid duplex qPCR. Robust *C. auris* PCR curves (green) demonstrate that all 3 strains are detected by POC.auris.

automated sample preparation and PCR protocol. Within the device, the motorized magnetic arm concentrated the DNA-bound magnetic beads into a pellet, transported it through the wash buffer well, and finally was delivered it to the PCR mix well (**Figure 3B**). In the PCR mix well, DNA dissociated from the beads before the beads were removed from the PCR mix well and PCR commenced. We were able to simultaneously detect 100 fg purified DNA from the 3 strains of *C. auris* and the control DNA plasmid, as well as only the control DNA plasmid in the absence of *C. auris* DNA (**Figure 3B**). Of note, the C_q values of the three magnetically extracted *C. auris* DNA samples were ~3 cycles higher than their directly spiked counterparts, suggesting ~10% efficiency in DNA capture and transport. Nevertheless, these results demonstrate that DNA was magnetically captured and

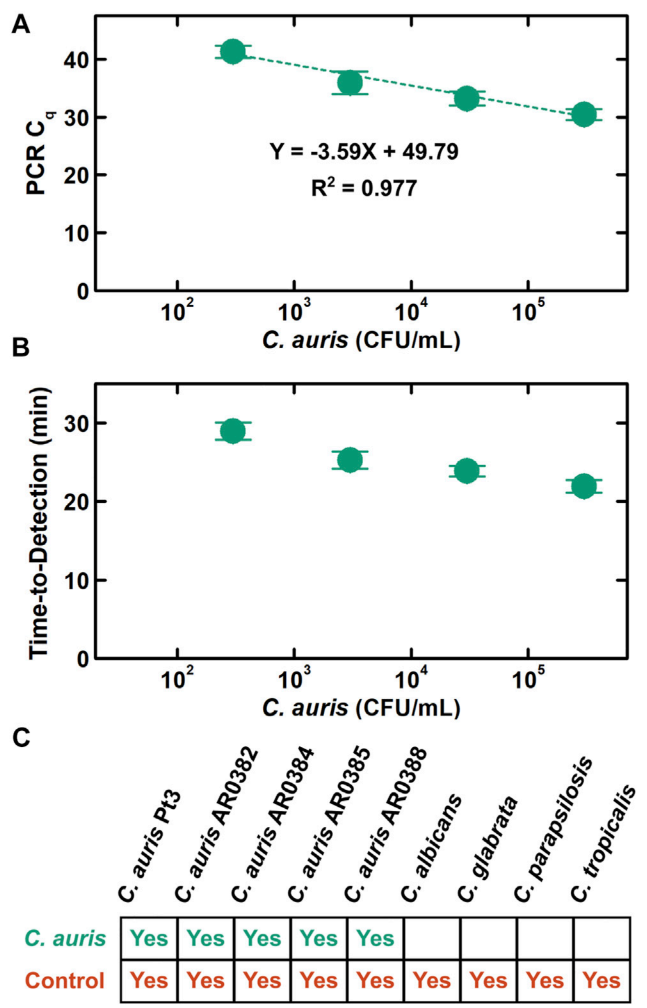

	C. auris Pt3	*C. auris* AR0382	*C. auris* AR0384	*C. auris* AR0385	*C. auris* AR0388	*C. albicans*	*C. glabrata*	*C. parapsilosis*	*C. tropicalis*
C. auris	Yes	Yes	Yes	Yes	Yes				
Control	Yes	Yes	Yes	Yes	Yes	Yes	Yes	Yes	Yes

FIGURE 4 | Analytical performance evaluation of POC.auris. **(A)** POC.auris detects $3{\times}10^5$, $3{\times}10^4$, $3{\times}10^3$, and 3×10^2 CFU/ml of *C. auris* strain 0382 (South Asia clade) in PBS with C_q values of 30.5 ± 1.0, 33.2 ± 1.2, 35.9 ± 2.0, and 41.3 ± 1.0, respectively (mean ±1 SD, $n \geq 3$). The slope (–3.59) of the linear fit (R^2 = 0.977) suggests efficient PCR in the DM assay cartridge and the DM device. **(B)** For $3{\times}10^5$, $3{\times}10^4$, $3{\times}10^3$, and 3×10^2 CFU/ml of *C. auris* strain 0382, the time-to-detection in POC.auris—the elapsed time between initiating the automated program in the DM device and detecting *C. auris* through a definitive C_q value measured by the DM device—are 21.9 ± 0.8, 23.9 ± 0.7, 25.3 ± 1.1, and 28.9 ± 1.1 min, respectively (mean ±1 SD, $n \geq 3$). **(C)** POC.auris specifically detects *C. auris*. When tested against 4 other *Candida* species including *C. albicans*, *C. glabrata*, *C. parapsilosis*, and *C. tropicalis*, POC.auris shows no cross reactivity and only detects the internal control DNA plasmid.

transported through the cartridge and directly eluted in the PCR mix.

As the final step of POC.auris development, we incorporated a simple, fast, and handheld method for lysing *C. auris* cells. To use this method, we employed a syringe-linked microbead-beating module that is battery-powered and disposable to mechanically lyse *C. auris* cells (**Supplementary Figure S9**) (Vandeventer Peter et al., 2011; Shin et al., 2017). For characterizing this method, we spiked 3×10^6 CFU/mL *C. auris* cells, which were cultured from the isolate from the South Asia clade, into PBS as the sample. We determined that 10 lysis cycles (i.e., passing the sample through the lysis module 10 times), which were completed in ~1—2 min, achieved effective lysis of *C. auris* (**Supplementary Figure S9**). To our knowledge, these results represent the first demonstration of such handheld lysis of *C. auris*.

We demonstrated the utility of full POC.auris—including handheld cell lysis, automated magnetic sample preparation, and rapid duplex qPCR—with multiple strains of *C. auris*. Here, we first challenged POC.auris against 5 strains of *C. auris*, which belong to the South Asia clade, the Africa clade, and the South America clade, in PBS suspension at ~3×10^3 CFU/ml, and we included a no-*C. auris* control (i.e., only PBS). After subjecting each sample and the control with 10 lysis cycles, we loaded the lysate along with the control DNA plasmid, human genomic DNA, and the magnetic bead buffer into the sample well of an assay cartridge and initiated our workflow. We were able to detect all 5 strains of *C. auris* along with their respective control DNA plasmid, and only the control DNA plasmid from the no-*C. auris* control (**Figure 3C** and **Supplementary Figure S10**). Moreover, we were able to detect *C. auris* strain from the South America clade suspended in a swab transport medium (**Supplementary Figure S11**). These results demonstrate that POC.auris could detect up to 5 strains of *C. auris* belonging to 3 major clades from either PBS or a swab transport medium.

Analytical Performance Evaluation of POC.auris

As part of analytical performance evaluation of POC.auris, we first assessed its analytical sensitivity. Here, we tested POC.auris against a 10-fold serial dilution series from $3{\times}10^5$ to 3×10^2 CFU/ml of *C. auris* cells cultured from the isolate of the South Asia clade and spiked into PBS. In these experiments, we continued employing PBS because PBS has been used as an elution and transport medium for *C. auris* swabs (Leach et al., 2018), and therefore is a clinically relevant medium. The C_q values for $3{\times}10^5$, $3{\times}10^4$, $3{\times}10^3$, and 3×10^2 CFU/ml measured by POC.auris were 30.5 ± 1.0, 33.2 ± 1.2, 35.9 ± 2.0, and 41.3 ± 1.0, respectively (mean ±1 SD; **Figure 4A**, $n \geq 3$). We observed strong linearity from our results (R^2 = 0.977). The slope of our linear fit was −3.59, which corresponds to ~90% efficiency. Finally, we note that these results were acquired on different days, the low coefficients of variation across the four target concentrations (all ≤5.4%; **Supplementary Figure S12**) thus demonstrate that POC.auris is reproducible.

To show the speed of POC.auris, we calculated the time-to-detection for each input concentration of *C. auris*. In this study, the time-to-detection represents the elapsed time between initiating the automated program in the DM device (i.e., immediately after mounting the DM assay cartridge in the DM device) and detecting *C. auris* through a definitive C_q value measured by the DM device. The time-to-detection thus includes the time for executing magnetic bead-based capture and transport of DNA. The time-to-detection values for $3{\times}10^5$, $3{\times}10^4$, $3{\times}10^3$, and 3×10^2 CFU/mL *C. auris* were 21.9 ± 0.8, 23.9 ± 0.7, 25.3 ± 1.1, and 28.9 ± 1.1 min, respectively (mean ±1 SD;

Figure 4B, n ≥ 3). These results illustrate that POC.auris can rapidly detect even low concentrations of *C. auris*.

Finally, we verified the analytical specificity of POC.auris against other *Candida* species. To do so, we cultured clinically isolated *C. albicans*, *C. glabrata*, *C. parapsilosis*, and *C. tropicalis* and tested POC.auris with these 4 species at 3×10^3 CFU/ml. These *Candida* species were undetected by the *C. auris* probe (**Figure 4C** and **Supplementary Figure S13**), which supported that POC.auris is specific for detecting *C. auris*. Importantly, the internal control DNA plasmids mixed with these *Candida* species could still be detected, which ascertained the functionality of the assay and illustrated the significance of the internal control in POC.auris.

DISCUSSION

We have developed POC.auris—an automated and portable DM device that detects *C. auris* with fast speed, high sensitivity, and high specificity. For developing POC.auris, we first employed a US CDC-approved duplex qPCR assay that detects *C. auris* and an assay control and we systematically modified the assay to ensure its compatibility with DM. The modifications include using a DM-compatible PCR mix, incorporating additives, shortening the assay time, and appending magnetic-based DNA purification upstream. We subsequently adapted the DM-compatible assay into the disposable thermoplastic DM cartridge and the integrated palm-sized DM device to actualize POC.auris. We established that the miniature thermocycling module and the portable fluorescence detector in the device facilitated rapid duplex qPCR, then verified that the motorized magnetic arm in the device automated magnetic DNA capture and transport across the assay cartridge, and finally incorporated a handheld, bead-beating-based cell lysis module that lysed *C. auris* cells with <2 min hands-on time. Using POC.auris, we can detect clinically isolated *C. auris* from 3 major clades in <30 min, with no cross reactivity against other *Candida* species and LOD of ~300 CFU/ml.

We made a few remarks to contextualize our work. First, while benchtop nucleic acid-based *C. auris* detection assays have been reported, POC.auris is unique because we have adapted our assay in our POC-amenable device. A recent review on *C. auris* diagnostics (Dennis et al., 2021) corroborates the lack of POC devices capable of nucleic acid-based detection of *C. auris*. Second, amid increasing popularity of isothermal nucleic acid amplification testing assays such as loop mediated isothermal amplification (LAMP), which has seen a report of benchtop LAMP assay for *C. auris* detection (Yamamoto et al., 2018), it is worth noting that miniaturized and rapid qPCR within POC.auris already delivers portability, speed, and simplicity through automation—potential "advantages" that isothermal assays promise to deliver. Moreover, isothermal assays still require sample preparation before testing, whereas POC.auris already integrates sample preparation. Third, although DM has been previously leveraged to develop POC diagnostic devices for other pathogens, POC.auris presents an advantage by incorporating an internal assay control, which represents an important benefit for POC diagnostic devices. Finally, throughout the development of POC.auris, we evaluated its sensitivity, specificity, hands-on time, turnaround time, and cost. These performance metrics should serve as the basis of comparison when future *C. auris* POC diagnostic devices are developed.

We envision several improvements for the current version of POC.auris to bring it a step closer to monitoring patients, screening close patient contacts, and testing environmental sources. First, isolates suspended in either PBS or a swab transport medium along with background human DNA were used as mock samples for the development and demonstration of POC.auris. A more extensive investigation into different sample types (e.g., clinical swabs and environmental sponges) with a range of sample volumes by adjusting the magnetic bead buffer and the sample well capacity of the assay cartridge is critical to assessing clinically relevant sensitivity and hence the clinical utility of POC.auris. Second, the current POC.auris involves brief but manual off-cartridge cell lysis and cartridge preparation. A simpler workflow using an improved assay cartridge that performs in-cartridge cell lysis and preloads all necessary reagents is critical to deploying POC.auris at POC and alleviating potential biosafety concerns from handling *C. auris*. Third, the current POC.auris can detect ~300 CFU/mL *C. auris* in <30 min. Enhancing the sensitivity and the turnaround time by further optimizing DNA extraction efficiency and accelerating PCR in the DM device may improve its usefulness at POC. Fourth, the current POC.auris employed a qPCR assay that focuses on detecting *C. auris*, but different PCR assays may be adapted toward detecting antifungal resistance gene markers (Hou et al., 2019; Kordalewska et al., 2019) or differentiating *C. auris* strains. Finally, both the one-time cost of the DM device and the cost per POC.auris assay can be reduced by employing inexpensive optical components such as a light-emitting diode (LED) and a complementary metal-oxide-semiconductor (CMOS) camera and exploring alternatives to the commercial cell lysis module. Based on the current performances and the potential for improvements, we envision a future version of POC.auris can become a useful diagnostic tool for combating *C. auris*.

DATA AVAILABILITY STATEMENT

The original contributions presented in the study are included in the article/Supplementary Material, further inquiries can be directed to the corresponding authors.

AUTHOR CONTRIBUTIONS

P-WL: methodology, investigation, validation, formal analysis, visualization, and writing—original draft, review, and editing. MT: methodology, investigation, and writing—review and editing. LC: conceptualization and methodology. F-EC: methodology and resources. AT: methodology and software. KS: resources. HN: resources. MJ: resources. KH: conceptualization, formal analysis, visualization, writing—original draft, review, editing, supervision, and

funding acquisition. SZ: conceptualization, writing—review and editing, supervision, and funding acquisition. T-HW: conceptualization, writing—review and editing, supervision, and funding acquisition.

FUNDING

This work was financially supported by the Sherrilyn and Ken Fisher Center for Environmental Infectious Diseases at Johns Hopkins University (FCDP-010ZHA2020) and the National Institutes of Health (R01AI137272, R01AI138978, and R61AI154628).

SUPPLEMENTARY MATERIAL

The Supplementary Material for this article can be found online at: https://www.frontiersin.org/articles/10.3389/fbioe.2022.826694/full#supplementary-material

REFERENCES

Adams, E., Quinn, M., Tsay, S., Poirot, E., Chaturvedi, S., Southwick, K., et al. (2018). Candida Auris in Healthcare Facilities, New York, USA, 2013-2017. *Emerg. Infect. Dis.* 24 (10), 1816–1824. doi:10.3201/eid2410.180649

Ahmad, A., Spencer, J. E., Lockhart, S. R., Singleton, S., Petway, D. J., Bagarozzi, D. A., Jr, et al. (2019). A High-throughput and Rapid Method for Accurate Identification of Emerging Multidrug-resistant Candida Auris. *Mycoses* 62 (6), 513–518. doi:10.1111/myc.12907

Arastehfar, A., Fang, W., Daneshnia, F., Al-Hatmi, A. M., Liao, W., Pan, W., et al. (2019). Novel Multiplex Real-Time Quantitative PCR Detecting System Approach for Direct Detection of Candida Auris and its Relatives in Spiked Serum Samples. *Future Microbiol.* 14 (1), 33–45. doi:10.2217/fmb-2018-0227

Armstrong, P. A., Rivera, S. M., Escandon, P., Caceres, D. H., Chow, N., Stuckey, M. J., et al. (20192016). Hospital-Associated Multicenter Outbreak of Emerging Fungus Candida Auris, Colombia, 2016. *Emerg. Infect. Dis.* 25 (7), 1339–1346. doi:10.3201/eid2507.180491

Bradley, S. F. (2019). What Is Known about Candida Auris. *JAMA* 322 (15), 1510–1511. doi:10.1001/jama.2019.13843

Bravo Ruiz, G., Ross, Z. K., Holmes, E., Schelenz, S., Gow, N. A. R., and Lorenz, A. (2019). Rapid and Extensive Karyotype Diversification in Haploid Clinical Candida Auris Isolates. *Curr. Genet.* 65 (5), 1217–1228. doi:10.1007/s00294-019-00976-w

Chen, F.-E., Lee, P.-W., Trick, A. Y., Park, J. S., Chen, L., Shah, K., et al. (2021a). Point-of-care CRISPR-Cas-Assisted SARS-CoV-2 Detection in an Automated and Portable Droplet Magnetofluidic Device. *Biosens. Bioelectron.* 190, 113390. doi:10.1016/j.bios.2021.113390

Chen, L., Wen, K., Chen, F.-E., Trick, A. Y., Liu, H., Shao, S., et al. (2021b). Portable Magnetofluidic Device for Point-of-Need Detection of African Swine Fever. *Anal. Chem.* 93 (31), 10940–10946. doi:10.1021/acs.analchem.1c01814

Chiou, C.-H., Jin Shin, D., Zhang, Y., and Wang, T.-H. (2013). Topography-assisted Electromagnetic Platform for Blood-To-PCR in a Droplet. *Biosens. Bioelectron.* 50, 91–99. doi:10.1016/j.bios.2013.06.011

Chowdhary, A., Prakash, A., Sharma, C., Kordalewska, M., Kumar, A., Sarma, S., et al. (2018). A Multicentre Study of Antifungal Susceptibility Patterns Among 350 Candida Auris Isolates (2009-17) in India: Role of the ERG11 and FKS1 Genes in Azole and Echinocandin Resistance. *J. Antimicrob. Chemother.* 73 (4), 891–899. doi:10.1093/jac/dkx480

Dennis, E. K., Chaturvedi, S., and Chaturvedi, V. (2021). So Many Diagnostic Tests, So Little Time: Review and Preview of Candida Auris Testing in Clinical and Public Health Laboratories. *Front. Microbiol.* 12, 757835. doi:10.3389/fmicb.2021.757835

Eyre, D. W., Sheppard, A. E., Madder, H., Moir, I., Moroney, R., Quan, T. P., et al. (2018). A Candida Auris Outbreak and its Control in an Intensive Care Setting. *N. Engl. J. Med.* 379 (14), 1322–1331. doi:10.1056/NEJMoa1714373

Hou, X., Lee, A., Jiménez-Ortigosa, C., Kordalewska, M., Perlin, D. S., and Zhao, Y. (2019). Rapid Detection of ERG11 -Associated Azole Resistance and FKS -Associated Echinocandin Resistance in Candida Auris. *Antimicrob. Agents Chemother.* 63 (1), e01811–01818. doi:10.1128/AAC.01811-18

Jainlabdin, M. H., Batra, A., Sánchez Paredes, E., Hernández Hernández, F., Fu, G., and Tovar-Torres, J. (2019). Single-tube, Dual Channel Pentaplexing for the Identification of Candida Strains Associated with Human Infection. *Sci. Rep.* 9 (1), 14692. doi:10.1038/s41598-019-51198-6

Jeffery-Smith, A., Taori, S. K., Schelenz, S., Jeffery, K., Johnson, E. M., Borman, A., et al. (2018). Candida Auris: a Review of the Literature. *Clin. Microbiol. Rev.* 31 (1), e00029–00017. doi:10.1128/CMR.00029-17

Kordalewska, M., Lee, A., Park, S., Berrio, I., Chowdhary, A., Zhao, Y., et al. (2018). Understanding Echinocandin Resistance in the Emerging Pathogen Candida Auris. *Antimicrob. Agents Chemother.* 62 (6), e00238–00218. doi:10.1128/AAC.00238-18

Kordalewska, M., Lee, A., Zhao, Y., and Perlin, D. S. (2019). Detection of Candida Auris Antifungal Drug Resistance Markers Directly from Clinical Skin Swabs. *Antimicrob. Agents Chemother.* 63 (12), e01754–01719. doi:10.1128/AAC.01754-19

Kordalewska, M., Zhao, Y., Lockhart, S. R., Chowdhary, A., Berrio, I., and Perlin, D. S. (2017). Rapid and Accurate Molecular Identification of the Emerging Multidrug-Resistant Pathogen Candida Auris. *J. Clin. Microbiol.* 55 (8), 2445–2452. doi:10.1128/JCM.00630-17

Ku, T. S. N., Walraven, C. J., and Lee, S. A. (2018). Candida Auris: Disinfectants and Implications for Infection Control. *Front. Microbiol.* 9, 726. doi:10.3389/fmicb.2018.00726

Leach, L., Russell, A., Zhu, Y., Chaturvedi, S., and Chaturvedi, V. (2019). A Rapid and Automated Sample-To-Result Candida Auris Real-Time PCR Assay for High-Throughput Testing of Surveillance Samples with the BD Max Open System. *J. Clin. Microbiol.* 57 (10), e00630–00619. doi:10.1128/jcm.00630-19

Leach, L., Zhu, Y., and Chaturvedi, S. (2018). Development and Validation of a Real-Time PCR Assay for Rapid Detection of Candida Auris from Surveillance Samples. *J. Clin. Microbiol.* 56 (2), e01223–01217. doi:10.1128/JCM.01223-17

Lima, A., Widen, R., Vestal, G., Uy, D., Silbert, S., and Land Geoffrey, A. (2019). A TaqMan Probe-Based Real-Time PCR Assay for the Rapid Identification of the Emerging Multidrug-Resistant Pathogen Candida Auris on the BD Max System. *J. Clin. Microbiol.* 57 (7), e01604–01618. doi:10.1128/JCM.01604-18

Meis, J. F., and Chowdhary, A. (2018). Candida Auris: a Global Fungal Public Health Threat. *Lancet Infect. Dis.* 18 (12), 1298–1299. doi:10.1016/s1473-3099(18)30609-1

Mizusawa, M., Miller, H., Green, R., Lee, R., Durante, M., Perkins, R., et al. (2017). Can Multidrug-Resistant Candidaauris Be Reliably Identified in Clinical Microbiology Laboratories? *J. Clin. Microbiol.* 55 (2), 638–640. doi:10.1128/JCM.02202-16

Park, J. Y., Bradley, N., Brooks, S., Burney, S., and Wassner, C. (2019). Management of Patients with Candida Auris Fungemia at Community Hospital, Brooklyn, New York, USA, 2016-20181. *Emerg. Infect. Dis.* 25 (3), 601–602. doi:10.3201/eid2503.180927

Schelenz, S., Hagen, F., Rhodes, J. L., Abdolrasouli, A., Chowdhary, A., Hall, A., et al. (2016). First Hospital Outbreak of the Globally Emerging Candida Auris in a European Hospital. *Antimicrob. Resist. Infect. Control.* 5, 35. doi:10.1186/s13756-016-0132-5

Sexton, D. J., Kordalewska, M., Bentz, M. L., Welsh, R. M., Perlin, D. S., and Litvintseva, A. P. (2018). Direct Detection of Emergent Fungal Pathogen Candida Auris in Clinical Skin Swabs by SYBR Green-Based Quantitative PCR Assay. *J. Clin. Microbiol.* 56 (12), e01337. doi:10.1128/JCM.01337-18

Shin, D. J., Athamanolap, P., Chen, L., Hardick, J., Lewis, M., Hsieh, Y. H., et al. (2017). Mobile Nucleic Acid Amplification Testing (mobiNAAT) for *Chlamydia trachomatis* Screening in Hospital Emergency Department Settings. *Sci. Rep.* 7, 4495. doi:10.1038/s41598-017-04781-8

Shin, D. J., Trick, A. Y., Hsieh, Y.-H., Thomas, D. L., and Wang, T.-H. (2018). Sample-to-Answer Droplet Magnetofluidic Platform for Point-of-Care

Hepatitis C Viral Load Quantitation. *Sci. Rep.* 8, 9793. doi:10.1038/s41598-018-28124-3

Shin, D. J., and Wang, T.-H. (2014). Magnetic Droplet Manipulation Platforms for Nucleic Acid Detection at the Point of Care. *Ann. Biomed. Eng.* 42 (11), 2289–2302. doi:10.1007/s10439-014-1060-2

Shin, D. J., Zhang, Y., and Wang, T.-H. (2014). A Droplet Microfluidic Approach to Single-Stream Nucleic Acid Isolation and Mutation Detection. *Microfluid. Nanofluid.* 17 (2), 425–430. doi:10.1007/s10404-013-1305-7

Srivastava, V., and Ahmad, A. (2020). Abrogation of Pathogenic Attributes in Drug Resistant Candida Auris Strains by Farnesol. *PLoS One* 15 (5), e0233102. doi:10.1371/journal.pone.0233102

Trick, A. Y., Melendez, J. H., Chen, F.-E., Chen, L., Onzia, A., Zawedde, A., et al. (2021). A Portable Magnetofluidic Platform for Detecting Sexually Transmitted Infections and Antimicrobial Susceptibility. *Sci. Transl. Med.* 13 (593), eabf6356. doi:10.1126/scitranslmed.abf6356

Tsay, S., Kallen, A., Jackson, B. R., Chiller, T. M., and Vallabhaneni, S. (2018). Approach to the Investigation and Management of Patients with Candida Auris, an Emerging Multidrug-Resistant Yeast. *Clin. Infect. Dis.* 66 (2), 306–311. doi:10.1093/cid/cix744

Vallabhaneni, S., Jackson, B. R., and Chiller, T. M. (2019). Candida Auris: An Emerging Antimicrobial Resistance Threat. *Ann. Intern. Med.* 171 (6), 432–433. doi:10.7326/m19-2205

Vallabhaneni, S., Kallen, A., Tsay, S., Chow, N., Welsh, R., Kerins, J., et al. (2017). Investigation of the First Seven Reported Cases of Candida Auris, a Globally Emerging Invasive, Multidrug-Resistant Fungus-United States, May 2013-August 2016. *Am. J. Transpl.* 17 (1), 296–299. doi:10.1111/ajt.14121

Vandeventer, P. E., Weigel, K. M., Salazar, J., Erwin, B., Irvine, B., Doebler, R., et al. (2011). Mechanical Disruption of Lysis-Resistant Bacterial Cells by Use of a Miniature, Low-Power, Disposable Device. *J. Clin. Microbiol.* 49 (7), 2533–2539. doi:10.1128/JCM.02171-10

Welsh, R. M., Bentz, M. L., Shams, A., Houston, H., Lyons, A., Rose, L. J., et al. (2017). Survival, Persistence, and Isolation of the Emerging Multidrug-Resistant Pathogenic Yeast Candida Auris on a Plastic Health Care Surface. *J. Clin. Microbiol.* 55 (10), 2996–3005. doi:10.1128/JCM.00921-17

Yamamoto, M., Alshahni, M. M., Tamura, T., Satoh, K., Iguchi, S., Kikuchi, K., et al. (2018). Rapid Detection of Candida Auris Based on Loop-Mediated Isothermal Amplification (LAMP). *J. Clin. Microbiol.* 56 (9), e00591–00518. doi:10.1128/JCM.00591-18

Zhang, Y., Park, S., Liu, K., Tsuan, J., Yang, S., and Wang, T.-H. (2011). A Surface Topography Assisted Droplet Manipulation Platform for Biomarker Detection and Pathogen Identification. *Lab. Chip* 11 (3), 398–406. doi:10.1039/c0lc00296h

Zhang, Y., and Wang, T.-H. (2013). Full-Range Magnetic Manipulation of Droplets *via* Surface Energy Traps Enables Complex Bioassays. *Adv. Mater.* 25 (21), 2903–2908. doi:10.1002/adma.201300383

Conflict of Interest: The authors declare that the research was conducted in the absence of any commercial or financial relationships that could be construed as a potential conflict of interest.

frontiers | Frontiers in Bioengineering and Biotechnology

REVIEW
published: 23 May 2022
doi: 10.3389/fbioe.2022.889431

Recent Advances in Aptasensors For Rapid and Sensitive Detection of *Staphylococcus Aureus*

Wei Chen[1,2,3,4]*, **Qingteng Lai**[3], **Yanke Zhang**[3] and **Zhengchun Liu**[3,4]*

[1]Department of Clinical Laboratory, Xiangya Hospital of Central South University, Changsha, China, [2]National Clinical Research Center for Geriatric Diseases, Xiangya Hospital of Central South University, Changsha, China, [3]Hunan Key Laboratory for Super Microstructure and Ultrafast Process, School of Physics and Electronics, Central South University, Changsha, China, [4]Department of Microbiology, School of Basic Medical Science, Central South University, Changsha, China

The infection of *Staphylococcus aureus (S.aureus)* and the spread of drug-resistant bacteria pose a serious threat to global public health. Therefore, timely, rapid and accurate detection of *S. aureus* is of great significance for food safety, environmental monitoring, clinical diagnosis and treatment, and prevention of drug-resistant bacteria dissemination. Traditional *S. aureus* detection methods such as culture identification, ELISA, PCR, MALDI-TOF-MS and sequencing, etc., have good sensitivity and specificity, but they are complex to operate, requiring professionals and expensive and complex machines. Therefore, it is still challenging to develop a fast, simple, low-cost, specific and sensitive *S. aureus* detection method. Recent studies have demonstrated that fast, specific, low-cost, low sample volume, automated, and portable aptasensors have been widely used for *S. aureus* detection and have been proposed as the most attractive alternatives to their traditional detection methods. In this review, recent advances of aptasensors based on different transducer (optical and electrochemical) for *S. aureus* detection have been discussed in details. Furthermore, the applications of aptasensors in point-of-care testing (POCT) have also been discussed. More and more aptasensors are combined with nanomaterials as efficient transducers and amplifiers, which appears to be the development trend in aptasensors. Finally, some significant challenges for the development and application of aptasensors are outlined.

Keywords: ***Staphylococcus aureus***, **aptasensor, optical biosensor, electrochemical biosensor, nanomaterials, POCT**

Edited by:
Han-Sheng Chuang,
National Cheng Kung University,
Taiwan

Reviewed by:
Nien-Tsu Huang,
National Taiwan University, Taiwan
Megan Yi-Ping Ho,
The Chinese University of Hong Kong,
China

***Correspondence:**
Wei Chen
573570494@qq.com
Zhengchun Liu
liuzhengchunseu@126.com

Specialty section:
This article was submitted to
Biosensors and Biomolecular
Electronics,
a section of the journal
Frontiers in Bioengineering and
Biotechnology

Received: 04 March 2022
Accepted: 12 April 2022
Published: 23 May 2022

Citation:
Chen W, Lai Q, Zhang Y and Liu Z
(2022) Recent Advances in
Aptasensors For Rapid and Sensitive
Detection of Staphylococcus Aureus.
Front. Bioeng. Biotechnol. 10:889431.
doi: 10.3389/fbioe.2022.889431

INTRODUCTION

S.aureus is one of the most pathogenic pathogens in the world and it was first discovered and named by Dr. Alexander Ogston in 1880 (Ogston, 1882). *S. aureus* is a major cause of foodborne poisoning (Hulme, 2017), with more than 240,000 cases annually in the United States, and it is a major public health concern (Zhang et al., 2019). *S. aureus* is also the most common pathogen in purulent infections in humans, and can enter any organ or enter the bloodstream when the host immunity is weakened or the skin and mucosal barriers are disrupted. It can cause skin and soft tissue infections (impetigo, folliculitis and scalded skin syndrome), and severe systemic diseases such as bacteremia, endocarditis, osteomyelitis, hemolytic pneumonitis, and toxic shock syndrome (Tong et al., 2015). Mild skin and mucosal infections are usually self-limiting, while severe systemic infections are usually associated with high mortality (20~50%), high recurrence rate (5~10%), and persistent injury (more than three points out of the survivors) (Kern and Rieg, 2020). Methicillin-resistant *S. aureus* (MRSA) has been a serious threat to global public health since it was first described in 1961 (Jevons, 1961). About 40~60% of nosocomial *S. aureus* infections are MRSA in developed countries such as the United States, Europe and Japan (Fluit et al., 2001), and the MRSA infection rate is higher in developing countries (>70%), probably due to the widespread and improper use of antibiotics, and the spread of drug-resistant bacteria (Chen and Huang, 2014).

The rapid and accurate detection of *S. aureus* is of great significance to food safety, environmental monitoring, clinical diagnosis and treatment, and prevention of the spread of drug-resistant bacteria. The gold standard for detecting *S. aureus* is still culture identification, the results are accurate and reliable, economical and simple, but it is very time-consuming, usually taking 1~2 days to form visible colonies on agar plates, and then 1~2 days for biochemical identification and serological typing. In recent years, several rapid and automated detection methods have been developed, such as enzyme-linked immunosorbent assay (ELISA) (Nouri et al., 2018), polymerase chain reaction (PCR) (Umesha and Manukumar, 2018), next-generation sequencing and matrix-assisted laser desorption/ionization time-of-flight mass spectrometry (MALDI-TOF-MS) (Gill et al., 2019; Rajapaksha et al., 2019), et al. But they are complex to operate, requiring professionals and expensive and complex machines. Therefore, it is still a hot issue to develop a fast, simple, low-cost, specific and sensitive *S. aureus* detection method.

In the past two decades, biosensors have been more and more widely used in pathogen detection due to fast, low cost, high sensitivity, low sample volume, automation and portability, and have been proposed as the most promising alternative to traditional pathogen detection methods (Furst and Francis, 2019; Cesewski and Johnson, 2020). The biosensor is mainly composed of three parts: bioreceptor, transducer and signal readout system (Yu et al., 2021). Biorecognition element refers to the "biological receptor" that can recognize the target with strong affinity and high specificity, and is the most critical part of the biosensor, which determines the specificity (selectivity) of the biosensor (Morales and Halpern, 2018). Antibodies, peptides and bacteriophages are the most commonly used biorecognition elements, among which antibodies are considered to be the gold standard recognition element in biosensors due to their high affinity and specificity between antibodies and antigens (Sharma et al., 2016). In the past few decades, antibody technology has developed rapidly and has made great contributions to the development of medicine and the entire life sciences. However, there are still many limitations in the application of antibodies such as the antibody development process is cumbersome and complicated and it is very challenging to generate antibodies that recognize small molecule targets (Zhou and Rossi, 2017; Liu et al., 2021a). Aptamers are another class of biorecognition elements that have attracted great interest in biosensing in recent years, and are known as "chemical antibodies" due to their ability to interact with their targets with strong affinity and high specificity similar to antigen-antibody interactions (Banerjee, 2010).

Aptamer is a specific oligonucleotide sequence (most commonly single-stranded DNA or RNA), usually ranging in length from 25 to 90 bases, and their binding to the target is based on the diversity of single-stranded nucleic acid structure and spatial conformation (Tok et al., 2000). In the presence of the target, aptamers pass through the pairing and electrostatic interactions between complementary bases in the chain, and self-adaptive folding into different types of secondary structures, including stems (Tok et al., 2000), inner loops, purine-rich bulges, hairpins, pseudoknots (Tuerk et al., 1992), kissing complexes (Boiziau et al., 1999), and G-quadruplex (Bock et al., 1992). Subsequently, these secondary structures assemble to form unique three-dimensional (3D) structures, resulting in strong affinity and high specificity for binding to target. Aptamers can efficiently and specifically attach to a wide range of targets, including small molecules, ions, peptides, proteins, viruses, bacteria and even cells (Shen et al., 2014). The affinity dissociation constants (Kd) of the aptamers with their cognate ligand are generally 1 pM~1 mM, most of them are between 1 and 10 nM, which is much larger than that of the related non-cognate ligand, indicating that aptamers have good specificity (Alizadeh et al., 2017). RNA-type oligonucleotide aptamers were fist found by Tuerk and Ellington in 1990 by phylogenetic evolution of ligands with exponential enrichment (SELEX) (Ellington and Szostak, 1990; Tuerk and Gold, 1990). Conventional SELEX consists of multiple cycles, each cycle including 5 main steps as shown in **Figure 1**: synthesis, binding, isolation, elution and amplification (Hamula et al., 2011; Teng et al., 2016). Since conventional SELEX is a very time-consuming process, many methods have been introduced in the past few decades to generate higher efficiency and reliability aptamers, such as Cell-SELEX (Dwivedi et al., 2013; Amraee et al., 2017; Li et al., 2018; He et al., 2019), Genomic SELEX (Lorenz et al., 2006), IP-SELEX (Wang et al., 2013), Capture-SELEX (Reinemann et al., 2016), CE-SELEX (Mendonsa and Bowser, 2004; Berezovski et al., 2006a; Berezovski et al., 2006b), M-SELEX (Lou et al., 2009), AFM-SELEX (Miyachi et al., 2010), AEGIS-SELEX (Sefah et al., 2014), Animal-SELEX (Cheng et al., 2013a), etc.

Aptamer-based biosensors are widely used in the rapid detection of *S. aureus* due to their fast, specific, low cost, low sample volume, automated, and portable. The commonly used aptamer sequences against *S. aureus* by SELEX technique are shown in **Table 1**. Therefore, this paper focuses on the latest progress of aptasensors based on different transducer (optical and electrochemical) for *S. aureus* detection. The detection principle, linear range, sensitivity and detection time of aptasensors are presented in **Table 2**. Furthermore, the applications of aptasensors in POCT have also been discussed. This review also highlights that more and more nanomaterials have been used as immobilized recognition elements or amplified detection signals to improve the sensitivity of aptasensors. Finally, some significant challenges for the development and application of aptasensors are outlined.

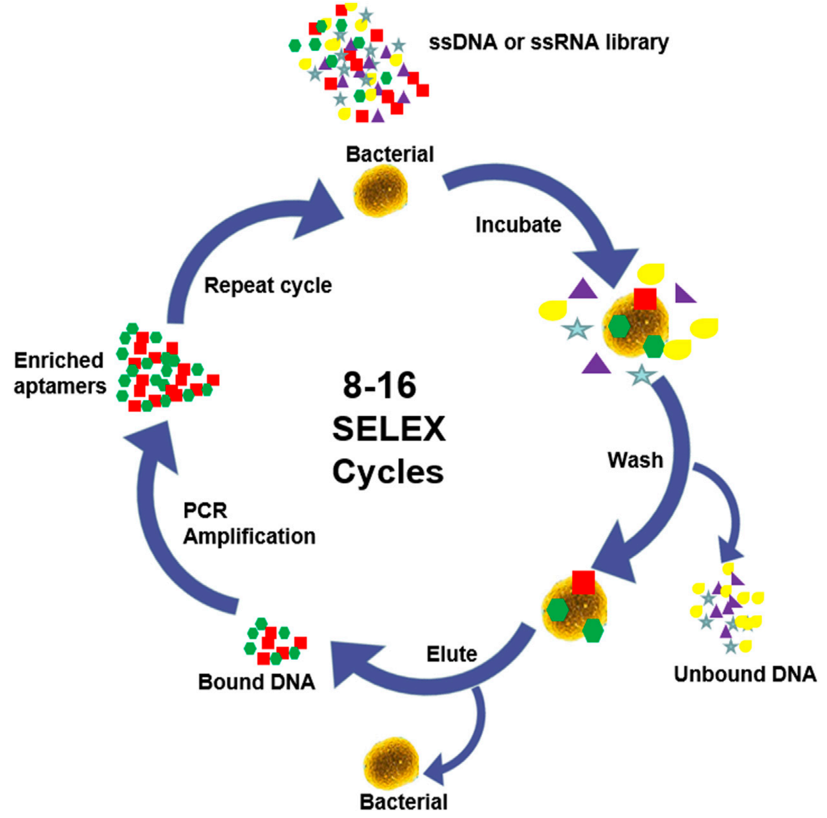

FIGURE 1 | SELEX process.

TABLE 1 | Aptamers selected against *S.aureus* by SELEX technique.

Aptamer name	Aptamer sequence (5–3′)	Kd (nM)	Ref
SA20	GCGCCCTCTCACGTGGCATCAGAGTGCCGGAAGTTCTGCGTTAT	70.86 ± 39.22	Cao et al. (2009)
SA23	GGGCTGGCCAGATCAGACCCCGGATGATCATCCTTGTGAGAACCA	61.50 ± 22.43	
SA31	TCCCACGATCTCATTAGTCTGTGGATAAGCGTGGGACGTCTATGA	82.86 ± 33.20	
SA34	CACAGTCACTCAGACGGCCGCTATTGTTGCCAGATTGCCTTTGGC	72.42 ± 35.23	
SA43	TCGGCACGTTCTCAGTAGCGCTCGCTGGTCATCCCACAGCTACGTC	210.70 ± 135.91	
SA17	TCCCTACGGCGCTAACCCCCCCAGTCCGTCCTCCCAGCCTCACACCGCCACCGTGCTACAAC	35.0	Chang et al. (2013)
SA61	TCCCTACGGCGCTAACCTCCCAACCGCTCCACCCTGCCTCCGCCTCGCCACCGTGCTACAAC	129.0	
A14	CACACCGCAGCAGTGGGAACGTTTCAGCCATGCAAGCATCACGCCCGT	3.49 ± 1.43	Moon et al. (2015)
RAB1	CGGGTGGGCTCCAATATGAATCGCTTGCCCTGACGCTATCT	56 ± 87	Ramlal et al. (2018)
RAB3	CGTAGTCTAGTGTCGATTAGTTTCCTTGAGACCTTGTGCT	37 ± 112	
RAB5	CGTAGTCTAGTGTCGATTAGTTTCCTTGCTATTGCAGACCTTGTGCT	58 ± 14	
RAB10	TCGAGAGGGATCTCGGGGCGTGCGATGATTTTGCCTTCAT	46 ± 24	
RAB20	GCGTTACGTTAGTGGCCGCCTATGAGGACAGGCGGTTGTA	128 ± 45	
RAB28	TGGACGTCGTGGCGGAGGTTTTATAAAACGGCGCCACTGT	49 ± 39	
RAB35	GGGGGGTTGTGCCATTTAAGATGACCGGTTGCCGCGATTT	34 ± 5	
SA25	GGGGAAGGTCGTCCGACGAACCCGGTCAGATAGGGTGGGG	44.92 ± 1.36	Nguyen et al. (2022)
SA28	GCGGCCACGGAGGGGGTGCCGGGCGTGGAATAAGATGTGG	77 ± 1.22	
SA35	CACAGGTGTGGGGAGGTCCCCATGGAGGTGGTTCAATG	58.77 ± 0.73	
SA37	AAAGACGGGGGGGGGGACCGGCGTATGAGTGAAGATGGGG	16.5 ± 3.41	
SA40	CGACGTGAAGCAATCATGGGTGGGGTACGTCGGGTCATGG	126.95 ± 0.51	
SA81	AACGAGGCGCAGGGGGAGGGGGTGGTACAGATAAGATGGGG	14.47 ± 8.18	

TABLE 2 | Available aptasensors for detect S.aureus.

Detection methods	Strategy/Assay	Linear range (CFU/ml)	LOD (CFU/ml)	Time	References
Colorimetric	Gold nanoparticle-based colorimetric aptasensor using tyramine signal amplification (TSA) technology	$10\sim10^6$	9	1~2 h	Yuan et al. (2014b)
Colorimetric	Visual detection based on aptamer recognition coupled to tyramine signal amplification	$10\sim10^7$	8	1~2 h	Yuan et al. (2014a)
Colorimetric	A colorimetric based on Cu-MOF-catalyzed chromogenic reaction with aptamer recognition and magnetic separation	$50\sim10^4$	20	~1 h	Wang et al. (2017a)
Colorimetric	A chemiluminescence biosensor based on nicking enzyme amplification reaction and rolling circle amplification	$5\sim10^4$	5	~2 h	Xu et al. (2018)
Colorimetric	A colorimetric biosensor based on specific aptamer and catalysis of dsDNA-SYBR Green I (SG I) complex	$10^2\sim10^7$	81	5~6 h	Yu et al. (2020)
Colorimetric	A novel colorimetric immunoassay based on a combination of immunomagnetic separation and signal amplification *via* etching-enhanced peroxidase-like catalytic activity of gold nanoparticles (AuNPs)	$10\sim10^6$	10	~1 h	Yao et al. (2020)
Colorimetric	on-site colorimetric based on aptamer-immobilized gold nanoparticles (aiGNPs)	$1.5 \times 10^7\sim5.3 \times 10^7$	1.5×10^7	~1 h	Lim et al. (2021)
Colorimetric	One-step colorimetric based on target-induced shielding against the peroxidase mimicking activity of aptamer-functionalized gold-coated iron oxide nanocomposites	$10\sim10^6$	10	12 min	Zhang et al. (2021b)
Colorimetric	A colorimetry and fluorescenc dual-signal strategy based on Upconversion Nanoprobes	$56\sim5.6 \times 10^6$	20	/	Ouyang et al. (2021a)
Colorimetric	A multicolorimetric assay based on oxidase mimicking activity of aptamer-functionalized manganese dioxide-coated ferriferrous oxide (apt-Fe_3O_4/MnO_2) nanocomposites and oxTMB etching of gold nanorods (AuNRs)	$10\sim10^6$	10 (bare eye) and 1.2~1.4(UV–visible spectrometry)	40 min	Zhang et al. (2021a)
Fluorescence	A sensitive luminescent bioassay based on dual-color upconversion nanoparticles (UCNPs) and aptamer-functionalized magnetic nanoparticles	$10\sim10^5$	8	40 min	Duan et al. (2012)
Fluorescence	Aptasensor simultaneous detection of various pathogenic bacteria based on multicolor upconversion nanoparticles (UCNPs)	$50\sim10^6$	25	40 min	Wu et al. (2014)
Fluorescent	A sensitive assay based on aptamer-functionalized silica magnetic nanoparticles and fluorophore loaded and nuclease resistant oligonucleotides-capped nanokeepers (mesoporous silica nanoparticles)	$800\sim10^4$	682	17 min	Borsa et al. (2016)
Fluorescence	A dual-excitation sensing method based on aptamer-functionalized quantum dots and upconverting nanoparticle	$50\sim10^6$	16	30 min	Kurt et al. (2016)
Fluorescence	A dual recognition strategy using aptamer-coated magnetic beads and antibiotic-capped gold nanoclusters	$32\sim10^8$	16	3~4 h	Cheng et al. (2016)
Fluorescence	A transcription aptasensor by using a light-up RNA aptamer	$10^2\sim10^6$	77	/	Sheng et al. (2019)
Fluorescent	A fluorescent detection based on a finely designed functional chimera sequence, a molecular beacon (MB), and strand displacement target recycling	$80\sim8 \times 10^6$	39	2~3 h	Cai et al. (2019)
Fluorescence	A highly selective platform based on aptamer-gated nano-materials	$10\sim10^3$	2 in buffer and 5 in blood	1 h	Pla et al. (2020)
Fluorescence	A fluorescent aptasensor based on strand displacement amplification (SDA) technology and unique self-assembled DNA hexagonal structure	$7\sim7 \times 10^7$	1.7	~5 h	Cai et al. (2020)
Fluorescent	A fluorescence biosensor based on a peptide-mediated immunomagnetic separation technique and an immunofluorescence quantum dot technique	$10\sim10^7$	5.407 in buffer, 19.9 in tap water and 10.7 in milk simulation	~4 h	Wang et al. (2020)
Fluorescence	A colorimetry and fluorescenc dual-signal strategy based on Upconversion Nanoprobes	$56\sim5.6 \times 10^6$	22	/	Ouyang et al. (2021a)
Fluorescence	A novel aptasensor based on aptamer-functionalized DNA–silver nanocluster nanofim	$10^7\sim10^{11}$	/	>12 h	Yang et al. (2021a)

(Continued on following page)

TABLE 2 | (*Continued*) Available aptasensors for detect S.aureus.

Detection methods	Strategy/Assay	Linear range (CFU/ml)	LOD (CFU/ml)	Time	References
Fluorescent	A new fluorescence biosensor using aptamer- and vancomycin -copper nanoclusters as dual recognition strategy	10^2~10^8	80	45 min	Pebdeni et al. (2021)
FRET	A multiplexed FRET-based aptamer biosensor using multicolor dyes as donors and carbon nanoparticles (CNPs) as a sole acceptor	10^2~10^6	50	>3 h	Duan et al. (2016)
FRET	A dual-recognition FRET sensor based on fluorescent vancomycin–gold nanoclusters and aptamer–gold nanoparticles	20~10^8	10	30 min	Yu et al. (2017)
FRET	A FRET aptasensor based on self-assembled Fe_3O_4 and multicolor fluorescent carbon dots (CDs)	50~10^7	8	30 min	Cui et al. (2019)
FRET	A biosensing platform based on the binding protection effect of aptamer-cell complex	10^2~10^7	64	1~2 h	Lu et al. (2020b)
FRET	A fluorescent turn-on aptasensor based on the FRET between green carbon quantum dot and gold nanoparticle	10~10^8	10	~2 h	Pebdeni et al. (2020)
FRET	A simple one-step FRET sensor based on the aptamer modified quantum dots (Aptamer-QDs) and antibiotic molecule of Teicoplanin functionalized-gold nanoparticles (Teico-AuNPs)	/	1/cell	~2 h	Fu et al. (2020)
FRET	An efficient FRET sensor based on stimuli-responsive nanoprobe PDANSs-FAM-Apt	0~3.5×10^8	1	~6 h	Ye et al. (2020)
FRET	A simple one-step FRET sensor based on aptamer-modified quantum dots (aptamer-QDs) w and antibiotic of teicoplanin functionalized-gold nanoparticles (Teico-AuNPs)	10~5×10^8	2 in buffer and 100 in milk	1 h	Tao et al. (2021)
FRET	A FRET aptasensor based on Aptamer-functionalized gold nanoparticles (AuNPs-aptamers) and cDNA-modified upconversion nanoparticles (UCNPs-cDNA)	47~4.7×10^7	10.7	17 min	Ouyang et al. (2021a) Ouyang et al. (2021b)
Ratiometric FRET	A dual-recognition ratiometric fluorescent nanosensor based on the blue fluorescence of novel π-rich CNPs and NIR fluorescent Apt-Van-QDs	0~10^6	1	30 min	Shen et al. (2020)
NSET	A one-step fluorometric strategy based on nanometal surface energy transfer (NSET) between carbon dots (CDs) and gold nanoparticles (AuNPs)	10~10^6	10	~1 h	Yao et al. (2021)
Fluorescence imaging	A fluorescence microscopy imaging based on positive dielectro-phoresis (pDEP) driven on-line enrichment and aptamer-fluorescent silica nanoparticle (FNP)	50~10^6	93 in deionized water and 270 in spiked water	1~2 h	Shangguan et al. (2015)
Fluorescence imaging	A quantitative fluorescence imaging platform on a smartphone based on aptamer-functionalized fluorescent magnetic nanoparticles	50~2000	10	10 min	Shrivastava et al. (2018)
SERS	A magnetically assisted SERS biosensor based on Ag-coated magnetic nanoparticles, AgMNPs as SERS substrate and AuNR–DTNB@Ag–DTNB core–shell plasmonic NPs or DTNB-labeled inside-and-outside plasmonic NPs, DioPNPs as SERS tag	10~10^5	10	50 min	Wang et al. (2015)
SERS	A SERS biosensor based on sandwich structure by using gold nanoparticles and MGNPs immmoblized with aptamers	10^2~10^7	35	2-3 h	Zhang et al. (2015a)
SERS	A microfluidic optical device based on SERS-encoded nanoparticles functionalized with aptamer	/	<15	10 min	Catala et al. (2016)
SERS	A label-free SERS detection based on aptamer dependent *in situ* formations of silver nanoparticles (AgNPs)	10~10^7	1.5	25 min	Gao et al. (2017)
SERS	Dual-recognition SERS biosensor based on vancomycin- -Au@MBA as SERS tags and aptamer-Fe_3O_4@Au as specific magnetic concentration and dual-SERS substrat	10~10^7	3	45 min	Pang et al. (2019)
SERS	Fluorescence and SERS dual-mode biosensor based on gold nanoparticle-modified polystyrene microspheres (Au/PS)	16~1.6×10^5	3	1~2 h	Lei et al. (2020)
SERS	A SERS aptasensor based on AuNPs functionalized polydimethylsiloxane (PDMS)film	43~4.3×10^7	13	>2 h	Zhu et al. (2021a)

(Continued on following page)

TABLE 2 | (*Continued*) Available aptasensors for detect S.aureus.

Detection methods	Strategy/Assay	Linear range (CFU/ml)	LOD (CFU/ml)	Time	References
SERS	A SERS aptasensor based on artificial peroxidase enzyme regulated multiple signal amplified system	10~10^6	1.95	>3 h	Liu et al. (2021b)
SERS	A simple and novel biosensor based on target-induced release of signal molecules from aptamer-gated aminated mesoporous silica nanoparticles (MSNs) coupled with surface-enhanced Raman scattering (SERS) technology	47~4.7×10^8	17	13 min	Zhu et al. (2021b)
SERS	A SERS biosensor based on aptamer-facilitated gold/silver nanodimers and magnetic separation enrichment	3.2×10^2~3.2×10^7	96	30 min	Ma et al. (2021)
SERS	A SERS biosensor based on the sandwich recognition of aptamer-functionalized magnetic beads and polyphenolic SERS nanotags	10^2~10^8	10^2	1~2 h	Huang et al. (2021)
SPR	The SPR aptasensors via a polyadenine-mediated immobilization method	10^5~10^8	10^6	/	Wang et al. (2019b)
LSPR	A LSPR sensors based on aptamer at nanostructured plasmonic elements	/	10^3	2 min	Khateb et al. (2020)
ECL	An electrochemiluminesce aptasensor based on the quenching effect of MoS_2-PtNPs-vancomycin to $S_2O_8^{2-}/O_2$ system	1.5×10^2~1.5×10^8	28	2~3 h	Han et al. (2019)
CRET	An enhanced chemiluminescence resonance energy transfer aptasensor based on rolling circle amplification and WS_2 nanosheet	50~1.5×10^5	15	1 h	Hao et al. (2017)
Potentiometric	Label-free potentiometric biosensors based on carbon nanotubes and aptamers	2.4×10^3~2.0×10^4	8×10^2	30 min	Zelada-Guillen et al. (2012)
Potentiometric	A potentiometric biosensor based on chemically modified graphene (transducer layer of the aptasensor) and aptamers (sensing layer)	/	1	1-2 min	Hernandez et al. (2014)
DPV	An electrochemical immunosensor based on dual-aptamer-based sandwich by using streptavidin coated magnetic beads (MB) and silver nanoparticles immmoblized with aptamers	10~10^6	1	30 min	Abbaspour et al. (2015)
DPV	A versatile signal-on electrochemical biosensor based on triple-helix molecular switch	30~3×10^8	8	>3 h	Cai et al. (2021a)
DPV	An electrochemical biosensor based on the electrodeposition of Cu metal–organic framework (Cu-MOF) thin film	7~7×10^6	1.9	30 min	Sun et al. (2021)
DPV	A dual signal amplification electrochemical biosensor based on a DNA walker and DNA nanoflower	60~6×10^7	9	140 min	Cai et al. (2021b)
EIS	Impedimetric aptasensor based on nanocomposite prepared from reduced graphene oxide and gold nanoparticles	10~10^6	10	60 min	Jia et al. (2014)
EIS	Impedimetric biosensor based on aptamer as biological recognition element	10~10^9	10	10 min	Reich et al. (2017)
EIS	An electrochemical aptasensor based on gold nanoparticles/carbon nanoparticles/cellulose nanofibers nano-composite (AuNPs/CNPs/CNFs) at the surface of glassy carbon electrode	12~1.2×10^8	1	30 min	Ranjbar and Shahrokhian, (2018)
Capacitance	A capacitance sensors array functionalized with aptamers	/	10	1 h	Jo et al. (2018)
Conductometric	Conductometric sensor based on magnetic analyte separation via aptamer	4.1×10^3~4.1×10^8	4.0×10^3	60 min	Zhang et al. (2020)
Volumetric bar-chart chip	A bacteria-detection V-Chip based on the extraordinary catalytic activity of platinum nanozyme and the aptamer-modified magnetic beads	1~10^8	1	1.5 h	Huang et al. (2019)
Flow cytometry	A dual-color flow cytometry assay based on aptamer recognition and fluorescent silica nanoparticles (FSiNPs)	/	150 in buffer and 760 in spiked milk	/	He et al. (2014)
Resonancelight-scattering	A biosensor combines aptamer-conjugated gold Nanoparticles and a resonance light-scattering-detection system	/	1	1.5 h	Chang et al. (2013)
Nanophotonic interferometric	A nanophotonic interferometric biosensor based on a bimodal waveguide interferometer (BiMW)	800~1.6×10^5	29	12 min	Maldonado et al. (2020)

(Continued on following page)

TABLE 2 | (*Continued*) Available aptasensors for detect S.aureus.

Detection methods	Strategy/Assay	Linear range (CFU/ml)	LOD (CFU/ml)	Time	References
Magnetoelastic	A magnetoelastic sensors based on an aptamer-modified magnetoelastic alloy	$10\sim10^{11}$	5	5~6 min	Rahman et al. (2015)
Piezoelectric	A novel aptamer/graphene interdigitated gold electrode piezoelectric sensor by employing aptamer as a biological recognition element	$41\sim4.1\times10^5$	41	~1 h	Lian et al. (2015)
Lateral flow test strip	A lateral flow test strip based on the sandwich-type format using primary aptamer conjugated with gold nanoparticles (AuNPs) as the signal probe and a secondary aptamer-coated membrane as a capture probe	/	10^4	10 min	Lu et al. (2020a)
Engineered aptasensor	A novel pathogen aptasensor swab based on functionalized nanobeads	$10^2\sim10^5$	<100 (visual) and 2 (theoretically)	5 min	Raji et al. (2021)
Microfluidic biochip	Microfluidic device based on a polydimethylsiloxane (PDMS)/paper/glass hybrid and aptamer-functionalized graphene oxide (GO)	$10^4\sim10^6$	800	10 min	Zuo et al. (2013)
Microfluidic chips	Paper-based microfluidic chips based on dual-aptamer-based sandwich	/	10^5	35 min	Wang et al. (2019a)
Pressure-based biosensor	POC testing protocol based on vancomycin (Van)-functionalized platinum nano-particles (PtNPs@Van) and aptamer-coated magnetic $CuFe_2O_4$ nanoprobes dual-recognition units and the catalyzed gas-generation reaction	$5\sim10^4$	1	30 min	Li et al. (2019a)
PGM-based biosensor	Magnetic-aptamer biosensor based on the PGM platform and hybridization chain reaction strategy	$3\sim3\times10^3$	2	>5 h	Yang et al. (2021b)

"/": Not mentioned.

APTASENSORS BASED ON OPTICAL TRANSDUCTION

Optical biosensors have been widely used in the detection of *S. aureus* due to simple, fast, low cost, high sensitivity, real-time monitoring capability and label-free possibility. Optical biosensors can be classified according to transduction mechanisms such as absorption, scattering, diffraction, reflection, refraction and luminescence (photoluminescence, chemiluminescence, electrochemiluminescence or bioluminescence) (Paniel et al., 2013). Colorimetric, fluorescence, chemiluminescence, surface plasmon resonance (SPR) and surface-enhanced Raman scattering (SERS) are the most commonly used optical techniques (Rubab et al., 2018).

Colorimetric-Based Aptasensor

Colorimetric is the simplest and oldest biosensors. It can detect the target by detecting the color change of the solution with the naked eye or a simple instrument such as a UV-Vis spectrophotometer. It has been widely used to monitor various targets due to its simplicity, stability and low cost (Wang et al., 2018). The key technology of colorimetric is the selection of catalytic enzymes and corresponding chromogenic substrates. Traditional catalytic enzymes such as horseradish peroxidase (HRP) show high substrate specificity and catalytic efficiency, and its substrates are usually 3,3',5,5'-tetramethylbenzidine (TMB) and 2,2'-azino-bis (3-ethylbenzothiazoline-6-sulfonic acid) (ABTS). Yuan et al. constructed a colorimetric-based aptasensor combining aptamer, HRP and tyramide signal amplification technology for the detection of *S. aureus* (Yuan et al., 2014a). With the help of tyramide signal amplification technology, the limit of detection (LOD) can reach to 8 CFU/ml, and the linear range is $10\sim10^7$ CFU/ml (Yuan et al., 2014a). G-quadruplex (G4) is a DNase with a steric configuration, which has been widely used in biosensors due to its ability to combine with hemin to form a DNA-mimicking enzyme with catalase activity. Xu et al. established an ultrasensitive colorimetric-based aptasensor for *S. aureus* detection by using nickase amplification reaction (NEAR), rolling circle cycle amplification technology (RCA) and G4/hemin complex (Xu et al., 2018). The results showed that the established biosensor exhibited good discrimination between live and dead *S. aureus* in addition to good specificity, low detection limit (5 CFU/ml), and wide linear range ($5\sim10^4$ CFU/ml) (Xu et al., 2018).

Although HRP and G4 show high substrate specificity and catalytic efficiency, they also have disadvantages such as difficulty in storage, poor stability, and catalytic activity is easily affected by external conditions (such as pH). Since Woo discovered that Fe_3O_4 nanoparticles exhibited peroxidase activity in 2013 (Woo et al., 2013), Fe_3O_4 nanoparticles have received great attention due to their outstanding peroxidase-like activity, physicochemical stability, low cost, non-toxicity, and magnetic properties that can be used for enrichment and isolation of targets. Coating metal catalysts on the surface of magnetic nanoparticles to form hybrid nanocomposites can not only avoid the oxidation of Fe_3O_4 nanoparticles, but also significantly improve their catalytic performance (Zhang et al., 2021a; Zhang et al., 2021b). Zhang et al. synthesized a gold-coated Fe_3O_4 nanocomposites to construct a colorimetric-based aptasensor for one-step detection of *S. aureus* in water, urine and milk samples. The

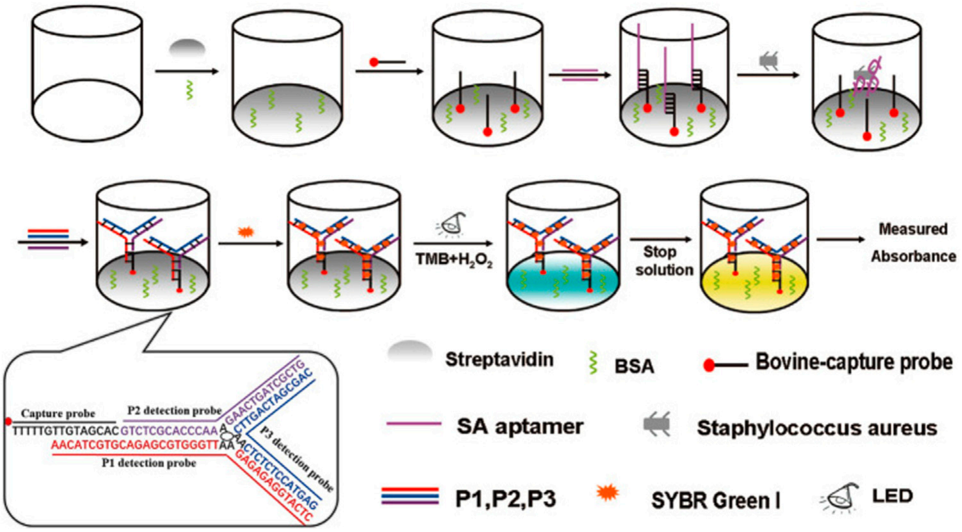

FIGURE 2 | Schematic illustration of the principle for detection of *S. aureus* with aptamer-high throughput colorimetric biosensor based on photocatalytic activity of dsDNA-SG I complex. Reproduced with permission (Yu et al., 2020).

detection process does not require enrichment, separation or washing steps, and the results can be obtained by naked eye in 12 min. Under the optimal reaction conditions, the LOD is 10 CFU/ml, and the linear range is 10~10^6 CFU/ml (Zhang et al., 2021b). Besides Fe_3O_4 nanoparticles, a variety of metal nanoparticles have also been synthesized as peroxide analogs in recent years, such as CeO_2 NPs, Cu-MOF NPs, Co_3O_4 NPs, $ZnFe_2O_4$NPs (Su et al., 2012; Wang et al., 2017a; Li et al., 2017b; Cheng et al., 2019).

There is also a class of enzyme-free colorimetric-based aptasensors, such as gold and silver metal nanoparticles, which are widely used as signal indicators due to their size- and distance-dependent optical properties (Mokhtarzadeh et al., 2015; Taghdisi et al., 2016). The color of AuNPs solution will change from red to blue or purple when the well-dispersed AuNPs aggregate under certain conditions, which was caused by the change of the surface resonance frequency of the AuNPs. Due to the high extinction coefficient of AuNPs, the sensitivity of colorimetric sensors based on AuNPs is higher than that of organic dyes (Ghosh and Pal, 2007). Chang et al. constructed an sensor based on aptamer and AuNPs for accurate identification of *S. aureus* from common pathogens (Chang et al., 2016). In the presence of *S. aureus*, the aptamer was removed by binding to *S. aureus*. Then the AuNPs aggregated when AuNPs and high salt were added, and the color of AuNPs solution will turned to blue or purple. In the absence of *S. aureus*, the color of the AuNPs solution was red because the unscavenged aptamers can adsorbed on the surface of AuNPs and protected AuNPs from ion-induced aggregation (Chang et al., 2016). Zhang et al. discovered that the dsDNA-SYBR Green I (SG I) complex has photocatalytic activity for the first time, which can utilize dissolved oxygen to catalyze the oxidation of the substrate TMB under light irradiation (Zhang et al., 2015b). Compared with HRP and G4, dsDNA-SG I complex has obvious advantages, such as simplicity, high sensitivity and label-free. Yu et al. constructed a colorimetric-based photoirradiation aptasensor for detection of *S. aureus* based on catalysis of dsDNA-SG I complex (**Figure 2**). The results shown that the biosensor could specifically, sensitively, rapidly and quantitatively detect *S. aureus*. In addition, this method can be used for high throughput analysis as it can detect 96 samples at once (Yu et al., 2020).

Fluorescence-Based Aptasensor

Fluorescence-based aptasensors mainly trigger or inactivate the fluorescence emission properties of fluorescent dyes or fluorescent nanomaterials through the interaction of aptamers with targets. Fluorescence-based aptasensors have become one of the most commonly used sensors for low-concentration analyte detection due to the advantages of the higher sensitivity, wider detection range and multiplex detection as compared with colorimetric-based aptasensors. It is relatively easy to construct distance-dependent fluorescence resonance energy transfer (FRET) aptasensors because aptamers can be easily modified with fluorophores or/and quenching dyes at the 3’ or 5’ end without affecting their binding affinity to the target. Traditional organic fluorescent dyes mainly include carboxyfluorescein (FAM), fluorescein isothiocyanate (FITC) and acridine orange, which have been widely used for a long time (Paniel et al., 2013). Lu et al. proposed an enzymatic cleavage aptasensor in which the aptamer act as biological recognition element for *S. aureus* in complex samples. The two ends of the molecular beacon were labeled with FAM (fluorophore) and BHQ1 (quencher) respectively, and can hybridize stably with aptamers. The aptamer can avoid being cleaved by exonuclease (Exonuclease I and III, Exo. I and III) when binging to *S. aureus* due to the enzymatic protection effect of aptamer-pathogen complex. The unscavenged aptamer then combined with the molecular beacon, which separated the fluorophore from the quencher, thereby

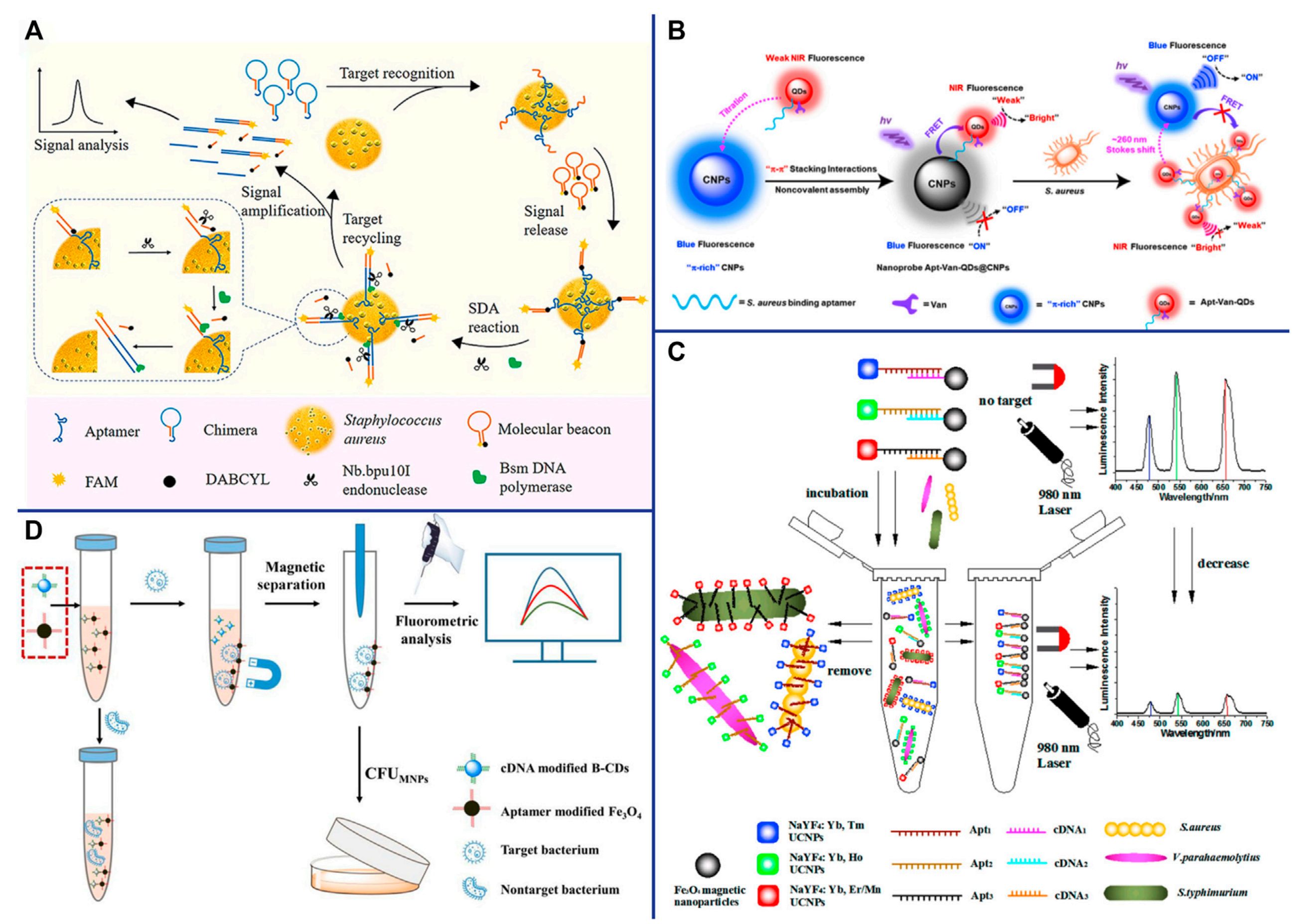

FIGURE 3 | (A) Schematic representation of the fluorescent detection of *S. aureus* based on a finely designed functional chimera sequence, a molecular beacon (MB), and strand displacement target recycling. Reproduced with permission (Cai et al., 2019). **(B)** General design of the vancomycin and aptamer dual-recognition moieties-based ratiometric fluorescent nanoprobe with a remarkably large Stokes shift for ultrafast and accurate management of *S. aureus* at the single-cell level. Reproduced with permission (Shen et al., 2020). **(C)** Schematic illustration of the multiplexed luminescence bioassay based on aptamers-modified UCNPs for the simultaneous detection of various pathogenic bacteria. Reproduced with permission (Wu et al., 2014). **(D)** Schematic illustration of the fluorometric aptasensor for high-sensitivity *S. aureus* detection based on FRET of the self-assembled dimer, B-CD/Fe_3O_4. Reproduced with permission (Cui et al., 2019).

restoring the fluorescence (Lu et al., 2020b). This detection system can be completed in the same tube without culture or separation, but its sensitivity (64 CFU/ml) need to be improved (Lu et al., 2020b).

DNA amplification systems such as rolling cycle amplification (RCA), strand displacement reaction (SDA) (Cai et al., 2020), hybridization Chain reaction (HCR) (Yang et al., 2021b) and hairpin DNA cascade hybridization reaction (HD-CHR) are often used to improve the sensitivity of aptasensor. The SDA is an isothermal amplification that does not require thermal cycling, which can exponentially expand the target sequence in less than 15 min (Wang et al., 2017b). Cai et al. designed an aptasensor for *S. aureus* detection based on functional chimera sequence, molecular beacon and SDA. The functional chimera sequence contains the *S. aureus* aptamer sequence and the molecular beacon complementary sequence, and it can form a hairpin structure. The molecular beacon was labeled with FAM (fluorophore) and DABCYL (quencher) in the end respectively. The distance between FAM and DABCYL in the hairpin structure of the molecular beacon is narrow, and the fluorescence signal of FAM is quenched by DABCYL. When the aptamer in the functional chimera sequence binds to *S. aureus*, the molecular beacon complementary sequence will be exposed and bound to the molecular beacon, keeping the FAM away from the DABCYL, and thereby emitting fluorescence (**Figure 3A**). The established aptasensor displays good detection limit (39 CFU/ml), wide linear range (8~8 × 10^8 CFU/ml), satisfactory recovery and repeatability (Cai et al., 2019). However, the use of traditional organic fluorescent dyes in sensors is limited due to low fluorescence intensity and rapid photobleaching. Compared with traditional organic fluorescent dyes, fluorescent nanomaterials such as quantum dots (QDs) (Fu et al., 2020; Tao et al., 2021), upconversion nanoparticles (UCNPs) (Wu et al., 2014; Ouyang et al., 2021b) and carbon dots (Cui et al., 2019; Pebdeni et al., 2020) that have emerged in recent years have many advantages, such as wider absorption spectra, size-tunable narrower emission spectra and better stability (Yao et al., 2014).

QDs are nanoscale semiconductors (1~20 nm in diameter), which can be effectively excited by any wavelength shorter than the emission peak and emit a narrow and symmetrical characteristic spectrum that varies with the size of the QD. Since QDs of different sizes can be excited by the same wavelength and emit different emission peaks, Wang et al. achieved the simultaneous detection of *Escherichia coli* O157: H7, *S. aureus* and *Vibrio* parahaemolyticus by modifying different aptamers with QDs of different sizes (Wang et al., 2020). Shen et al. constructed a ratiometric FRET-based aptasensor which involves target-induced emission intensity changes at two or more different wavelengths to reduces interference from various target-independent factors (Shen et al., 2020). They employed novel π-electron-rich carbon nanoparticles (CNPs) with high photostability and blue fluorescence as energy donors, and bilayer-modified QDs with aptamers and vancomycin as energy acceptors (Apt-Van-QDs). Due to the π−π stacking interaction, the Apt-Van-QDs will bind to the surface of π-rich CNPs, thereby promoting FRET between QDs and CNPs, and resulting in strong blue fluorescence quenching at ~465 nm for the CNPs and fluorescence enhancement at ~725 nm for Apt-Van-QDs (Shen et al., 2020). The FRET between QDs and CNPs was disrupted and exhibited a large Stokes shift of ~260 nm when Apt-Van-QDs binds to *S. aureus* and moves away from CNPs (**Figure 3B**). The dual-recognition ratiometric fluorescent nanosensor showed an ultrahigh specificity and can detect a single bacteria with 30 min (Shen et al., 2020). The use of a suitable donor-acceptor is crucial to improve the efficiency of FRET. AuNPs serve as excellent energy acceptors for ultrasensitive molecular detection due to easy synthesis, good optical and colloidal stability, and high extinction coefficient. Fu et al. established a dual-recognition FRET-based aptasensor for the detection of *S. aureus* by using aptamer-modified QDs as donors and teicoplanin-modified AuNPs as acceptors. This dual-recognition FRET-based aptasensor can detect a single *S. aureus* in cells, providing a simple, specific, sensitive and rapid diagnostic method for the detection of intracellular bacteria (Fu et al., 2020). QDs are typically extracted from a mixture of lead, cadmium and silicon that are often toxic and environmentally hazardous, which limiting their applications.

Lanthanide-doped NIR-to-visible UCNPs are able to emit intense visible light upon excitation by NIR (usually 980 nm), which is not absorbed by biological samples and does not cause autofluorescence and light scattering background (Wang et al., 2010; Cheng et al., 2013b). The optical properties of UCNPs can be tuned by changing their lanthanide dopants (including Er^{3+}, Tm^{3+}, and Ho^{3+}) (Liu et al., 2013). Wu et al. constructed a sensitive and specific biosensor based on multicolor UCNPs as luminescent labels and aptamers as biological recognition elements for simultaneous detection of *S. aureus*, *Vibrio* parahaemolyticus and *Salmonella typhimurium* (**Figure 3C**). Under the optimal reaction conditions, the LOD of the sensor was 25 CFU/ml and the linear range was 50~10^6 CFU/ml (Wu et al., 2014). AuNPs are considered as efficient fluorescence quenchers due to their large surface-to-volume ratio and strong surface plasmon absorption in the NIR and IR (Zhu et al., 2010). Taking advantage of the high fluorescence quenching effect of AuNPs, Ouyang et al. established a more sensitive FRET-based aptasensor for the detection of *S. aureus*. Aptamer-complementary sequence-modified UCNPs were used as the donor and aptamer-modified AuNPs were used as the acceptor. The fluorescence of the aptamer-complementary sequence-modified UCNPs were restored when it was replaced by *S. aureus* and released from the aptamer-modified AuNPs. The sensitivity of this detection system was 10.7 CFU/ml, and the linear range was 47~4.7 × 10^7 CFU/ml (Ouyang et al., 2021b). UCNPs have been widely used in sensors due to their advantages of high quantum yield, narrow emission peak, good photostability, long fluorescence lifetime, large anti-Stokes shift, and resistance to photobleaching. However, there are still some limitations, for example, it is difficult for the naked eye to distinguish different target concentrations under excitation by a 980 nm laser beam.

CDs are spherical carbon particles (or graphite fragments) luminescent materials smaller than 10 nm with semiconductor quantum effect and up-conversion function. CDs have been widely used in FRET-based sensors due to their outstanding properties, such as easy synthesis, low cost, strong fluorescence emission, high water solubility, good biocompatibility, and resistance to photobleaching. Cui et al. synthesized multi-color fluorescent CDs with long fluorescence lifetime and high photostability for *S. aureus* detection. The aptamer complementary sequences modified CDs were used as energy donors, and their fluorescence signals could be quenched by the aptamer-modified Fe_3O_4 through FRET. The fluorescence of the aptamer complementary sequences modified CDs were restored when they were replaced by *S. aureus* and released from the aptamer-modified Fe_3O_4 (**Figure 3D**) (Cui et al., 2019). Their result shown that the sensor has fast detection speed (<30 min), good sensitivity (8 CFU/ml) and wide linear range (50~10^7 CFU/ml). What's more, CDs can be used as fluorescent probes for *in vitro* and *in vivo* bioimaging due to their excellent biocompatibility and low toxicity, providing a new platform for pathogen bioimaging detection (Cui et al., 2019). Yao et al. constructed an enzyme-free and label-free nano-metal surface energy transfer (NSET) aptasensor based on CDs (donor) and AuNPs (acceptor) for one-step detection of *S. aureus* (Yao et al., 2021). In this study, linker DNA was used to connect aptamer-modified CDs and aptamer-complementary sequence-modified AuNPs. Compared with the direct hybridization of CDs and AuNPs, the fluorescence of CDs was quenched by AuNPs as high as 63.5% in linker DNA based hybridization, which significantly improved the detection limit of *S. aureus* (Yao et al., 2021).

Nanomaterials are playing an increasingly important role in improving sensors for the detection of bacterial pathogens due to their unique optical properties, and are considered as one of the most promising candidates for accurate reporting of pathogens. Novel metal nanoclusters (NCs) are a new type of nanoparticles with diameters less than 2 nm, and are composed of less than 150 metal atoms. It has attracted more and more attention due to its

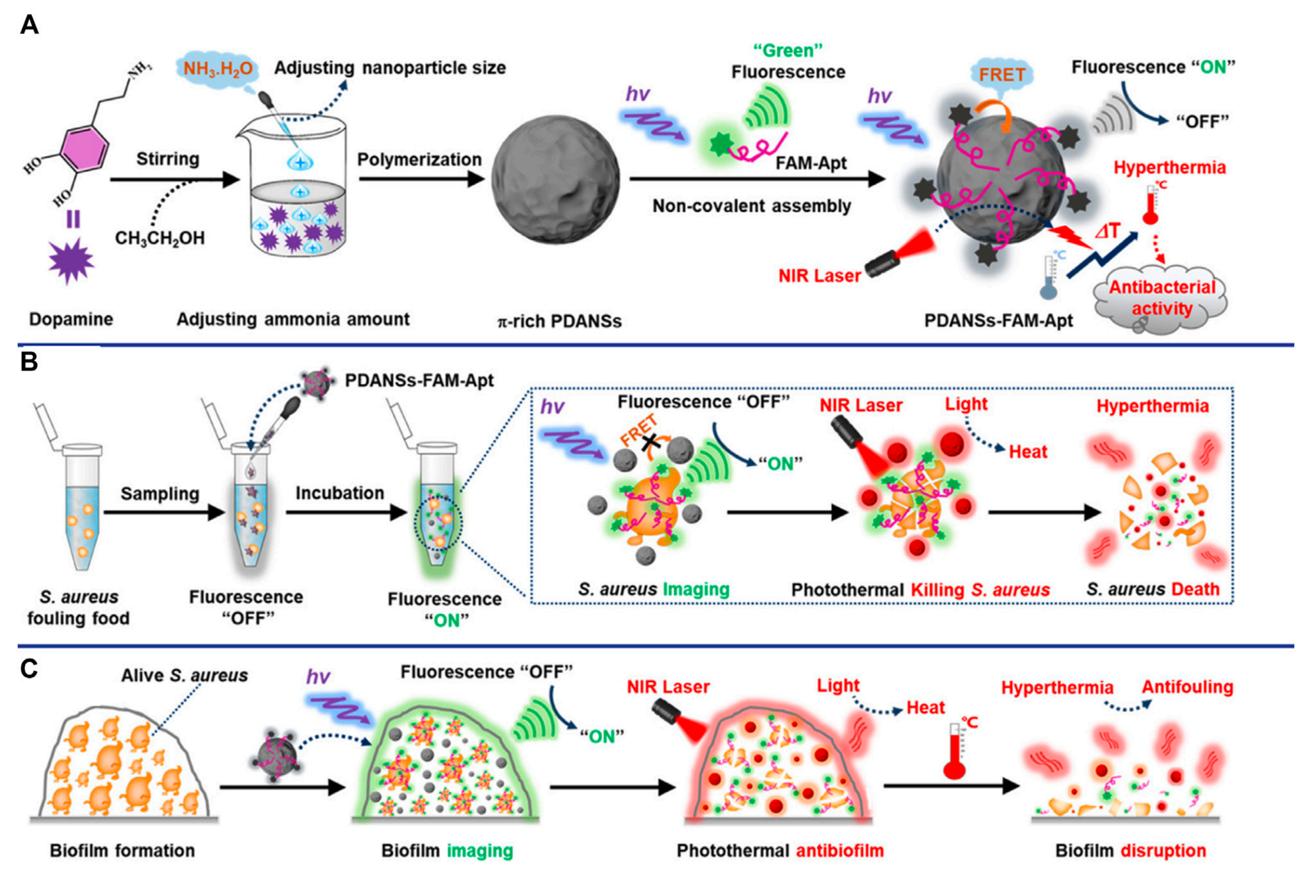

FIGURE 4 | General design of the smart nanoprobe PDANSs-FAM-Apt for accurate fluorescence detection and imaging-guided precise photothermal antibacteria. **(A)** Illustration of the assembly procedure of the nanoprobe PDANSs-FAM-Apt. **(B)** Diagram of the FRET-based assay procedure for PDANSs-FAM-Apt responsive to living *S. aureus* and imaging-guided photothermal killing of *S. aureus*. **(C)** Schematic of imaging-guided photothermal antifouling of the nanoprobe PDANSs-FAM-Apt for the destruction of *S. aureus* biofilms. Reproduced with permission (Ye et al., 2020).

outstanding advantages such as water solubility, high fluorescence and quantum yield, remarkable catalytic behavior, good biocompatibility and stability, etc (Munoz-Bustos et al., 2017; Yu et al., 2017; Pebdeni et al., 2021). Pebdeni et al. proposed a sensitive and specific *S. aureus* detection sensor based on vancomycin and aptamer dual receptor functionalized copper nanoclusters (CuNCs). CuNCs have photoluminescence properties and can induce fluorescence signal enhancement during the aggregation which was caused by *S. aureus*. Their result shown that the selectivity and sensitivity of this fluorescence sensor was enhanced by aptamer-CuNCs (Pebdeni et al., 2021). NCs not only possess unique fluorescent properties, but also have received extensive attention for their antibacterial properties (Javani et al., 2016). Yang et al. achieve a novel approach for visual detection and effective elimination of *S. aureus* by combing DNA-templated silver nanoclusters (DNA-AgNCs) and aptamers (Yang et al., 2021a). Compared with general fluorescent nanomaterials, polymer-based fluorescent nanomaterials exhibit excellent biocompatibility and biodegradability, and are easily prepared by self-polymerization (Zhang et al., 2015c). Polydopamine nanospheres (PDANS) have been used as excellent energy receptors for the construction of aptamer-based FRET biosensors because of its tunable diameters, broad absorption bands, and surface-conjugated rigid planar structures that facilitate PDANS binding interactions with aptamers *via* π-π stacking (Ye et al., 2020). Ye et al. designed a stimuli-responsive nanoprobe (PDANSs-FAM-Apt) for the detection of *S. aureus* at single-cell level, and it was able to destroy *S. aureus* and its biofilm on demand *via* NIR light-activated photothermal activity (**Figure 4**) (Ye et al., 2020). Porous materials with "molecular gates" have also been widely used in sensors for biomolecule detection. Nanoporous anodic aluminum (NAA) is widely used in aptasensors due to its stability, non-degradation in aqueous solution, multiple reuses after calcination, and support of nucleic acids (DNA, RNA, or aptamers) as molecular gates (Chen et al., 2015; Ribes and Aznar, 2019; Pla et al., 2020). Pla et al. installed the fluorescent indicator rhodamine B in the NAA well, and the entrance of the well was covered by DNA aptamer. The fluorescent indicator rhodamine B will be released when the orifice was opened by *S. aureus* binding to aptamer (Pla et al., 2020). This nanodevice can specific and sensitive (2 and 5 CFU in buffer and blood, respectively) detection of *S. aureus* in less than 1 h (Pla et al., 2020).

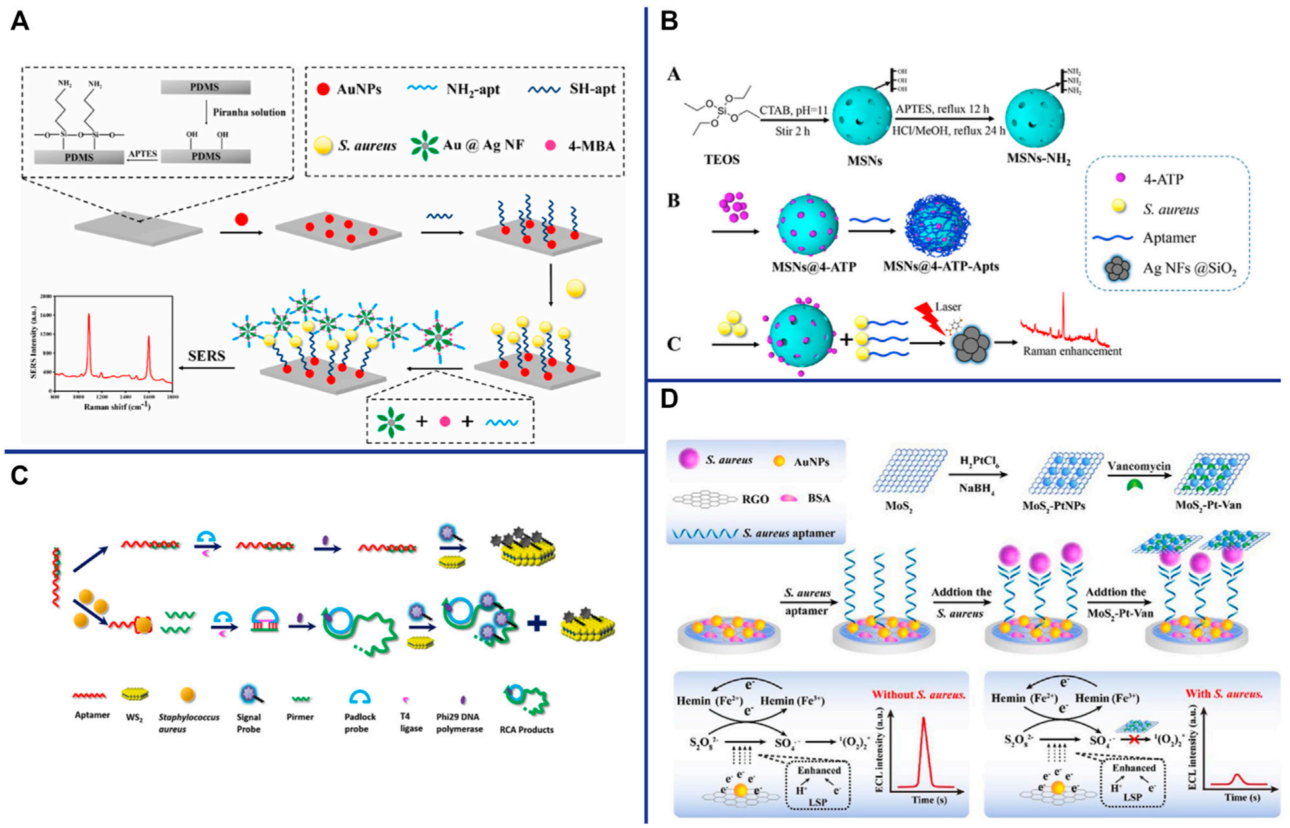

FIGURE 5 | (A) Schematic illustration of the developed SERS biosensor based on aptamer functionalized PDMS film for the detection of *S. aureus*. Reproduced with permission (Zhu et al., 2021a). **(B)** Schematic illustration of *S. aureus* detection based on the target-responsive release of 4-ATP molecules from aptamer-gated MSNs. Reproduced with permission (Zhu et al., 2021b). **(C)** Schematic illustration of the CRET biosensor for the detection of *S. aureus* based on Co^{2+}/ABEI-AuNFs and WS_2 nanosheet. Reproduced with permission (Hao et al., 2017). **(D)** Schematic illustration of the enzyme-free ECL aptasensor for *S. aureus* detection based on AuNPs/hemin as the regenerable enhancers of $S_2O_8^{2-}/O_2$ and the quenching effect of MoS_2-PtNPs on $S_2O_8^{2-}/O_2$. Reproduced with permission (Han et al., 2019).

Surface Enhanced Raman Scattering-Based Aptasensor

“Raman scattering” means that the molecules in the substance absorb part of the energy from excitation light and vibrate in different ways and degrees (for example: the wobbling and twisting of atoms, the wobbling and vibration of chemical bonds), and then scatter lower frequency light. The frequency of Raman scattering is determined by the characteristics of the substance. The Raman scattering can be enhanced by several orders of magnitude when different molecules or ions are adsorbed on the surface of metal nanomaterials (Ag, Cu, Au and other metal nanomaterials), which is related to the submicroscopic surface roughness of metal nanomaterials. SERS-based aptasensors are widely used in pathogen detection due to their ultra-sensitive, simple and rapid, excellent photostability, label-free and non-destructive fingerprint recognition (Xu et al., 2019). Zhang et al. constructed a “capture probe-target-signal probe” sandwich sensor for *S. aureus* detection by using Raman molecules and aptamer-modified AuNPs as signal probes, and aptamer-modified Fe_3O_4 magnetic gold nanoparticles (MGNPs) as capture probes (Zhang et al., 2015a). Although this method is simple, rapid, wide linearity (10^2~10^7 CFU/ml), high sensitivity (35 CFU/ml) and strong specificity, it is time-consuming (2~3 h) (Zhang et al., 2015a). Gao et al. constructed a label-free SERS-based aptasensor with only 25 min for the detection of *S. aureus* (Gao et al., 2017). Using the aptamer that specifically recognizes and binds to *S. aureus* as a template, silver nanoparticles were synthesized *in situ* to directly obtain the SERS fingerprint spectrum (Gao et al., 2017). This strategy is simple, rapid and low-cost, creating an idea for *in situ* detection of pathogens on microarrays. SERS-based sensors are generally used in liquid systems, which greatly limit their application due to the large number of detection steps and high cost. Zhu et al. construct a reliable, rapid, sensitive and specific biosensor for *S. aureus* detection by using aptamer-AuNPs-polydimethylsiloxane (PDMS) as capture substrate, mercaptobenzoic acid (4-MBA) and aptamer-modified gold-silver Core-shell nanoflowers (Au@Ag NFs) as signal probes (**Figure 5A**) (Zhu et al., 2021a). The SERS spectra will change when the sandwich structure “capture substrate-*S. aureus*-signal probe” was formed in the presence of the *S. aureus*.

The SERS aptasensor has high sensitivity (13 CFU/ml), and exhibits a good linear relationship in the range of 4.3 × 10 CFU/ml~4.3 × 10^7 CFU/ml. Au and Ag are the most popular SERS substrates, but their applications are limited due to their easy aggregation, high chemical activity, and easy chemical reaction with external substances (Jiao et al., 2021). Core-shell structures have recently been widely used as SERS substrates due to thin shells composed of inert materials can successfully prevent noble metal cores from contacting the external environment. Silica is an ideal shell material because it has no absorbance in the visible wavelength band and is somewhat hydrophilic (Li et al., 2017a). Zhu et al. proposed a SERS sensor for the detection of *S. aureus*, which based on *S. aureus* can induce release of the Raman dye 4-aminothiophenol (4-ATP) from mesoporous silica nanoparticles (MSNs) by binding to the gating aptamer (**Figure 5B**) (Zhu et al., 2021b). The SERS sensor is low-cost, fast, high sensitivity (17 CFU/ml), wide linearity (4.7 × 10 CFU/ml-4.7 × 10^8 CFU/ml), and is more reliable for detection of foodborne pathogens (Zhu et al., 2021b). The nanodimer and nanotrimer are also widely used as SERS substrates and show a greater increase in SERS signal compared to monodisperse particles (Ma et al., 2021).

Surface Plasmon Resonance-Based Aptasensor

Surface plasmon resonance (SPR) is a physical phenomenon that can cause resonance due to the light energy absorption of free electrons when incident light irradiates on the surface of plasmonic elements. The SPR was enhanced when light is irradiated onto plasmonic nanoparticles (eg, gold, silver, copper) or nanostructured and was called localized surface plasmon resonances (LSPRs) (Csáki et al., 2018). LSPR-based aptasensors have the advantages of ultrasensitive, real-time monitoring, label-free, miniaturization, and portability (Hoa et al., 2007). The LSPR frequency and strength primarily depends on the size, shape, geometry, interparticle spacing, and dielectric properties of the material. AuNPs have been widely used in LSPR-based aptasensors due to their easy preparation, high density, large dielectric constant, and good biocompatibility. Khateb et al. successfully constructed a simple, portable, and label-free LSPR-based aptasensor for *S. aureus* detection with short detection times of 120s (Khateb et al., 2020). Their results showed that the thickness of the sensing layer was critical, with a significantly greater responses for the thinner aptamer layer compared to antibody-based recognition elements (Khateb et al., 2020). They also measured the optical response experimentally through finite-difference time-domain simulations of differently sized metal nanostructures (100 and 200 nm disks) based sensor, and showed that the sensitivity of the 200 nm diameter disk structure was significantly higher compared to the 100 nm diameter disk structure, which is due to the increase in bulk refractive index sensitivity and the extent to which the local field extends from the metal surface (Khateb et al., 2020). The LSPR can also be simply tuned by changing the shape of the NPs, for example, only one LSPR has occurred in the 520 nm range (red color) for gold nanospheres (2~50 nm), while two were detected in the range of 522 nm (transverse LSPR) and 698 nm (longitudinal LSPR) for gold nanorods (Sharifi et al., 2020).

Chemiluminescence-Based Aptasensor

Chemiluminescence (CL)-based biosensors are a promising detection method because their energy is generated by chemical reactions and the sample does not require photoexcitation, thus avoiding interference from light scattering, unstable light source, and high background (Dodeigne et al., 2000). Hao et al. constructed a Chemiluminescence resonance energy transfer-based aptasensor for *S. aureus* detection using Co^{2+}-enhanced N-(aminobutyl) N-(ethylisoluminol) (ABEI)-modified AuNFs (Co^{2+}/ABEI-AuNFs) as the donor and WS_2 nanosheets as the acceptor (**Figure 5C**). The limits of detection of the electrochemiluminescence (ECL)-based aptasensor was 15 CFU/ml with the help of RCA amplification technology (Hao et al., 2017). Han et al. constructed an ECL aptasensor for *S. aureus* detection based on AuNPs/hemin as a regenerable enhancer for $S_2O_8^{2-}/O_2$ and MoS_2-PtNPs as a quencher for $S_2O_8^{2-}/O_2$ (**Figure 5D**) (Han et al., 2019). RGO was coated on the GCE to increase the specific surface area and electronic conductivity. The thiol-modified aptamers were then immobilized on the AuNPs which were electrochemically deposited on the RGO surface. In the presence of *S. aureus*, the signal was turned off because aptamer-*S. aureus* -MoS_2-PtNP-Van sandwich complex formed which act as quencher for $S_2O_8^{2-}/O_2$. Conversely, in the absence of *S. aureus*, the signal was turned on (Han et al., 2019). The results shown that the ECL-based aptasensor has high specificity and sensitivity (28 CFU/ml), and can be used for the detection of *S. aureus* in urine samples (Han et al., 2019).

APTASENSORS BASED ON ELECTROCHEMICAL TRANSDUCTION

The electrochemical aptasensors refers to that when the aptamer immobilized on the electrode surface binds to the target, it will cause a change that can be converted into a measurable electrical signal (current, impedance, potential or conductance, etc.) (Li et al., 2019b). Electrochemical sensors are one of the preferred biosensors for their high sensitivity, low cost, multi-analyte analysis, reproducibility, miniaturization and portability (Maduraiveeran et al., 2018). Electrochemical sensors can be classified into potentiometric, amperometric/voltammetric, impedimetric and conductometric sensors according to the electrical signal measured (Paniel et al., 2013).

Potentiometric-Based Aptasensor

Potentiometric biosensor is one of the oldest electrochemical techniques and is widely used due to its low cost and simple operation. Recent studies have shown that an increasing number

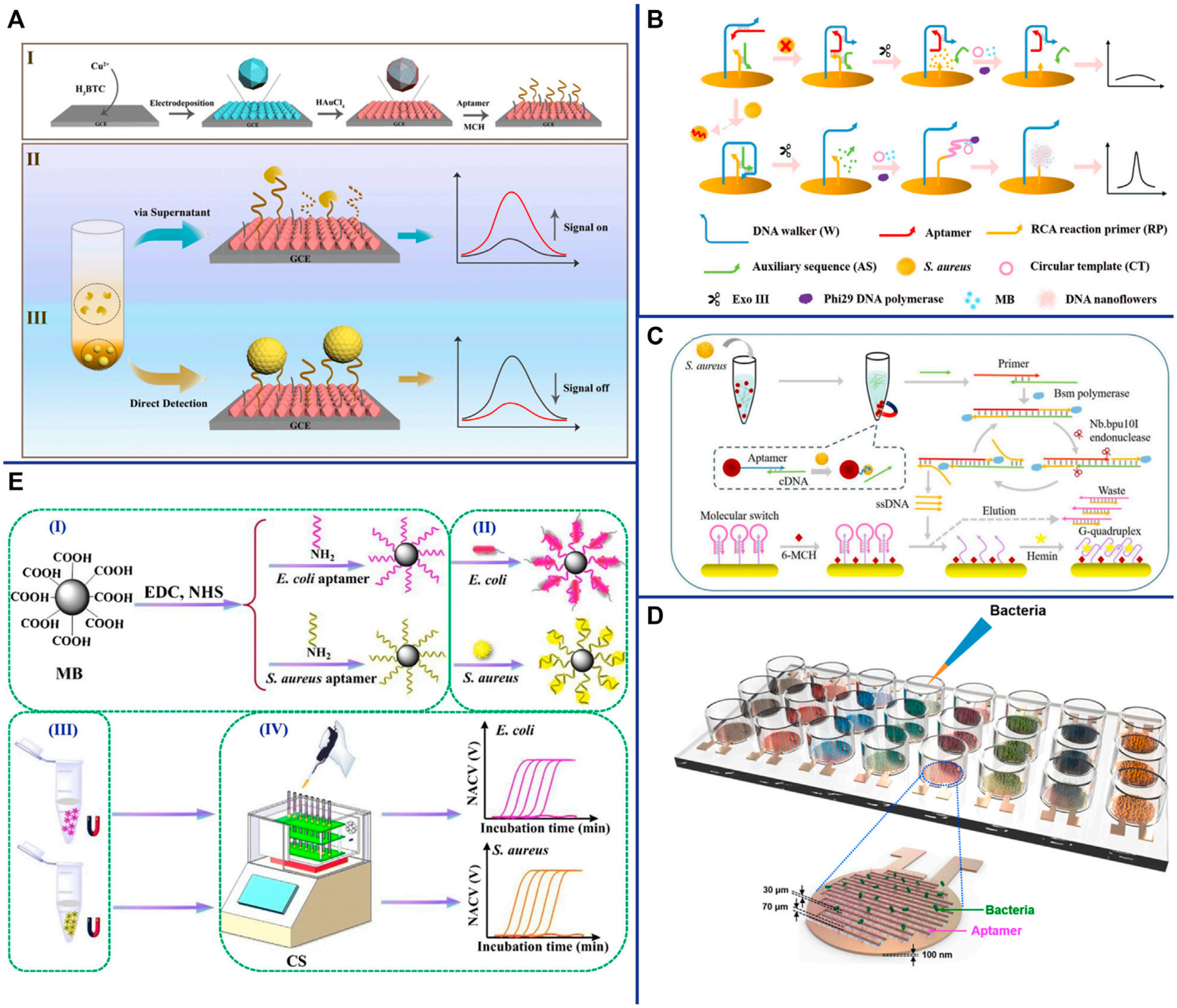

FIGURE 6 | (A) (I) Fabrication of the DNA/AuNPs/MOFs-based sensing platform; (II) Schematic diagrams of the electrochemical biosensor for the detection of *S. aureus* via supernatants; and (III) pathogen cells. Reproduced with permission (Sun et al., 2021). **(B)** Schematic representation of the biosensor for *S. aureus* detection based on a DNA walker and DNA nanoflower. Reproduced with permission (Cai et al., 2021b). **(C)** Schematic representation of the versatile signal-on electrochemical biosensor for *S. aureus* detection based on triple-helix molecular switch. Reproduced with permission (Cai et al., 2021a). **(D)** Schematic of aptamer-functionalized capacitance sensor array for real-time monitoring of bacterial growth and antibiotic susceptibility. Reproduced with permission (Jo et al., 2018). **(E)** Schematic representation of the multichannel conductometric sensor for *S. aureus* detection based on magnetic analyte separation *via* aptamer. (I)the preparation of aptamer-functionalized magnetic beads, (II) selective capture and (III) separation of bacterial cells, and (IV) determination of viable bacteria by the conductometric sensor. Reproduced with permission (Zhang et al., 2020).

of electrochemical sensors employ nanomaterials as efficient transducers and amplifiers. Carbon nanotubes have been widely used as transducers in electrochemical sensors due to their strong ability to promote electron transfer between electroactive species and electrodes. Zelada-Guillén et al. construct a highly sensitive potentiometric sensor for real-time detection of *S. aureus* without labeling based on aptamers as biorecognition elements and single-walled carbon nanotubes (SWCNTs) as potential transducers (Zelada-Guillen et al., 2012). The results shown that the sensor could detect S. aureus in skin in real time with good stability and specificity (Zelada-Guillen et al., 2012). Graphene oxide (GO) and reduced graphene oxide (RGO) are the preferred material for fabricating highly sensitive sensing platforms due to their unique thermal, mechanical, and electrical properties. Hernández et al. constructed a potentiometric aptasensor based on GO and RGO for the detection of S. aureus. The potentiometric aptasensor has strong selectivity and high sensitivity and can detect single live *S. aureus*. However, when the potentiometric aptasensor was applied to real samples, it is necessary to filter out the electroactive substances in the sample that interfere with the detection (Hernandez et al., 2014).

Amperometric/Voltammetric-Based Aptasensor

Amperometric/voltammetric is the most common and successful electrochemical techniques for *S. aureus* detection. Abbaspour et al. constructed a voltammetric-based aptasensor for *S. aureus* detection, which based on aptamer-modified magnetic beads as capture probes and aptamer-modified silver nanoparticles (Apt-AgNPs) as signal probes. Apt/*S. aureus*/apt-AgNP sandwich complexes form in the presence of *S. aureus*, resulting in current changes (Abbaspour et al., 2015). This approach with good sensitivity (1.0 CFU/ml) and wild linear range ($10\sim10^6$ CFU/ml) due to the combination of magnetic bead separation and signal amplification of AgNPs (Abbaspour et al., 2015). Besides metallic nanomaterials, other nanomaterials as efficient amplifiers have also become an integral part of electrochemical biosensor. For example, metal-organic framework (MOF) is a unique inorganic-organic hybrid nanomaterial, which has been widely used in many fields due to its flexibility, uniform structure, good chemical stability, and good biocompatibility (Han et al., 2020). Sun et al. electrodeposited Cu metal-organic framework (Cu-MOF) thin films on electrodes and *in situ* reduced AuNPs on their surfaces to enhance their electrical conductivity and form complexes (DNA/AuNPs/MOFs) with aptamers *via* Au-S bonds to construct electrochemical biosensors for dual detection of *S. aureus* (**Figure 6A**) (Sun et al., 2021). This aptasensor not only has high specificity and high sensitivity (1.9 CFU/ml), but also is easy to operate and requires no additional signal components (Sun et al., 2021). With the development of DNA nanotechnology, various nanomaterials constructed from DNA have also been widely used in electrochemical sensors. Cai et al. constructed a dual-signal amplifying electrochemical aptasensor based on DNA walker and DNA nanoflowers for high-sensitivity detection of *S. aureus* (Cai et al., 2021b). Two sets of double-stranded DNA were modified on the surface of the Au electrode. When the aptamer was bound to *S. aureus*, the DNA walker bound to the aptamer was released. With the help of exonuclease III (Exo III), the DNA walker moves along the electrode surface and continuously hydrolyzes the anchored short double-stranded DNA. The introduction of circular DNA and phi29 DNA polymerase initiates RCA and in turn forms nanoflowers, which provide binding sites for electroactive methylene blue (MB), resulting in a strong electrochemical signal (**Figure 6B**) (Cai et al., 2021b). The results shown that the electrochemical aptasensor has high sensitivity, high specificity and good anti-interference ability, which can distinguish *S. aureus* in mixed samples from other non-target bacteria (Cai et al., 2021b). In addition to nanomaterials, nucleic acid-based RCA, SDR, HCR, and HD-CHR amplification systems are also widely used as amplifiers in electrochemical sensors. Cai et al. constructed a multifunctional electrochemical sensor based on SDA and triple helix molecular switch for *S. aureus* detection (Cai et al., 2021a). In the presence of *S. aureus*, the aptamer binds to *S. aureus* and releases the complementary sequence (cDNA) into the solution, which initiates the SDA reaction under the action of primers and enzymes, and resulting in a large number of ssDNA probes. Subsequently, the interaction of the ssDNA probe with the triple helix molecular switch on the electrode leads to the release of the G-quadruplex-rich capture sequence, which reacts with hemin to form an electroactive G-quadruplex/heme complex and then turns on the electrochemical signal (**Figure 6C**) (Cai et al., 2021a). The results shown that this aptasensor has high sensitivity (8 CFU/ml), high specificity, and can detect *S. aureus* in lake water, tap water and honey samples (Cai et al., 2021a).

Impedimetric-Based Aptasensor

In recent years, impedimetric-based aptasensor has attracted interest for the detection of *S. aureus* due to its high sensitivity, no matrix interference, simple measurement, no labeling, and automation (Paniel et al., 2013). Jia et al. constructed an sensitive, specific and label-free impedimetric-based aptasensor for rapid and quantitative detection of *S. aureus* (Jia et al., 2014). This system adopts a novel nanocomposite material (rGO-ssDNA-AuNPs) that enhances electron transfer and electrochemical signals as an amplifier to improve the detection sensitivity (10 CFU/ml) (Jia et al., 2014). An effective strategy to improve the performance of biosensors is to increase the reaction surface area and thus capture the target more effectively. In recent years, cellulose nanofibers (CNFs) have been widely used in biosensing due to their large surface area, high aspect ratio, extensive chemical modification ability, good biocompatibility and adhesion (Golmohammadi et al., 2017). Ranjbar et al. using carbon nanoparticles (CNPs) and AuNPs to overcome the poor electrical conductivity of CNFs to construct nanocomposites (AuNPs/CNPs/CNFs) with large surface area, excellent electrical conductivity and good biocompatibility for constructing impedimetric aptasensor (Ranjbar and Shahrokhian, 2018). Studies have shown that the aptasensor has high sensitivity (1 CFU/ml), wide linear range ($1.2 \times 10\sim1.2 \times 10^8$ CFU/ml), and can be applied to the accurate detection of *S. aureus* in human serum samples (Ranjbar and Shahrokhian, 2018). Electrochemical aptasensor not only used for *S. aureus* detection, but also be used for rapid antibiotic susceptibility testing (AST) of *S. aureus*. The aptamers were immobilized between the two finger electrodes of an interdigitated gold electrode (IDE). When *S. aureus* was captured by the aptamer, it can act as a dielectric particle connecting electrode, thereby increasing the capacitance (**Figure 6D**) (Jo et al., 2018). The result shown that this aptamer-functionalized capacitive sensor array can not only rapidly and specifically recognize *S. aureus* (1 h), but also monitor bacterial growth in real time with high sensitivity (10 CFU/ml), which can be used for AST of *S. aureus* (Jo et al., 2018).

Conductometric-Based Aptasensor

Conductometric is a measurement of monitoring the conductivity of solution using a low-amplitude alternating current potential, which relies on the change in conductivity that occurs in the sample through the production or consumption of charged species. The working electrode must be in contact with

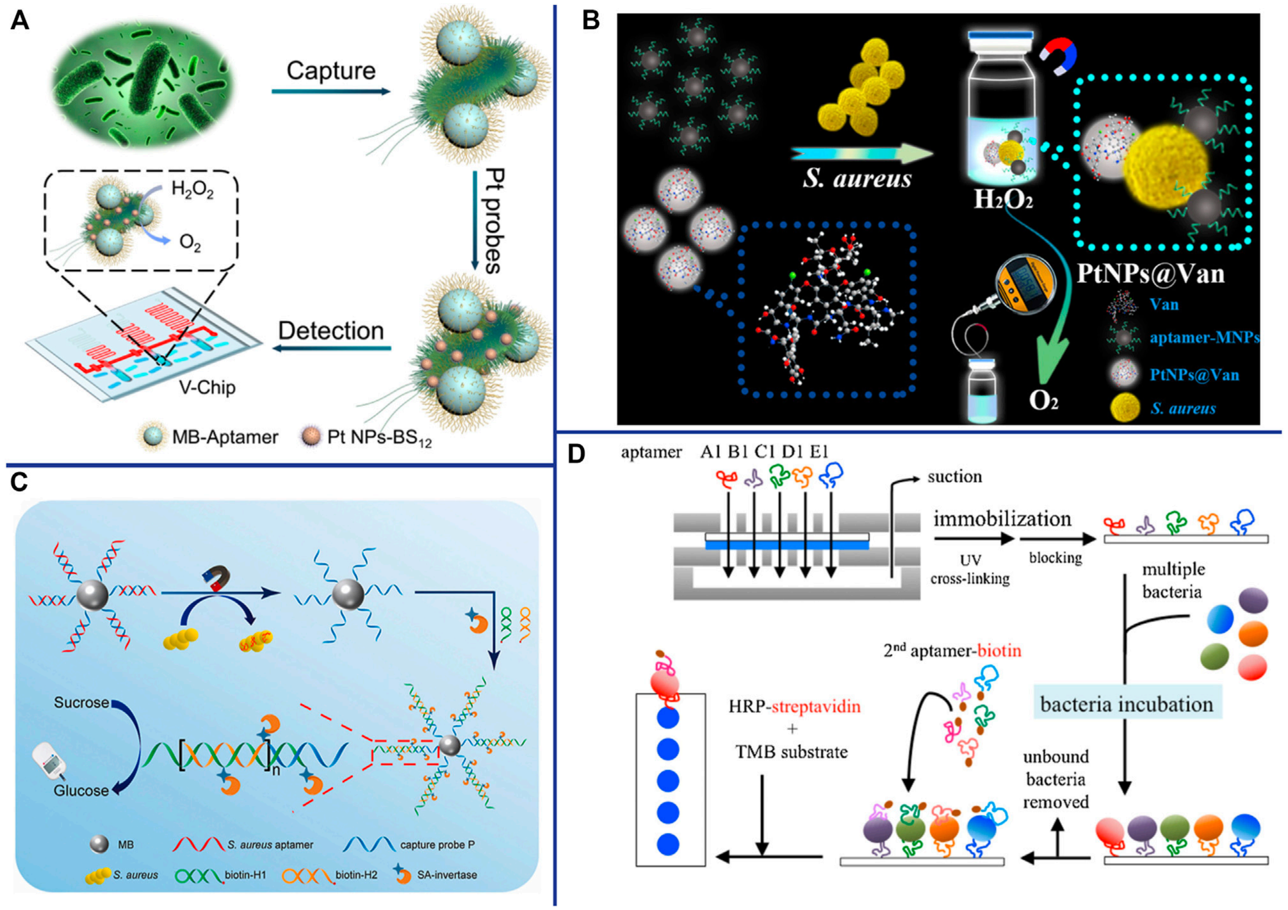

FIGURE 7 | (A) Working principle for detection of bacteria using BV-Chip. Reproduced with permission (Huang et al., 2019). **(B)** Schematic illustration of gas pressure-based POC testing protocol for highly sensitive and specific detection of *S. aureus*. Reproduced with permission (Li J. et al., 2019a). **(C)** Schematic illustration of the principle for portable detection of *S. aureus* using PGM based on HCR strategy. Reproduced with permission (Yang et al., 2021b). **(D)** The experimental procedure for multi-bacterial detection *via* bacteria-specific aptamers immobilized on a nitrocellulose (NC) membrane. 2nd (secondary) aptamer-biotin conjugated with biotin. Reproduced with permission (Wang et al., 2019a).

the solution in traditional electrochemical sensors, which inevitably causes electrode degradation and non-specific capture. To solve these problems, Zhang et al. developed a conductometric for real-time quantifying the number of live bacteria by using aptamer-modified magnetic beads to separate *S. aureus* and then a capacitively-coupled non-contact conductivity detector to measure and record conductivity changes. The bacteria captured by aptamer-modified magnetic beads can also be used for AST (**Figure 6E**) (Zhang et al., 2020).

APTASENSOR FOR POCT

Point-of-care testing (POCT) refers to a miniature mobile detection system that is close to the test sample in a non-laboratory environment and reports the results quickly. Although POCT does not require tedious operating steps, professional operators, and expensive and sophisticated instruments, the development and popularization of highly sensitive and specific POCT technology is still a major challenge in the field of science and engineering. A major strategy of POCT is to infiltrate liquid reagents into filter paper and various water-absorbing materials, and fix them on rigid substrates after drying. Paper-based lateral flow strips (LFS), also known as test strips, have been widely used for POCT and are the most promising method for POCT in various fields. In addition to being sensitive and specific, LFS is simple to operate and does not require complicated and expensive instruments, and the detection results can be observed with the naked eye. Lu et al. constructed an aptamer- and AuNPs-based LFS for rapid detection of *S. aureus*, with a detection time of only 10 min and no cross-reaction with other common bacteria (Lu et al., 2020a). Raji et al. developed a novel aptamer-based swab sensor for qualitative and quantitative detection of MRSA on environmental surfaces (Raji et al., 2021). In the presence of MRSA on environmental surfaces, MRSA can be combined with aptamers immobilized on cotton swabs and aptamers modified by blue nanobeads to form an "aptamer-MRSA-aptamer" sandwich structure (Raji et al., 2021). The swab sensor is fast (5 min), sensitive (theoretical value 2 CFU/ml), specific, and can be read directly by the naked eye without the need for laboratory equipment (Raji et al., 2021). This novel aptasensor holds great promise because of its good detection performance, ease of use and relatively inexpensive to produce.

Another major strategy of POCT is to miniaturize the analytical instrument and simplify the operation method, making it a portable and palm-like device. Huang et al. have developed a microfluidic device based on volumetric bar-chart chip (V-Chip) technology for rapid and visually intuitive quantification of pathogenic bacteria in urine (Huang et al., 2019). Bacteria can combine with aptamer-modified magnetic beads and 2-(dodecyldimethylamino) acetate (BS-12) modified platinum nanoparticles (PtNPs-BS12) to form an "aptamer-bacteria-PtNPs-BS12" sandwich complex. Pt NPs with extremely high catalase-like activity can catalyze the decomposition of H_2O_2 to generate O_2, thereby pushing the pink ink in the V-Chip into the S-shaped readout channel (**Figure 7A**) (Huang et al., 2019). Due to the fast detection speed (1.5 h) and high sensitivity (as low as 1 CFU/ml) of the device, and the detection results of clinical urine samples are consistent with the plate counting, the V-Chip can significantly improve the early diagnosis rate of bacterial infection (Huang et al., 2019). A pressure measuring instrument is an ideal POCT that is simple, portable and capable of quantitative detection. Li et al. constructed a pressure-based POCT for the detection of *S. aureus* using vancomycin-modified functionalized platinum nanoparticles (PtNPs@Van) and aptamer-modified magnetic $CuFe_2O_4$ nanoprobes. The Pt NPs catalyzed the decomposition of H_2O_2 to O_2 in a sealed device, resulting in a significant increase in pressure that can be detected with a hand-held digital pressure gauge (**Figure 7B**) (Li et al., 2019a). Personal Glucose Meters (PGMs) also has been widely used as a readout means for highly sensitive non-glucose target identification and quantification due to its advantages of portability, speed, low cost, easy operation and reliable results. Yang et al. designed a novel aptasensor for *S. aureus* detection based on HCR and PGMs (**Figure 7C**). This aptasensor is specific, sensitive (2 CFU/ml) and accurate, providing a new perspective for the development of sensitive and portable pathogen detection solution in the future (Yang et al., 2021b). Wang et al. developed an aptamer-based micro-microfluidic chip for multi-pathogen detection, replacing the traditional single-pathogen detection (**Figure 7D**). The results shown that this new microfluidic chip has faster detection time (35 min) and smaller size (7.0 cm × 5.0 cm × 1.2 cm), higher specificity, and simultaneous detected multiple pathogens compared with traditional chips (Wang et al., 2019a). Therefore, it promises to be a powerful POCT for multibacterial diagnosis.

CONCLUSION AND PERSPECTIVES

This review presented an overview on the latest progress of aptasensors based on optical (colorimetric, fluorescence, SPR and SERS) and electrochemical (potentiometric, voltammetric, impedimetric and conductometric) for *S. aureus* detection. Overall, colorimetric-based aptasensors are simplicity, fast, low-cost, and the results can be quickly judged by the naked eye or simple instruments. However, its low sensitivity still needs to be improved when applying to practical detection. Fluorescence-based aptasensors have become one of the most commonly used sensors for low-concentration analyte detection due to their high sensitivity, but their results are susceptible to interference by autofluorescence or background fluorescence, and the fluorescent molecules used are unstable and prone to photobleaching. Novel optical transduction mechanisms such as SPR and SERS have also been used for *S. aureus* detection due to their advantages of ultra-sensitivity, real-time monitoring, and label-freeness, but their widespread application is limited by cumbersome sample preparation and the expensive equipment required. Compared with optical based aptasensors, electrochemical based aptasensors demonstrate the potential for the fabrication of POCT due to their fastness, simplicity, sensitivity, miniaturization and portability.

Although the development of aptasensors is the most active research topic in recent years, there are still some significant challenges in practical applications: First, since most of the existing aptamers are screened by time-consuming and inefficient traditional SELEX, it is necessary to introduce new technologies and new methods (such as Cell-SELEX, Genomic SELEX, IP-SELEX, Capture-SELEX, CE-SELX, M-SELEX, AFM-SELEX, AEGIS-SELEX, Animal-SELEX) to improve the screening efficiency and generate higher affinity and specificity aptamers. Second, aptamer density, aptamer orientation, surface charge and steric hindrance during the progress of aptamer immobilization should also be systematically studied to further improve aptamer properties and biostability. Although nanomaterials play an important role in increasing the immobilization density and orientation of aptamers, high-density immobilization will limit the formation of normal configurations of aptamers. Third, although most studies have shown that the aptasensors have good specificity and could distinguish other co-existing foodborne pathogens in artificially contaminated samples (recoveries ranged from 85.0 to 110.0%), the interference effects of various metal ions, anions and antioxidants that may be present in the real sample also require further studies to ensure the existing aptasensors compatibility in complex biological and clinical samples. Fourth, the stability and reproducibility of nanomaterials that play an increasingly important role in aptasensors still need to be improved. Fifth, how to achieve simultaneous detection of multiple pathogens is still a major challenge in a short period of time.

Overall, although there are still some challenges to be solved, aptasensors have great potential in the field of *S. aureus* detection. Rapid, sensitive, specific, high-throughput, simple operation, small sample size, low cost, reagent-safe, portable, and wearable aptamer based novel microfluidic chip will become the focus of future biosensor research, and will have a significant impact on human health and well-being.

AUTHOR CONTRIBUTIONS

WC Designed the manuscript, conducted literature search, wrote the manuscript, revised and proofread manuscript. QTL performed literature search and helped write the manuscript. YKZ performed literature search, helped write the manuscript. ZCL provide the principal idea, designed the manuscript, helped revised and proofread manuscript.

FUNDING

This work was supported financially by the National Natural Science Foundation of China (Grant no. 61771493) and the Natural Science Foundation of Hunan province (Grant No. 2018JJ2532).

REFERENCES

Abbaspour, A., Norouz-Sarvestani, F., Noori, A., and Soltani, N. (2015). Aptamer-conjugated Silver Nanoparticles for Electrochemical Dual-Aptamer-Based Sandwich Detection of staphylococcus Aureus. *Biosens. Bioelectron.* 68, 149–155. doi:10.1016/j.bios.2014.12.040

Alizadeh, N., Memar, M. Y., Moaddab, S. R., and Kafil, H. S. (2017). Aptamer-assisted Novel Technologies for Detecting Bacterial Pathogens. *Biomed. Pharmacother.* 93, 737–745. doi:10.1016/j.biopha.2017.07.011

Amraee, M., Oloomi, M., Yavari, A., and Bouzari, S. (2017). DNA Aptamer Identification and Characterization for *E. coli* O157 Detection Using Cell Based SELEX Method. *Anal. Biochem.* 536, 36–44. doi:10.1016/j.ab.2017.08.005

Banerjee, J. (2010). Antibodies Are Challenged. *Indian J. Med. Sci.* 64, 144–147.

Berezovski, M., Musheev, M., Drabovich, A., and Krylov, S. N. (2006a). Non-SELEX Selection of Aptamers. *J. Am. Chem. Soc.* 128, 1410–1411. doi:10.1021/ja056943j

Berezovski, M. V., Musheev, M. U., Drabovich, A. P., Jitkova, J. V., and Krylov, S. N. (2006b). Non-SELEX: Selection of Aptamers without Intermediate Amplification of Candidate Oligonucleotides. *Nat. Protoc.* 1, 1359–1369. doi:10.1038/nprot.2006.200

Bock, L. C., Griffin, L. C., Latham, J. A., Vermaas, E. H., and Toole, J. J. (1992). Selection of Single-Stranded DNA Molecules that Bind and Inhibit Human Thrombin. *Nature* 355, 564–566. doi:10.1038/355564a0

Boiziau, C., Dausse, E., Yurchenko, L., and Toulmé, J.-J. (1999). DNA Aptamers Selected against the HIV-1trans-Activation-Responsive RNA Element Form RNA-DNA Kissing Complexes. *J. Biol. Chem.* 274, 12730–12737. doi:10.1074/jbc.274.18.12730

Borsa, B. A., Tuna, B. G., Hernandez, F. J., Hernandez, L. I., Bayramoglu, G., Arica, M. Y., et al. (2016). Staphylococcus Aureus Detection in Blood Samples by Silica Nanoparticle-Oligonucleotides Conjugates. *Biosens. Bioelectron.* 86, 27–32.

Cai, R., Yin, F., Chen, H., Tian, Y., and Zhou, N. (2020). A Fluorescent Aptasensor for *Staphylococcus aureus* Based on Strand Displacement Amplification and Self-Assembled DNA Hexagonal Structure. *Microchim. Acta* 187, 304. doi:10.1007/s00604-020-04293-9

Cai, R., Yin, F., Zhang, Z., Tian, Y., and Zhou, N. (2019). Functional Chimera Aptamer and Molecular Beacon Based Fluorescent Detection of *Staphylococcus aureus* with Strand Displacement-Target Recycling Amplification. *Anal. Chim. Acta* 1075, 128–136. doi:10.1016/j.aca.2019.05.014

Cai, R., Zhang, S., Chen, L., Li, M., Zhang, Y., and Zhou, N. (2021b). Self-Assembled DNA Nanoflowers Triggered by a DNA Walker for Highly Sensitive Electrochemical Detection of *Staphylococcus aureus*. *ACS Appl. Mat. Interfaces* 13, 4905–4914. doi:10.1021/acsami.0c22062

Cai, R., Zhang, Z., Chen, H., Tian, Y., and Zhou, N. (2021a). A Versatile Signal-On Electrochemical Biosensor for *Staphylococcus aureus* Based on Triple-Helix Molecular Switch. *Sensors And Actuators B-Chemical* 326, 128842. doi:10.1016/j.snb.2020.128842

Cao, X., Li, S., Chen, L., Ding, H., Xu, H., Huang, Y., et al. (2009). Combining Use of a Panel of ssDNA Aptamers in the Detection of *Staphylococcus aureus*. *Nucleic Acids Res.* 37, 4621–4628. doi:10.1093/nar/gkp489

Catala, C., Mir-Simon, B., Feng, X., Cardozo, C., Pazos-Perez, N., Pazos, E., et al. (2016). Online SERS Quantification of Staphylococcus aureus and the Application to Diagnostics in Human Fluids. *Adv. Mater. Technol.* 1.

Cesewski, E., and Johnson, B. N. (2020). Electrochemical Biosensors for Pathogen Detection. *Biosens. Bioelectron.* 159, 112214. doi:10.1016/j.bios.2020.112214

Chang, T., Wang, L., Zhao, K., Ge, Y., He, M., and Li, G. (2016). Duplex Identification of *Staphylococcus aureus* by Aptamer and Gold Nanoparticles. *J. Nanosci. Nanotechnol.* 16, 5513–5519. doi:10.1166/jnn.2016.11656

Chang, Y. C., Yang, C. Y., Sun, R. L., Cheng, Y. F., Kao, W. C., and Yang, P. C. (2013). Rapid Single Cell Detection of *Staphylococcus aureus* by Aptamer-Conjugated Gold Nanoparticles. *Sci. Rep.* 3, 1863. doi:10.1038/srep01863

Chen, C.-J., and Huang, Y.-C. (2014). New Epidemiology of *Staphylococcus aureus* Infection in Asia. *Clin. Microbiol. Infect.* 20, 605–623. doi:10.1111/1469-0691.12705

Chen, Y., Santos, A., Wang, Y., Kumeria, T., Li, J., Wang, C., et al. (2015). Biomimetic Nanoporous Anodic Alumina Distributed Bragg Reflectors in the Form of Films and Microsized Particles for Sensing Applications. *ACS Appl. Mat. Interfaces* 7, 19816–19824. doi:10.1021/acsami.5b05904

Cheng, D., Yu, M., Fu, F., Han, W., Li, G., Xie, J., et al. (2016). Dual Recognition Strategy for Specific and Sensitive Detection of Bacteria Using Aptamer-Coated Magnetic Beads and Antibiotic-Capped Gold Nanoclusters. *Anal. Chem.* 88, 820–825.

Cheng, C., Chen, Y. H., Lennox, K. A., Behlke, M. A., and Davidson, B. L. (2013a). *In Vivo* SELEX for Identification of Brain-Penetrating Aptamers. *Mol. Ther. - Nucleic Acids* 2, e67. doi:10.1038/mtna.2012.59

Cheng, L., Wang, C., and Liu, Z. (2013b). Upconversion Nanoparticles and Their Composite Nanostructures for Biomedical Imaging and Cancer Therapy. *Nanoscale* 5, 23–37. doi:10.1039/c2nr32311g

Cheng, X., Huang, L., Yang, X., Elzatahry, A. A., Alghamdi, A., and Deng, Y. (2019). Rational Design of a Stable Peroxidase Mimic for Colorimetric Detection of H2O2 and Glucose: A Synergistic CeO2/Zeolite Y Nanocomposite. *J. Colloid Interface Sci.* 535, 425–435. doi:10.1016/j.jcis.2018.09.101

Csáki, A., Stranik, O., and Fritzsche, W. (2018). Localized Surface Plasmon Resonance Based Biosensing. *Expert Rev. Mol. Diagnostics* 18, 279–296. doi:10.1080/14737159.2018.1440208

Cui, F., Sun, J., de Dieu Habimana, J., Yang, X., Ji, J., Zhang, Y., et al. (2019). Ultrasensitive Fluorometric Angling Determination of *Staphylococcus aureus In Vitro* and Fluorescence Imaging *In Vivo* Using Carbon Dots with Full-Color Emission. *Anal. Chem.* 91, 14681–14690. doi:10.1021/acs.analchem.9b03916

Dodeigne, C., Thunus, L., and Lejeune, R. (2000). Chemiluminescence as Diagnostic Tool. A Review. *Talanta* 51, 415–439. doi:10.1016/s0039-9140(99)00294-5

Duan, N., Gong, W., Wang, Z., and Wu, S. (2016). An Aptasensor Based on Fluorescence Resonance Energy Transfer for Multiplexed Pathogenic Bacteria Determination. *Anal. Methods* 8, 1390–1395.

Duan, N., Wu, S., Zhu, C., Ma, X., Wang, Z., Yu, Y., et al. (2012). Dual-Color Upconversion Fluorescence and Aptamer-Functionalized Magnetic Nanoparticles-Based Bioassay for the Simultaneous Detection of Salmonella Typhimurium and Staphylococcus Aureus. *Analytica. Chimica. Acta.* 723, 1–6.

Dwivedi, H. P., Smiley, R. D., and Jaykus, L.-A. (2013). Selection of DNA Aptamers for Capture and Detection of Salmonella Typhimurium Using a Whole-Cell SELEX Approach in Conjunction with Cell Sorting. *Appl. Microbiol. Biotechnol.* 97, 3677–3686. doi:10.1007/s00253-013-4766-4

Ellington, A. D., and Szostak, J. W. (1990). *In Vitro* selection of RNA Molecules that Bind Specific Ligands. *Nature* 346, 818–822. doi:10.1038/346818a0

Fluit, A., Verhoef, J., Schmitz, F., and Sentry Participants, T. E. (2001). Frequency of Isolation and Antimicrobial Resistance of Gram-Negative and Gram-Positive

Bacteria from Patients in Intensive Care Units of 25 European University Hospitals Participating in the European Arm of the SENTRY Antimicrobial Surveillance Program 1997-1998. *Eur. J. Clin. Microbiol. Infect. Dis.* 20, 617–625. doi:10.1007/s100960100564

Fu, F., Zhang, Y., Li, L., Wang, H., Li, Q., Tao, X., et al. (2020). Intracellular Pathogen Detection Based on Dual-Recognition Units Constructed Fluorescence Resonance Energy Transfer Nanoprobe. *Anal. Chem.* 92, 11462–11468. doi:10.1021/acs.analchem.0c02695

Furst, A. L., and Francis, M. B. (2019). Impedance-Based Detection of Bacteria. *Chem. Rev.* 119, 700–726. doi:10.1021/acs.chemrev.8b00381

Gao, W., Li, B., Yao, R., Li, Z., Wang, X., Dong, X., et al. (2017). Intuitive Label-free SERS Detection of Bacteria Using Aptamer-Based *In Situ* Silver Nanoparticles Synthesis. *Anal. Chem.* 89, 9836–9842. doi:10.1021/acs.analchem.7b01813

Ghosh, S. K., and Pal, T. (2007). Interparticle Coupling Effect on the Surface Plasmon Resonance of Gold Nanoparticles: from Theory to Applications. *Chem. Rev.* 107, 4797–4862. doi:10.1021/cr0680282

Gill, A. A. S., Singh, S., Thapliyal, N., and Karpoormath, R. (2019). Nanomaterial-based Optical and Electrochemical Techniques for Detection of Methicillin-Resistant *Staphylococcus aureus*: a Review. *Microchim. Acta* 186, 114. doi:10.1007/s00604-018-3186-7

Golmohammadi, H., Morales-Narváez, E., Naghdi, T., and Merkoçi, A. (2017). Nanocellulose in Sensing and Biosensing. *Chem. Mat.* 29, 5426–5446. doi:10.1021/acs.chemmater.7b01170

Hamula, C. L. A., Zhang, H., Li, F., Wang, Z., Chris Le, X., and Li, X.-F. (2011). Selection and Analytical Applications of Aptamers Binding Microbial Pathogens. *TrAC Trends Anal. Chem.* 30, 1587–1597. doi:10.1016/j.trac.2011.08.006

Han, D., Yan, Y., Wang, J., Zhao, M., Duan, X., Kong, L., et al. (2019). An Enzyme-free Electrochemiluminesce Aptasensor for the Rapid Detection of *Staphylococcus aureus* by the Quenching Effect of MoS2-PtNPs-Vancomycin to S2O82−/O2 System. *Sensors Actuators B Chem.* 288, 586–593. doi:10.1016/j.snb.2019.03.050

Han, X., Hong, Y., Ma, Y., Lu, W., Li, J., Lin, L., et al. (2020). Adsorption of Nitrogen Dioxide in a Redox-Active Vanadium Metal-Organic Framework Material. *J. Am. Chem. Soc.* 142, 15235–15239. doi:10.1021/jacs.0c06414

Hao, L., Gu, H., Duan, N., Wu, S., Ma, X., Xia, Y., et al. (2017). An Enhanced Chemiluminescence Resonance Energy Transfer Aptasensor Based on Rolling Circle Amplification and WS2 Nanosheet for *Staphylococcus aureus* Detection. *Anal. Chim. Acta* 959, 83–90. doi:10.1016/j.aca.2016.12.045

He, J., Wang, J., Zhang, N., Shen, L., Wang, L., Xiao, X., et al. (2019). *In Vitro* selection of DNA Aptamers Recognizing Drug-Resistant Ovarian Cancer by Cell-SELEX. *Talanta* 194, 437–445. doi:10.1016/j.talanta.2018.10.028

He, X., Li, Y., He, D., Wang, K., Shangguan, J., and Shi, H (2014). Aptamer-Fluorescent Silica Nanoparticles Bioconjugates Based Dual-Color Flow Cytometry for Specific Detection of Staphylococcus aureus. *J. Biomed. Nanotechnol.* 10, 1359–1368.

Hernández, R., Vallés, C., Benito, A. M., Maser, W. K., Xavier Rius, F., and Riu, J. (2014). Graphene-based Potentiometric Biosensor for the Immediate Detection of Living Bacteria. *Biosens. Bioelectron.* 54, 553–557. doi:10.1016/j.bios.2013.11.053

Hoa, X. D., Kirk, A. G., and Tabrizian, M. (2007). Towards Integrated and Sensitive Surface Plasmon Resonance Biosensors: a Review of Recent Progress. *Biosens. Bioelectron.* 23, 151–160. doi:10.1016/j.bios.2007.07.001

Huang, L., Sun, D-W., Wu, Z., Pu, H., and Wei, Q. (2021). Reproducible, Shelf-Stable, and Bioaffinity SERS Nanotags Inspired by Multivariate Polyphenolic Chemistry for Bacterial Identification. *Analytica. Chimica. Acta.* 1167.

Huang, T., Yang, J., Zhou, W., Liu, X., Pan, Y., and Song, Y. (2019). Rapid Identification of Urinary Tract Infections Based on Ultrasensitive Bacteria Detection Using Volumetric Bar-Chart Chip. *Sensors Actuators B-Chemical* 298. doi:10.1016/j.snb.2019.126885

Hulme, J. (2017). Recent Advances in the Detection of Methicillin Resistant *Staphylococcus aureus* (MRSA). *BioChip J.* 11, 89–100. doi:10.1007/s13206-016-1201-9

Javani, S., Lorca, R., Latorre, A., Flors, C., Cortajarena, A. L., and Somoza, Á. (2016). Antibacterial Activity of DNA-Stabilized Silver Nanoclusters Tuned by Oligonucleotide Sequence. *ACS Appl. Mat. Interfaces* 8, 10147–10154. doi:10.1021/acsami.6b00670

Jevons, M. P. (1961). "Celbenin" - Resistant Staphylococci. *Bmj* 1, 124–125. doi:10.1136/bmj.1.5219.124-a

Jia, F., Duan, N., Wu, S., Ma, X., Xia, Y., Wang, Z., et al. (2014). Impedimetric Aptasensor for *Staphylococcus aureus* Based on Nanocomposite Prepared from Reduced Graphene Oxide and Gold Nanoparticles. *Microchim. Acta* 181, 967–974. doi:10.1007/s00604-014-1195-8

Jiao, T., Mehedi Hassan, M., Zhu, J., Ali, S., Ahmad, W., Wang, J., et al. (2021). Quantification of Deltamethrin Residues in Wheat by Ag@ZnO NFs-Based Surface-Enhanced Raman Spectroscopy Coupling Chemometric Models. *Food Chem.* 337, 127652. doi:10.1016/j.foodchem.2020.127652

Jo, N., Kim, B., Lee, S.-M., Oh, J., Park, I. H., Jin Lim, K., et al. (2018). Aptamer-functionalized Capacitance Sensors for Real-Time Monitoring of Bacterial Growth and Antibiotic Susceptibility. *Biosens. Bioelectron.* 102, 164–170. doi:10.1016/j.bios.2017.11.010

Kern, W. V., and Rieg, S. (2020). Burden of Bacterial Bloodstream Infection-A Brief Update on Epidemiology and Significance of Multidrug-Resistant Pathogens. *Clin. Microbiol. Infect.* 26, 151–157. doi:10.1016/j.cmi.2019.10.031

Khateb, H., Klös, G., Meyer, R. L., and Sutherland, D. S. (2020). Development of a Label-free LSPR-Apta Sensor for *Staphylococcus aureus* Detection. *ACS Appl. Bio Mat.* 3, 3066–3077. doi:10.1021/acsabm.0c00110

Kurt, H., Yuce, M., Hussain, B., and Budak, H. (2016). Dual-Excitation Upconverting Nanoparticle and Quantum Dot Aptasensor for Multiplexed Food Pathogen Detection. *Biosens. Bioelectron.* 81, 280–286.

Lei, M., Xu, C., Shan, Y., Xia, C., Wang, R., Ran, H-H., et al. (2020). Plasmon-Coupled Microcavity Aptasensors for Visual and Ultra-Sensitive Simultaneous Detection of Staphylococcus aureus and Escherichia coli. *Anal. Bioanal. Chem.* 412, 8117–8126.

Li, H., Chen, Q., Mehedi Hassan, M., Chen, X., Ouyang, Q., Guo, Z., et al. (2017a). A Magnetite/PMAA Nanospheres-Targeting SERS Aptasensor for Tetracycline Sensing Using Mercapto Molecules Embedded Core/shell Nanoparticles for Signal Amplification. *Biosens. Bioelectron.* 92, 192–199. doi:10.1016/j.bios.2017.02.009

Li, J., Jiang, H., Rao, X., Liu, Z., Zhu, H., and Xu, Y. (2019a). Point-of-Care Testing of Pathogenic Bacteria at the Single-Colony Level via Gas Pressure Readout Using Aptamer-Coated Magnetic CuFe2O4 and Vancomycin-Capped Platinum Nanoparticles. *Anal. Chem.* 91, 1494–1500. doi:10.1021/acs.analchem.8b04584

Li, W.-M., Zhou, L.-L., Zheng, M., and Fang, J. (2018). Selection of Metastatic Breast Cancer Cell-specific Aptamers for the Capture of CTCs with a Metastatic Phenotype by Cell-SELEX. *Mol. Ther. - Nucleic Acids* 12, 707–717. doi:10.1016/j.omtn.2018.07.008

Li, Y.-Z., Li, T.-T., Chen, W., and Song, Y.-Y. (2017b). Co4N Nanowires: Noble-Metal-Free Peroxidase Mimetic with Excellent Salt- and Temperature-Resistant Abilities. *ACS Appl. Mat. Interfaces* 9, 29881–29888. doi:10.1021/acsami.7b09861

Li, Z., Mohamed, M. A., and Vinu Mohan, A. M. (2019b). Application of Electrochemical Aptasensors toward Clinical Diagnostics, Food, and Environmental Monitoring: Review. *Sensors (Basel)* 19, 5435. doi:10.3390/s19245435

Lian, Y., He, F., Wang, H., and Tong, F. (2015). A New Aptamer/Graphene Interdigitated Gold Electrode Piezoelectric Sensor for Rapid and Specific Detection of Staphylococcus aureus. *Biosens. Bioelectron.* 65, 314–319.

Lim, S. H., Ryu, Y. C., and Hwang, B. H. (2021). Aptamer-immobilized Gold Nanoparticles Enable Facile and On-site Detection of Staphylococcus aureus. *Biotechnol. Bioprocess Eng.* 26, 107–113.

Liu, L. S., Wang, F., Ge, Y., and Lo, P. K. (2021a). Recent Developments in Aptasensors for Diagnostic Applications. *ACS Appl. Mat. Interfaces* 13, 9329–9358. doi:10.1021/acsami.0c14788

Liu, S., Li, H., Hassan, M. M., Ali, S., and Chen, Q. (2021b). SERS Based Artificial Peroxidase Enzyme Regulated Multiple Signal Amplified System for Quantitative Detection of Foodborne Pathogens. *Food Control* 123.

Liu, Y., Tu, D., Zhu, H., and Chen, X. (2013). Lanthanide-doped Luminescent Nanoprobes: Controlled Synthesis, Optical Spectroscopy, and Bioapplications. *Chem. Soc. Rev.* 42, 6924–6958. doi:10.1039/c3cs60060b

Lorenz, C., von Pelchrzim, F., and Schroeder, R. (2006). Genomic Systematic Evolution of Ligands by Exponential Enrichment (Genomic SELEX) for the Identification of Protein-Binding RNAs Independent of Their Expression Levels. *Nat. Protoc.* 1, 2204–2212. doi:10.1038/nprot.2006.372

Lou, X., Qian, J., Xiao, Y., Viel, L., Gerdon, A. E., Lagally, E. T., et al. (2009). Micromagnetic Selection of Aptamers in Microfluidic Channels. *Proc. Natl. Acad. Sci. U.S.A.* 106, 2989–2994. doi:10.1073/pnas.0813135106

Lu, C., Gao, X., Chen, Y., Ren, J., and Liu, C. (2020a). Aptamer-Based Lateral Flow Test Strip for the Simultaneous Detection of *Salmonella typhimurium*, *Escherichia coli* O157:H7 and *Staphylococcus aureus*. *Anal. Lett.* 53, 646–659. doi:10.1080/00032719.2019.1663528

Lu, Y., Yuan, Z., Bai, J., Lin, Q., Deng, R., Luo, A., et al. (2020b). Directly Profiling Intact *Staphylococcus aureus* in Water and Foods via Enzymatic Cleavage Aptasensor. *Anal. Chim. Acta* 1132, 28–35. doi:10.1016/j.aca.2020.07.058

Ma, X., Lin, X., Xu, X., and Wang, Z. (2021). Fabrication of Gold/silver Nanodimer SERS Probes for the Simultaneous Detection of *Salmonella typhimurium* and *Staphylococcus aureus*. *Microchim. Acta* 188, 202. doi:10.1007/s00604-021-04791-4

Maduraiveeran, G., Sasidharan, M., and Ganesan, V. (2018). Electrochemical Sensor and Biosensor Platforms Based on Advanced Nanomaterials for Biological and Biomedical Applications. *Biosens. Bioelectron.* 103, 113–129. doi:10.1016/j.bios.2017.12.031

Maldonado, J., Estevez, M. C., Fernandez-Gavela, A., Jose Gonzalez-Lopez, J., Belen Gonzalez-Guerrero, A., and Lechuga, L. M. (2020). Label-free Detection of Nosocomial Bacteria Using a Nanophotonic Interferometric Biosensor. *Analyst.* 145, 497–506.

Mendonsa, S. D., and Bowser, M. T. (2004). *In Vitro* evolution of Functional DNA Using Capillary Electrophoresis. *J. Am. Chem. Soc.* 126, 20–21. doi:10.1021/ja037832s

Miyachi, Y., Shimizu, N., Ogino, C., and Kondo, A. (2010). Selection of DNA Aptamers Using Atomic Force Microscopy. *Nucleic Acids Res.* 38, e21. doi:10.1093/nar/gkp1101

Mokhtarzadeh, A., Ezzati Nazhad Dolatabadi, J., Abnous, K., de la Guardia, M., and Ramezani, M. (2015). Nanomaterial-based Cocaine Aptasensors. *Biosens. Bioelectron.* 68, 95–106. doi:10.1016/j.bios.2014.12.052

Moon, J., Kim, G., Park, S., Lim, J., and Mo, C. (2015). Comparison of Whole-Cell SELEX Methods for the Identification of Staphylococcus Aureus-specific DNA Aptamers. *SENSORS* 15, 8884–8897. doi:10.3390/s150408884

Morales, M. A., and Halpern, J. M. (2018). Guide to Selecting a Biorecognition Element for Biosensors. *Bioconjugate Chem.* 29, 3231–3239. doi:10.1021/acs.bioconjchem.8b00592

Muñoz-Bustos, C., Tirado-Guízar, A., Paraguay-Delgado, F., and Pina-Luis, G. (2017). Copper Nanoclusters-Coated BSA as a Novel Fluorescence Sensor for Sensitive and Selective Detection of Mangiferin. *Sensors Actuators B Chem.* 244, 922–927. doi:10.1016/j.snb.2017.01.071

Nguyen, T. T.-Q., Kim, E. R., and Gu, M. B. (2022). A New Cognate Aptamer Pair-Based Sandwich-type Electrochemical Biosensor for Sensitive Detection of *Staphylococcus aureus*. *Biosens. Bioelectron.* 198, 113835. doi:10.1016/j.bios.2021.113835

Nouri, A., Ahari, H., and Shahbazzadeh, D. (2018). Designing a Direct ELISA Kit for the Detection of *Staphylococcus aureus* Enterotoxin A in Raw Milk Samples. *Int. J. Biol. Macromol.* 107, 1732–1737. doi:10.1016/j.ijbiomac.2017.10.052

Ogston, A. (1882). Micrcoccus Poisoning. *J. Anat. Physiol.* 17, 24–58.

Ouyang, Q., Wang, L., Ahmad, W., Yang, Y., and Chen, Q. (2021a). Upconversion Nanoprobes Based on a Horseradish Peroxidase-Regulated Dual-Mode Strategy for the Ultrasensitive Detection of Staphylococcus aureus in Meat. *J. Agric. Food Chem.* 69, 9947–9956.

Ouyang, Q., Yang, Y., Ali, S., Wang, L., Li, H., and Chen, Q. (2021b). Upconversion Nanoparticles-Based FRET System for Sensitive Detection of *Staphylococcus aureus*. *Spectrochimica Acta Part a-Molecular And Biomol. Spectrosc.* 255, 119734. doi:10.1016/j.saa.2021.119734

Pang, Y., Wan, N., Shi, L., Wang, C., Sun, Z., Xiao, R., et al. (2019). Dual-Recognition Surface-Enhanced Raman Scattering(SERS) Biosensor for Pathogenic Bacteria Detection by Using Vancomycin-SERS Tags and Aptamer-Fe3O4@Au. *Analytica. Chimica. Acta.* 1077, 288–296.

Paniel, N., Baudart, J., Hayat, A., and Barthelmebs, L. (2013). Aptasensor and Genosensor Methods for Detection of Microbes in Real World Samples. *Methods* 64, 229–240. doi:10.1016/j.ymeth.2013.07.001

Pebdeni, A. B., Hosseini, M., and Ganjali, M. R. (2020). Fluorescent Turn-On Aptasensor of *Staphylococcus aureus* Based on the FRET between Green Carbon Quantum Dot and Gold Nanoparticle. *Food Anal. Methods* 13, 2070–2079. doi:10.1007/s12161-020-01821-4

Pebdeni, A. B., Mousavizadegan, M., and Hosseini, M. (2021). Sensitive Detection of *S.Aureus* Using Aptamer- and Vancomycin-Copper Nanoclusters as Dual Recognition Strategy. *Food Chem.* 361, 130137. doi:10.1016/j.foodchem.2021.130137

Pla, L., Santiago-Felipe, S., Angeles Tormo-Mas, M., Peman, J., Sancenon, F., Aznar, E., et al. (2020). Aptamer-Capped Nanoporous Anodic Alumina for *Staphylococcus aureus* Detection. *Sensors Actuators B-Chemical* 320, 128281. doi:10.1016/j.snb.2020.128281

Rahman, M. R. T., Lou, Z., Wang, H., and Ai, L. (2015). Aptamer Immobilized Magnetoelastic Sensor for the Determination of Staphylococcus aureus. *Analytical Letters.* 48, 2414–2422.

Rajapaksha, P., Elbourne, A., Gangadoo, S., Brown, R., Cozzolino, D., and Chapman, J. (2019). A Review of Methods for the Detection of Pathogenic Microorganisms. *Analyst* 144, 396–411. doi:10.1039/c8an01488d

Raji, M. A., Suaifan, G., Shibl, A., Weber, K., Cialla-May, D., Popp, J., et al. (2021). Aptasensor for the Detection of Methicillin Resistant *Staphylococcus aureus* on Contaminated Surfaces. *Biosens. Bioelectron.* 176, 112910. doi:10.1016/j.bios.2020.112910

Ramlal, S., Mondal, B., Lavu, P. S., N., B., and Kingston, J. (2018). Capture and Detection of *Staphylococcus aureus* with Dual Labeled Aptamers to Cell Surface Components. *Int. J. Food Microbiol.* 265, 74–83. doi:10.1016/j.ijfoodmicro.2017.11.002

Ranjbar, S., and Shahrokhian, S. (2018). Design and Fabrication of an Electrochemical Aptasensor Using Au Nanoparticles/carbon Nanoparticles/cellulose Nanofibers Nanocomposite for Rapid and Sensitive Detection of *Staphylococcus aureus*. *Bioelectrochemistry* 123, 70–76. doi:10.1016/j.bioelechem.2018.04.018

Reich, P., Stoltenburg, R., Strehlitz, B., Frense, D., and Beckmann, D. (2017). Development of An Impedimetric Aptasensor for the Detection of Staphylococcus aureus. *Int. J. Mol. Sci.* 18.

Reinemann, C., Freiin von Fritsch, U., Rudolph, S., and Strehlitz, B. (2016). Generation and Characterization of Quinolone-specific DNA Aptamers Suitable for Water Monitoring. *Biosens. Bioelectron.* 77, 1039–1047. doi:10.1016/j.bios.2015.10.069

Ribes, À., Aznar, E., Santiago-Felipe, S., Xifre-Perez, E., Tormo-Mas, M. Á., Pemán, J., et al. (2019). Selective and Sensitive Probe Based in Oligonucleotide-Capped Nanoporous Alumina for the Rapid Screening of Infection Produced by Candida Albicans. *ACS Sens.* 4, 1291–1298. doi:10.1021/acssensors.9b00169

Rubab, M., Shahbaz, H. M., Olaimat, A. N., and Oh, D.-H. (2018). Biosensors for Rapid and Sensitive Detection of *Staphylococcus aureus* in Food. *Biosens. Bioelectron.* 105, 49–57. doi:10.1016/j.bios.2018.01.023

Sefah, K., Yang, Z., Bradley, K. M., Hoshika, S., Jiménez, E., Zhang, L., et al. (2014). *In Vitro* selection with Artificial Expanded Genetic Information Systems. *Proc. Natl. Acad. Sci. U.S.A.* 111, 1449–1454. doi:10.1073/pnas.1311778111

Shangguan, J., Li, Y., He, D., He, X., Wang, K., Zou, Z., et al. (2015). A Combination of Positive Dielectrophoresis Driven on-Line Enrichment and Aptamer-Fluorescent Silica Nanoparticle Label for Rapid and Sensitive Detection of Staphylococcus aureus. *Analyst.* 140, 4489–4497.

Sharifi, M., Hosseinali, S. H., Hossein Alizadeh, R., Hasan, A., Attar, F., Salihi, A., et al. (2020). Plasmonic and Chiroplasmonic Nanobiosensors Based on Gold Nanoparticles. *Talanta* 212, 120782. doi:10.1016/j.talanta.2020.120782

Sharma, A., Catanante, G., Hayat, A., Istamboulie, G., Ben Rejeb, I., Bhand, S., et al. (2016). Development of Structure Switching Aptamer Assay for Detection of Aflatoxin M1 in Milk Sample. *Talanta* 158, 35–41. doi:10.1016/j.talanta.2016.05.043

Shen, J., Li, Y., Gu, H., Xia, F., and Zuo, X. (2014). Recent Development of Sandwich Assay Based on the Nanobiotechnologies for Proteins, Nucleic Acids, Small Molecules, and Ions. *Chem. Rev.* 114, 7631–7677. doi:10.1021/cr300248x

Shen, Y., Wu, T., Zhang, Y., Ling, N., Zheng, L., Zhang, S.-L., et al. (2020). Engineering of a Dual-Recognition Ratiometric Fluorescent Nanosensor with a Remarkably Large Stokes Shift for Accurate Tracking of Pathogenic Bacteria at the Single-Cell Level. *Anal. Chem.* 92, 13396–13404. doi:10.1021/acs.analchem.0c02762

Sheng, L., Lu, Y., Deng, S., Liao, X., Zhang, K., Ding, T., et al. (2019). A Transcription Aptasensor: Amplified, Label-Free and Culture-Independent Detection of Foodborne Pathogens via Light-up RNA Aptamers. *Chem. Commun.* 55, 10096–10099.

Shrivastava, S., Lee, W-I., and Lee, N-E. (2018). Culture-Free, Highly Sensitive, Quantitative Detection of Bacteria From Minimally Processed Samples Using Fluorescence Imaging by Smartphone. *Biosens. Bioelectron.* 109, 90–97.

Su, L., Feng, J., Zhou, X., Ren, C., Li, H., and Chen, X. (2012). Colorimetric Detection of Urine Glucose Based ZnFe2O4 Magnetic Nanoparticles. *Anal. Chem.* 84, 5753–5758. doi:10.1021/ac300939z

Sun, Z., Peng, Y., Wang, M., Lin, Y., Jalalah, M., Alsareii, S. A., et al. (2021). Electrochemical Deposition of Cu Metal-Organic Framework Films for the Dual Analysis of Pathogens. *Anal. Chem.* 93, 8994–9001. doi:10.1021/acs.analchem.1c01763

Taghdisi, S. M., Danesh, N. M., Beheshti, H. R., Ramezani, M., and Abnous, K. (2016). A Novel Fluorescent Aptasensor Based on Gold and Silica Nanoparticles for the Ultrasensitive Detection of Ochratoxin A. *Nanoscale* 8, 3439–3446. doi:10.1039/c5nr08234j

Tao, X., Liao, Z., Zhang, Y., Fu, F., Hao, M., Song, Y., et al. (2021). Aptamer-quantum Dots and Teicoplanin-Gold Nanoparticles Constructed FRET Sensor for Sensitive Detection of *Staphylococcus aureus*. *Chin. Chem. Lett.* 32, 791–795. doi:10.1016/j.cclet.2020.07.020

Teng, J., Yuan, F., Ye, Y., Zheng, L., Yao, L., Xue, F., et al. (2016). Aptamer-Based Technologies in Foodborne Pathogen Detection. *Front. Microbiol.* 7, 1426. doi:10.3389/fmicb.2016.01426

Tok, J. B.-H., Cho, J., and Rando, R. R. (2000). RNA Aptamers that Specifically Bind to a 16S Ribosomal RNA Decoding Region Construct. *Nucleic Acids Res.* 28, 2902–2910. doi:10.1093/nar/28.15.2902

Tong, S. Y. C., Davis, J. S., Eichenberger, E., Holland, T. L., and Fowler, V. G., Jr. (2015). *Staphylococcus aureus* Infections: Epidemiology, Pathophysiology, Clinical Manifestations, and Management. *Clin. Microbiol. Rev.* 28, 603–661. doi:10.1128/cmr.00134-14

Tuerk, C., and Gold, L. (1990). Systematic Evolution of Ligands by Exponential Enrichment: RNA Ligands to Bacteriophage T4 DNA Polymerase. *Science* 249, 505–510. doi:10.1126/science.2200121

Tuerk, C., MacDougal, S., and Gold, L. (1992). RNA Pseudoknots that Inhibit Human Immunodeficiency Virus Type 1 Reverse Transcriptase. *Proc. Natl. Acad. Sci. U.S.A.* 89, 6988–6992. doi:10.1073/pnas.89.15.6988

Umesha, S., and Manukumar, H. M. (2018). Advanced Molecular Diagnostic Techniques for Detection of Food-Borne Pathogens: Current Applications and Future Challenges. *Crit. Rev. Food Sci. Nutr.* 58, 84–104. doi:10.1080/10408398.2015.1126701

Wang, C.-H., Wu, J.-J., and Lee, G.-B. (2019a). Screening of Highly-specific Aptamers and Their Applications in Paper-Based Microfluidic Chips for Rapid Diagnosis of Multiple Bacteria. *Sensors Actuators B Chem.* 284, 395–402. doi:10.1016/j.snb.2018.12.112

Wang, C.-W., Chung, W.-H., Cheng, Y.-F., Ying, N.-W., Peck, K., Chen, Y.-T., et al. (2013). A New Nucleic Acid-Based Agent Inhibits Cytotoxic T Lymphocyte-Mediated Immune Disorders. *J. Allergy Clin. Immunol.* 132, 713–722. e711. doi:10.1016/j.jaci.2013.04.036

Wang, D., Lian, F., Yao, S., Liu, Y., Wang, J., Song, X., et al. (2020). Simultaneous Detection of Three Foodborne Pathogens Based on Immunomagnetic Nanoparticles and Fluorescent Quantum Dots. *ACS Omega* 5, 23070–23080. doi:10.1021/acsomega.0c02833

Wang, F., Banerjee, D., Liu, Y., Chen, X., and Liu, X. (2010). Upconversion Nanoparticles in Biological Labeling, Imaging, and Therapy. *Analyst* 135, 1839–1854. doi:10.1039/c0an00144a

Wang, J., Li, H., Li, T., and Ling, L. (2018). Determination of Bacterial DNA Based on Catalytic Oxidation of Cysteine by G-Quadruplex DNAzyme Generated from Asymmetric PCR: Application to the Colorimetric Detection of *Staphylococcus aureus*. *Microchim. Acta* 185, 410. doi:10.1007/s00604-018-2935-y

Wang, J., Wu, X., Wang, C., Shao, N., Dong, P., Xiao, R., et al. (2015). Magnetically Assisted Surface-Enhanced Raman Spectroscopy for the Detection of Staphylococcus aureus Based on Aptamer Recognition. *ACS Appl. Mater. Interfaces* 7, 20919–20929.

Wang, S., Deng, W., Yang, L., Tan, Y., Xie, Q., and Yao, S. (2017a). Copper-Based Metal-Organic Framework Nanoparticles with Peroxidase-like Activity for Sensitive Colorimetric Detection of *Staphylococcus aureus*. *ACS Appl. Mat. Interfaces* 9, 24440–24445. doi:10.1021/acsami.7b07307

Wang, W. W., Han, X., and Chu, L. Q. (2019b). Polyadenine-mediated Immobilization of Aptamers on a Gold Substrate for the Direct Detection of Bacterial Pathogens. *Anal Sci.* 35, 967–972.

Wang, X., Liu, W., Yin, B., Sang, Y., Liu, Z., Dai, Y., et al. (2017b). An Isothermal Strand Displacement Amplification Strategy for Nucleic Acids Using Junction Forming Probes and Colorimetric Detection. *Microchim. Acta* 184, 1603–1610. doi:10.1007/s00604-017-2158-7

Woo, M.-A., Kim, M., Jung, J., Park, K., Seo, T., and Park, H. (2013). A Novel Colorimetric Immunoassay Utilizing the Peroxidase Mimicking Activity of Magnetic Nanoparticles. *Ijms* 14, 9999–10014. doi:10.3390/ijms14059999

Wu, S., Duan, N., Shi, Z., Fang, C., and Wang, Z. (2014). Simultaneous Aptasensor for Multiplex Pathogenic Bacteria Detection Based on Multicolor Upconversion Nanoparticles Labels. *Anal. Chem.* 86, 3100–3107. doi:10.1021/ac404205c

Xu, J., Guo, J., Maina, S. W., Yang, Y., Hu, Y., Li, X., et al. (2018). An Aptasensor for staphylococcus Aureus Based on Nicking Enzyme Amplification Reaction and Rolling Circle Amplification. *Anal. Biochem.* 549, 136–142. doi:10.1016/j.ab.2018.03.013

Xu, K., Zhou, R., Takei, K., and Hong, M. (2019). Toward Flexible Surface-Enhanced Raman Scattering (SERS) Sensors for Point-of-Care Diagnostics. *Adv. Sci.* 6, 1900925. doi:10.1002/advs.201900925

Yang, M., Chen, X., Zhu, L., Lin, S., Li, C., Li, X., et al. (2021a). Aptamer-Functionalized DNA-Silver Nanocluster Nanofilm for Visual Detection and Elimination of Bacteria. *ACS Appl. Mat. Interfaces* 13, 38647–38655. doi:10.1021/acsami.1c05751

Yang, Y., Wu, T., Xu, L. P., and Zhang, X. (2021b). Portable Detection of *Staphylococcus aureus* Using Personal Glucose Meter Based on Hybridization Chain Reaction Strategy. *Talanta* 226, 122132. doi:10.1016/j.talanta.2021.122132

Yao, J., Yang, M., and Duan, Y. (2014). Chemistry, Biology, and Medicine of Fluorescent Nanomaterials and Related Systems: New Insights into Biosensing, Bioimaging, Genomics, Diagnostics, and Therapy. *Chem. Rev.* 114, 6130–6178. doi:10.1021/cr200359p

Yao, S., Zhao, C., Shang, M., Li, J., and Wang, J. (2021). Enzyme-free and Label-free Detection of *Staphylococcus aureus* Based on Target-Inhibited Fluorescence Signal Recovery. *Food Chem. Toxicol.* 150, 112071. doi:10.1016/j.fct.2021.112071

Yao, S., Li, J., Pang, B., Wang, X., Shi, Y., Song, X., et al. (2020). Colorimetric Immunoassay for Rapid Detection of Staphylococcus aureus Based on Etching-Enhanced Peroxidase-like Catalytic Activity of Gold Nanoparticles. *Microchimica Acta.* 187.

Ye, Y., Zheng, L., Wu, T., Ding, X., Chen, F., Yuan, Y., et al. (2020). Size-Dependent Modulation of Polydopamine Nanospheres on Smart Nanoprobes for Detection of Pathogenic Bacteria at Single-Cell Level and Imaging-Guided Photothermal Bactericidal Activity. *ACS Appl. Mat. Interfaces* 12, 35626–35637. doi:10.1021/acsami.0c07784

Yu, H., Alkhamis, O., Canoura, J., Liu, Y., and Xiao, Y. (2021). Advances and Challenges in Small-Molecule DNA Aptamer Isolation, Characterization, and Sensor Development. *Angew. Chem. Int. Ed.* 60, 16800–16823. doi:10.1002/anie.202008663

Yu, M., Wang, H., Fu, F., Li, L., Li, J., Li, G., et al. (2017). Dual-Recognition Förster Resonance Energy Transfer Based Platform for One-step Sensitive Detection of Pathogenic Bacteria Using Fluorescent Vancomycin-Gold Nanoclusters and Aptamer-Gold Nanoparticles. *Anal. Chem.* 89, 4085–4090. doi:10.1021/acs.analchem.6b04958

Yu, T., Xu, H., Zhao, Y., Han, Y., Zhang, Y., Zhang, J., et al. (2020). Aptamer Based High Throughput Colorimetric Biosensor for Detection of staphylococcus Aureus. *Sci. Rep.* 10, 9190. doi:10.1038/s41598-020-66105-7

Yuan, J., Yu, Y., Li, C., Ma, X., Xia, Y., Chen, J., et al. (2014a). Visual Detection and Microplate Assay for *Staphylococcus aureus* Based on Aptamer Recognition Coupled to Tyramine Signal Amplification. *Microchim. Acta* 181, 321–327. doi:10.1007/s00604-013-1120-6

Yuan, J., Wu, S., Duan, N., Ma, X., Xia, Y., Chen, J., et al. (2014b). A Sensitive Gold Nanoparticle-Based Colorimetric Aptasensor for Staphylococcus aureus. *Talanta.* 127, 163–168.

Zelada-Guillén, G. A., Sebastián-Avila, J. L., Blondeau, P., Riu, J., and Rius, F. X. (2012). Label-free Detection of *Staphylococcus aureus* in Skin Using Real-Time Potentiometric Biosensors Based on Carbon Nanotubes and Aptamers. *Biosens. Bioelectron.* 31, 226–232. doi:10.1016/j.bios.2011.10.021

Zhang, H., Liu, Y., Yao, S., Shang, M., Zhao, C., Li, J., et al. (2021a). A Multicolor Sensing System for Simultaneous Detection of Four Foodborne Pathogenic Bacteria Based on Fe3O4/MnO2 Nanocomposites and the Etching of Gold Nanorods. *Food Chem. Toxicol.* 149, 112035. doi:10.1016/j.fct.2021.112035

Zhang, H., Ma, X., Liu, Y., Duan, N., Wu, S., Wang, Z., et al. (2015a). Gold Nanoparticles Enhanced SERS Aptasensor for the Simultaneous Detection of *Salmonella typhimurium* and *Staphylococcus aureus*. *Biosens. Bioelectron.* 74, 872–877. doi:10.1016/j.bios.2015.07.033

Zhang, H., Yao, S., Song, X., Xu, K., Wang, J., Li, J., et al. (2021b). One-step Colorimetric Detection of *Staphylococcus aureus* Based on Target-Induced Shielding against the Peroxidase Mimicking Activity of Aptamer-Functionalized Gold-Coated Iron Oxide Nanocomposites. *Talanta* 232, 122448. doi:10.1016/j.talanta.2021.122448

Zhang, X., Wang, X., Yang, Q., Jiang, X., Li, Y., Zhao, J., et al. (2020). Conductometric Sensor for Viable *Escherichia coli* and *Staphylococcus aureus* Based on Magnetic Analyte Separation via Aptamer. *Mikrochim. Acta* 187, 43. doi:10.1007/s00604-019-3880-0

Zhang, X., Huang, C., Xu, S., Chen, J., Zeng, Y., Wu, P., et al. (2015b). Photocatalytic Oxidation of TMB with the Double Stranded DNA-SYBR Green I Complex for Label-free and Universal Colorimetric Bioassay. *Chem. Commun.* 51, 14465–14468. doi:10.1039/c5cc06105a

Zhang, X., Wang, K., Liu, M., Zhang, X., Tao, L., Chen, Y., et al. (2015c). Polymeric AIE-Based Nanoprobes for Biomedical Applications: Recent Advances and Perspectives. *Nanoscale* 7, 11486–11508. doi:10.1039/c5nr01444a

Zhang, Y., Tan, W., Zhang, Y., Mao, H., Shi, S., Duan, L., et al. (2019). Ultrasensitive and Selective Detection of *Staphylococcus aureus* Using a Novel IgY-Based Colorimetric Platform. *Biosens. Bioelectron.* 142, 111570. doi:10.1016/j.bios.2019.111570

Zhou, J., and Rossi, J. (2017). Aptamers as Targeted Therapeutics: Current Potential and Challenges. *Nat. Rev. Drug Discov.* 16, 181–202. doi:10.1038/nrd.2016.199

Zhu, A., Ali, S., Xu, Y., Ouyang, Q., and Chen, Q. (2021a). A SERS Aptasensor Based on AuNPs Functionalized PDMS Film for Selective and Sensitive Detection of *Staphylococcus aureus*. *Biosens. Bioelectron.* 172, 112806. doi:10.1016/j.bios.2020.112806

Zhu, A., Jiao, T., Ali, S., Xu, Y., Ouyang, Q., and Chen, Q. (2021b). SERS Sensors Based on Aptamer-Gated Mesoporous Silica Nanoparticles for Quantitative Detection of *Staphylococcus aureus* with Signal Molecular Release. *Anal. Chem.* 93, 9788–9796. doi:10.1021/acs.analchem.1c01280

Zhu, J., Li, J.-j., Wang, A.-q., Chen, Y., and Zhao, J.-w. (2010). Fluorescence Quenching of Alpha-Fetoprotein by Gold Nanoparticles: Effect of Dielectric Shell on Non-radiative Decay. *Nanoscale Res. Lett.* 5, 1496–1501. doi:10.1007/s11671-010-9668-0

Zuo, P., Li, X., Dominguez, D. C., and Ye, B.-C. (2013). A PDMS/Paper/Glass Hybrid Microfluidic Biochip Integrated With Aptamer-Functionalized Graphene Oxide Nano-Biosensors for One-Step Multiplexed Pathogen Detection. *LAB ON A CHIP* 13, 3921–3928.

Conflict of Interest: The authors declare that the research was conducted in the absence of any commercial or financial relationships that could be construed as a potential conflict of interest.

frontiers | Frontiers in Bioengineering and Biotechnology

ORIGINAL RESEARCH
published: 01 June 2022
doi: 10.3389/fbioe.2022.884271

Osmotic Processor for Enabling Sensitive and Rapid Biomarker Detection *via* Lateral Flow Assays

***Sheng-You Chen*[1†]*, Abe Y. Wu*[2†]*, Ruby Lunde*[2†] *and James J. Lai*[2*]**

[1]Department of Mechanical Engineering, University of Washington, Seattle, WA, United States, [2]Department of Bioengineering, University of Washington, Seattle, WA, United States

Urine is an attractive biospecimen for *in vitro* diagnostics, and urine-based lateral flow assays are low-cost devices suitable for point-of-care testing, particularly in low-resource settings. However, some of the lateral flow assays exhibit limited diagnostic utility because the urinary biomarker concentration is significantly lower than the assay detection limit, which compromises the sensitivity. To address the challenge, we developed an osmotic processor that statically and spontaneously concentrated biomarkers. The specimen in the device interfaces with the aqueous polymer solution via a dialysis membrane. The polymer solution induces an osmotic pressure difference that extracts water from the specimen, while the membrane retains the biomarkers. The evaluation demonstrated that osmosis induced by various water-soluble polymers efficiently extracted water from the specimens, ca. 5–15 ml/h. The osmotic processor concentrated the specimens to improve the lateral flow assays' detection limits for the model analytes—human chorionic gonadotropin and SARS-CoV-2 nucleocapsid protein. After the treatment via the osmotic processor, the lateral flow assays detected the corresponding biomarkers in the concentrated specimens. The test band intensities of the assays with the concentrated specimens were very similar to the reference assays with 100-fold concentrations. The mass spectrometry analysis estimated the SARS-CoV-2 nucleocapsid protein concentration increased ca. 200-fold after the osmosis. With its simplicity and flexibility, this device demonstrates a great potential to be utilized in conjunction with the existing lateral flow assays for enabling highly sensitive detection of dilute target analytes in urine.

Keywords: biomarker concentration, osmosis, polymers, lateral flow tests, limit of detection, biospecimen processing, point-of-care diagnostics

Edited by:
Tzong-Rong Ger,
Chung Yuan Christian University,
Taiwan

Reviewed by:
Zhenpeng Qin,
The University of Texas at Dallas,
United States
Alfredo De La Escosura-Muñiz,
University of Oviedo, Spain

****Correspondence:***
James J. Lai
jilai@uw.edu

[†]These authors have contributed equally to this work

Specialty section:
This article was submitted to Biosensors and Biomolecular Electronics, a section of the journal Frontiers in Bioengineering and Biotechnology

Received: *26 February 2022*
Accepted: *19 April 2022*
Published: *01 June 2022*

Citation:
Chen S-Y, Wu AY, Lunde R and Lai JJ (2022) Osmotic Processor for Enabling Sensitive and Rapid Biomarker Detection via Lateral Flow Assays. Front. Bioeng. Biotechnol. 10:884271. doi: 10.3389/fbioe.2022.884271

1 INTRODUCTION

Urine is one of the most used biospecimens next to blood that can be easily collected in large quantities with noninvasive procedures (Hadland and Levy, 2016). Urine is routinely used at the point-of-care and in laboratory settings to detect pregnancies, diagnose diseases, and screen potential health problems (Tuuminen, 2012). Molecules in urine originate from glomerular filtration of plasma, renal tubule excretion, and shedding of various cells, representing a biomarker repertoire that can be exploited for diagnosis and monitoring of renal as well as systemic diseases (Harpole et al., 2016). Urine is composed of mostly water and solutes like urea, small ions, creatinine, albumin, bilirubin, and low concentrations of other small proteins (Simerville et al., 2005; Taylor and Curhan, 2006). Solute concentrations as well as the presence of other uncommon molecules are reflective of physiological conditions and can be utilized for disease diagnosis such as urinary tract infection (Simerville et al., 2005). However, urinary biomarkers can present in concentrations well below the limits of detection (LOD) of common diagnostic assays (Nimse et al., 2016). For example, the concentration of human growth hormone (hGH), a urinary biomarker, is ca. 100-fold below the immunoassays' LOD (Fredolini et al., 2008). Urinary cell-free DNA can be utilized as a biomarker for cancer and infectious disease diagnostics (e.g., tuberculosis), but the dilute concentration and fragmented nature of the analyte impair the efficiency of extraction methods and consequently lower the diagnostic sensitivity (Oreskovic et al., 2019). The presence of high salts and interfering molecules (e.g., biotin) in urine also hinders the development and clinical implementation of urine-based diagnostic tests (Wong and Tse, 2009; Bowen et al., 2019).

Lateral flow assays (LFAs) are low-cost immunoassays for rapid biomarker detection, which have been widely used in medicine, environmental health, and quality control (Koczula and Gallotta, 2016). However, the LFAs' detection limits are higher than the corresponding laboratory-based assays, so their sensitivities are significantly impacted by the low analyte concentrations and interferences (Moghadam et al., 2015; Zhang et al., 2020). For example, the Alere Determine TB-LAM Ag, a LFA for detecting urinary tuberculosis (TB) antigen lipoarabinomannan (LAM), has been proven to be highly specific and exhibits potential to be a high-impact point-of-care test (Peter et al., 2015). However, the estimated assay sensitivities are ~18% for HIV-negative and ~42% for HIV-positive individuals, caused by the low analyte concentration (Bulterys et al., 2019). The LAM concentration in urine for TB-positive patients can be as low as 14 pg/ml, which is significantly lower than the assay LOD, 500–1,000 pg/ml (Bulterys et al., 2019; García et al., 2019). Thus, the test cannot be utilized for general TB screening (World Health Organization, 2020).

Techniques have been developed to improve the sensitivities of LFAs, including kinetics and transport control (Yang et al., 2013; Rivas et al., 2014; Tang et al., 2017; Ishii et al., 2018), biochemical signal amplification (Hu et al., 2013; Parolo et al., 2013; Panferov et al., 2016), improved labeling (Choi et al., 2010), and sample enrichment. Sample enrichment techniques include centrifugal filtration (Corstjens et al., 2015), immunomagnetic separation (Panferov et al., 2017; Ben Aissa et al., 2021), electrophoretic and phasic separation (Wu et al., 2014; Chiu et al., 2015; Kim et al., 2017), isotachophoresis (Moghadam et al., 2015), dialysis (Tang et al., 2016), and test-zone pre-enrichment (Zhang et al., 2020). These systems are not suitable for low-resource, point-of-care settings as they require expensive reagents, equipment, and/or complex procedures. On the other hand, paper-based methods using dialysis or test-zone pre-enrichment lead to suboptimal enrichment and have limited processing capacity (Tang et al., 2016; Zhang et al., 2020). Therefore, there is a need for simple, versatile and effective approaches that enrich analytes to improve the LFA sensitivity.

To enable sensitive and rapid urinary biomarker detection *via* LFAs, this work presents the osmotic processor—a device that concentrates analytes via osmosis. The process spontaneously removes water molecules from the urine specimen while retaining the target analyte. The device includes a urine specimen compartment and a polymer compartment, which are separated by a semipermeable membrane. The polymer solution induces a strong osmotic pressure difference across the semipermeable membrane, which drives water molecules in the urine specimen across the membrane into the polymer solution (Nelson, 2017). Additionally, the membrane's molecular weight cutoff (MWCO) is significantly smaller than that of the target analyte, allowing small ions and solutes that may interfere with the assay to be removed. Concentrating urinary analytes *via* osmosis has been demonstrated by McFarland, using cellulose acetate membrane and sucrose (polymer) to concentrate the analytes 5-fold for gel electrophoresis (McFarlane, 1964).

Compared to existing enrichment approaches, the osmotic processor demonstrates the potential to streamline its interface with existing LFAs, its simplicity with a spontaneous process, its flexibility to process a large specimen volume, and its capability to simultaneously recondition the concentrated specimen (remove inhibitory factors) for optimal assay performance. In this work the device was utilized to improve the detection limits of commercially available LFAs using human chorionic gonadotropin (hCG) and SARS-CoV-2 nucleocapsid (N) protein as model analytes. The osmotic processor has demonstrated ca. 100-fold concentration from a 10 ml sample for both analytes.

2 MATERIALS AND METHODS

2.1 Materials

Polyethylene glycol 1,500/PEG 1500 (Sigma-Aldrich, St. Louis, MO, United States)**,** Polyethylene glycol 4,000/PEG 4000 (Sigma-Aldrich, St. Louis, MO, United States), Polyethylene glycol 35,000/PEG 35000 (Sigma-Aldrich, St. Louis, MO, United States), Poly (sodium 4-styrenesulfonate)/PSS (Sigma-Aldrich, St. Louis, MO, United States), Pectin (Spectrum Chemical Mfg. Corp, Gardena, CA, United States), Poly (acrylic acid sodium salt)/PAA (Sigma-Aldrich, St. Louis, MO, United States), Polyethyleneimine/PEI (Sigma-Aldrich, St. Louis, MO, United States), Spectra/Por 1 Dry Standard Grade Regenerated Cellulose (RC) Dialysis Tubing (Repligen, Waltham, MA, United States, 32 mm flat width, 6 kD, 1 m), SnakeSkin Dialysis Tubing (Thermo Fisher Scientific, Waltham, MA, United States, 3.5 K, 35 mm dry inner diameter, 35 feet), Original Prusa i3 MK3S + Printer (Prusa Research 3D, Prague, Czech Republic), Polylactic Acid (PLA) 1.75 mm Filament (Hatchbox3D, Pomona, CA, United States), Ammonium bicarbonate (ThermoFisher Scientific, Waltham, MA, United States, 99% for analysis), Chorionic gonadotropin human (Sigma-Aldrich, St. Louis, MO, United States, 5000 IU lyophilized powder), AimStep Pregnancy Urine Cassette Test (Germaine Laboratories, Inc. San Antonio, TX, United States of America), Nucleocapsid Protein 95% COVID-19 (ACROBiosystems, Newark, DE, United States), Quidel QuickVue at-Home OTC COVID-19 Test (Quidel

TABLE 1 | Polymers prepared at maximum mass concentration.

Polymer	Maximum mass Concentration (g/ml)	Molecular weight (daltons)	Charge
PEG 1500	2	1,500	neutral
PEG 4000	1.5	4,000	neutral
PEG 35000	0.8	35,000	neutral
PSS	0.6	1,000,000	negative
Pectin	0.25	Unknown	neutral
PAA	1	5,100	negative
PEI	1	25,000	positive

Corporation, San Diego, CA, United States), Urea (Bio Rad Lab, Hercules, CA, United States, Pkg of 1, 250 g), TCEP (Promega Corporation, Madison, WI, 15 mg), Iodoacetamide (Thermo Fisher Scientific, Waltham, MA, United States), Dithiothreitol (Bio Rad Lab, Hercules, CA, United States, 1 g), Trypsin (Sigma-Aldrich, St. Louis, MO, United States, 1x Gamma-Irradiated 0.25% Porcine Trypsin 1:250 in HBSS w/0.1% EDTA-NA2 w/o CA and MG), formic acid (Fisher Scientific, Waltham, MA, United States, 0.1% in water, Optima LC/MS, Solvent Blends), Orbitrap Exploris 480 mass spectrophotometer (Thermo Fisher Scientific, Waltham, MA, United States), EASYnLC 1200 UPLC system (Thermo Fisher Scientific, Waltham, MA, United States), Analytical column (New Objective, Inc., Woburn, MA, ID 75 μm), Integrafrit trap column (New Objective, Inc., Woburn, MA, ID 100 μm), ReprosilPur C18AQ 5 μm beads (Dr. Maisch, Tubigen, Germany), formic acid (Fisher Scientific, Waltham, MA, United States, 0.1% in acetonitrile, Optima LC/MS, Solvent Blends), Water (Fisher Scientific, Waltham, MA, United States, Optima™ LC/MS Grade)

2.2 Methods

2.2.1 Water Soluble Polymers for Osmosis

Various water-soluble polymers were utilized to evaluate the rate of water movement across the membrane, driven by osmosis. The evaluation included polymers with different compositions, molecular weights, and charge properties. The polymer characteristics and the solution concentrations are summarized in **Table 1**.

In this study, 10 ml deionized water was loaded in the Spectra/Por 1 dialysis tubing with 32 mm flat width and 6–8 kDa MWCO. Then, the sealed dialysis bags were immersed in 80 ml of a polymer solution, listed in **Table 1**. After 30 min, the dialysis bag was removed from the polymer solution, and then briefly rinsed with DI water to remove excess polymer. The remaining water in the dialysis bag was transferred to a graduated cylinder for volume measurement. The volume difference between the initial 10 ml solution and remaining liquid was the total water removed, which was divided by the processing time (0.5 h) to estimate the water removal rate.

2.2.2 Effect of Polymer Molecular Weight on Osmosis

To evaluate the effect of polymer molecular weight on the rate of water transport across the membrane, the study utilized polyethylene glycol (PEG) at three different molecular weights, 1.5, 4, and 35 kDa. All polymer solutions were prepared by pre-dissolving the polymers in deionized water at 0.8 g/ml to drive the osmosis. For the evaluation, 10 ml deionized water was loaded in the Spectra/Por 1 dialysis tubing with 32 mm flat width and 6–8 kDa MWCO. Then, the sealed dialysis bags were immersed in 80 ml of the PEG solution. After 30 min, the dialysis bag was removed from the polymer solution, and then briefly rinsed with DI water to remove excess polymer. The remaining water in the dialysis bag was transferred to a graduated cylinder for volume measurement. The volume difference between the initial 10 ml solution and remaining liquid was the total water removed, which was divided by the processing time (0.5 h) to estimate the water removal rate.

2.2.3 Effect of Polymer Solution Mass Concentration on Osmosis

To evaluate the effect of polymer solution mass concentration on the rate of water transport across the membrane, the polymer solutions were prepared using PEG 1500 (1.5 kDa PEG) to drive the osmosis. Specifically, PEG 1500 was dissolved in deionized water at concentrations of 0.125, 0.25, 0.5, 1.0, or 2.0 g/ml. For the evaluation, 10 ml deionized water was loaded in the Spectra/Por 1 dialysis tubing with 32 mm flat width and 6–8 kDa MWCO. Then, the sealed dialysis bags were immersed in 80 ml of the PEG solution. After 30 min, the dialysis bag was removed from the polymer solution, and then briefly rinsed with DI water to remove excess polymer. The remaining water in the dialysis bag was transferred to a graduated cylinder for volume measurement. The volume difference between the initial 10 ml solution and remaining liquid was the total water removed, which was divided by the processing time (0.5 h) to estimate the water removal rate.

2.2.4 Osmotic Processor Fabrication and Assembly

Scheme 1 shows the device components, dimension, and assembly workflow. The urine compartment, polymer container lid, polymer container, base, and collection cap components of the osmotic processor (**Scheme 1A**) were fabricated using the fused filament fabrication (FFF) 3D printing method on the Original Prusa i3 MK3S + printer (Prusa Research 3D, Prague, Czech Republic) with 1.75 mm PLA filament. The height and diameter of the assembled device were 136 and 22 mm, respectively (**Scheme 1B**). **Scheme 1C** illustrates the assembly workflow. 1) The sample collection cap was secured to the base of the device. 2) The outer specimen compartment was inserted into 150 mm of SnakeSkin

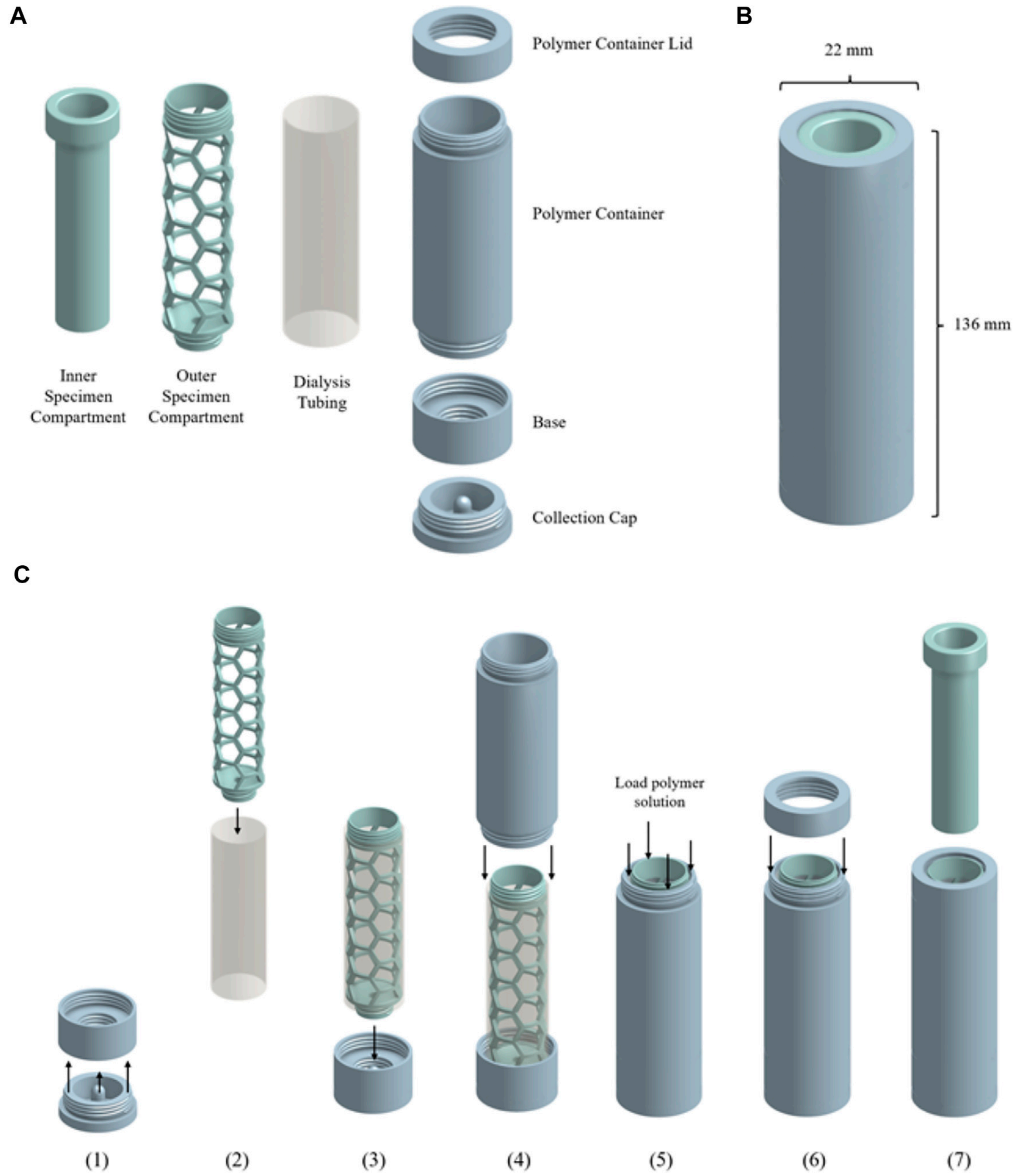

SCHEME 1 | (A) Components of the osmotic processor: urine compartment, dialysis tubing, polymer container lid, polymer container, base and collection cap. **(B)** Dimensions of the osmotic processor. **(C)** Assembly workflow of the osmotic processor. (Created with Onshape).

dialysis tubing with 35 mm inner diameter to hold the structure of the membrane. 3) The outer urine compartment was screwed onto the base to secure the bottom end of the dialysis tubing. 4) The polymer container was screwed onto the base. 5) The polymer container was filled with 50 ml of polymer solution. 6) The polymer container was sealed with the polymer container lid. 7) The assembled device is ready for specimen to be added. See **Scheme 3** for the osmotic processing workflow.

2.2.5 Concentrating Human Chorionic Gonadotropin (hCG) Hormone for Improved Lateral Flow Assay Detection Limit

hCG solutions were processed using the osmotic processor, and then the concentrated specimens were assayed using the AimStep pregnancy test, a LFA. The osmotic processor utilized 50 ml of PEG 1500 at 2 g/ml and the 6–8 kDa Spectra/Por 1 dialysis tubing. Specimens were prepared by diluting hCG in deionized water. 10 ml of the 0.02 μg/ml hCG solution was processed for 45 min, and the resulting 100 μl sample was assayed using the AimStep pregnancy test by following the vendor's protocol. 0 μg/ml hCG solution was also processed and assayed as a negative control. For reference, the stock solutions with 0, 0.02, and 2 μg/ml hCG wereassayed using the AimStep pregnancy test. The results were recorded by capturing the images of the assays, using an Epson Perfection v39 photo scanner. The test band intensity of the hCG LFA was analyzed with ImageJ (Schneider et al., 2012), an image-processing software, to produce semi-quantitative comparison between the specimens before and after the osmosis. The signal was measured in arbitrary units by inverting the image color, selecting an area on the test band, and measuring the raw integrated pixel density of the selected area. For the semi-quantitative comparison, the test line signals were further processed by normalizing against the background noise, signals from a no color membrane area away from the test and control bands.

2.2.6 Concentrating SARS-CoV-2 Nucleocapsid (N) Protein for Improved Lateral Flow Assay Detection Limit

Solutions of SARS-CoV-2 N protein were processed using the osmotic processor, and then assayed with the QuickVue test, a LFA. The osmotic processor utilized 50 ml of PEG 35000 at 0.8 g/ml and the 3.5 kDa SnakeSkin dialysis tubing. Specimens were prepared by diluting the SARS-CoV-2 N protein in the 50 mM ammonium bicarbonate buffer. 10 ml of the 0.04 ng/mL N protein solution was concentrated by the osmotic processor for 1.5 h, and the resulting 100 μl sample was assayed using the QuickVue test. 0 ng/ml N protein solution was also processed and assayed as a negative control. For reference, the stock solutions with 0, 0.04, and 4 ng/mL N protein were assayed using the QuickVue test. The results were recorded by capturing the assay membrane images, using an Epson Perfection v39 photo scanner. The test band intensity of the SARS-CoV-2 LFA was analyzed with ImageJ (Schneider et al., 2012), an image-processing software, to produce semi-quantitative comparison between the specimens before and after the osmosis process. The signal was measured in arbitrary units by inverting the image color, selecting an area on the test band, and measuring the raw integrated pixel density of the selected area. For the semi-quantitative comparison, the test line signals were further processed by normalizing against the background noise, signals from a no color membrane area away from the test and control bands.

2.2.7 Mass Spectrometry Assays for Quantitating Analyte Enrichment via the Osmosis Processor

The analyte enrichment was also characterized via mass spectrometry using SARS-CoV-2 N protein as the model analyte. To accommodate the mass spectrometry LOD, which is significantly higher than LFA, the evaluation utilized specimens with 4 μg/ml N protein. The aforementioned approach (2.2.6) was employed to concentrate SARS-CoV-2 N protein via the osmotic processor. A calibration was generated by performing mass spec analysis using 100 μL of standard solutions with 0, 0.08, 0.4, 2, 10 and 40 μg/ml N protein.

Specimen preparation for mass spectrometry followed a published protocol (Beynon et al., 1989). In brief, reduction was carried out by incubating 100 μl of each sample with 2.5 μl of 200 mM TCEP at 37°C for 1 h, followed by alkylation with 20 μl of 200 mM iodoacetamide at room temperature in the dark. Excess iodoacetamide was quenched by incubation of the sample with 20 μl 200 mM DTT at room temperature. The samples were diluted by adding 700 μl of 50 mM ammonium bicarbonate, after which tryptic digestion was carried out at 37°C overnight. Prior to liquid chromatography/mass spectrometry (LC/MS) analysis, all samples were dried down and resuspended in 0.1% formic acid in water.

All samples were analyzed on an Orbitrap Exploris 480 mass spectrophotometer equipped with an EASYnLC 1200 UPLC system and an in-house developed nano spray ionization source. Samples (5 μl at various concentrations) were loaded from the autosampler onto a 100 μm ID Integrafrit trap packed with Reprosil-Pur C18-AQ 120 Å 5 μm material to a bed length of 2.5 cm with a volume of 18 μl at a flow rate of 2.5 μl/min. After loading and desalting with 0.1% formic acid in water, the trap was brought in-line with a pulled fused-silica capillary tip (75-μm i. d.) packed with 35 cm of Reprosil-Pur C18-AQ 120 Å 5 μm. Peptides were separated using a linear gradient, from 6–45% solvent B (LCMS grade 0.1% formic acid, 80% acetonitrile in water) in 60 min at a flow rate of 300 nL/min. Peptides were detected using a targeted Parallel Reaction Monitoring (PRM) method. After the survey scan, targeted MS/MS was performed based on the inclusion list of 23 precursors (m/z, charge state) generated by Skyline (Pino et al., 2020). Precursors were isolated in the quadrupole with an isolation width of 2 m/z. Higher-energy collisional dissociation (HCD) fragmentation was applied with a normalized collision energy of 30% and resulting fragments were detected in the Orbitrap mass analyzer at 15 k resolution (at 200 m/z) with a 300% ion count (AGC) target and a maximum injection time of 22 ms. The loop count was set to 'All', to generate 23 fragment ion spectra per MS1 scan.

Data processing and analysis were performed using Skyline (Pino et al., 2020). The raw data were imported and R. ITFGGPSDSTGSNQNGER.S [15, 32], the peptide sequence, was selected for analysis due to its high abundance. The peak area under the intensity vs. retention time curve of the selected sequence was calculated by the Skyline software and correlated to the N protein standards' concentration as the calibration. Then, the peak areas of the unprocessed and processed N protein samples were used to estimate the specimen concentration via the calibration.

3 RESULTS AND DISCUSSION

3.1 Osmosis Driven by the Polymer Solutions

To concentrate the urinary biomarkers, we have designed and fabricated devices that employ osmosis to remove water molecules from the specimens, illustrated in **Scheme 2**. The beaker contains an aqueous polymer solution and a dialysis

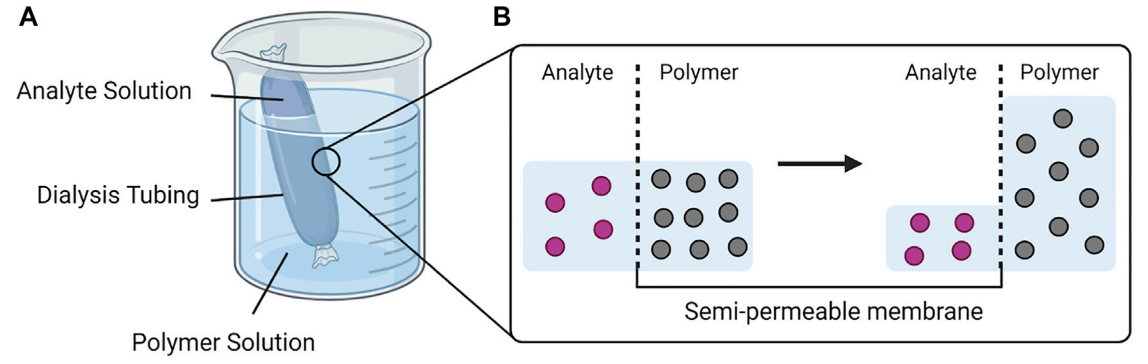

SCHEME 2 | The process of osmosis applied in the urine specimen processor. **(A)** The analyte solution in a sealed dialysis tubing is immersed in a highly concentrated polymer solution. **(B)** The osmotic pressure difference drives the water molecules from the analyte solution across the semipermeable membrane to the polymer solution until equilibrium is reached. (Created with BioRender).

bag with the specimen inside (e.g., urine). The osmosis occurs when the dialysis bag is placed in the polymer solution due to the osmotic pressure generated by the polymer solution. The membrane MWCO is small enough to retain the analyte while allowing the transport of water and other smaller molecules. The rate of water transport across the semipermeable membrane with regard to osmotic pressure (π) can be described by the following equation (Lucke et al., 1931):

$$\frac{dV}{dt} = k \times S \times (\pi - P_{ex}) \tag{1}$$

where dV/dt is the rate of change of volume, k is the membrane permeability, S is the surface area of the membrane and P_{ex} is the surrounding pressure. The osmotic pressure (π) produced by non-ideal polymer solutions can be described using the Flory-Huggins equation (Flory, 1942; Huggins, 1942):

$$\pi = c \times R \times T\left(M^{-1} + A_2c + A_3c^2 + \cdots\right) \tag{2}$$

where c is the mass concentration of the polymer solution, R is the gas constant, T is the system temperature, M is the polymer molecular weight, and A_2 and A_3 are osmotic virial constants that describe the polymer-solvent interaction. The van't Hoff theory is commonly applied to describe principle of osmosis in "ideal" solutions by assuming the solute and solvent particles are of similar sizes and occupy similar volumes (Kendall, 1921). However, the equation cannot be used here because the polymer (solute) is much larger in size and occupies more volume than the water molecules (solvent). Therefore, the Flory-Huggins equation is applied here to reflect the contribution of non-ideality to the solution osmotic pressure due to the difference in solute and solvent molecular sizes.

The water removal *via* osmosis was demonstrated using various water soluble polymers (**Table 1**), including poly (ethylene glycol)/PEG, poly (acrylic acid)/PAAc, polyethylenimine/PEI, poly (sodium 4-styrenesulfonate)/PSS, and pectin. The evaluation utilized the apparatus illustrated in **Scheme 2**. The rate of water removed from the dialysis bag varied from ca. 5–15 ml/h, and was highest for PEG 1500, followed by PAA, PEI, PEG 4000, PEG 35000, PSS and Pectin (**Figure 1A**). Because lower molecular weight leads to higher water solubility, PEG 1500 was prepared at a higher mass concentration (2 mg/ml), resulting in a higher osmotic pressure (**Eq. 2**) across the dialysis membrane to drive 15.2 ± 0.1 ml/h water removal. The removal rates were 10.5 ± 0.1 and 8.6 ± 0.2 ml/h for PEG 4000 and PEG 35000 respectively. The stronger polymer-water interaction via charge and the low molecular weight, 5.1 kDa, allowed the PAA solution to be prepared at a higher mass concentration, 1 g/ml, resulting in 15.2 ± 0.1 ml/h of water removed. The removal rates were 10.9 ± 0.3 and 8.1 ± 0.3 ml/h for PEI and PSS, respectively. The slower water removal associated with PEI and PSS is likely caused by lower osmotic pressure, which is a function of mass concentration (**Eq. 2**). While PEI and PSS are both charged polymers, higher molecular weights (25 kDa for PEI and 1,000 kDa for PSS) limit the solubilities, which lead to lower osmotic pressures. Pectin is not charged and likely has high molecular weight given the low maximum mass concentration, with 4.7 ± 0.3 ml/h water removed.

According to the Flory-Huggins equation (**Eq. 2**), the osmotic pressure is a function of polymer molecular weight. Therefore, we further evaluate the osmosis using polymer solutions prepared by PEG with different molecular weights. All polymer solutions had the same mass concentration, 0.8 g/ml. The results are summarized in **Figure 1B**. As the molecular weight of PEG increases from 1.5 to 35 kDa, the rate of water removal from the dialysis tubing decreased from 14.8 ± 0.4 to 8.6 ± 0.6 ml/h. The observed phenomenon aligns with the inverse relationship between polymer molecular weight and osmotic pressure (**Eq. 2**). Higher polymer molecular weight results in lower osmotic pressure, which slows down the change in water volume over time in the dialysis tubing (**Eq. 1**).

We also evaluated the impact of polymer solution mass concentration for osmosis. According to the Flory-Huggins equation (**Eq. 2**), higher mass concentration leads to stronger osmotic pressure. PEG 1500 solutions at concentrations of 0.125, 0.25, 0.5, 1, and 2 g/ml were prepared for the evaluation. The results are summarized in **Figure 1C**. As the polymer solution concentration increased from 0.125 to 2 g/ml, the rate of water removal from the dialysis tubing increased from 3.3 ± 1.4 to 14.6 ± 1.4 ml/h. The increase in polymer mass concentration results in a proportional increase of osmotic

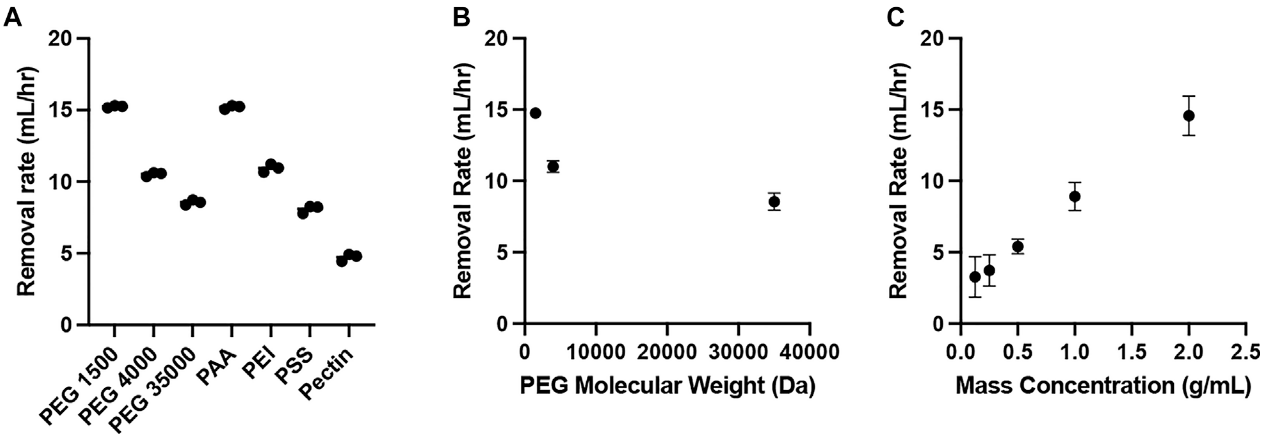

FIGURE 1 | Water removal rate (*n* = 3). **(A)** Various polymers, including PEG 1500, PEG 4000, PEG 35000, PAA, PEI, PSS, and Pectin; **(B)** Polymer solutions (0.8 g/ml) using PEG with 1500, 4000 and 35000 Da molecular weights; **(C)** Polymer solutions using PEG 1500 with mass concentrations of 0.125, 0.25, 0.5, 1.0 and 2.0 g/ml.

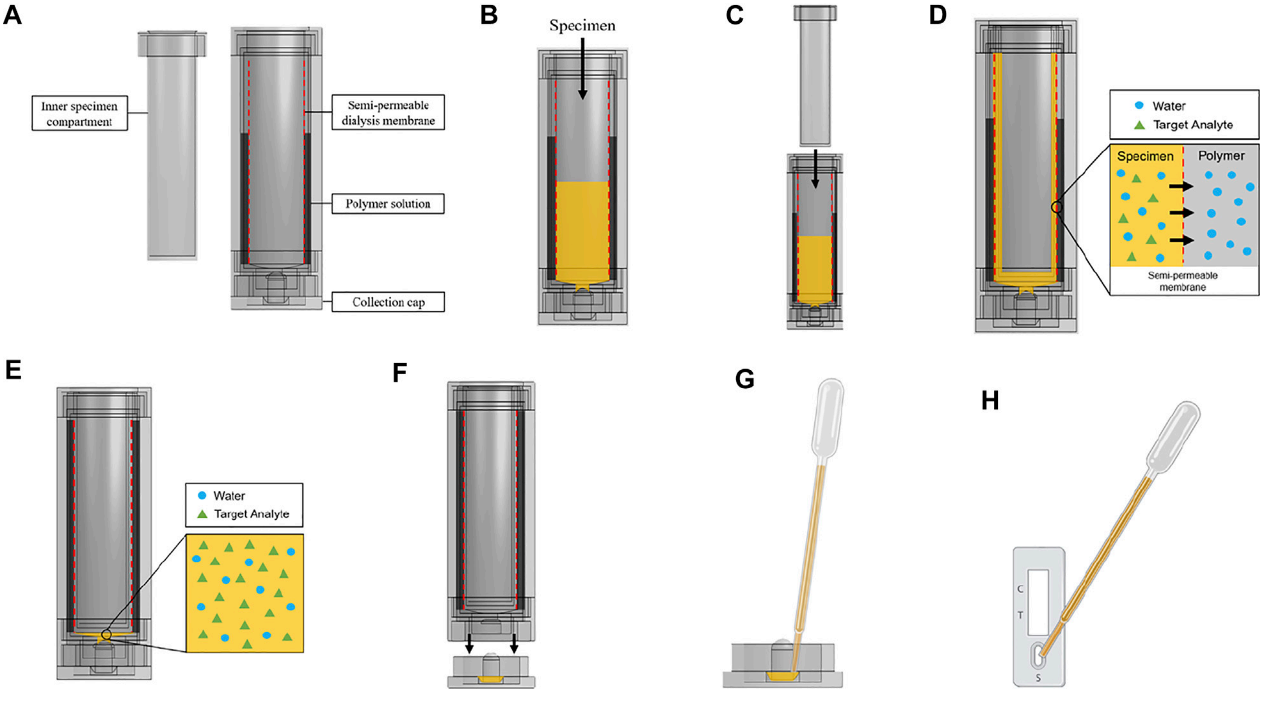

SCHEME 3 | Osmotic specimen processing device design and workflow. **(A)** Device components. **(B)** Load sample into urine compartment. **(C)** Insert inner component of urine compartment to create thin specimen layer against dialysis membrane. **(D)** Water from the analyte solution is drawn out by the polymer solution through the process of osmosis. The target analyte is retained by a semipermeable membrane. **(E)** The processed specimen is collected at the bottom of the urine compartment with a specific volume cutoff. **(F)** The specimen flows from the urine compartment to the collection cap when the collection cap is unscrewed. **(G)** The processed specimen is pipetted from the collection cap. **(H)** The processed specimen is deposited onto the lateral flow test. (Created with OnShape and BioRender).

pressure, increasing the rate of water transport across the membrane (**Eqs 1** and **2**).

3.2 Osmotic Processor Design Specifications and Workflow

Based on our evaluation (**Figures 1A–C**), the Flory-Huggins equation (**Eq. 2**), and reagent availability, PEG was chosen for the osmotic processor. Assembled components of the specimen processor are shown in **Scheme 3A**. The workflow starts from adding the specimen to the device (**Scheme 3B**). Then, the inner component is insert to the urine compartment to create a thin specimen layer (**Scheme 3C**). To maximize membrane surface area (**Eq. 1**), the interface between the specimen and the polymer solution, the urine specimen compartment is designed to create a thin cylindrical layer that presses against the semipermeable

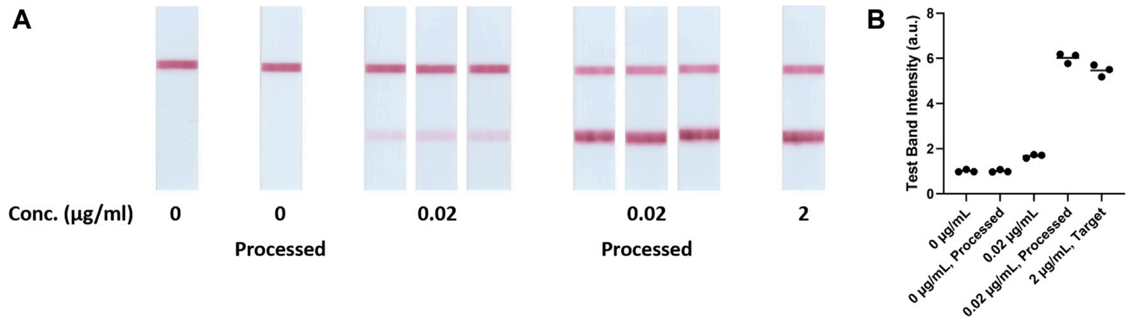

FIGURE 2 | (A) 0 μg/mL, 0 μg/mL processed, 0.02 μg/mL, 0.02 μg/mL processed and 2 μg/mL target hCG samples on AimStep hCG Pregnancy Lateral Flow Cassette (*n* = 3). **(B)** Test band intensities of blank, unprocessed, target and processed hCG LFA tests (*n* = 3).

membrane in contact with the surrounding polymer solution. The 3.5 kDa MWCO, 35 mm dry inner diameter SnakeSkin dialysis tubing was selected to effectively retain the targeted analytes such as hCG (~36 kDa) and the SARS-CoV-2 N protein (~114 kDa). The polymer solution creates a pressure difference across the membrane, driving water transport from the urine compartment to the polymer container (**Scheme 3D**). To prevent the over-concentration and sample dry-out, a small collection cup (**Scheme 3E**) that has no contact with the membrane was designed at the bottom of the specimen compartment. Therefore, the final volume of the concentrated specimen is fixed at 100 μl. To collect the processed sample, the collection cup can be detached from the bottom of the device (**Scheme 3F**), and the sample can be deposited onto the lateral assay by pipetting (**Schemes 3G,H**).

3.3 Concentrating Human Chorionic Gonadotropin Hormone to Improve Lateral Flow Assay Detection Limit

To demonstrate the improved LFA detection limit, hCG hormone and AimStep® Pregnancy (a LFA) were used as a model system. The qualitative results were recorded by capturing the images of the assays (**Figure 2A**), which were analyzed by quantitating the test line intensities as the assay signals (**Figure 2B**). In this evaluation, assays with 0, 0.02, and 2 μg/ml hCG solutions were used as references. The device was utilized to process a 10 ml solution with 0 and 0.02 μg/ml hCG. After 45 min, the resulting 100 μl concentrated specimens were assayed using AimStep® Pregnancy. Assays with both 0 μg/ml and processed 0 μg/ml hCG solutions resulted in only a visible control line, which were correctly determined as negatives. Solutions with 0.02 and 2 μg/ml hCG resulted in both visible control and test lines, which were classified as positives. The 0.02 μg/ml hCG solutions led to faint test lines, and the test line intensities of the assays with 2 μg/ml hCG specimens were significantly higher (**Figure 2A**). After the osmotic processing, the 0.02 μg/ml hCG specimens resulted in much stronger test line intensities, which were similar to the 2 μg/ml hCG assays. Assay signals, generated via ImageJ analysis (**Figure 2B**), were 1.01 ± 0.06, 1.68 ± 0.08, and 5.46 ± 0.27 for specimens with 0, 0.02, and 2 μg/ml hCG respectively. After the osmosis, the assay signals of the 0 μg/ml hCG controls was 1.01 ± 0.06. The assay signals for the processed 0.02 μg/ml specimens increased to 6.02 ± 0.23, which were almost the same as the assays with 2 μg/ml hCG, indicating a ca. 100-fold concentration.

3.4 Concentrating SARS-CoV-2 Nucleocapsid Protein to Improve Lateral Flow Assay Detection Limit

To further demonstrate the device versatility for improving LFA detection limit, SARS-CoV-2 nucleocapsid (N) protein and the

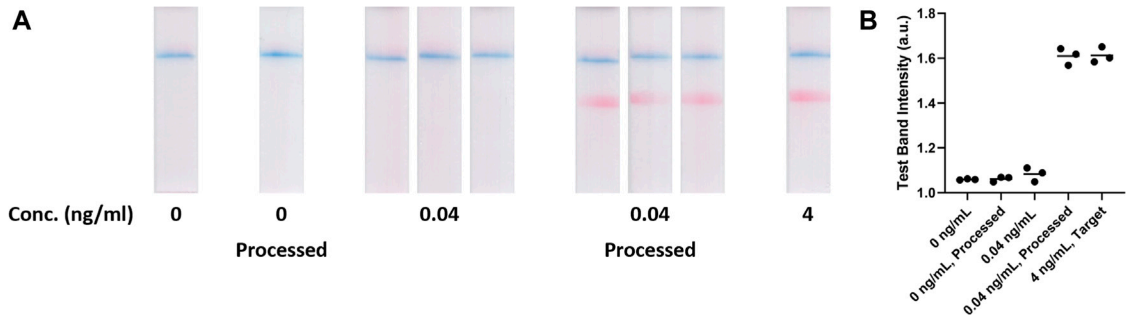

FIGURE 3 | (A) 0 ng/mL, 0 ng/mL processed, 0.04 ng/mL, 0.04 ng/mL processed and 4 ng/mL target N protein samples on Quidel QuickVue SARS-CoV-2 Lateral Flow Assays (*n* = 3). **(B)** Test band intensities of blank, unprocessed, target and processed SARS-CoV-2 LFA tests (*n* = 3).

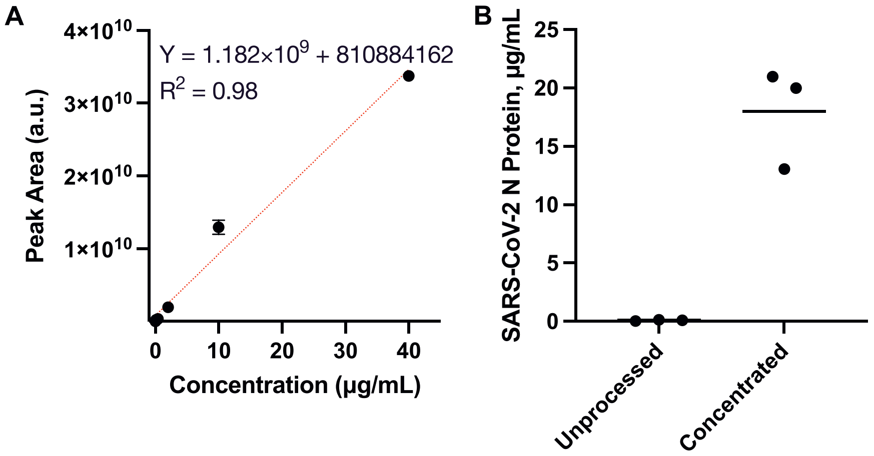

FIGURE 4 | Mass spectrometry analysis for quantitating SARS-CoV-2 N protein concentration by measuring the area under the ionization intensity vs. retention time peaks of the peptide sequence R.ITFGGPSDSTGSNQNGER.S [15, 32]. **(A)** Calibration using standards, 0, 0.08, 0.4, 2, 10 and 40 μg/ml SARS-CoV-2 N protein; **(B)** Specimens' SARS-CoV-2 N protein concentrations before and after the osmosis. The solution average concentration was 0.09 ± 0.06 μg/ml prior to the process. Then, the concentration increased to 18.0 ± 4.3 μg/ml N protein, nearly 200-fold, after the enrichment.

TABLE 2 | Analyte enrichment by various concentration techniques.

Method	Sample type	Biomarker	Enrichment fold (ca.)
Osmotic Processor	Ammonium bicarbonate buffer	Human chorionic gonadotropin (hCG); SARS-CoV-2 N protein	100
Centrifugal Filtration (Corstjens et al., 2015)	Urine	Circulating cathodic antigen	100
Dialysis (Tang et al., 2016)	Water	Human Immunodeficiency Virus nucleic acid (HIV NA); myoglobin (MYO)	HIV NA: 4; MYO: 10
Electrophoresis (Wu et al., 2014)	Saline Sodium Citrate	DNA of H5 subtype of avian influenza virus	400
Aqueous two-phase system (Chiu et al., 2015)	PBS, FBS, synthetic urine	Transferrin	100
Isotachophoresis (Moghadam et al., 2015)	TE (*Glycine*, Bis-Tris, pH7.4)	Goat anti-rabbit IgG; Goat anti-mouse IgG	160–400
Test-zone pre-enrichment (Zhang et al., 2020)	human blood serum; PBS	miR-210 mimic; hCG	miR-210 mimic: 10–100; hCG: 10
Immunomagnetic separation (Panferov et al., 2017; Ben Aissa et al., 2021)	PBST; PBS	Potato virus X (PVX); 16S rRNA gene for *Myobacterium* (rGM)	PVX: 6; rGM: 10

QuickVue test (a LFA) were used as a model system. The evaluation was carried out using an approach similar to the aforementioned hCG model system. The qualitative results were recorded by capturing images of the assays (**Figure 3A**), which were analyzed by quantitating the test line intensities as the assay signals (**Figure 3B**). In this evaluation, assays with 0, 0.04, and 4 ng/ml N protein solutions were used as references. **Figure 3A** shows the assays with 0 ng/ml and processed 0 ng/ml N protein resulted in only a visible control line, which were determined as negatives. Specimens with 0.04 ng/ml N protein resulted in only a visible control line but specimens with 4 ng/ml N protein resulted in both visible control and test lines. The results indicated that the specimens with 0.04 ng/ml N protein were below the assay LOD. After the osmotic processing, the 0.04 ng/ml N protein specimens resulted in much stronger test lines, which were similar to the 4 ng/ml N protein assays. Assay signals, generated *via* ImageJ analysis (**Figure 3B**), were 1.06 ± 0.01, 1.08 ± 0.03, and 1.61 ± 0.03 for specimens with 0, 0.04, and 4 ng/ml N protein, respectively. After the osmosis, the assay signal for the 0 ng/ml N protein solution was 1.06 ± 0.01. The assay signal for the processed 0.04 ng/ml N protein specimens increased to 1.61 ± 0.04, which was almost the same as the assays with 4 ng/ml N protein, indicating a ca. 100-fold concentration.

Mass spectrometry was utilized to quantitate SARS-CoV-2 N protein concentrations, which were used to estimate the enrichment factor via the osmotic processor. The enrichment factors are the concentration ratios of the processed specimens over the unprocessed solutions. To accommodate the mass spectrometry dynamic range, the evaluation utilized specimens with 4 μg/ml SARS-CoV-2 N protein for the concentration process. Skyline, a software for targeted proteomics data analysis, was utilized to measure the area under the ionization intensity vs. retention time peaks of the peptide sequence R. ITFGGPSDSTGSNQNGER.S [15, 32] for the standards (0, 0.08, 0.4, 2, 10 and 40 μg/ml SARS-CoV-2 N protein) as well as the specimens before and after the concentration process

(**Supplementary Materials**, the peak near 26 min in **Supplementary Figure S1**). Because of the trypsin digestion, the specimens were diluted 10-fold prior to the mass spectrometry. The standards were utilized to generate a calibration (**Figure 4A**), which was used to determine the specimen concentrations. Prior to osmosis, the specimens' average N protein concentration was 0.09 ± 0.06 μg/ml (**Figure 4B**). After the concentration process, the specimens contained 18.0 ± 4.3 μg/ml N protein. The mass spectrometry analysis indicated that the osmotic processor concentrated the specimen nearly 200-fold. The specimen concentrations were lower than the theoretical values, which might be caused by the loss during the sample preparation.

In this study, an osmotic processor was developed to spontaneously concentrate analytes for improving the LOD of existing LFAs. The processor employed solutions with water-soluble polymers to create osmotic pressure difference across the membrane to drive the water transport, removing water from the specimen to concentrate analytes. Several polymers were evaluated and have demonstrated the capability to induce osmosis. However, the rate of water transport varies because of the polymer properties (e.g., molecular weight, charge properties). The systematic evaluations showed that faster water transport can be induced using PEG with lower molecular weights and the polymer solutions with higher mass concentration. According to the Flory-Huggins principle (**Eq. 2**), these PEG solutions resulted in higher osmotic pressures, which drove faster water transport *via* osmosis (**Eq. 1**). Therefore, PEG solutions were incorporated into the osmotic processor. To further increase the water transport rate, the specimen compartment of the processor utilizes an insert that results in a thin layer specimen solution on the membrane to maximize the contact surface area. The osmotic processor was utilized to concentrate analytes for more sensitive biomarker detections via LFAs, using hCG and SARS-CoV-2 N protein as the model analytes. After the osmosis, LFAs showed strong signals for the solutions with low analyte concentration. The analyses for the LFA membranes suggest the analyte concentrations were increased nearly 100-fold for both model analytes. Additional quantitative analyses via mass spectrometry showed the concentration of SARS-CoV-2 N protein increases ca. 200-fold. **Table 2** summarizes various analyte concentration approaches, which were utilized for proteins as well as nucleic acids. These approaches concentrated analytes from few to 400-fold. Compared to the existing approaches, the osmotic processor can achieve similar enrichment and can concentrate analyte spontaneously. The osmotic processor can be utilized in conjunction with LFAs to improve biomarker detection, which can potentially increase the assay sensitivity.

4 CONCLUSION

We have fabricated an osmotic processor that can spontaneously concentrate specimens' analyte to improve biomarker detections via LFA. Using hCG and SARS-CoV-2 N protein as model analytes, the osmotic processor has demonstrated the concentration process qualitatively and quantitatively. Specimens originally with analytes below the LFA LOD became detectable after the osmosis, indicating the osmotic processor concentrated the analyte to above the assay LOD. The quantitative analysis via mass spectrometry suggested ≥ 100-fold analyte concentration via the device. The device can potentially improve biomarker detection by interfacing with urine-based LFAs, a lot of which have problems with low-sensitivity. The analyte concentration via the osmotic processor is very comparable to other existing concentration approaches. The current design requires the transfer of enriched specimen to lateral flow test strips by manual pipetting. For further improvements in the point-of-care diagnostic workflow, the osmotic processor may be modified to seamlessly integrate with existing LFAs, where the concentrated specimen is directly released onto the sample pad of LFAs. Additionally, the device is easy to use, and does not depend on a power source, which can potentially enable many point-of-care tests (e.g., TB screening via urinary LAM) in low-resources settings.

DATA AVAILABILITY STATEMENT

The original contributions presented in the study are included in the article/**Supplementary Material**, further inquiries can be directed to the corresponding author.

AUTHOR CONTRIBUTIONS

S-YC, AW, and RL conducted the experiments and performed data analysis. S-YC led data visualization. JL provided technical insights on discussion and oversaw the study. All authors contributed to writing this manuscript and approved the final version for submission.

FUNDING

The study was supported by the University of Washington Royalty Research Fund (RRF).

ACKNOWLEDGMENTS

We are grateful to P. von Haller at the University of Washington's Proteomics Resource (UWPR95794) for the assistance with mass spectrometry analysis.

SUPPLEMENTARY MATERIAL

The Supplementary Material for this article can be found online at: https://www.frontiersin.org/articles/10.3389/fbioe.2022.884271/full#supplementary-material

REFERENCES

Ben Aissa, A., Araújo, B., Julián, E., Boldrin Zanoni, Mv., and Pividori, M. I. (2021). Immunomagnetic Separation Improves the Detection of Mycobacteria by Paper-Based Lateral and Vertical Flow Immunochromatographic Assays. *Sensors (Basel)* 21. doi:10.3390/s21185992

Beynon, R. J., Bond, J. S., Beynon, R. J., and Bond, J. S. (1989). *Proteolytic Enzymes : A Practical Approach*. Oxford New York, Oxford New York: IRL Press at Oxford University Press.

Bowen, R., Benavides, R., Colón-Franco, J. M., Katzman, B. M., Muthukumar, A., Sadrzadeh, H., et al. (2019). Best Practices in Mitigating the Risk of Biotin Interference with Laboratory Testing. *Clin. Biochem.* 74, 1–11. doi:10.1016/j.clinbiochem.2019.08.012

Bulterys, M. A., Wagner, B., Redard-Jacot, M., Suresh, A., Pollock, N. R., Moreau, E., et al. (2019). Point-Of-Care Urine LAM Tests for Tuberculosis Diagnosis: A Status Update. *J. Clin. Med.* 9. doi:10.3390/jcm9010111

Chiu, R. Y. T., Thach, A. V., Wu, C. M., Wu, B. M., and Kamei, D. T. (2015). An Aqueous Two-phase System for the Concentration and Extraction of Proteins from the Interface for Detection Using the Lateral-Flow Immunoassay. *PLoS One* 10, e0142654. doi:10.1371/journal.pone.0142654

Choi, D. H., Lee, S. K., Oh, Y. K., Bae, B. W., Lee, S. D., Kim, S., et al. (2010). A Dual Gold Nanoparticle Conjugate-Based Lateral Flow Assay (LFA) Method for the Analysis of Troponin I. *Biosens. Bioelectron.* 25, 1999–2002. doi:10.1016/j.bios.2010.01.019

Corstjens, P. L., Nyakundi, R. K., De Dood, C. J., Kariuki, T. M., Ochola, E. A., Karanja, D. M., et al. (2015). Improved Sensitivity of the Urine CAA Lateral-Flow Assay for Diagnosing Active Schistosoma Infections by Using Larger Sample Volumes. *Parasites Vectors* 8, 241. doi:10.1186/s13071-015-0857-7

Flory, P. J. (1942). Thermodynamics of High Polymer Solutions. *J. Chem. Phys.* 10, 51–61. doi:10.1063/1.1723621

Fredolini, C., Meani, F., Alex Reeder, K., Rucker, S., Patanarut, A., Botterell, P. J., et al. (2008). Concentration and Preservation of Very Low Abundance Biomarkers in Urine, Such as Human Growth Hormone (hGH), by Cibacron Blue F3G-A Loaded Hydrogel Particles. *Nano Res.* 1, 502–518. doi:10.1007/s12274-008-8054-z

García, J. I., Kelley, H. V., Meléndez, J., De León, R. A. A., Castillo, A., Sidiki, S., et al. (2019). Improved Alere Determine Lipoarabinomannan Antigen Detection Test for the Diagnosis of Human and Bovine Tuberculosis by Manipulating Urine and Milk. *Sci. Rep.* 9, 18012. doi:10.1038/s41598-019-54537-9

Hadland, S. E., and Levy, S. (2016). Objective Testing. *Child Adolesc. Psychiatric Clin. N. Am.* 25, 549–565. doi:10.1016/j.chc.2016.02.005

Harpole, M., Davis, J., and Espina, V. (2016). Current State of the Art for Enhancing Urine Biomarker Discovery. *Expert Rev. Proteomics* 13, 609–626. doi:10.1080/14789450.2016.1190651

Hu, J., Wang, L., Li, F., Han, Y. L., Lin, M., Lu, T. J., et al. (2013). Oligonucleotide-linked Gold Nanoparticle Aggregates for Enhanced Sensitivity in Lateral Flow Assays. *Lab. Chip* 13, 4352–4357. doi:10.1039/c3lc50672j

Huggins, M. L. (1942). Some Properties of Solutions of Long-Chain Compounds. *J. Phys. Chem.* 46, 151–158. doi:10.1021/j150415a018

Ishii, M., Preechakasedkit, P., Yamada, K., Chailapakul, O., Suzuki, K., and Citterio, D. (2018). Wax-Assisted One-step Enzyme-Linked Immunosorbent Assay on Lateral Flow Test Devices. *Anal. Sci.* 34, 51–56. doi:10.2116/analsci.34.51

Kendall, J. (1921). The Application of Ideal Solution Equations To Dilute Aqueous Solutions. *J. Am. Chem. Soc.* 43, 1391–1396. doi:10.1021/ja01440a002

Kim, C., Yoo, Y. K., Han, S. I., Lee, J., Lee, D., Lee, K., et al. (2017). Battery Operated Preconcentration-Assisted Lateral Flow Assay. *Lab. Chip* 17, 2451–2458. doi:10.1039/c7lc00036g

Koczula, K. M., and Gallotta, A. (2016). Lateral Flow Assays. *Essays Biochem.* 60, 111–120. doi:10.1042/ebc20150012

Lucke, B., Hartline, H. K., and Mccutcheon, M. (1931). Further Studies on the Kinetics of Osmosis in Living Cells. *J. Gen. Physiol.* 14, 405–419. doi:10.1085/jgp.14.3.405

McFarlane, H. (1964). A Simple Rapid Method of Concentrating Urine For Protein Electrophoresis. *Clin. Chim. Acta* 9, 376–380. doi:10.1016/0009-8981(64)90029-4

Moghadam, B. Y., Connelly, K. T., and Posner, J. D. (2015). Two Orders of Magnitude Improvement in Detection Limit of Lateral Flow Assays Using Isotachophoresis. *Anal. Chem.* 87, 1009–1017. doi:10.1021/ac504552r

Nelson, P. H. (2017). Osmosis and Thermodynamics Explained by Solute Blocking. *Eur. Biophys. J.* 46, 59–64. doi:10.1007/s00249-016-1137-y

Nimse, S. B., Sonawane, M. D., Song, K.-S., and Kim, T. (2016). Biomarker Detection Technologies and Future Directions. *Analyst* 141, 740–755. doi:10.1039/c5an01790d

Oreskovic, A., Brault, N. D., Panpradist, N., Lai, J. J., and Lutz, B. R. (2019). Analytical Comparison of Methods for Extraction of Short Cell-free DNA from Urine. *J. Mol. Diagnostics* 21, 1067–1078. doi:10.1016/j.jmoldx.2019.07.002

Panferov, V. G., Safenkova, I. V., Varitsev, Y. A., Drenova, N. V., Kornev, K. P., Zherdev, A. V., et al. (2016). Development of the Sensitive Lateral Flow Immunoassay with Silver Enhancement for the Detection of Ralstonia Solanacearum in Potato Tubers. *Talanta* 152, 521–530. doi:10.1016/j.talanta.2016.02.050

Panferov, V. G., Safenkova, I. V., Zherdev, A. V., and Dzantiev, B. B. (2017). Setting up the Cut-Off Level of a Sensitive Barcode Lateral Flow Assay with Magnetic Nanoparticles. *Talanta* 164, 69–76. doi:10.1016/j.talanta.2016.11.025

Parolo, C., De La Escosura-Muñiz, A., and Merkoçi, A. (2013). Enhanced Lateral Flow Immunoassay Using Gold Nanoparticles Loaded with Enzymes. *Biosens. Bioelectron.* 40, 412–416. doi:10.1016/j.bios.2012.06.049

Peter, J., Theron, G., Chanda, D., Clowes, P., Rachow, A., Lesosky, M., et al. (2015). Test Characteristics and Potential Impact of the Urine LAM Lateral Flow Assay in HIV-Infected Outpatients under Investigation for TB and Able to Self-Expectorate Sputum for Diagnostic Testing. *BMC Infect. Dis.* 15, 262. doi:10.1186/s12879-015-0967-z

Pino, L. K., Searle, B. C., Bollinger, J. G., Nunn, B., Maclean, B., and Maccoss, M. J. (2020). The Skyline Ecosystem: Informatics for Quantitative Mass Spectrometry Proteomics. *Mass Spec. Rev.* 39, 229–244. doi:10.1002/mas.21540

Rivas, L., Medina-Sánchez, M., De La Escosura-Muñiz, A., and Merkoçi, A. (2014). Improving Sensitivity of Gold Nanoparticle-Based Lateral Flow Assays by Using Wax-Printed Pillars as Delay Barriers of Microfluidics. *Lab. Chip* 14, 4406–4414. doi:10.1039/c4lc00972j

Schneider, C. A., Rasband, W. S., and Eliceiri, K. W. (2012). NIH Image to ImageJ: 25 Years of Image Analysis. *Nat. Methods* 9, 671–675. doi:10.1038/nmeth.2089

Simerville, J. A., Maxted, W. C., and Pahira, J. J. (2005). Urinalysis: a Comprehensive Review. *Am. Fam. Physician* 71, 1153–1162. Available at: https://www.aafp.org/afp/2005/0315/p1153.html

Tang, R., Yang, H., Choi, J. R., Gong, Y., Hu, J., Feng, S., et al. (2016). Improved Sensitivity of Lateral Flow Assay Using Paper-Based Sample Concentration Technique. *Talanta* 152, 269–276. doi:10.1016/j.talanta.2016.02.017

Tang, R., Yang, H., Gong, Y., Liu, Z., Li, X., Wen, T., et al. (2017). Improved Analytical Sensitivity of Lateral Flow Assay Using Sponge for HBV Nucleic Acid Detection. *Sci. Rep.* 7, 1360. doi:10.1038/s41598-017-01558-x

Taylor, E. N., and Curhan, G. C. (2006). Body Size and 24-hour Urine Composition. *Am. J. Kidney Dis.* 48, 905–915. doi:10.1053/j.ajkd.2006.09.004

Tuuminen, T. (2012). Urine as a Specimen to Diagnose Infections in Twenty-First Century: Focus on Analytical Accuracy. *Front. Immun.* 3, 45. doi:10.3389/fimmu.2012.00045

Wong, R. C., and Tse, H. Y. (2009). *Lateral Flow Immunoassay*. New York, NY: Springer.

World Health Organization (2020). *Global Tuberculosis Report 2020*. Geneva, Switzerland: World Health Organization.

Wu, J.-C., Chen, C.-H., Fu, J.-W., and Yang, H.-C. (2014). Electrophoresis-enhanced Detection of Deoxyribonucleic Acids on a Membrane-Based Lateral Flow Strip Using Avian Influenza H5 Genetic Sequence as the Model. *Sensors* 14, 4399–4415. doi:10.3390/s140304399

Yang, M., Goolia, M., Xu, W., Bittner, H., and Clavijo, A. (2013). Development of a Quick and Simple Detection Methodology for Foot-And-Mouth Disease Virus Serotypes O, A and Asia 1 Using a Generic RapidAssay Device. *Virol. J.* 10, 125. doi:10.1186/1743-422x-10-125

Zhang, Y., Liu, X., Wang, L., Yang, H., Zhang, X., Zhu, C., et al. (2020). Improvement in Detection Limit for Lateral Flow Assay of Biomacromolecules by Test-Zone Pre-enrichment. *Sci. Rep.* 10, 9604. doi:10.1038/s41598-020-66456-1

Conflict of Interest: The authors declare that the research was conducted in the absence of any commercial or financial relationships that could be construed as a potential conflict of interest.

frontiers | Frontiers in Bioengineering and Biotechnology

ORIGINAL RESEARCH
published: 05 August 2022
doi: 10.3389/fbioe.2022.930800

Flexible Terahertz Metamaterial Biosensor for Ultra-Sensitive Detection of Hepatitis B Viral DNA Based on the Metal-Enhanced Sandwich Assay

Yumin Li[1,2†], Xiaojing Wang[3†], Yu Liu[2], Weidong Jin[2], Huiyan Tian[2], Fengxin Xie[2], Ke Xia[2], Xiuming Zhang[1]*, Weiling Fu[2]* and Yang Zhang[4]*

[1]Medical Laboratory of the Third affiliated Hospital of Shenzhen University, Shenzhen, China, [2]Department of Laboratory Medicine, Southwest Hospital, Third Military Medical University (Army Medical University), Chongqing, China, [3]Department of Laboratory Medicine, Chifeng Municipal Hospital, Chifeng, China, [4]Department of Laboratory Medicine, Chongqing University Cancer Hospital, Chongqing, China

The high sensitivity and specificity of terahertz (THz) biosensing are both promising and challenging in DNA sample detection. This study produced and refined a flexible THz MM biosensor for ultrasensitive detection of HBV in clinical serum samples based on a gold magnetic nanoparticle-mediated rolling circle amplification (GMNPs@RCA) sandwich assay under isothermal conditions. Typically, solid-phase RCA reactions mediated by circular padlock probes (PLPs) are triggered under isothermal conditions in the presence of HBV DNA, resulting in long single-stranded DNA (ssDNA) with high fidelity and specificity. Then, the resultant ssDNA was conjugated with detection probes (DPs) immobilized on gold nanoparticles (DP@AuNPs) to form GMNPs-RCA-AuNPs sandwich complexes. The HBV DNA concentrations were quantified by introducing GMNPs-RCA-AuNPs complexes into the metasurface of a flexible THz metamaterial-based biosensor chip and resulting in a red shift of the resonance peak of the THz metamaterials. This biosensor can lead to highly specific and sensitive detection with one-base mismatch discrimination and a limit of detection (LOD) down to 1.27E + 02 IU/ml of HBV DNA from clinical serum samples. The HBV DNA concentration was linearly correlated with the frequency shift of the THz metamaterials within the range of 1.27E + 02~1.27E + 07 IU/ml, illustrating the applicability and accuracy of our assay in real clinical samples. This strategy constitutes a promising THz sensing method to identify virus DNA. In the future, it is hoped it can assist with pathogen identification and clinical diagnosis.

Keywords: terahertz metamaterials, biosensors, virus DNA, gold magnetic nanoparticles, clinical diagnosis

Edited by:
Yu-Jui Fan,
Taipei Medical University, Taiwan

Reviewed by:
Parikshit Moitra,
University of Maryland, Baltimore, United States
Chan-Shan Yang,
National Taiwan Normal University, Taiwan
Tsung-Rong Kuo,
Taipei Medical University, Taiwan

***Correspondence:**
Xiuming Zhang
zxm0760@163.com
Weiling Fu
fwl@tmmu.edu.cn
Yang Zhang
millen001@163.com

†These authors have contributed equally to this work

Specialty section:
This article was submitted to Biosensors and Biomolecular Electronics, a section of the journal Frontiers in Bioengineering and Biotechnology

Received: *28 April 2022*
Accepted: *23 June 2022*
Published: *05 August 2022*

Citation:
Li Y, Wang X, Liu Y, Jin W, Tian H, Xie F, Xia K, Zhang X, Fu W and Zhang Y (2022) Flexible Terahertz Metamaterial Biosensor for Ultra-Sensitive Detection of Hepatitis B Viral DNA Based on the Metal-Enhanced Sandwich Assay. Front. Bioeng. Biotechnol. 10:930800. doi: 10.3389/fbioe.2022.930800

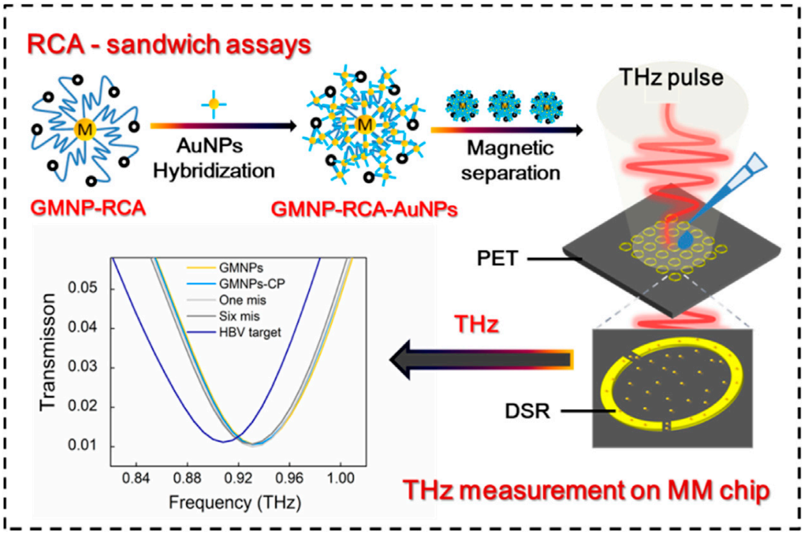

GRAPHICAL ABSTRACT | Li et al. presented a new terahertz (THz) biosensing strategy for serum Hepatitis B virus DNA (HBV DNA) detection in clinical samples based on a flexible MM chip with an ultrathin polyethylene terephthalate (PET) substrate and gold magnetic nanoparticle-mediated rolling circle amplification (GMNPs@RCA) sandwich assay under isothermal conditions. This THz biosensing strategy demonstrates excellent analytical performance towards serum HBV DNA with high sensitivity, ultralow detection limit, excellent specificity and accuracy, as well as good stability, suggesting a promising THz sensing platform for virus DNA in clinical diagnosis, pathogen detection, and environmental monitoring in the future.

INTRODUCTION

Virus infection remains a worldwide public health problem. Virus infections are diagnosed using traditional immunoassays to detect certain antigens and antibodies (Amini et al., 2017; Abusalah et al., 2020; Ong et al., 2021; Inoue et al., 2021). Alternatively, nucleic acid tests can be deployed to target a given genomic sequence. Virus nucleic acids are used as key markers of virus infection and replication. In addition, quantification of viral nucleic acids can be utilized in the early diagnosis, treatment, and assessment of how an individual is responding to antiviral therapy (Amini et al., 2017; Hsieh et al., 2022a). There is an urgent need to produce a diagnostic device, such as biosensing for infectious samples detection, which can carry out rapid, sensitive, and accurate detection of viral infection and replication during its early stages (Moitra et al., 2021; Hsieh et al., 2022b; Guo et al., 2022; Dighe et al., 2022; Liang et al., 2022; Moitra et al., 2022).

Terahertz (THz) spectroscopy has proven to have the potential to detect nucleic acids. THz spectroscopy utilizes forms of radiation that are positioned between microwave radiation and infrared radiation in the electromagnetic spectrum. The frequency range of the radiation used here is between 0.1 and 10 THz. Nucleic acids consist of nucleotide linear polymers joined together by phospholipid bonds. Nucleic acids' THz spectrums can be used to determine the molecules' configuration characteristics and their intermolecular collective and lattice vibrations. THz time-domain spectroscopy (TDS) has been readily applied to analyze nucleic acids in a label-free manner, such as in the identification of nucleotide bases (Fischer et al., 2002; Pickwell-MacPherson and Wallace, 2009; Wang et al., 2017), nucleic acid chain molecules (both single and double) (Bolivar et al., 2002), DNA mutations (Tang et al., 2015), transgenic genome (Yang et al., 2018), microcystin aptamer (Zhang et al., 2019), and even in the quantitative detection of DNA in aqueous solution (Arora et al., 2012; Hu et al., 2016; Yang et al., 2017; Zhou R. et al., 2021). However, there is an urgent need for new techniques and materials that are highly sensitive to THz-TDS for use in DNA detection.

Metamaterial (MM)-based THz biosensor chips have recently become a promising protein or DNA detection platform (Geng et al., 2017; Xu et al., 2017; Yang et al., 2018; Zhou R. et al., 2021). THz MM biosensor was designed as a planar array of metal double-split rings (DSRs) with asymmetric structures to obtain a tailored electromagnetic response, which is very sensitive to microenvironment medium change on the surface of the MM (Yang et al., 2018; Zhou J. et al., 2021; Zhou R. et al., 2021). These biosensors overcame the limit in sensitivity with typical THz-TDS systems, which might be attributed to the following factors: Firstly, asymmetric split resonators were designed to produce an exceptionally sharp resonance and achieve a great frequency shift of the THz transmission spectra. Secondly, low-permittivity materials were used to fabricate the substrates of the THz MM biosensor in an effort to minimize induced capacitance and transmission loss. Polyethylene terephthalate (PET) is an ideal flexible MM and a popular electro-optical substrate for various THz biosensor applications due to its low dispersion and loss in the THz range, high optical transparency, good surface smoothness, and simple fabrication of different thicknesses (Chen and Pickwell-MacPherson, 2019; Xia et al., 2019; Hu, et al., 2019; Zheng, et al., 2020; Wang, et al., 2021).

TABLE 1 | Sequences of oligonucleotides used in the study.

Oligonucleotides	Sequences (5′-3′)
Padlock probe (PLP)	5′-Phosphate-TGCAGTTTCCGTCCGTAGTAGAATGAAGATAGC**GCATCGTAGGAGGACGGAGG**ATGATGGGTATGGGAATACAGG-3′
HBV target sequence	5′-CTACGGACGGAAACTGCACCTGTATTCCCATACCCATCAT-3′
Single-base mismatch	5′-CTACGGACGGAAACTGCA*A*CTGTATTCCCATACCCATCAT-3′
Six-base mismatch	5′-CTACGGACGGAAACTGC*GAGCCG*ATTCCCATACCCATCAT-3′
Capture probe (CP)	5′-SH-TTTTTTTTTT**CCTCCGTCCTCCTACGATGC**-3′
Detection probe (DP)	5′-CCGTAGTAGAATGAAGATAGCGCATCG-SH-3′

The sequence underlined in the PLP matches the underlined sequence in the HBV target sequence, and the bold sequence in the PLP is complementary to the bold sequence in the capture probe (CP). A non-complementary sequence to the PLP was used as a control sequence, which included single-base mismatched and six-base mismatched sequences (italics).

In addition, in DNA detection, THz-TDS sensitivity can be boosted through the utilization of signal amplification methods, including but not limited to rolling circle amplification (RCA) and polymerase chain reaction (PCR) (Arora et al., 2012; Yang et al., 2017). The target oligonucleotide hybridizes with the circular-shaped RCA template, which is a padlock probe (PLP), and then the long nucleic acid products with high fidelity are generated at a constant temperature (Hu and Zhang, 2010; Tong et al., 2012; Ding et al., 2013). Meanwhile, due to their unique physicochemical properties and large surface area, gold nanoparticles (AuNPs) are increasingly applied to develop RCA assays. AuNPs allow stable immobilization of oligonucleotide probes due to their adhesion to metal surfaces *via* thiol groups. RCA is then performed again following successful hybridization with the probes on the gold slide and the target sequence. Besides, AuNPs are also able to bind to RCA products; the effect of this is to enhance the plasmon resonance of incident light excitation whilst also elevating the transduction of small refractive index changes on the surface. Based on these considerations, the RCA combined with the AuNPs method has been subjected to a lot of attention for its use in the ultrasensitive detection of DNA, including AuNPs-RCA-based surface plasmon resonance (SPR) biosensors and RCA-surface enhanced Raman spectroscopy (SERS) sandwich assays (Shi et al., 2014; Guven et al., 2015).

AuNPs have also been introduced into THz MM biosensors. By integrating the THz plasmonic metasurface and AuNPs with each other, the metasensor's sensitivity can be increased whilst also achieving a large resonance (Ahmadivand et al., 2018). However, when using RCA in combination with THz spectroscopy, the RCA products and complex matrix components (buffer) must be separated to minimize the background signal before THz measurements are taken (Yang et al., 2017). The use of gold magnetic nanoparticles (GMNPs) possesses not only the advantage of superparamagnetism to enable the isolation or extraction of target nucleic acids (Guven et al., 2015), but also the outstanding properties of AuNPs to enhance the capturing of targets in the surrounding medium of the THz MM and improve the sensitivity of the metasurface.

This research involved the fabrication of a THz flexible MM biosensor for the highly sensitive, highly selective determination of hepatitis B virus (HBV) DNA in clinical serum samples using a gold magnetic nanoparticle-mediated rolling circle amplification (GMNPs@RCA) sandwich assay under isothermal conditions. The flexible MM chip with a transparent and ultrathin PET substrate was designed as a planar array of metal double-split rings (DSRs) with asymmetric structures. The inherent properties of the excellent specificity of the circular PLP mediated specific target binding and the signal amplification of solid-phase RCA on GMNPs can maintain the high fidelity and sensitivity of this THz MM biosensor. In order to further enhance the detection signal, the AuNPs immobilized with the detection probes (DPs) are used to bind to the RCA products to form the GMNPs-RCA-AuNPs complex, which will achieve triple signal amplification of THz MM sensing. This THz biosensing strategy demonstrates excellent analytical performance in relation to HBV DNA with high sensitivity, ultra-low detection limits, excellent specificity and accuracy, as well as good stability. Together, these features indicate we have developed a promising THz sensing platform to identify viral DNA that can be used to carry out pathogen detection, clinical diagnosis, and environmental monitoring in the future.

EXPERIMENTAL METHODS

Reagents and Materials

E.coli DNA ligase, Exonuclease I, Exonuclease III, dNTPs, DL2000 DNA Maker, and 50 bp DNA Ladder were bought from Takara Biomedical Tech Co., Ltd. (Dalian, China). The Qlysisi-V Kit was bought from Sangon Biotech Co., Ltd. (Shanghai, China). The Phi 29 DNA polymerase was obtained from Thermo Scientific (United States). Gold magnetic nanoparticles (GMNPs) with a diameter of 100 nm and gold nanoparticles (AuNPs) with a diameter of 40 nm were from XFNANO Materials Tech Co., Ltd. (Nanjing, China). Only analytical reagent grade chemicals are used in this study. Finally, a Milli-Q water purification system was used to prepare high-purity deionized water (Millipore Co., Bedford, United States).

Oligonucleotides

All of the oligonucleotides used in this research were synthesized and purified by Takara Biotechnology Co., Ltd. (Dalian, China) through high-performance liquid chromatography (HPLC). The related sequences are listed in **Table 1**. The details of the HBV target sequence selection and its complementary padlock probe

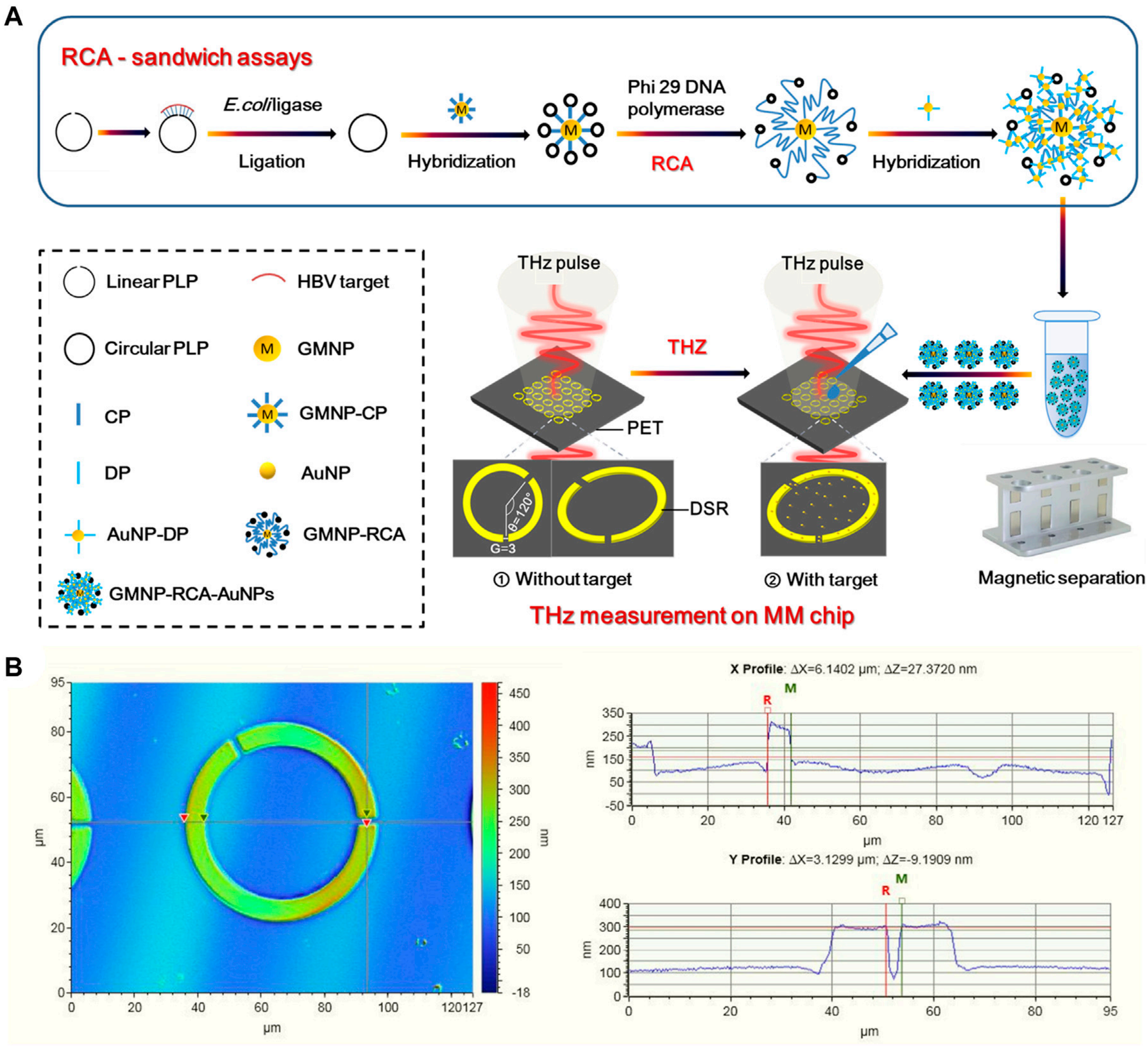

FIGURE 1 | THz biosensing strategy for HBV DNA detection. **(A)** Schematic description of the THz MM biosensor chip for HBV DNA detection based on the GMNPs-RCA-AuNPs sandwich assay. **(B)** Characterization of DSR cell in a square lattice with dimensions of width and (G).

(PLP) design can be referred to in our previous report (Yao et al., 2013). PLP's 5′ end was phosphorylated to achieve ligation. The 5′ end of the capture probe (CP) was altered by the addition of an SH group onto the GMNPs for immobilization. The 3′ end of the detection probe (DP) was also altered by the addition of an SH group onto the AuNPs for immobilization.

Gold Magnetic Nanoparticle-Rolling Circle Amplification-AuNPs Sandwich Assay Designs

The CP-coated gold magnetic nanoparticles (GMNPs-CP) were prepared. The 1 ml of GMNPs (0.05 mg/ml) was immobilized with 50 μl of 1% SDS and one OD CP by incubating for 20 min at room temperature to form an Au-S covalent bond. Then, 25 μl of 2 M NaCl was incorporated into the above mixture for 10 s in Ultrasonic. The mixture was then incubated at room temperature for 20 min. Subsequently, 25 μl of 2 M NaCl and 0.25 μl of 1% SDS were added to the above mixture for 10 s in ultrasonic, and the mixture was incubated for 20 min at room temperature. After repeating this process 20 times, the final solutions containing 0.9~1.0 M NaCl and 0.01% SDS were incubated overnight at room temperature. Afterwards, the mixture was spun in a centrifuge to remove excess CPs. Finally, the GMNPs-CP were collected and resuspended in 0.01% SDS solutions.

The schematic illustration of the stepwise assay design process of the solid-phase RCA reaction on GMNPs was shown in **Figure 1A**. At the first step to prepare the circular PLP, 17 μl of solutions containing 600 nM HBV target sequence, 100 nm linear PLP, and *E. coli* ligase buffer (30 mM Tris-HCl (pH 8.0), 4 mM $MgCl_2$, 10 mM $(NH_4)_2SO_4$, 1.2 mM EDTA, and 100 μM NAD) were denatured by heating them to 95°C for 5 min before cooling them to 4°C. Next, 10 U of *E. coli* ligase and 0.005% BSA were added to the mixture, which was then incubated at 16°C for

60 min. Subsequently, 10 U of each Exonuclease I and 200 U of Exonuclease III were incorporated into the ligation mixture at 37°C for 30 min. The purpose of this step was to remove any unligated PLPs or excess linear oligonucleotides in 40 µl of the reaction mixture [67 mM glycine-KOH (pH 9.5), 6.7 mM $MgCl_2$, and 1 mM dithiothreitol (DTT)]. After holding at 95°C for 5 min, the reaction was terminated. After ligation and enzyme digestion reactions, 2 µl of GMNPs-CP and 20 µl of ligation and exonuclease products (circular PLPs) were introduced to microcentrifuge tubes at 37°C for 30 min to perform the first stage of hybridization between CP and circular PLPs. Once the hybridization step was completed, the GMNPs were washed with PBS buffer twice to detach any unhybridized oligonucleotides from the GMNPs' surface. Next, 10 U of Phi 29 DNA polymerase and 2 µl of 100 µM dNTPs were introduced into the hybridization mixture at 40°C for 60 min to perform solid-phase RCA in 30 µl of the reaction mixture [33 mM of Tris-acetate (pH 7.9), 10 mM of Mg-acetate, 66 mM of K-acetate, 0.1% Tween 20, and 1 mM of DTT] (Yao et al., 2013). After the RCA step, PBS buffer was used to rinse the GMNPs with immobilized RCA products (GMNPs-RCA) twice.

AuNPs and GMNPs were used for the same purpose to prepare for probes coated with nanoparticles. Therefore, the same protocol was applied for AuNPs to prepare for DP-coated AuNPs (DP-AuNPs). At the second hybridization step, the GMNPs-RCA and DP-AuNPs were mixed in 50 µl of the reaction mixture (10 mM Tris, 1 mM EDTA, and 50 mM NaCl). After 15 min at 60°C, PBS was used to rinse the hybridization products (GMNPs-RCA-AuNPs complex) twice. They were then resuspended in the same volume of deionized water in preparation for subsequent THz measurements.

Terahertz Metamaterial Chip Design and Fabrication

Figure 1A presents a diagram of a THz MM-based biosensor. To increase detection sensitivity, the designed MM metal split-ring (SR) resonators are composed of double splits with an asymmetric structure fabricated on an ultrathin PET film with a low intrinsic loss. The DSR sensor features strong sensing characteristics relating to the resonance shift loaded with a dielectric material (Geng et al., 2017; Yang et al., 2018). The THz MM chip consists of fundamental circuit elements. Moreover, its sensing mechanism is that the equivalent capacitance of the DSRs is sensitive to the change of environment refractive index. Notably, the equivalent capacitance changes when the sample on the DSRs-MM structure is altered; this then prompts the resonant frequency shift, which is an indicator of the sample's presence. The period of DSR has a cell size of 90 $\mu m^2 \times 90\ \mu m^2$. As a DSR resonator, the central angle formed by the two radius crossing the center of two gaps was 120° (**Figure 1A**) and the gap (G) was 3 µm (**Figure 1B**), the width of the split ring was 6 µm (**Figure 1B**), and the inner radius and outer radius were 24 and 30 µm (**Supplementary Figure S1**), respectively. A 200-nm-thickness of gold was deposited on a PET sheet with thickness of 25 microns by radio frequency magnetron sputtering method. The main fabrication processes included lithography to form DSRs patterns, Au deposition, and lift-off. An image of the THz MM chip is shown in the supplementary information (**Supplementary Figure S2**).

Extraction of Hepatitis B Virus DNA

The specimens were gathered from an HBV infected patient in Chifeng Municipal Hospital (Chifeng, China), which initially confirmed that the patient did not have the viruses that cause hepatitis A, C, D, E or human immunodeficiency virus (HIV) infections. The serum sample with HBV DNA concentration of 1.27E + 7 IU/ml was diluted to a concentration at 1.27E + 2 IU/ml with the negative serum, and then a series of samples with six equally spaced concentrations were provided for the sensitivity assay. HBV DNA was extracted from 200 µl of serum samples by following the procedure set out by the manufacturer, Qlysisi-V Kit, from Sangon Biotech Co., Ltd. (Shanghai, China). The aforementioned RCA protocol was used to detect HBV DNA extractives.

Terahertz Spectroscopy Measurement

In the present study, THz spectroscopic measurements were carried out using a commercial THz-TDS system set to transmission mode (TAS7500SP, Advantest). The measured frequency range was from 0.1 to 2 THz with a frequency resolution of 7.6 GHz. The transmission measurements were carried out using linearly polarized THz waves at normal incidence, with the electric field positioned parallel to the gap. The samples were measured in a dry nitrogen atmosphere at 25°C. A blank PET sheet identical to the array substrate was employed to derive the THz reference pulse. The THz MM chip was used as the THz detection pulse, both with and without the target (**Figure 1A**). Once the THz measurements were taken, a Fourier transformation was applied to obtain the frequency domain data from the time-domain. A frequency shift was calculated by $\Delta f = f_{target} - f_{\text{without } target}$, where f_{target} represents the resonance peak frequency of the samples, and $f_{\text{without } target}$ symbolizes the resonance peak frequency of the bare THz metamaterial chip without samples.

RESULTS AND DISCUSSION

Principle of Terahertz Biosensing Strategy for Hepatitis B Virus DNA Detection

Three steps were demonstrated in the THz biosensing strategy (**Figure 1A**). Firstly, the solid-phase RCA reaction on GMNPs was performed to realize the first detection signal amplification of the target sequence, and then the AuNPs immobilized with the DPs were used to bind to the RCA products to form the GMNPs-RCA-AuNPs complex, which further realizes the second detection signal amplification of RCA products. Secondly, the THz MM chip with a transparent and ultrathin PET substrate was designed as a planar array of gold DSRs with asymmetric structures. This chip can sense significant shifts in the resonance frequency caused by changes in the metasurface's dielectric environment. Thirdly, by introducing the GMNPs-

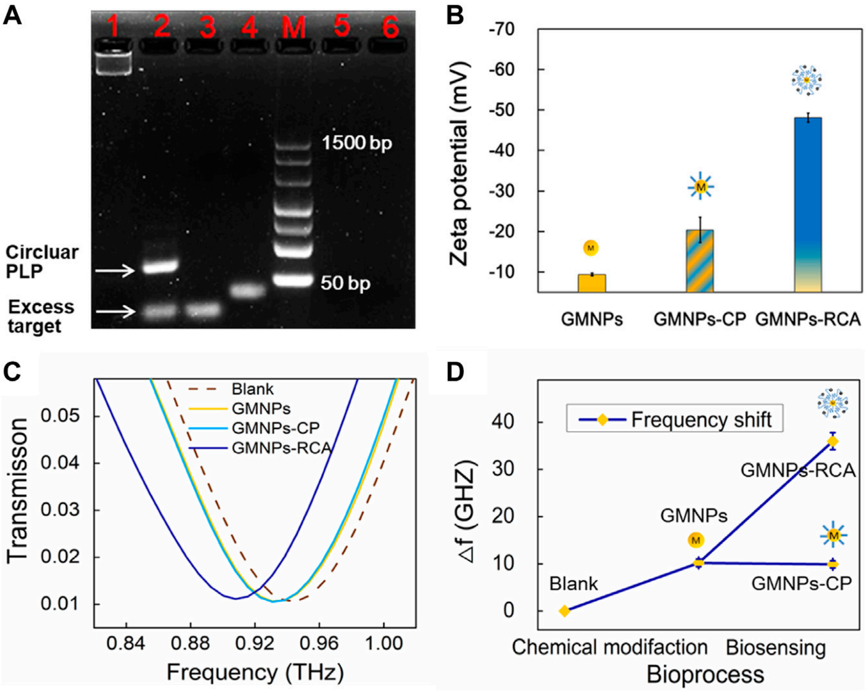

FIGURE 2 | GMNPs-RCA assay for HBV target sequence. **(A)** Electrophoretic identification of the ligation reaction mixture and RCA products. Lanes 1, 2, 3, 4, 5, and 6 represent the RCA products, ligation products (circular PLP), target, linear PLP, single-base mismatched sequences, and six-base mismatched sequences, respectively. **(B)** Zeta potential of GMNPs, GMNPs-CP, and GMNPs-RCA. Error bars indicate the SD (*n* = 3). **(C)** THz measurements of the bare THz MM chip (Blank), GMNPs, GMNPs-CP, and GMNPs-RCA. **(D)** The corresponding THz frequency shifts (*Δf*) of **Figure 2C**. Error bars indicate the SD (*n* = 3). $\Delta f = f_{target} – f_{\text{without target}}$ of which *f* represents the resonance peak frequency.

RCA-AuNPs complex to the THz MM chip, the target DNA was detected by THz measurements with high sensitivity and accuracy, which will realize the third detection signal amplification. Therefore, this strategy will achieve triple signal amplification of THz MM sensing.

Feasibility of Terahertz Metamaterial Biosensing Based on Gold Magnetic Nanoparticle-Mediated Rolling Circle Amplification

3% agarose gel electrophoresis was used to assess the RCA reaction performance of Ligation and RCA products. Theoretically, when the linear PLP is hybridized with a mismatched strand, neither a specific reaction of circularization nor a series of amplification reactions are expected to occur in the follow-up process. As shown in **Figure 2A**, the PLPs could not hybridize with the single-base and six-base mismatched sequences. Additionally, as the subsequent exonuclease treatment removed any non-circularized PLPs, no amplification template remained to conduct RCA through agarose gel electrophoresis analysis. The circular PLP migrated at a slower rate than the linear PLP and the target sequence. The RCA products could not enter the gels because they were too large. Furthermore, zeta potential was used to validate the RCA reaction that occurred on the GMNP surface. This validation method was selected due to the negative charge on the ssDNA; specifically, the conjugation of GMNPs with ssDNA should give rise to negative charged conjugates that will render the zeta potential negative. As shown in **Figure 2B**, there was an observable change in the non-modified GMNPs' value (−9.37 ± 0.37 mV) for the GMNPs-CP (−20.40 ± 3.15 mV). This shift indicates that the CPs were appropriately connected with the GMNPs. Following amplification, a marked shift to −48.13 ± 1.08 mV (**Figure 2B**) was recorded. This indicates that the GMNPs were covered with amplified DNA that had a greater negative charge.

The DSRs MM chips were used to detect different GMNPs by THz spectroscopy measurements. It should be noted that the asymmetric structure of DSRs had two dips. The low-frequency resonance peak (dip 1) and high-frequency resonance peak (dip 2) are at the sites of 0.259 and 0.946 THz (**Supplementary Figure S3**). The different GMNP suspensions were evaporated at 42°C in an oven. This ensured the DNA was not denatured and could later be used for THz spectroscopy measurements. **Figure 2C** shows the measured transmission spectra of dip 2 with the bare THz MM chip (blank), GMNPs, GMNPs-CP, and GMNPs-RCA (HBV target). The difference in the frequency of transmission spectra between GMNPs and GMNPs-CP was negligible, whereas the readily apparent difference between GMNPs and GMNPs-RCA was recorded due to the amplified DNA products on the GMNPs' surfaces. The frequency shift was 25.8 GHz before and after the RCA procedure (**Figure 2D**). The results demonstrated that the gold magnetic nanoparticle-mediated RCA products

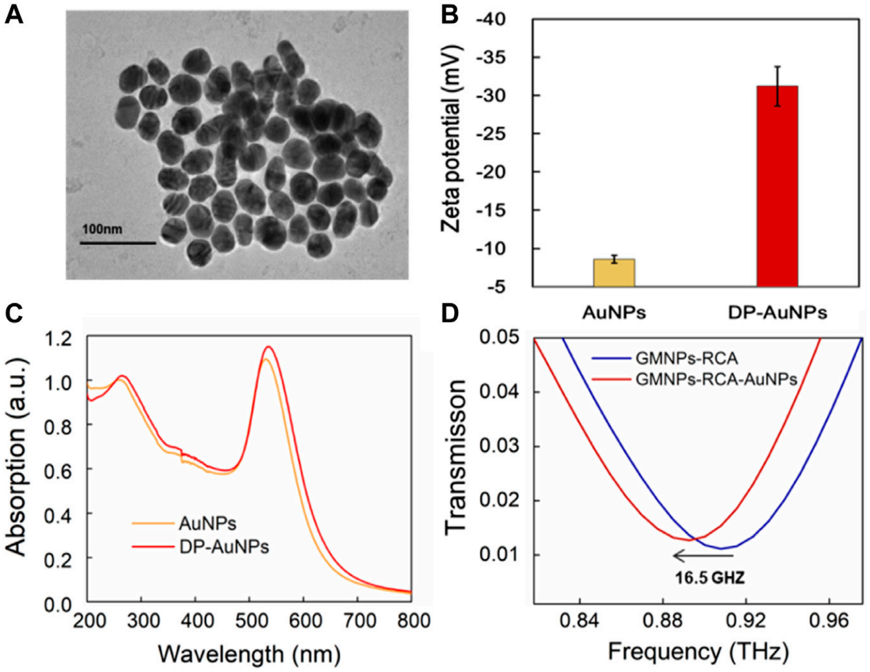

FIGURE 3 | THz measurement for the GMNPs-RCA-AuNPs complex. **(A)** The TEM images of the AuNPs. **(B)** The zeta potential of AuNPs and DP-AuNPs. Error bars indicate the SD (*n* = 3). **(C)** The UV-Visible absorbance spectra of the AuNPs (Yellow) and the DP-AuNPs (Red). **(D)** The frequency shift of THz transmission spectra for GMNPs-RCA-AuNPs compared to GMNPs-RCA.

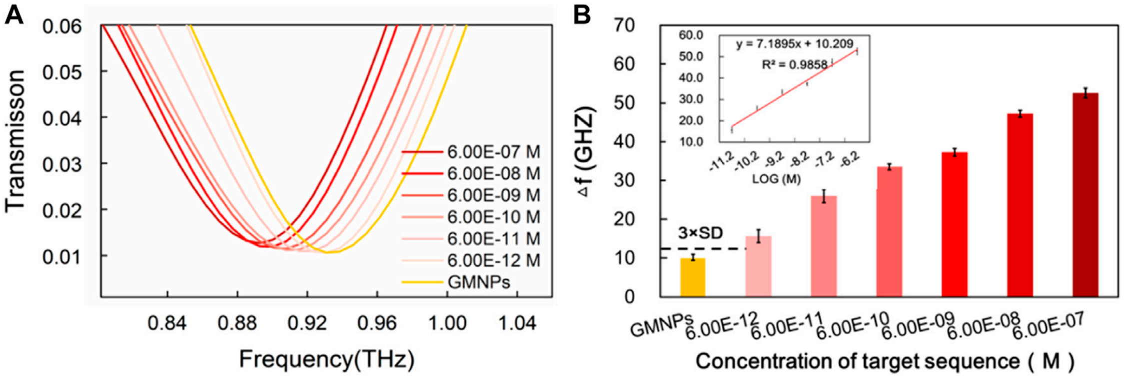

FIGURE 4 | Sensitivity of THz biosensing strategy for HBV target sequence detection. **(A)** The frequencies of the THz transmission spectra for blank GMNPs and GMNPs-RCA-AuNPs amplified with different concentrations of the HBV target sequence. **(B)** The THz frequencies shifts (*Δf*) for blank GMNPs and GMNPs-RCA-AuNPs amplified with different concentrations of the HBV target sequence. Error bars indicate the SD (*n* = 3). The inset graph shows the linear fit of the frequencies (Δf) versus the logarithm of the HBV target sequence concentration. The error bars indicate the SD (*n* = 3).

could be sensitively captured on the THz MM chip surface for biosensing.

Enhancement of Terahertz Sensitivity Using Gold Nanoparticles

The localized electric field present in the gaps of the MM chip enhanced the interactions between the DNA and THz wave, which was further enhanced by the gold nanoparticles (AuNPs) due to their high refractive index, thus verifying that AuNPs can increase the THz biosensing signal (Yang et al., 2021; Zhan et al., 2021). Here, the GMNPs-RCA-AuNPs sandwich assay was refined to improve the sensitivity of DNA detection based on the THz MM biosensor. The impact of AuNP diameter on metamaterial sensing was explored to better understand the role it plays in signal enhancement, relative to the GMNPs-RCA method. AuNPs with an average diameter of 40 nm assume an almost round shape and exhibit good monodispersity, as shown in the TEM images (**Figure 3A**). They

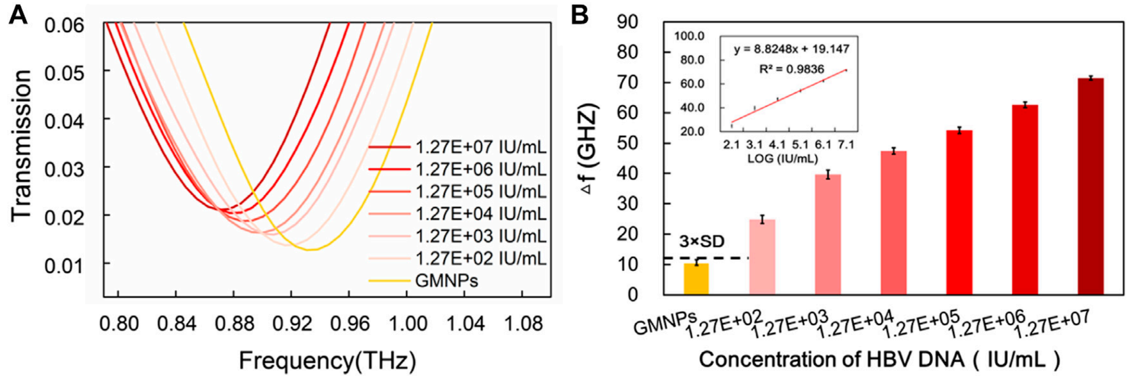

FIGURE 5 | Sensitivity of THz biosensing strategy for HBV DNA detection in serum sample. **(A)** The frequencies of THz transmission spectra for blank GMNPs and GMNPs-RCA-AuNPs amplified with different concentrations of the HBV DNA. **(B)** The THz frequencies shifts (*Δf*) for blank GMNPs and GMNPs-RCA-AuNPs amplified with different concentrations of the HBV DNA. Error bars indicate the SD (*n* = 3). The inset graph shows the linear fit of the frequencies versus the logarithm of the HBV DNA concentration. The error bars indicate the SD (*n* = 3).

also undergo a shift to more negative values, as was observed in the zeta potential of AuNPs (−8.60 ± 0.53 mV) when the coverage by DP (−31.20 ± 2.59 mV) was higher (**Figure 3B**). Moreover, the AuNPs have a plasmon resonance at 531 nm (black line); meanwhile, the DP-modified AuNPs underwent a red shift from 531 to 536 nm (red curve, respectively), demonstrating that functionalization of the AuNPs for DP was successfully completed (**Figure 3C**). Then, it was obvious to see that the GMNPs-RCA-AuNPs complexes could be readily determined amongst GMNPs-RCA due to their higher THz frequency shift signals. There was a further frequency shift of transmission spectra at 16.5 GHz (**Figure 3D**) before and after the formation of the GMNPs-RCA-AuNPs complexes, exhibiting the larger magnitude of target DNA detection signal amplification by the THz biosensing strategy based on the GMNPs-RCA-AuNPs sandwich assay and MM chip, compared to the traditional RCA-THz MM biosensor method, which may be due to the gold-mediated nanoparticles' (including GMNPs and AuNPs) high refractive index.

Sensitivity of Terahertz Biosensing Strategy for Hepatitis B Virus Target Sequence

The frequencies of the THz transmission spectra for various synthetic HBV target sequence concentrations are shown in **Figure 4A**. Improved frequency shift was remarkably observed with the increase of the HBV target sequence. The dose-dependent manner was further explored upon the addition of different concentrations of the HBV target. As it was producing a signal equal to the blank GMNPs signal plus three times its standard deviation (SD), a detection limit for the HBV target was estimated to be 6.00E-12M (**Figure 4B**), indicating that 6.00E-12M of the target sequence can be effectively detected. As can be seen from **Figure 4B**, the frequency and the logarithm of the HBV target sequence exhibited a notable linear correlation (y = 7.1895x + 10.209, R^2 = 0.9858) at concentrations in the range of 6.00E-12~6.00E-07M.

Compared to the reported RCA-based methods, the current assay's sensitivity (6.00E-12M) is inferior to the AuNPs-RCA-based SPR biosensor assay (5.00E-13M) and the AuNPs-RCA-SERS assay (1.00E-13M) (Shi et al., 2014; Guven et al., 2015), but it is comparable with the RCA-SPR biosensor assay (5.00E-12M) and greatly exceeded our previous THz measurements for bacterial DNA using magnetic bead-based RCA (1.00E-10M) (Xiang et al., 2013; Yang et al., 2017). There are several factors that could produce the high sensitivity of the assay. Firstly, the circular DSR resonators made of double splits were specifically designed to produce highly sensitive THz MM chips. Secondly, the RCA produces large DNA sequences, which are conjugated on the GNMPs to improve the sensitivity of the THz MM chips. Thirdly, it is possible for a significant quantity of AuNPs to hybridize with the ssDNA products, which include tandem repeats numbering in the thousands, thereby further enhancing the sensitivity of THz MM chips. Moreover, magnetic separation of RCA products, extracts any interferences from the complex sample matrix when conducting THz measurements, which presents a time-saving replacement and allows the flexibility of applying DNA end point detection methods. Thus, the results of the present study suggest that a specific oligonucleotide sequence can be detected in a more sensitive and selective manner using the current assay compared to similar reported methods of DNA detection under THz spectroscopy conditions (Arora et al., 2012; Yang et al., 2017).

Sensitivity of Terahertz Biosensing Strategy for Hepatitis B Virus DNA in Serum Sample

To further investigate the applicability of the proposed assay in a real biological environment, serum samples were selected to detect HBV DNA. As shown in **Supplementary Figure S4**, analysis of HBV DNA was performed on a 1% agarose gel after the RCA reaction. To assess the extent of this method's sensitivity, serially diluted serum samples were measured (**Figure 5A**). Much like with the synthetic target sequence, THz transmission spectra's analytical frequencies also exhibited a good linear relationship with the logarithm of the HBV DNA at concentrations in the range of 1.27E + 02~1.27E + 07 IU/ml (y = 8.8248x + 19.147, R^2 = 0.9836) range (**Figure 5B**). For the proposed strategy, the HBV DNA detection limit was estimated to be 1.27E + 02 IU/ml. This provides for a signal that is larger than the blank GMNPs signal plus three times its SD (**Figure 5B**).

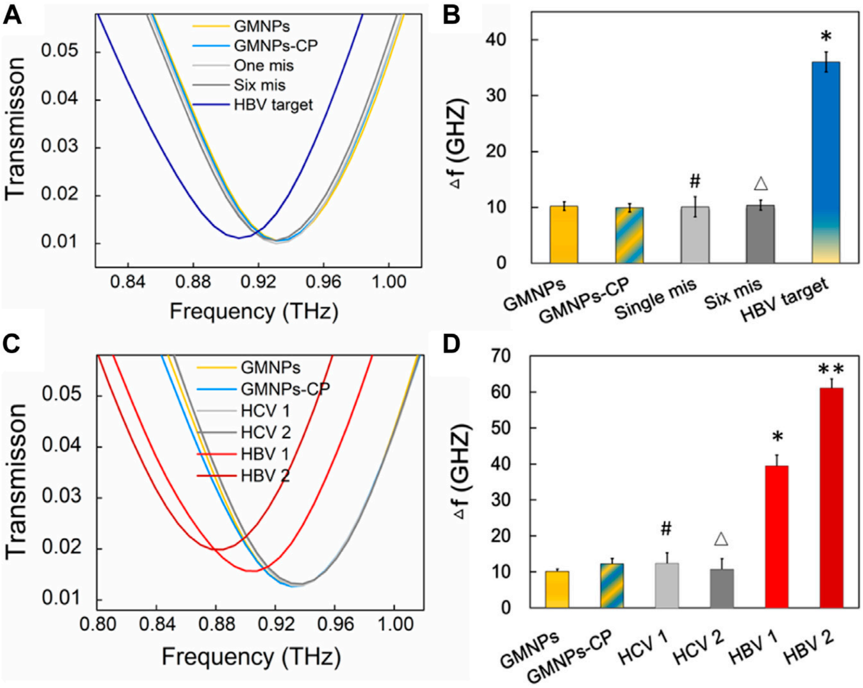

FIGURE 6 | Specificity verification of the THz biosensing strategy. **(A)** THz transmission spectra for HBV target and mismatched sequence. **(B)** The frequency shifts (*Δf*) of THz transmission spectra. Error bars indicate the SD (*n* = 3). Significance was determined using one-way ANOVA; $^{*}p < 0.05$, HBV target versus GMNPs; $^{\#}p > 0.05$, single-base mismatched sequence versus GMNPs; and $^{\triangle}p > 0.05$, six-base mismatched sequence versus GMNPs. **(C)** THz transmission spectra for HBV and HCV in serum samples. **(D)** The frequency shifts (*Δf*) of THz transmission spectra. Error bars indicate the SD (*n* = 3). Significance was determined using one-way ANOVA, $^{*}p < 0.05$, HBV 1 (1.74E + 03 IU/ml) versus GMNPs, $^{**}p < 0.05$, HBV 2 (1.58E + 06 IU/ml) versus GMNPs, $^{\#}p > 0.05$, HCV 1 (4.03E + 03 IU/ml) versus GMNPs, and $^{\triangle}p > 0.05$, HCV 2 (2.45E + 06 IU/ml) versus GMNPs.

TABLE 2 | Determination results of HBV DNA in clinical serum samples (*n* = 4).

Samples	Added	Measured	RSD (%)	Recovery (%)
1	5.32E + 02 IU/ml	5.13E + 02 IU/ml	3.99	99.1
2	1.74E + 03 IU/ml	1.90E + 03 IU/ml	2.94	101.0
3	1.79E + 04 IU/ml	2.73E + 04 IU/ml	3.97	103.7
4	1.50E + 05 IU/ml	2.28E + 05 IU/ml	4.47	102.7
5	1.58E + 06 IU/ml	1.38E + 06 IU/ml	3.51	98.4
6	1.27E + 07 IU/ml	2.80E + 07 IU/ml	3.91	104.0

The sensitivity of the current assay (1.27E + 02 IU/ml) is similar or superior to existing HBV detection methods reported elsewhere, including the loop-mediated isothermal amplification (LAMP) assay (100 IU/ml) (Akram et al., 2018), nanostructured impedance biosensor assay (1,000 copies/ml) (Chen et al., 2016), and the RCA-based quartz crystal microbalance (QCM) biosensor assay (10,000 copies/ml) (Yao et al., 2013). The experiment results suggested that THz spectroscopy measurements of HBV DNA by GMNPs-RCA-AuNPs sandwich assay integrated with the MM biosensor chip provided a new alternative method for early diagnosis and treatment of HBV. A recent study revealed that the highly efficient electrochemiluminescence (ECL) biosensor could realize the ultrasensitive detection of HBV DNA from 100 aM to 1 nM while the limit of detection was 18.08 aM (Guo et al., 2022). The more suitable metamaterials and better signal amplification strategies would be considered to further improve sensitivity of THz biosensor in the future study.

Specificity of the Terahertz Biosensing Strategy

In order to assess the specificity of the THz biosensing strategy for HBV DNA detection, the frequency shifts brought about by the HBV target sequence were compared with the shifts stemming from single-base and six-base mismatched oligonucleotides under the same detection conditions. The THz signals (**Figure 6A**) were measured along with GMNPs, GMNPs-CP, HBV target, single-base mismatched, and six-base mismatched sequences. As shown in **Figure 6B**, the Δf of the HBV target was significantly greater than that of blank GMNPs ($p < 0.05$), GMNPs-CP, single-base mismatched and six-base mismatched sequences, respectively. The results demonstrated that the GMNPs-RCA reaction was highly selective for single-base discrimination. Moreover, the long ssDNA strands could be produced in a specificity sequence-dependent manner which enjoyed high fidelity. Additionally, no amplified frequency signal could be detected in the presence of mismatched sequences. Further detection results of clinical serum samples (**Figures 6C,D**) revealed that the HBV DNA in serum induced significantly greater frequency shifts (Δf) than blank GMNPs ($p < 0.05$), respectively. However, it is not significantly different between GMNPs and Hepatitis C (HCV) as the RCA products were absent ($p > 0.05$), respectively. The results suggest that the THz biosensing strategy developed here enjoys high selectivity and specificity for HBV DNA detection.

Clinical Application of the Terahertz Biosensing Strategy and Reproducibility

A recovery experiment was performed by detecting six clinical human serum samples with different concentrations of HBV DNA over the linear range to assess the proposed THz biosensing strategy's analytical reliability. The recovery rate was calculated (**Table 2**), the results of which aligned with the spiked amounts for the targets. This suggests that the measured and actual values in the serum sample are consistent. To evaluate the THz biosensing strategy's reproducibility, the relative standard deviation (RSD) was calculated based on the four replicate measurements of the clinical human serum samples. The RSDs (%) were determined to be 2.94%–4.47%, indicating that the reproducibility is acceptable. The results showed that the proposed method exhibits sound precision and recovery when applied to clinical serum samples. It is recommended that clinical transformation should be further explored in future research.

CONCLUSION

This research developed a new assay for THz spectroscopy measurement of HBV DNA by using the combination of GMNPs-RCA-AuNPs sandwich assay and the THz MM biosensor chip. Leveraging the high amplification efficiency, specificity, and fidelity of RCA under isothermal conditions, as well as the intrinsically high sensitivity of the gold-mediated nanoparticles and THz MM biosensor chip, as low as 1.27E + 02 IU/ml of serum HBV DNA was detected by THz spectroscopy. The results also indicate there is a linear relationship between THz transmission spectra frequencies and HBV DNA logarithm at concentrations in excess of the 1.27E + 02~1.27E + 07 IU/ml range. It is, therefore, pointed out that the proposed THz biosensing strategy can be employed to carry out the specific, sensitive, selective, and quantitative detection of virus DNA in clinical samples.

DATA AVAILABILITY STATEMENT

The original contributions presented in the study are included in the article/**Supplementary Material**; further inquiries can be directed to the corresponding authors.

AUTHOR CONTRIBUTIONS

YmL: Conceptualization, Methodology, Software, Investigation, Data Curation, Writing-Original Draft. XW: Conceptualization, Methodology, Software, Writing-Review, and Editing. YuL: Methodology, Formal Analysis. WJ: Software, Data Curation. HT: Resources, Investigation. KX: Conceptualization, Resources. FX: Conceptualization, Resources. XZ: Resources, Validation, Data Curation, Project Administration. WF: Supervision, Methodology, Writing-Review, and Editing, Funding Acquisition, Administration, Data Curation. YZ: Supervision, Methodology, Writing-Review, and Editing, Funding Acquisition, Administration, Data Curation.

FUNDING

This work was partially supported by the National Natural Science Foundation of China (81920108024 and 82172374), the Sanming Project of Medicine in Shenzhen (SZSM201601062), the Shenzhen Key Medical Discipline Construction Fund (SZXK054), and the 2019-nCoV Emergency Research Project of China (No. CWS20C008).

SUPPLEMENTARY MATERIAL

The Supplementary Material for this article can be found online at: https://www.frontiersin.org/articles/10.3389/fbioe.2022.930800/full#supplementary-material

REFERENCES

Abusalah, M. A. H., Gan, S. H., Al-Hatamleh, M. A. I., Irekeola, A. A., Shueb, R. H., and Yean Yean, C. (2020). Recent Advances in Diagnostic Approaches for Epstein-Barr Virus. *Pathogens* 9 (3), 226. doi:10.3390/pathogens9030226

Ahmadivand, A., Gerislioglu, B., Tomitaka, A., Manickam, P., Kaushik, A., Bhansali, S., et al. (2018). Extreme Sensitive Metasensor for Targeted Biomarkers Identification Using Colloidal Nanoparticles-Integrated Plasmonic Unit Cells. *Biomed. Opt. Express* 9 (2), 373–386. doi:10.1364/boe.9.000373

Akram, A., Islam, S. M. R., Munshi, S. U., and Tabassum, S. (2018). Detection of Hepatitis B Virus DNA Among Chronic and Potential Occult HBV Patients in Resource-Limited Settings by Loop-Mediated Isothermal Amplification Assay. *J. Viral Hepat.* 25 (11), 1306–1311. doi:10.1111/jvh.12931

Amini, A., Varsaneux, O., Kelly, H., Tang, W., Chen, W., Boeras, D. I., et al. (2017). Diagnostic Accuracy of Tests to Detect Hepatitis B Surface Antigen: A Systematic Review of the Literature and Meta-Analysis. *BMC Infect. Dis.* 17 (1), 698. doi:10.1186/s12879-017-2772-3

Arora, A., Luong, T. Q., Krüger, M., Kim, Y. J., Nam, C.-H., Manz, A., et al. (2012). Terahertz-time Domain Spectroscopy for the Detection of PCR Amplified DNA in Aqueous Solution. *Analyst* 137 (3), 575–579. doi:10.1039/c2an15820e

Bolivar, P. H., Brucherseifer, M., Nagel, M., Kurz, H., Bosserhoff, A., and Buttner, R. (2002). Label-free Probing of Genes by Time-Domain Terahertz Sensing. *Phys. Med. Biol.* 47, 3815–3821. doi:10.1088/0031-9155/47/21/320

Chen, C.-C., Lai, Z.-L., Wang, G.-J., and Wu, C.-Y. (2016). Polymerase Chain Reaction-free Detection of Hepatitis B Virus DNA Using a Nanostructured Impedance Biosensor. *Biosens. Bioelectron.* 77, 603–608. doi:10.1016/j.bios.2015.10.028

Chen, X., and Pickwell-MacPherson, E. (2019). A Sensitive and Versatile Thickness Determination Method Based on Non-inflection Terahertz Property Fitting. *Sensors* 19 (19), 4118. doi:10.3390/s19194118

Dighe, K., Moitra, P., Alafeef, M., Gunaseelan, N., and Pan, D. (2022). A Rapid RNA Extraction-free Lateral Flow Assay for Molecular Point-Of-Care

Detection of SARS-CoV-2 Augmented by Chemical Probes. *Biosens. Bioelectron.* 200, 113900. doi:10.1016/j.bios.2021.113900

Ding, C., Wang, N., Zhang, J., and Wang, Z. (2013). Rolling Circle Amplification Combined with Nanoparticle Aggregates for Highly Sensitive Identification of DNA and Cancercells. *Biosens. Bioelectron.* 42, 486–491. doi:10.1016/j.bios.2012.10.015

Fischer, B. M., Walther, M., and Jepsen, P. U. (2002). Far-infrared Vibrational Modes of DNA Components Studied by Terahertz Time-Domain Spectroscopy. *Phys. Med. Biol.* 47, 3807–3814. doi:10.1088/0031-9155/47/21/319

Geng, Z., Zhang, X., Fan, Z., Lv, X., and Chen, H. (2017). A Route to Terahertz Metamaterial Biosensor Integrated with Microfluidics for Liver Cancer Biomarker Testing in Early Stage. *Sci. Rep.* 7 (1), 16378–16411. doi:10.1038/s41598-017-16762-y

Guo, Y.-Z., Liu, J.-L., Chen, Y.-F., Chai, Y.-Q., Li, Z.-H., and Yuan, R. (2022). Boron and Nitrogen-Codoped Carbon Dots as Highly Efficient Electrochemiluminescence Emitters for Ultrasensitive Detection of Hepatitis B Virus DNA. *Anal. Chem.* 94 (21), 7601–7608. doi:10.1021/acs.analchem.2c00763

Guven, B., Boyaci, I. H., Tamer, U., Acar-Soykut, E., and Dogan, U. (2015). Development of Rolling Circle Amplification Based Surface-Enhanced Raman Spectroscopy Method for 35S Promoter Gene Detection. *Talanta* 136, 68–74. doi:10.1016/j.talanta.2014.11.051

Hsieh, H.-Y., Luo, J.-X., Shen, Y.-H., Lo, S.-C., Hsu, Y.-C., Tahara, H., et al. (2022a). A Nanofluidic Preconcentrator Integrated with an Aluminum-Based Nanoplasmonic Sensor for Epstein-Barr Virus Detection. *Sensors Actuators B Chem.* 355, 131327. doi:10.1016/j.snb.2021.131327

Hsieh, H.-Y., Chang, R., Huang, Y.-Y., Juan, P.-H., Tahara, H., Lee, K.-Y., et al. (2022b). Continuous Polymerase Chain Reaction Microfluidics Integrated with a Gold-Capped Nanoslit Sensing Chip for Epstein-Barr Virus Detection. *Biosens. Bioelectron.* 195, 113672. doi:10.1016/j.bios.2021.113672

Hu, J., and Zhang, C.-y. (2010). Sensitive Detection of Nucleic Acids with Rolling Circle Amplification and Surface-Enhanced Raman Scattering Spectroscopy. *Anal. Chem.* 82, 8991–8997. doi:10.1021/ac1019599

Hu, X., Xu, G., Wen, L., Wang, H., Zhao, Y., Zhang, Y., et al. (2016). Metamaterial Absorber Integrated Microfluidic Terahertz Sensors. *Laser & Photonics Rev.* 10, 962–969. doi:10.1002/lpor.201600064

Hu, J., Lang, T., Xu, W., Liu, J., and Hong, Z. (2019). Experimental Demonstration of Electromagnetically Induced Transparency in a Conductively Coupled Flexible Metamaterial with Cheap Aluminum Foil. *Nanoscale Res. Lett.* 14, 359. doi:10.1186/s11671-019-3180-y

Inoue, T., Matsui, T., and Tanaka, Y. (2021). Novel Strategies for the Early Diagnosis of Hepatitis B Virus Reactivation. *Hepatology Res.* 51 (10), 1033–1043. doi:10.1111/hepr.13699

Liang, L., Jiang, Y. J., Zhang, L. C., Liu, H., Li, Y. F., Li, C. M., et al. (2022). Rational Fabrication of a DNA Walking Nanomachine on Graphene Oxide Surface for Fluorescent Bioassay. *Biosens. Bioelectron.* 211, 114349. doi:10.1016/j.bios.2022.114349

Moitra, P., Alafeef, M., Dighe, K., Sheffield, Z., Dahal, D., and Pan, D. (2021). Synthesis and Characterisation of N-Gene Targeted NIR-II Fluorescent Probe for Selective Localisation of SARS-CoV-2. *Chem. Commun.* 57 (51), 6229–6232. doi:10.1039/d1cc01410b

Moitra, P., Chaichi, A., Abid Hasan, S. M., Dighe, K., Alafeef, M., Prasad, A., et al. (2022). Probing the Mutation Independent Interaction of DNA Probes with SARS-CoV-2 Variants through a Combination of Surface-Enhanced Raman Scattering and Machine Learning. *Biosens. Bioelectron.* 208, 114200. doi:10.1016/j.bios.2022.114200

Ong, D. S. Y., Fragkou, P. C., Schweitzer, V. A., Chemaly, R. F., Moschopoulos, C. D., and Skevaki, C. (2021). How to Interpret and Use COVID-19 Serology and Immunology Tests. *Clin. Microbiol. Infect.* 27 (7), 981–986. doi:10.1016/j.cmi.2021.05.001

Pickwell-MacPherson, E., and Wallace, V. P. (2009). Terahertz Pulsed Imaging-A Potential Medical Imaging Modality? *Photodiagnosis Photodyn. Ther.* 6, 128–134. doi:10.1016/j.pdpdt.2009.07.002

Shi, D., Huang, J., Chuai, Z., Chen, D., Zhu, X., Wang, H., et al. (2014). Isothermal and Rapid Detection of Pathogenic Microorganisms Using a Nano-Rolling Circle Amplification-Surface Plasmon Resonance Biosensor. *Biosens. Bioelectron.* 62, 280–287. doi:10.1016/j.bios.2014.06.066

Tang, M., Huang, Q., Wei, D., Zhao, G., Chang, T., Kou, K., et al. (2015). Terahertz Spectroscopy of Oligonucleotides in Aqueous Solutions. *J. Biomed. Opt.* 20 (9), 095009. doi:10.1117/1.JBO.20.9.095009

Tong, P., Zhao, W.-W., Zhang, L., Xu, J.-J., and Chen, H.-Y. (2012). Double-probe Signal Enhancing Strategy for Toxin Aptasensing Based on Rolling Circle Amplification. *Biosens. Bioelectron.* 33, 146–151. doi:10.1016/j.bios.2011.12.042

Wang, F., Zhao, D., Dong, H., Jiang, L., Liu, Y., and Li, S. (2017). Terahertz Spectra of DNA Nucleobase Crystals: A Joint Experimental and Computational Study. *Spectrochim. Acta A Mol. Biomol. Spectrosc.* 179, 255–260. doi:10.1016/j.saa.2017.02.037

Wang, J., Lang, T., Hong, Z., Xiao, M., and Yu, J. (2021). Design and Fabrication of a Triple-Band Terahertz Metamaterial Absorber. *Nanomaterials* 11 (5), 1110. doi:10.3390/nano11051110

Xia, L., Cui, H.-L., Zhang, M., Dang, S., and Du, C. (2019). Broadband Anisotropy in Terahertz Metamaterial with Single-Layer Gap Ring Array. *Materials* 12 (14), 2255. doi:10.3390/ma12142255

Xiang, Y., Deng, K., Xia, H., Yao, C., Chen, Q., Zhang, L., et al. (2013). Isothermal Detection of Multiple Point Mutations by a Surface Plasmon Resonance Biosensor with Au Nanoparticles Enhanced Surface-Anchored Rolling Circle Amplification. *Biosens. Bioelectron.* 49, 442–449. doi:10.1016/j.bios.2013.04.044

Xu, W., Xie, L., and Ying, Y. (2017). Mechanisms and Applications of Terahertz Metamaterial Sensing: A Review. *Nanoscale* 9, 13864–13878. doi:10.1039/c7nr03824k

Yang, X., Yang, K., Zhao, X., Lin, Z., Liu, Z., Luo, S., et al. (2017). Terahertz Spectroscopy for the Isothermal Detection of Bacterial DNA by Magnetic Bead-Based Rolling Circle Amplification. *Analyst* 142 (24), 4661–4669. doi:10.1039/c7an01438d

Yang, Y., Xu, D., and Zhang, W. (2018). High-sensitivity and Label-free Identification of a Transgenic Genome Using a Terahertz Meta-Biosensor. *Opt. Express* 26 (24), 31589–31598. doi:10.1364/oe.26.031589

Yang, K., Li, J., Lamy de la Chapelle, M., Huang, G., Wang, Y., Zhang, J., et al. (2021). A Terahertz Metamaterial Biosensor for Sensitive Detection of microRNAs Based on Gold-Nanoparticles and Strand Displacement Amplification. *Biosens. Bioelectron.* 175, 112874. doi:10.1016/j.bios.2020.112874

Yao, C., Xiang, Y., Deng, K., Xia, H., and Fu, W. (2013). Sensitive and Specific HBV Genomic DNA Detection Using RCA-Based QCM Biosensor. *Sensors Actuators B Chem.* 181, 382–387. doi:10.1016/j.snb.2013.01.063

Zhan, X., Yang, S., Huang, G., Yang, L., Zhang, Y., Tian, H., et al. (2021). Streptavidin-functionalized Terahertz Metamaterials for Attomolar Exosomal microRNA Assay in Pancreatic Cancer Based on Duplex-specific Nuclease-Triggered Rolling Circle Amplification. *Biosens. Bioelectron.* 188, 113314. doi:10.1016/j.bios.2021.113314

Zhang, M., Yang, Z., Tang, M., Wang, D., Wang, H., Yan, S., et al. (2019). Terahertz Spectroscopic Signatures of Microcystin Aptamer Solution Probed with a Microfluidic Chip. *Sensors (Basel)* 19 (3), 1–12. doi:10.3390/s19030534

Zheng, Q., Xia, L., Tang, L., Du, C., and Cui, H. (2020). Low Voltage Graphene-Based Amplitude Modulator for High Efficiency Terahertz Modulation. *Nanomaterials* 10 (3), 585. doi:10.3390/nano10030585

Zhou, J., Zhao, X., Huang, G., Yang, X., Zhang, Y., Zhan, X., et al. (2021). Molecule-Specific Terahertz Biosensors Based on an Aptamer Hydrogel-Functionalized Metamaterial for Sensitive Assays in Aqueous Environments. *ACS Sens.* 6 (5), 1884–1890. doi:10.1021/acssensors.1c00174

Zhou, R., Wang, C., Huang, Y., Huang, K., Wang, Y., Xu, W., et al. (2021). Label-free Terahertz Microfluidic Biosensor for Sensitive DNA Detection Using Graphene-Metasurface Hybrid Structures. *Biosens. Bioelectron.* 188, 113336. doi:10.1016/j.bios.2021.113336

Conflict of Interest: The authors declare that the research was conducted in the absence of any commercial or financial relationships that could be construed as a potential conflict of interest.

frontiers | Frontiers in Bioengineering and Biotechnology

TYPE Original Research
PUBLISHED 23 September 2022
DOI 10.3389/fbioe.2022.987669

OPEN ACCESS

EDITED BY
Yu-Jui Fan,
Taipei Medical University, Taiwan

REVIEWED BY
Tsung-Rong Kuo,
Taipei Medical University, Taiwan
Chia Wen Tsao,
National Central University, Taiwan
Shih-hao Huang,
National Taiwan Ocean University,
Taiwan

*CORRESPONDENCE
Laura Cerqueira,
lcerqueira@fe.up.pt
João M. Miranda,
jmiranda@fe.up.pt

SPECIALTY SECTION
This article was submitted to Biosensors and Biomolecular Electronics, a section of the journal Frontiers in Bioengineering and Biotechnology

RECEIVED 06 July 2022
ACCEPTED 08 August 2022
PUBLISHED 23 September 2022

CITATION
Barbosa VB, Rodrigues CF, Cerqueira L, Miranda JM and Azevedo NF (2022), Microfluidics combined with fluorescence in situ hybridization (FISH) for Candida spp. detection. *Front. Bioeng. Biotechnol.* 10:987669. doi: 10.3389/fbioe.2022.987669

Microfluidics combined with fluorescence *in situ* hybridization (FISH) for *Candida spp.* detection

Violina Baranauskaite Barbosa[1,2], Célia F. Rodrigues[1,2], Laura Cerqueira[1,2]*, João M. Miranda[2,3]* and Nuno F. Azevedo[1,2]

[1]LEPABE–Laboratory for Process Engineering, Environment, Biotechnology and Energy, Department of Chemical Engineering, Faculty of Engineering of University of Porto, Porto, Portugal, [2]ALiCE–Associate Laboratory in Chemical Engineering, Faculty of Engineering, University of Porto, Porto, Portugal, [3]CEFT–Transport Phenomena Research Center, Department of Chemical Engineering, Faculty of Engineering of University of Porto, Porto, Portugal

One of the most prevalent healthcare-associated infection is the urinary tract infection (UTI), caused by opportunistic pathogens such as *Candida albicans* or non-albicans *Candida* species (NACS). Urine culture methods are routinely used for UTI diagnostics due to their specificity, sensitivity and low-cost. However, these methods are also laborious, time- and reagent-consuming. Therefore, diagnostic methods relying on nucleic acids have been suggested as alternatives. Nucleic acid-based methods can provide results within 24 h and can be adapted to point-of-care (POC) detection. Here, we propose to combine fluorescence *in situ* hybridization (FISH) with a microfluidic platform for the detection of *Candida* spp. As a case study we used *C. tropicalis*, which is reported as the second most common NACS urine isolate obtained from patients suspected with UTI. The microfluidic platform proposed in this study relies on hydrodynamic trapping, and uses physical barriers (e.g., microposts) for the separation of target cells from the suspension. Using a specific peptide nucleic acid (PNA) probe, the FISH procedure was applied onto previously trapped *C. tropicalis* cells present inside the microfluidic platform. Fluorescence signal intensity of hybridized cells was captured directly under the epifluorescence microscope. Overall, the PNA probe successfully detected *C. tropicalis* in pure culture and artificial urine (AU) using FISH combined with the microfluidic platform. Our findings reveal that FISH using nucleic acid mimics (PNA) in combination with microfluidics is a reliable method for the detection of microorganisms such as *C. tropicalis*. As such, this work provides the basis for the development of a POC detection platform in the future.

KEYWORDS

FISH, microfluidics, UTI, detection, *C. tropicalis*

Abbreviations: PNA, FISH Peptide nucleic acid fluorescence *in situ* hybridization; TCF, total cell fluorescence; ID, integrated density; CA, Cell area; MBF, Mean background fluorescence; MCF, Mean cell fluorescence; MIF, Mean image fluorescence; N, Number of cells; MCF_i, Mean fluorescence of each cell; CA_i, Area of each cell.

1 Introduction

Urinary tract infections (UTI) represent one of the most common healthcare-associated infection across EU countries, accounting for 18.9% of all cases (OECD/European Union, 2018). These infections are caused by microbial pathogens, either bacteria or fungi. While *Candida* species are natural residents of the genitourinary, gastrointestinal tract and skin human flora (Kauffman, 2014), they are also considered as opportunistic pathogens and can cause fungal infections (Richardson, 1991; Fisher, 2011). Infections resulting from *Candida albicans* and non-*Candida albicans Candida* (NCAC) species have increased significantly in the last decade. The presence of *Candida* species in urine–candiduria - is a common clinical finding, particularly in hospitalized patients, mainly with the use of medical devices and/or immunosuppression (e.g., antibiotic therapy, diabetes) (Alvarez-Lerma et al., 2003; Kauffman, 2014; Rodrigues C. F. et al., 2019; Gajdacs et al., 2019). Candiduria denotes a diagnostic and therapeutic challenge for physicians from primary care or infectious diseases, intensive medicine and surgery (Bongomin et al., 2017), because it may be linked to numerous conditions that require careful interpretation, from sample contamination to UTI or even disseminated candidiasis. The identification of *Candida* isolates to species level is necessary due to different antifungal susceptibility patterns, which is important for administration of appropriate therapeutic strategy (Kauffman et al., 2011). *Candida albicans* is the most prevalent species isolated from urine samples (51.8%) (Kauffman et al., 2000; Fisher, 2011). However, recent studies indicate increased incidence of NCAC in clinical samples (Goyal et al., 2016; Taei et al., 2019). For instance, *Candida tropicalis* is reported as the second most common NCAC (14.3%) identified in urine samples obtained from patients suspected with UTI (Gharanfoli et al., 2019). It is also a frequent isolate detected in urine samples of both inpatients (8.95%) and outpatients (8.69%) (Gajdacs et al., 2019).

In clinical microbiology, urine culture methods are used for UTI diagnosis. At first the causative microorganism is identified from urine culture which takes 18–48 h. Afterwards, the antimicrobial susceptibility testing (AST) is performed, which takes additional 24 h (Wilson and Gaido, 2004; Davenport et al., 2017). While these culture methods are used for routine urine examination (Aspevall et al., 2001) due to their cost-effectiveness and specificity, although some limitations are also present (Kauffman, 2014). Besides standard urine culture-based methods, *Candida* spp. Can be detected through microscopy visualization with the aid of Gram staining (e.g., *Candida albicans* appear in budding yeast 4–10 μm in diameter) (Kauffman et al., 2011). Other diagnostic techniques include the imaging studies, such as ultrasonography, ultrasound or computed tomography urograms (Kauffman et al., 2011; Kauffman, 2014).

This diagnostic delay may eventually result in increased severity of the infection. As such, molecular detection methods that rely on proteins or nucleic acids have also been suggested for routine urine analysis. These methods identify microorganisms at the species level within 24 h, which is important for selecting appropriate therapeutics. One example of a molecular method is fluorescence *in situ* hybridization, that relies on fluorescently labelled nucleic acids [DNA, RNA or nucleic acid mimics (NAM's)] probes (Almeida et al., 2013c; Cerqueira et al., 2013; Mendes et al., 2016; Ferreira et al., 2017; Azevedo et al., 2019) to bind to target sequences of the microorganism of interest by complementary base pairing (Gall and Pardue, 1969). The hybrid complex can then be visualised directly with an epifluorescence microscope (Moter and Gobel, 2000). The miniaturization concept found application in biotechnology, due to certain advantages such as single-cell analysis or high surface area to volume (S/V) ratio, which results in reduced mass and heat transfer times and shorter diffusion distances (Walker et al., 2004). As such, the biochemical reaction time is improved which is important for reducing the overall diagnostic time (Asghar et al., 2019; Sohrabi et al., 2020). Also, upon microfluidics integration with molecular methods, the amount of sample required is reduced and doesn't compromise the sensitivity and specificity of the system (Hsieh et al., 2022). Moreover, for sample analysis, different visualization devices can be combined with microfluidic platform, allowing spatiotemporal resolution and high detection efficiency (Fan et al., 2021). While other study developed mobile platform with a sensitivity comparable to that of a conventional microscope (Muller et al., 2018). Microchannel geometries are also prone to massive parallelization, allowing high-throughput analysis (Mach and Di Carlo, 2010). Equally important, microfluidic platforms allow to concentrate and separate target microorganisms from biological fluids, thus reducingcircumventing lengthy culture times (Wang et al., 2012; Beech et al., 2018). A number of studies have explored hydrodynamic filtration (Yamada and Seki, 2005), deterministic lateral displacement (DLD) (Inglis et al., 2011), microfiltration (Ji et al., 2008) methods, which allow to separate or enrich microorganisms. These methods do not require any external force field (passive cell separation), making them simple, low-cost and label-free, which simplifies the overall procedure (Zhou et al., 2019). Such passive separation techniques rely on inherent hydrodynamic forces, channel geometries and physical obstacles, such as micropost arrays, microfiltration, microwells and chambers (Luan et al., 2020). The use of these techniques eliminates the need for sophisticated and expensive devices. Hydrodynamic cell trapping has shown to be applicable for single cell imaging and quantification (Park et al., 2011), microorganism enrichment (Whang et al., 2018) and size-selective trapping and sorting (Kim et al., 2014).

The FISH method robustness and implementation as molecular diagnostic tool greatly improves when using

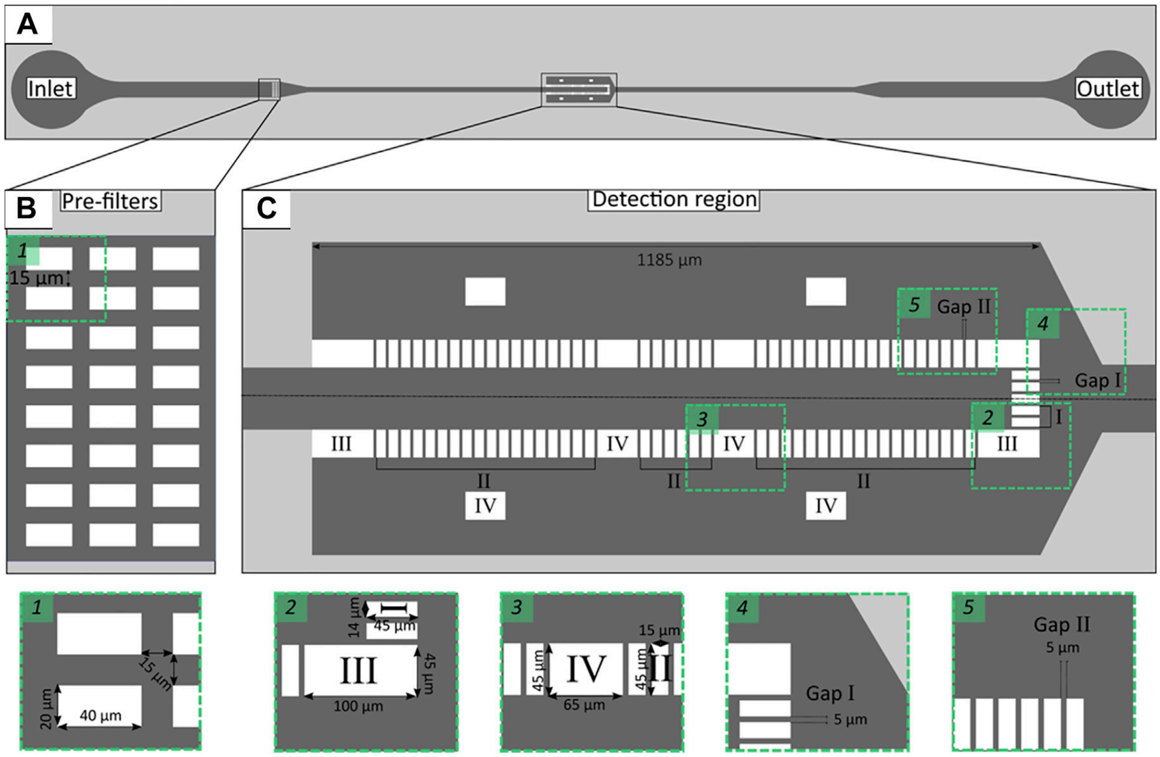

FIGURE 1
Schematic representation of microfluidic channel layout with single inlet and outlet **(A)**. Enlarged view representing pre-filters **(B)** and the detection region **(C)** containing microposts of different geometries: front (Micropost I), lateral (Micropost II) and support (Micropost III and IV). *Rectangles 1–5* enlarged microchannel layout sections.

NAM's, which have enhanced sensitivity and specificity, when compared to DNA or RNA probes (Nacher-Vazquez et al., 2022). Moreover, when combined with microfluidics, the analysis time is reduced when compared to standard FISH method (Chien-Hsuan et al., 2013). In spite of its great potential, the integration of FISH and microfluidics has been achieved in a limited number of works (Ferreira et al., 2017; Nguyen et al., 2017; Lee et al., 2022), especially for the diagnostics of fungal infections (Hussain et al., 2020). Therefore, the goal of this work is to develop a microfluidic platform combined with FISH for the detection of *Candida* spp. The proposed method was tested using *C. tropicalis* as a case study.

2 Materials and methods

2.1 Cell culture maintenance and microbial cell suspension preparation

C. tropicalis reference strain (ATCC 750) from the American Type Culture Collection was used in this work. For inoculum preparation, cells were grown overnight (≈16 h) at 37C° and 120 rpm, under aerobic conditions. The growth rate under these conditions was determined by measuring optical density (OD 600 nm) (VWR V-1200 spectrophotometer, United States) over time. Subsequently, cell concentration was adjusted by OD for a final single cell concentration of 1×10^8 cells/ml or 1×10^5 cells/ml (for artificial urine (AU)). To assess cultivability, 1:10 dilutions were prepared in Phosphate Buffered Saline (PBS, 180 mM NaCl, 3 mM KCl, 9 mM $Na_2HPO_4.2H_2O$, and 1.5 mM KH_2PO_4, pH 7.4) and plated onto SD agar plates and incubated overnight, at 37°C, under aerobic conditions (Rodrigues et al., 2018). Then, colony forming units (CFU) were counted to confirm microbial cell concentration (CFU/ml). Finally, 1 ml of *C. tropicalis* cell suspension was centrifuged at 13.000 g for 10 min and resuspended in 1 ml of PBS before proceeding to fluorescence *in situ* hybridization and microfluidic experiments.

2.2 Microfluidic platform development

The microchannel geometry was designed using AutoCAD 2013® software (Autodesk Inc., United States) and then a silicon master mold was fabricated at the International Iberian

Nanotechnology Laboratory-INL facilities (Braga, Portugal) combining direct laser write lithography and deep reactive ion etching. The microchannel layout proposed in this study consisted of an inlet, an outlet and a widened detection region (500 µm) (Figure 1A). The depth of the microchannel was set to 30 µm, because low *height*/*width* ratio provides better micropost stability (Ferreira et al., 2017). Also, the depth of 30 µm was calculated to be the maximum value at which low *height*/*width* ratio is still maintained. This is an important parameter, as on one hand low *height*/*width* ratio provides better micropost stability and on the other high depths maximise the flow rate.

In comparison to a previous design (Ferreira et al., 2017), three rows of pre-filters (Figure 1B) were introduced to separate target microorganisms from particles or other cells that may be present in clinical samples (e.g., blood or urine). The detection region consisted of different micropost geometries designed to trap cells larger than 5 µm (such as *C. tropicalis*) (Figure 1C, Micropost I and II), while larger microposts provided structural support to the larger cross-sectional area of the microchannel (Figure 1C, Micropost III and IV). The gaps were set to 5 µm throughout the whole trapping array (Figure 1C, Gap I and II).

2.2.1 Microchannel fabrication

The microchannels were produced using the soft-lithography method–a replication of the silicon mold. At first the master mold was placed in a laminar flow chamber with a few drops of trichlorosilane (UCT Specialities, United States) for 1 h. The vapour of trichlorosilane allows an easier removal of the elastomer block (Jung et al., 2005). The two-part polydimethyl-siloxane (PDMS) silicone elastomer kit (Sylgard 184; Dow Corning, United States) was used to produce the liquid polymer. To produce a negative PDMS slab, 5:1 ratio (5 parts of base polymer by weight to one part of curing agent by weight) and mixed for 10 min with vortex mixer (VV3, VWR) at 2,500 min^{-1}. Afterwards, the mixture was placed in a desiccator connected to a vacuum line for degassing to remove air bubbles. Then, the liquid polymer was poured onto a master mold, subjected again to degassing and eventually cured for 20 min at 80°C in the incubator (FD 23, Binder, Germany). Afterwards, the negative PDMS slab containing the microchannels was cut out and peeled off from the master mold. Finally, the inlet and outlet holes were punched with a precision tip (7018178, 20 GA, Nordson EFD, United States). For PDMS-glass bonding, the imprinted surface of the negative PDMS stamp and clean ultra-thin cover glass (631.0178, VWR International) were subjected to oxygen plasma treatment (ZEPTO, Diener electronic GmbH, Germany) at 20 W and 1.2 mBar for 30 s, with subsequent joining of the two surfaces. The PDMS-glass was left in contact for 5 min to form an irreversible bond. Before the oxygen plasma treatment, the cover glass was cleaned with acetone (20063.365, VWR Chemicals, France) then rinsed with high-purity water (HPW) and dried with compressed air.

2.2.2 Microchannel geometrical characterization

First, each fabrication microchannel geometry was inspected visually for any geometrical errors or structural instabilities (e.g., micropost bending) using a microscope (*see section: 2.6.2*).

Afterwards, the experimental geometry characterization was performed. For this, one PDMS slab of each design was cut to obtain the channel cross section and placed downwards onto a glass slide. Then, images were recorded (*see section: 2.6.2*) and subsequently processed with Fiji® (ImageJ.net) software (Schindelin et al., 2012) in order to measure the height (H) and width (W) of the microchannel (inlet/outlet and micropost array). The characterization was performed in triplicate and measurements were used to calculate the percent error (%) between nominal and experimental values (Supplementary Table S1).

2.2.3 Computational fluid dynamics (CFD)

The 2D CAD geometry of the microchannel was extruded to obtain a 3D geometry and was imported to OpenSCAD. In OpenSCAD, the boundaries of the domain were created and exported as STL files. As the geometry is symmetric relatively to two planes (Figure 2A), the flow was solved for 1/4 of the domain (Figure 2B). The boundaries were subsequently named and merged in a single file. This file was used as input to generate the mesh (Figure 2B) using snappyMesh, a mesh generator available on the OpenFOAM framework (version 4.1). The mesh is refined in the gaps (inset in Figure 2B) to ensure an accurate solution of the velocity field.

The flow in the microchannel was solved using the icoFoam solver (OpenFOAM framework, version 4.1), modified to enable an adjustable time step, with the following boundary conditions (Figure 2A): **Inlet:** i) Uniform velocity corresponding to the flow rate of 1 µl/min; ii) pressure gradient normal to the boundary equal to zero; **Outlet:** i) Velocity gradient normal to the boundary equal to zero; ii) pressure set to zero. **Walls:** i) No-slip boundary conditions; ii) pressure gradient normal to the boundary equal to zero. **Symmetry planes:** i) Velocity gradient normal to the boundary equal to zero; ii) pressure gradient normal to the boundary equal to zero. The flow conditions for the simulation are discussed in section 3.1.1. The primary results obtained were the velocity and pressure fields in the domain. These fields were visualized in paraFoam and post-processed to obtain the velocities in the gaps using openFoam post-processing tools.

2.3 Fluid handling

For fluid injection in the microchannel and FISH experiments in microfluidic device, gravity- and/or pressuredriven low systems were used (Figure 3). The gravity-driven system was composed of fluid reservoir (e.g., syringe without a plunger) attached to a Tygon microtube (0.44 mm ID) and connected to the inlet of

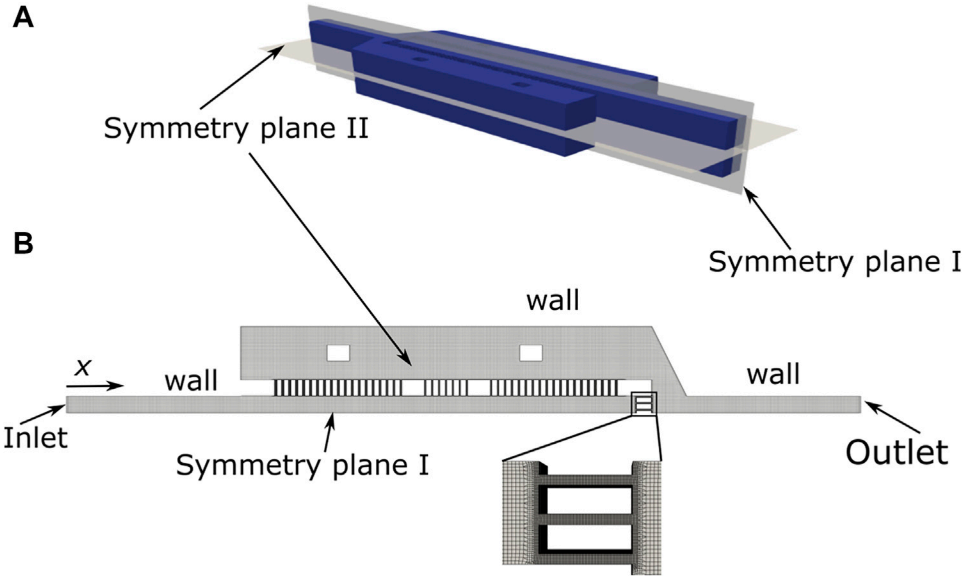

FIGURE 2
Schematic representation of the device computational domain **(A)** and detailed view of the mesh (inset) **(B)**.

microfluidic platform. The pressure-driven flow system consisted of 500 µl syringe (Hamilton Company, Bonaduz, Switzerland) connected to the inlet of microfluidic platform through Tygon microtube (0.44 mm ID). To achieve pressure-induced laminar flow, the syringe was mounted on a neMESYS low pressure syringe pump (Cetoni, neMESYS syringe pump, Germany), which was controlled through computer software and with the flow rate set to 1 µl/min. In both fluid handling systems, the single microtube was filled with different solutions, which were separated with an air microbubble.

2.4 PNA probe design

The PNA-probe targeting *Candida* 18S rRNA was designed by Oliveira (Oliveira, 2018) using BLAST (https://blast.ncbi.nlm.nih.gov/Blast.cgi) and Clustal W (https://www.ebi.ac.uk/Tools/msa/clustalo/) programs for selection and alignment of gene sequences, respectively. Also, the theoretical specificity (%) of 96.04 was calculated. Finally, the PNA-probe containing the following sequence 5′-Alexa488-OO-CACCCACAAAATCAA-3′ was synthesized and HPLC-purified at >90% (BioPortugal, Portugal).

2.5 PNA-FISH adaptation to microfluidic environment

2.5.1 PNA-FISH off chip

The hybridization procedure was performed as previously reported (Perry-O'Keefe et al., 2001) with some modifications. A *C. tropicalis* cell suspension (1×10^8 cells/mL) was centrifuged at 10.000 *g* for 5 min (Centrifuge 5,418, Eppendorf, Germany) and resuspended in 500 µl of 4% (w/v) paraformaldehyde (Acros Organics, Belgium) with subsequent incubation for 1 h at room temperature. Then, cells were centrifuged again at 10.000 *g* for 5 min, the pellets re-suspended in 50% (v/v) ethanol (VWR Chemicals, Belgium), and incubated for at least 30 min at -20°C. Subsequently, *C. tropicalis* cells were re-suspended in hybridization solution (pH 7.5) containing 200 nM PNA probe and incubated (FD 23, Binder, Germany) for 1 h at 53°C. The hybridization solution was composed of 10 mM NaCl (VWR Chemicals); 30% (v/v) formamide (VWR, United States); 0.1% (w/v) sodium pyrophosphate (Acros Organics, Spain); 0.2% (w/v) polyvinylpyrrolidone (Sigma-Aldrich, China); 0.2% (w/v) Ficoll® 400 (Sigma-Aldrich, United States); 50 mM di-sodium EDTA (Panreac Quimica, Spain); 50 mM Tris-HCl (Fisher Scientific, United States); 0.1% (v/v) Triton X-100 (Panreac Quimica, Spain) and 10% (w/v) dextran Sulfate (Fisher Scientific, United States) (Cruz-Moreira, 2014). A negative control was performed using hybridization solution without PNA probe. Afterwards, hybridized *C. tropicalis* cells were re-suspended in 500 µl washing solution (pH 10), 5 mM Tris Base (Fisher Scientific, United States), 15 mM NaCl (VWR Chemicals), and 1% (v/v) Triton X-100 (Panreac Quimica), further incubated at 53°C, for 30 min and re-suspended in 500 µl of sterile water. Next, 10 µl of the suspension was injected into microfluidic channel using pressure-driven flow, set at 1 µl/min flow rate (*see section: 2.3*). Cell fluorescent signal was detected by epifluorescence microscopy (*see section: 2.6.1*). In parallel, 20 µl of the previously re-suspended pellets were placed on a glass slide (Hecht Assistent®, Germany), dried, mounted with BacLightTM mounting oil (Invitrogene, United States) and covered with a cover slip (24 × 60 mm) for microscopy visualization (Almeida et al., 2013c).

2.5.2 PNA-FISH on chip

The standard PNA-FISH protocol was adapted to work inside the microfluidic device. For this, 20 µL of *C. tropicalis* cell suspension or artificially contaminated urine samples were injected into the microfluidic device by gravity-driven flow (*see section: 2.3*). The artificially contaminated samples were prepared by resuspension of *C. tropicalis* cell pellets (1×10^5 cells/mL) in 1,000 µl of artificial urine (AU) ($CaCl_2$, 0.65 g/L; $MgCl_2$, 0.65 g/L; NaCl, 4.6 g/L; Na_2SO_4, 2.3 g/L; $Na_3C_3H_5O(CO_2)_3$, 0.65 g/L; $Na_2C_2O_4$, 0.02 g/L; KH_2PO_4, 2.8 g/L; KCl, 1.6 g/L; NH_4Cl, 1.0 g/L; urea, 25.0 g/L; creatinine, 1.1 g/L; and glucose, 0.3% and adjusted to pH 6.5) (Negri et al., 2011). Subsequently, trapped cells were exposed to 20 µl of 4% (w/v) paraformaldehyde and 20 µl of 50% (v/v) ethanol by gravity-driven flow. Next, 10 µl of hybridization solution with PNA probe (200 nM) or hybridization solution alone (control), 10 µl wash buffer and 10 µl of sterile water were introduced through pressure-driven flow system (*see section: 2.3*). The incubation times and temperatures were maintained as described above. For keeping the temperature during the hybridization and washing steps, a heating plate (Leica TPX-TypeF, Leica Microsystems, Germany) was used. Finally, trapped *C. tropicalis* were visualised under the microscope (*see section: 2.6.1*).

2.6 Microscopy visualisation

2.6.1 PNA-FISH signal

Images were acquired with a Nikon EclipseT*i* SR inverted epifluorescence microscope (Nikon Instruments, Netherlands) connected to a DS-Ri2 camera (Nikon Instruments). The microscope was equipped with a FITC (fluorescein isothiocyanate) filter sensitive to the Alexa Fluor® 488 fluorophore labelled PNA probe (Excitation 465–495 nm; Barrier 515–555 nm; Dichroic mirror 505 nm). The microscope software NIS-elements 4.13.04 (Nikon Instruments, Amsterdam, Netherlands) was used and parameters such as exposure, gain and saturation were maintained constant in all experiments involving FISH. The acquired images were used for fluorescence signal quantification (*see section: 2.7*).

2.6.2 Geometrical characterisation and cell trapping

Images were recorded with Leica DMI 5000 inverted microscope (Leica Microsystems, Germany) coupled with Leica DFC350 FX camera (Leica Microsystems) and imaging software Leica Application Suite 3.7.0 (Leica Microsystems). To assure the reproducibility and consistency among experimental assays, the microscope parameters (exposure, gain and saturation) were maintained the same in each microscope.

2.7 Fluorescence quantification

The fluorescence signal intensity of *C. tropicalis* cells, from 3 independent assays, was quantified from images using Fiji® Software and the procedures described in (Schindelin et al., 2012; Fontenete et al., 2016), with minor modifications. Initially, the original RGB channels (red, green, and blue light) were split and the green channel (where the fluorescence was emitted) was used for fluorescence signal intensity analysis.

The total cell fluorescence, *TCF*, of individual cell was determined as follows:

$$\boldsymbol{TCF} = \frac{\boldsymbol{ID} - \boldsymbol{CA} \times \boldsymbol{MBF}}{\boldsymbol{CA}} \tag{1}$$

where *ID* is the integrated density, *CA* the selected cell area and *MBF* the mean background fluorescence.

This would provide cell size independent quantification and measure of contrast. Then, the mean fluorescence intensity of each cell (considering the cell area), was calculated by:

$$\boldsymbol{MCF} = \frac{\boldsymbol{TCF}}{\boldsymbol{CA}} \tag{2}$$

where *MCF* is the mean cell fluorescence.

Then mean image fluorescence, *MIF*, was determined as follows:

$$\boldsymbol{MIF} = \frac{\sum_{i=1}^{N} \boldsymbol{MCF_i}}{\sum_{i=1}^{N} \boldsymbol{CA_i}} \tag{3}$$

where N is the number of cells, MCF_i is the mean fluorescence of each cell and CA_i is the area of each cell.

2.8 Statistical analysis

All experiments ("PNA-FISH on chip" *see section: 2.5.2*) were repeated three times in independent assays. Statistical analysis was performed using GraphPad Prism 9 (GraphPad Software, CA, United States). The normality of distribution was tested with D'Agostino-Pearson test, followed by comparison between conditions with the *t*-test. All experimental data are presented as mean ± standard error of the mean (SEM) and statistical significance set at $p < 0.05$.

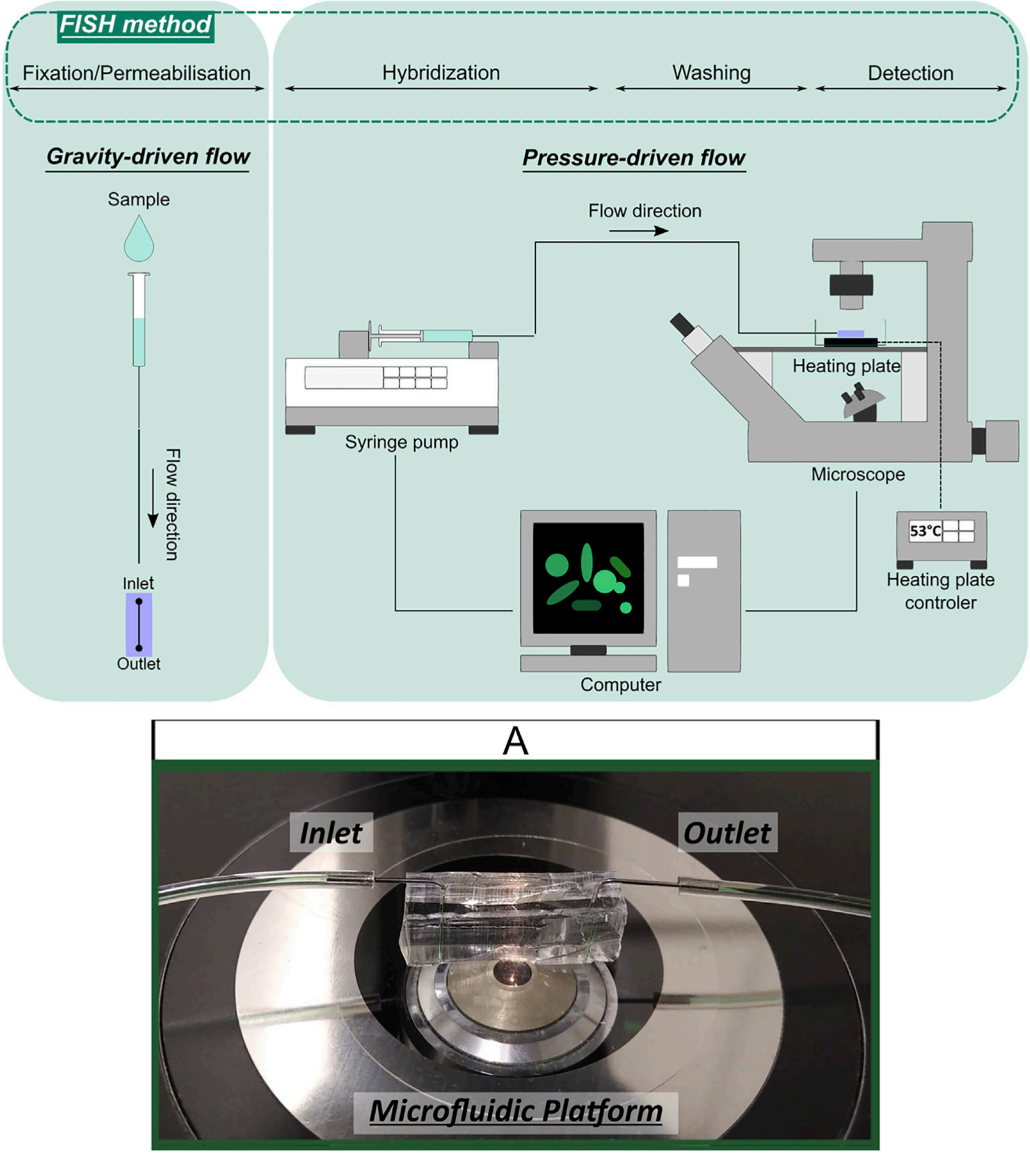

FIGURE 3
Schematic representation of gravity- and pressure-driven fluid handling systems applied in FISH integration with microfluidics experiments and microfluidic device illustration **(A)**.

3 Results

3.1 Microfluidic channel characterization

After fabrication, visual examination of the microfluidic channels revealed that microposts were not visibly bent or deformed and that the microchannel had a well-defined rectangular shape (data not shown) with a vertical side wall (Figure 4). As expected, minor differences in microposts height were observed (Figure 4A, white dashed line). To understand if microposts would fail to bond to glass substrate due to differences in height, we applied oxygen plasma treatment to the microfluidic channel (Ferreira et al., 2017). After treatment it was observed that the surface of all microposts were in contact with the glass substrate (Figure 4B, black dashed line).

Afterwards, the nominal height (*H*) and width (*W*) of the proposed microchannel geometry were compared with the experimental dimensions. Therefore, the microchannel dimensions were measuredat different regions, namely the inlet/outlet and the detection region and the percent error was determined (Supplementary Table S1). It was observed that

TABLE 1 Hydrodynamic flow conditions (nominal).

	Flow rate (Q, μl/min)	Velocity (V, m/s)	Reynolds number (Re)
Inlet/Outlet	1	0.006	0.51
Detection region	1	0.001	0.13

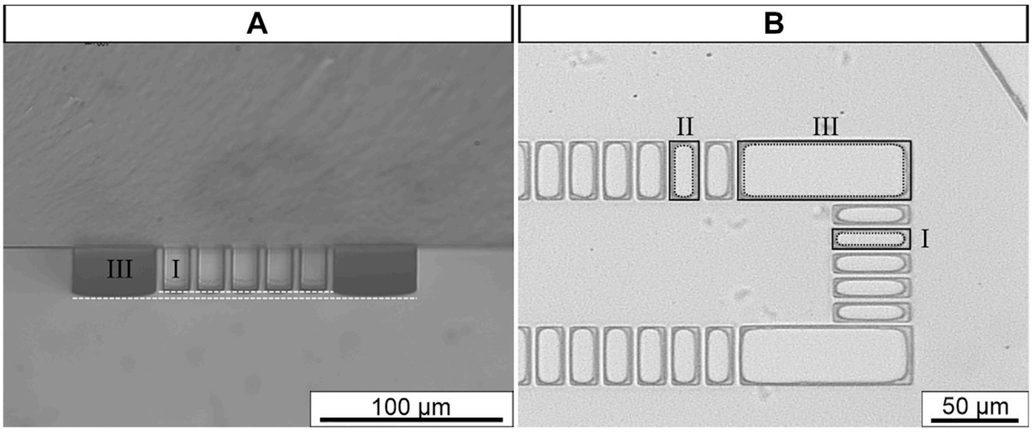

FIGURE 4
Representative examples of microfluidic channel detection region at cross-section **(A)** and horizontal view **(B)**. *White dashed line* represents micropost height. *Black line* micropost contour; *Black dashed line* micropost contact with glass substrate. Original magnification 400 *X* **(A)**, 100 *X* **(B)**.

width percent error ranged between 1.6 and 17.2%. The higher percent error was found to be in the gaps. This was expected because the percent error is generally higher in smaller dimensions (Pinto et al., 2013). Moreover, the height percent error was 10.9–16.0%, suggesting that the master mold height was below 30 μm.

3.1.1 Flow conditions

The next step was to assess hydrodynamic flow conditions by calculating the flow rate (Q, μl/min), mean velocity (V, m/s) and Reynolds number (Re) (Table 1). Since the microchannel has different dimensions of cross-sectional area along the microchannel, the Re number was calculated at different regions. Based on previous studies (Ferreira et al., 2017), an inlet velocity of 0.006 m/s was set, which corresponds to an inlet flow rate of 1 μl/min in a cross-section of 100 μm × 30 μm, where the fluid was assumed to be water (ρ = 998.2 kg/m^3; μ = 0.001003 kg m^{-1}. s^{-1}) (Table 1). As expected, the Re number varied 0.51–0.13 among different regions (inlet/outlet and detection region). These values confirm low Re, thus indicating laminar flow and consistency with other microfluidic devices. This data was then used as a starting point to perform computational fluid dynamics (CFD) simulations.

3.1.2 CFD simulations

The results obtained by the CFD simulations are represented in Figure 5. More specifically, Figure 5A shows the velocity magnitude field at the device horizontal plane of symmetry (Symmetry plane II, Figure 2A). When the fluid enters the trapping region the velocity starts decreasing in the retentate side and increases along the x axis in the permeate side, due to the fluid flowing through the gaps. The maximum velocity in the gaps decreases along the x direction (Figure 5B) in the first two sets of gaps and stabilizes in the third set of gaps. The maximum velocity ranges from 0.0014 m/s to 0.0031 m/s. As shown in Figure 5C, the velocity magnitudes in the lateral gaps are very similar and it can be assumed that the flow does not have preferential paths. The velocity profile of the front microposts is also similar to the velocity profile of the lateral microposts. The maximum velocity ranges from 0.0009 m/s, in the central gaps, to 0.0018 m/s in the lateral gaps.

3.2 Integration of FISH method to microfluidic environment

In here, the sample was introduced to microfluidic channel using gravity-driven flow, while the fixation, hybridization and

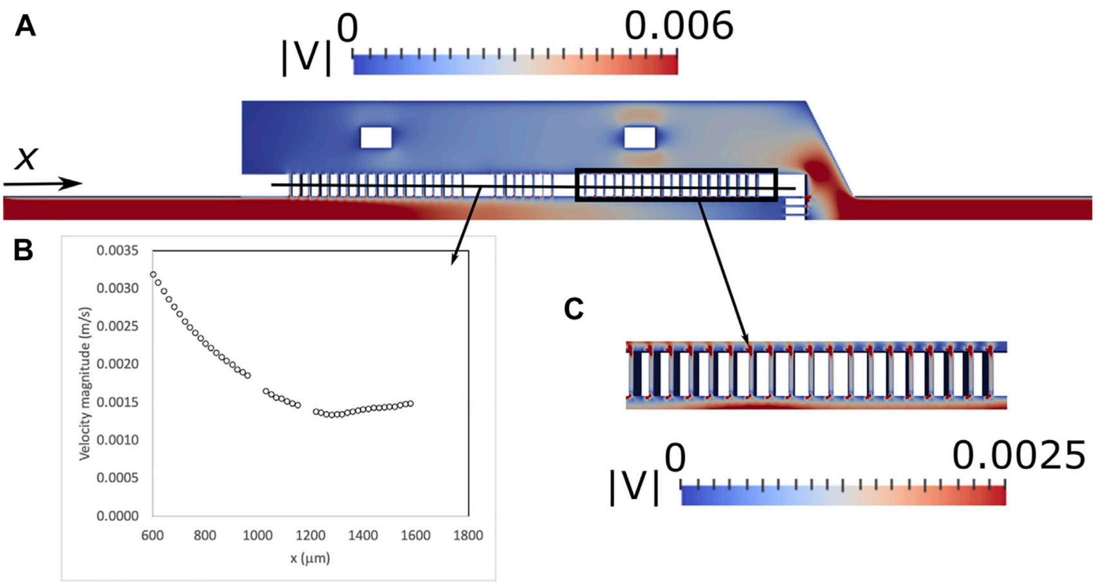

FIGURE 5
Contours of the velocity magnitude (m/s) for proposed microfluidic devices along the horizontal plane of symmetry (Symmetry plane II, **Figure 2A**) predicted by the CFD simulations **(A)**, maximum velocity along the lateral gaps **(B)** and detail of the contours of the velocity magnitude in the lateral gaps **(C)**.

washing solutions were injected using the pressure-driven flow system. The experimental set-up used in these assays is outlined in Figure 3. At first, using gravity-driven flow, viable *C. tropicalis* cells were introduced into the microfluidic channel, so that they could be retained along the microposts. Then, using the same flow system, the fixation/permeabilization solutions of the FISH protocol were applied onto trapped *C. tropicalis* cells. During this step the microorganism was permeabilized while preserving the morphological structure of the cells, so that the probe can be internalized in the hybridization step. Cell trapping was confirmed with bright field microscopy (Figures 6A,B). *C. tropicalis* was mainly trapped along the lateral (Figure 6A, black dashed arrow) and front microposts (Figures 6A,B, black arrow). Subsequently, using pressure-driven flow, subsequent hybridization and washing steps were performed. Overall, *C. tropicalis* cells revealed strong fluorescence signal. This confirmed that the PNA probe successfully hybridized to the target microorganism and that FISH steps were performed correctly in the microfluidic environment. Some *C. tropicalis* cells were observed in different focus planes (Figure 6D, white arrow) which may partly explain differences in the fluorescence signal of different cells. Because the microchannel height (≈30 µm) is higher that *C. tropicalis* cell dimension, single or multiple cells can be found in different positions along the microchannel height. As such, images should be acquired at different focus planes.

Different morphological growth forms were observed among *C. tropicalis* cells during integration studies [i.e., yeast, hyphae, pseudohyphae (Figures 7A–C)]. Islam *et al.* (Islam et al., 2020) also assessed *Candida* spp. Cell morphology before microfluidic experiments. In the case of *C. tropicalis* they revealed several morphologies: first spherical (with larger diameter of $x = y =$ 5.98 ± 0.75 µm) and then pseudosphere with ellipsoidal morphology (length of the pseudohyphae ranged from 7 to 27 µm with an average width of 1.89 ± 0.4 µm). These findings are in the agreement with our observations. Thus, it is possible that elongated filamentous *C. tropicalis* cells may pass through the gaps because of their orientation (e.g., minor length) when flowing in the microchannel.

3.3 Microfluidic platform validation in artificially contaminated samples

Finally, the proposed method was tested in artificially contaminated samples, where AU was contaminated with *C. tropicalis* at 10^5 cells/mL, a representative concentration for UTI (Fisher et al., 2011). At first, 20 µl of AU contaminated with *C. tropicalis* was introduced to the microfluidic channel. Subsequently, the solutions of FISH protocol were applied sequentially onto already trapped *C. tropicalis* cells using the same fluid handling system as described previously. A negative control with *C. tropicalis* exposed to HS alone was included. Finally, cell trapping was confirmed with bright field microscopy (Figures 8A,C, black arrow). Overall, strong fluorescence signal of *C. tropicalis* cells was observed (Figure 8D) when subjected to PNA probe, compared to cells hybridized in HS alone (Figure 8B,

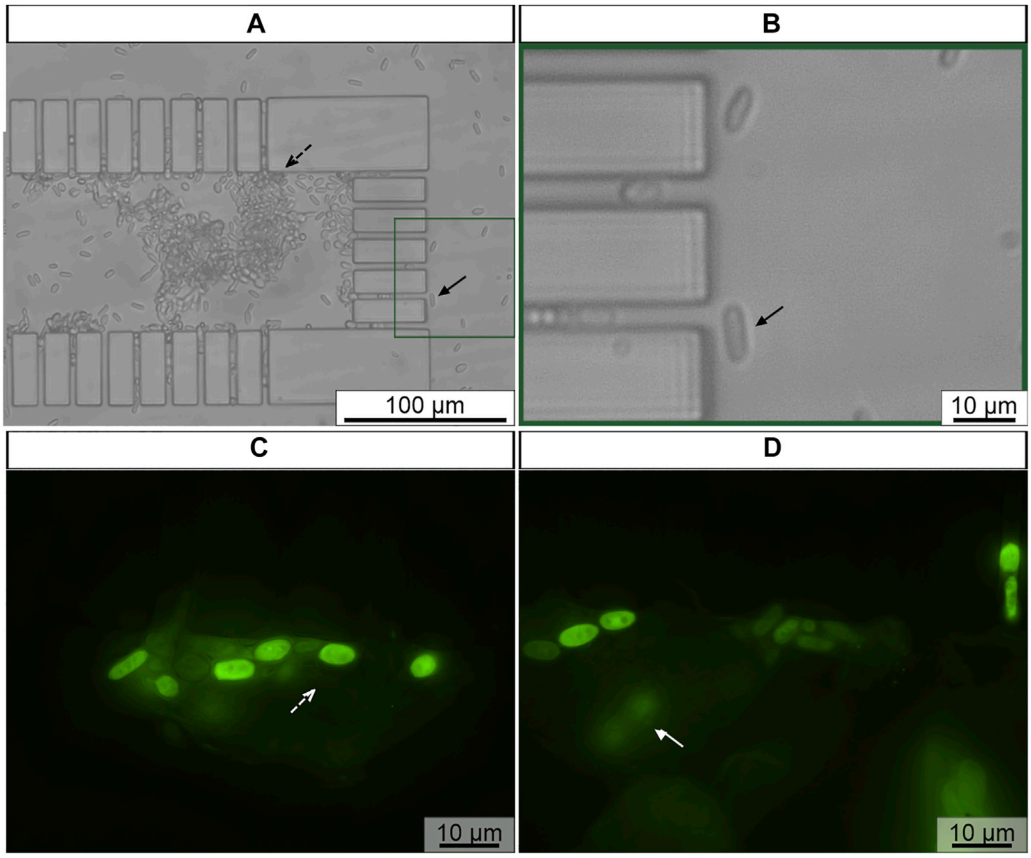

FIGURE 6
Representative example of *C. tropicalis* subjected to FISH in microchannel **(A,B)** Previously trapped *C. tropicalis* (≈1 × 10^8 cells/mL) after fixation/permeabilization, **(C,D)** hybridization and washing steps of FISH protocol. The microscope parameters maintained the same. *Black dashed arrow* represents cells at lateral microposts; *Rectangle* enlarged microchannel section; *Black arrow* trapped cell cells at front microposts; *White dashed arrow* fluorescence cells; *White arrow* fluorescence cells in different focus plane. Original magnification 400 *X* **(A,B)**, 1,000 *X* **(C,D)**.

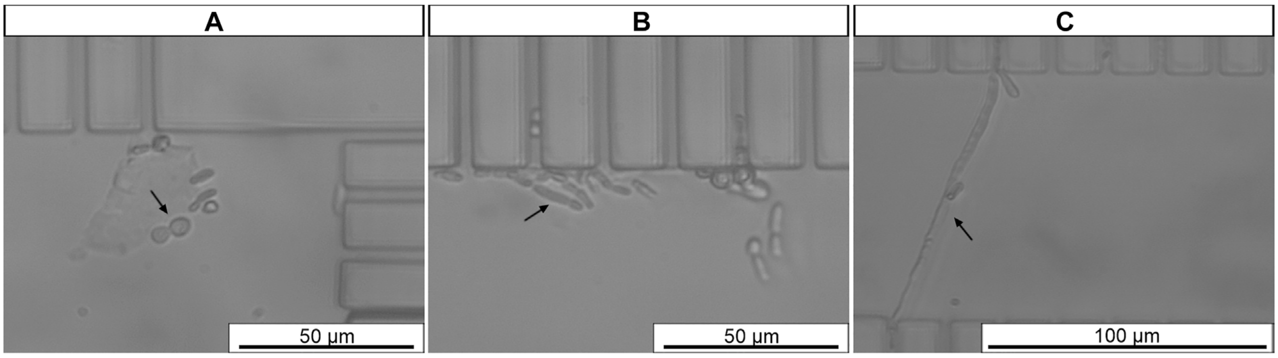

FIGURE 7
Morphological growth forms of *C. tropicalis*: **(A)** yeast, **(B)** pseudohyphae, **(C)** hyphae. The microscope parameters maintained the same. *Black arrow* represents trapped cell. Original magnification 400 *X* **(A–C)**.

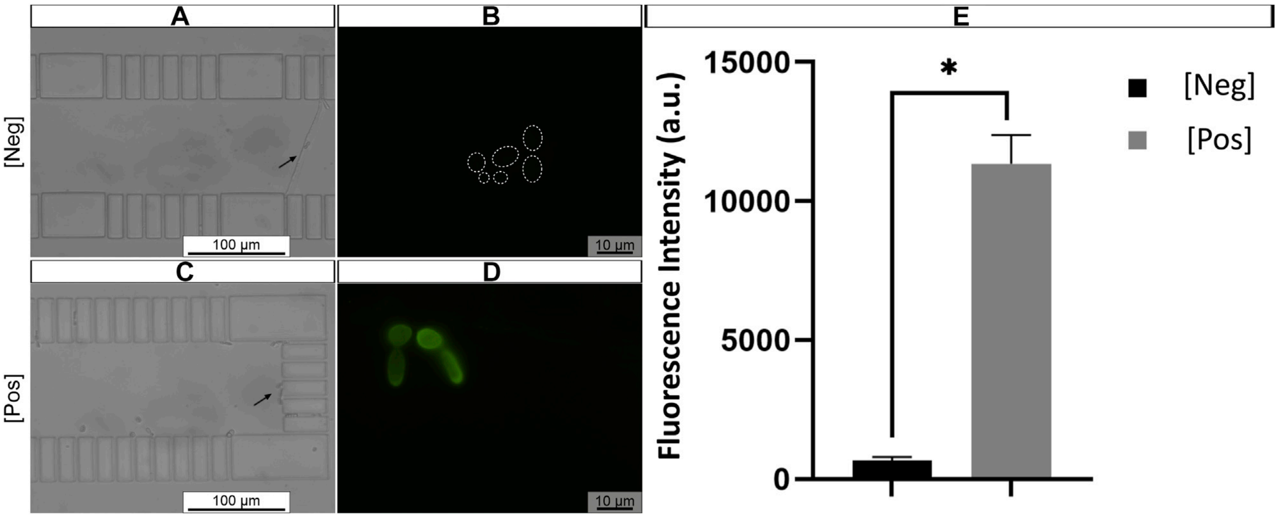

FIGURE 8
Representative example of artificial urine (AU) contaminated with *C. tropicalis* subjected to microchannel integrated FISH method **(A,C)**. Previously trapped *C. tropicalis* (≈1 × 10^5 cells/mL) after fixation/permeabilization step. And subjected to hybridization solution (HS) alone (control, *dashed circles*) **(B)** or **(D)** PNA probe suspended in HS (200 nM). The microscope parameters were kept the same. *Black arrow* represents trapped cell; *Dashed circle* hybridized cell contour. Original magnification 400 *X* **(A,C)**, 1,000 *X* **(B,D)** **(E)** The fluorescence signal quantification of *C. tropicalis*. The data is shown as mean fluorescence intensity (arbitrary units a. u.) ± SEM. *p*>0.05: * vs HS alone [Neg], HS + PNA probe [Pos].

dashed circle). Additionally, the fluorescence signal quantification results revealed that the signal intensity was significantly higher in *C. tropicalis* cells hybridized with probe, when compared to cells subjected to hybridization solution alone (Figure 8E). These findings corroborate with previous observations of visual detection using microfluidic PNA-FISH method (Figure 8D).

4 Discussion

The proposed microfluidic channel was fabricated using the silicon-based organic polymer–PDMS. This material is widely used in biological studies (Ferreira et al., 2017) since it presents several advantages, such as biocompatibility, optical transparency, low-cost, and rapid prototyping (Torino et al., 2018). PDMS is composed of -O-Si(CH_3)$_2$- repeating units and the CH_3 is responsible for hydrophobic surface properties. As such, it is difficult to wet with aqueous solutions and may result in microchannel blocking by air bubbles (Sia and Whitesides, 2003). This challenge can be circumvented by exposing PDMS to oxygen plasma treatment, during which the silanol groups (SiOH) are replaced by methyl groups ($SiOH_3$) (Duffy et al., 1998; Kim et al., 2004; Bodas and Khan-Malek, 2007). This changes PDMS surface properties to hydrophilic, thus resulting in surface wetting (Bartali et al., 2017). Additionally, PDMS can be joined with different surfaces through reversible or irreversible seals to form closed microfluidic channel (Tan et al., 2010; Xiong et al., 2014). In this study we used the irreversible seal, where the PDMS block and the glass substrate were exposed to plasma oxidation following by immediate bonding forming a closed microchannel. This type of bonding withstands higher pressures (30–50 psi) when compared to the reversible seal (5 psi) (Sia and Whitesides, 2003) and is more suitable for pressure-driven flow systems. Simultaneously, oxygen plasma treatment also was used for PDMS surface hydrophilization.

Flow in the device is crucial to adequate cell sieving. If the flow velocity in the gaps is too high, cells may be dragged through the gaps. One of the goals of CFD simulations was the analysis of possible preferential paths due large asymmetries in flow resistance in the device. Preferential paths lead to high velocities in specific regions of the device, favouring cell dragging through the gaps. CFD results show that the velocity in the gaps is higher in the first set of gaps. To balance the flow between the gaps, the flow resistance must be increased in the gaps with higher velocity by increasing the gap length. Nonetheless, the maximum velocity in the gaps is 0.0031 m/s and in a previous work we showed that the velocity in the gaps can be as high as 0.02 m/s without significant cell dragging (Ferreira et al., 2017).

The dimensional deviations of the fabricated microchannels were also evaluated, as microchannel and gap dimensions impact fluid velocity and sieving performance during experimental assays. For example, non-vertical side walls may result in different velocity contours and streamlines, when compared with numerical simulations (e.g., CFD), which may impact cell trajectories when flowing in microfluidic channel (Karthikeyan et al., 2018). Additionally, the percent error was determined as a measure of fabrication accuracy. Fabrication accuracy was assessed by Sampaio *et al.* (Sampaio et al., 2015) and Lepowsky *et al.* (Lepowsky et al., 2018) in microfluidic chips fabricated by soft-lithography and 3D-printing methods, respectively. For instance, Lepowsky *et al.* reported varying width percent errors from 5.38 to 10.75% in different microchannel regions. These findings are similar to the microchannel proposed in the present study. Overall, the developed microfluidic geometry had minor differences in microchannel height among different microposts which did not prevent from successful microchannel bonding to glass substrate, after oxygen plasma treatment. Therefore, it was assumed that minor differences in micropost heights should not impact overall microfluidic platform performance in further experiments.

The main objective of this study was to integrate microfluidic channel based on hydrodynamic cell trapping with PNA-FISH. This can provide several advantages for UTI diagnostics from clinical urine samples, such as direct target visualisation (Moter and Gobel, 2000) in complex biological matrices (Almeida et al., 2013a; Almeida et al., 2013b), using epifluorescence microscope - a standard equipment found in clinical laboratories. Also, target microorganisms can be detected within a few hours, while the standard culture-based method would require several days (Almeida et al., 2013b). Furthermore, studies showed that the pre-enrichment time can be reduced using PNA-FISH technique (Almeida et al., 2013c; Cerqueira et al., 2020). Nevertheless, the PNA probes can be designed to target microorganisms at species or genus level (Almeida et al., 2013b; Cerqueira et al., 2013; Rocha et al., 2019) and in this case, it is important for the quick identification of *Candida* spp. Isolates and initiation of appropriate treatment (Oliveira Santos et al., 2018; Rodrigues M. E. et al., 2019). Moreover, biological fluids and matrices may contain inhibitory substances, that may interfere with molecular method performance (Morshed et al., 2007; Schrader et al., 2012).

In FISH, one the main challenge is the autofluorescence arising from biological matrices and inorganic debris. This natural fluorescence could impact microscopic sample examination (Moter and Gobel, 2000; Rohde et al., 2015). Clinical samples, such as urine, may exhibit different fluorescence depending on individuals' health status (Anwer et al., 2009; Spakova et al., 2020). Finally, the microfluidic device can be operated with small volumes (in μl range), resulting in lower costs of probes used in FISH assays.

Despite the successful PNA-FISH procedure integration with a microfluidic platform was attained, some adjustments to microfluidic design should be further considered. For instance, it was observed that some *C. tropicalis* cells pass through the gaps (Figure 6B, black arrow). Kim *et al.* showed that elongated cells moving with the flow in microchannels follow different trajectories than spherical shape cells. Using computational simulations, it was observed, that elongated cell orientation varied through the flipping motion (Kim et al., 2011). Therefore, the microchannel gap size should be adjusted, taking into consideration the width of *C. tropicalis*.

To further decrease the time of the proposed method several strategies could be applied. Such as, optimising laboratory infrastructures and experimental set-up would streamline the process. Also, the pressure-driven flow could be applied for the entire PNA-FISH method in microchannel. Thus, using one type of liquid handling system would simplify the overall procedure. Finally, the incubation times of hybridization and washing steps could be reduced without compromising the fluorescence signal intensity.

5 Concluding remarks

The combination of FISH with microfluidics demonstrated number of advantages, such as cell separation from fluid with subsequent pre-enrichment, also reduced reagent consumption and analysis time. However, this integration was achieved in a limited number of works, especially for the diagnostics of fungal infections (Asghar et al., 2019; Hussain et al., 2020). As such, the work presented in this manuscript aimed to develop a microfluidic platform combined with FISH for the detection of *C. tropicalis*. Overall, the obtained results confirm that FISH worked well in microfluidic channels and demonstrated successful *C. tropicalis* detection in biologically-relevant samples, such as AU. Using our proposed PNA-FISH integrated microfluidic platform, *C. tropicalis* was visually detected in AU in 6 h, which is faster than current urine culture method that takes 18–48 h (Wilson and Gaido, 2004; Davenport et al., 2017). Ultimately, this work provides the necessary fundaments towards development of future POC detection platform.

Data availability statement

The original contributions presented in the study are included in the article/Supplementary Material, further inquiries can be directed to the corresponding authors.

Author contributions

NFA and JMM conceptualized and designed the study. CFR, LC, JMM and NFA supervised, provided the necessary resources, performed manuscript revision and editing. VBB performed the experiments, data curation, analysis and writing the original manuscript. JMM performed CFD numerical simulations, data analysis and writing of the respective section. Formal analysis and result validation was conducted by VBB, CFR, LC, JMM, NFA. The research project administration and funding acquisition performed by CFR, LC, JMM and NFA.

Funding

This work was financially supported by LA/P/0045/2020 (ALiCE), UIDB/00511/2020 - UIDP/00511/2020 (LEPABE) and UIDP/00532/2020 (CEFT) funded by national funds through FCT/MCTES (PIDDAC); POCI-01-0145-FEDER-031011 and POCI-01-0145-FEDER-029961, funded by FEDER funds through COMPETE2020—Programa Operacional Competitividade e Internacionalização (POCI) and by national funds (PIDDAC) through FCT/MCTES. This work was also financed by Project NORTE-01-0247-FEDER-046970.

Conflict of interest

The authors declare that the research was conducted in the absence of any commercial or financial relationships that could be construed as a potential conflict of interest.

Publisher's note

Supplementary material

The Supplementary Material for this article can be found online at: https://www.frontiersin.org/articles/10.3389/fbioe.2022.987669/full#supplementary-material

References

Almeida, C., Azevedo, N. F., Bento, J. C., Cerca, N., Ramos, H., Vieira, M. J., et al. (2013a). Rapid detection of urinary tract infections caused by *Proteus* spp. using PNA-FISH. *Eur. J. Clin. Microbiol. Infect. Dis.* 32, 781–786. doi:10.1007/s10096-012-1808-2

Almeida, C., Cerqueira, L., Azevedo, N. F., and Vieira, M. J. (2013b). Detection of *Salmonella enterica* serovar Enteritidis using real time PCR, immunocapture assay, PNA FISH and standard culture methods in different types of food samples. *Int. J. Food Microbiol.* 161, 16–22. doi:10.1016/j.ijfoodmicro.2012.11.014

Almeida, C., Sousa, J. M., Rocha, R., Cerqueira, L., Fanning, S., Azevedo, N. F., et al. (2013c). Detection of *Escherichia coli* O157 by peptide nucleic acid fluorescence *in situ* hybridization (PNA-FISH) and comparison to a standard culture method. *Appl. Environ. Microbiol.* 79, 6293–6300. doi:10.1128/AEM.01009-13

Alvarez-Lerma, F., Nolla-Salas, J., Leon, C., Palomar, M., Jorda, R., Carrasco, N., et al. (2003). Candiduria in critically ill patients admitted to intensive care medical units. *Intensive Care Med.* 29, 1069–1076. doi:10.1007/s00134-003-1807-y

Anwer, A. G., Sandeep, P. M., Goldys, E. M., and Vemulpad, S. (2009). Distinctive autofluorescence of urine samples from individuals with bacteriuria compared with normals. *Clin. Chim. Acta* 401, 73–75. doi:10.1016/j.cca.2008.11.021

Asghar, W., Sher, M., Khan, N. S., Vyas, V. M., and Demirci, U. (2019). Microfluidic chip for detection of fungal infections. *ACS Omega* 4, 7474–7481. doi:10.1021/acsomega.9b00499

Aspevall, O., Hallander, H., Gant, V., and Kouri, T. (2001). European guidelines for urinalysis: a collaborative document produced by European clinical microbiologists and clinical chemists under ECLM in collaboration with ESCMID. *Clin. Microbiol. Infect.* 7, 173–178. doi:10.1046/j.1198-743x.2001.00237.x

Azevedo, A. S., Sousa, I. M., Fernandes, R. M., Azevedo, N. F., and Almeida, C. (2019). Optimizing locked nucleic acid/2'-O-methyl-RNA fluorescence *in situ* hybridization (LNA/2'OMe-FISH) procedure for bacterial detection. *PLoS One* 14, e0217689. doi:10.1371/journal.pone.0217689

Bartali, R., Morganti, E., Lorenzelli, L., Micheli, V., Gottardi, G., Scarpa, M., et al. (2017). Oxygen plasma treatments of polydimethylsiloxane surfaces: effect of the atomic oxygen on capillary flow in the microchannels. *Micro Nano Lett.* 12, 754–757. doi:10.1049/mnl.2017.0230

Beech, J. P., Ho, B. D., Garriss, G., Oliveira, V., Henriques-Normark, B., and Tegenfeldt, J. O. (2018). Separation of pathogenic bacteria by chain length. *Anal. Chim. Acta X.* 1000, 223–231. doi:10.1016/j.aca.2017.11.050

Bodas, D., and Khan-Malek, C. (2007). Hydrophilization and hydrophobic recovery of PDMS by oxygen plasma and chemical treatment—an SEM investigation. *Sensors Actuators B Chem.* 123, 368–373. doi:10.1016/j.snb.2006.08.037

Bongomin, F., Gago, S., Oladele, R. O., and Denning, D. W. (2017). Global and multi-national prevalence of fungal diseases-estimate precision. *J. Fungi (Basel).* 3, 57–29. doi:10.3390/jof3040057

Cerqueira, L., Fernandes, R. M., Ferreira, R. M., Oleastro, M., Carneiro, F., Brandao, C., et al. (2013). Validation of a fluorescence *in situ* hybridization method using peptide nucleic acid probes for detection of *Helicobacter pylori* clarithromycin resistance in gastric biopsy specimens. *J. Clin. Microbiol.* 51, 1887–1893. doi:10.1128/JCM.00302-13

Cerqueira, L., Moura, S., Almeida, C., Vieira, M. J., and Azevedo, N. F. (2020). Establishment of a new PNA-FISH method for *Aspergillus fumigatus* identification: First insights for future use in pulmonary samples. *Microorganisms* 8, 1950. doi:10.3390/microorganisms8121950

Chien-Hsuan, T., Chung-Liang, H., Ya-Lan, C., Wan, C. L., and Gwo-Bin, L. (2013). A novel integrated microfluidic platform to perform fluorescence *in situ* hybridization for chromosomal analysis. *Microfluid. Nanofluidics* 15, 745–752. doi:10.1007/s10404-013-1190-0

Cruz-Moreira, D. (2014). "Integration of microfluidics and fluorescence *in situ* hybridization (FISH) for the rapid identification of microorganisms," in *Master's Thesis. Porto: Faculdade de Engenharia da Universidade do Porto - FEUP, Laboratório de Engenharia de Processos Ambiente - LEPABE.*

Davenport, M., Mach, K. E., Shortliffe, L. M. D., Banaei, N., Wang, T.-H., and Liao, J. C. (2017). New and developing diagnostic technologies for urinary tract infections. *Nat. Rev. Urol.* 14, 296–310. doi:10.1038/nrurol.2017.20

Duffy, D. C., McDonald, C. J., Schueller, O. J. A., and Whitesides, G. M. (1998). Rapid prototyping of microfluidic systems in poly(dimethylsiloxane). *Anal. Chem.* 70, 4974–4984. doi:10.1021/ac980656z

Fan, Y.-J., Hsieh, H.-Y., Tsai, S.-F., Wu, C.-H., Lee, C.-M., Liu, Y.-T., et al. (2021). Microfluidic channel integrated with a lattice lightsheet microscopic system for continuous cell imaging. *Lab. Chip* 21, 344–354. doi:10.1039/d0lc01009j

Ferreira, A. M., Cruz-Moreira, D., Cerqueira, L., Miranda, J. M., and Azevedo, N. F. (2017). Yeasts identification in microfluidic devices using peptide nucleic acid fluorescence *in situ* hybridization (PNA-FISH). *Biomed. Microdevices* 19, 11. doi:10.1007/s10544-017-0150-y

Fisher, J. F. (2011). *Candida* urinary tract infections--epidemiology, pathogenesis, diagnosis, and treatment: executive summary. *Clin. Infect. Dis.* 52 (6), S429–S432. doi:10.1093/cid/cir108

Fisher, J. F., Sobel, J. D., Kauffman, C. A., and Newman, C. A. (2011). *Candida* urinary tract infections--treatment. *Clin. Infect. Dis.* 52 (6), S457–S466. doi:10.1093/cid/cir112

Fontenete, S., Carvalho, D., Lourenco, A., Guimaraes, N., Madureira, P., Figueiredo, C., et al. (2016). FISHji: New ImageJ macros for the quantification of fluorescence in epifluorescence images. *Biochem. Eng. J.* 112, 61–69. doi:10.1016/j.bej.2016.04.001

Gajdacs, M., Doczi, I., Abrok, M., Lazar, A., and Burian, K. (2019). Epidemiology of candiduria and *Candida* urinary tract infections in inpatients and outpatients: results from a 10-year retrospective survey. *Cent. Eur. J. Urol.* 72, 209–214. doi:10.5173/ceju.2019.1909

Gall, J. G., and Pardue, M. L. (1969). Molecular hybridization of radioactive DNA to the DNA of cytological preparations. *Proc. Natl. Acad. Sci. U. S. A.* 64, 600–604. doi:10.1073/pnas.64.2.600

Gharanfoli, A., Mahmoudi, E., Torabizadeh, R., Katiraee, F., and Faraji, S. (2019). Isolation, characterization, and molecular identification of *Candida* species from urinary tract infections. *Curr. Med. Mycol.* 5, 33–36. doi:10.18502/cmm.5.2.1159

Goyal, R. K., Sami, H., Mishra, V., Bareja, R., and Behara, R. N. (2016). Non-albicans candiduria: An emerging threat. *J. Appl. Pharm. Sci.* 6, 048–050. doi:10.7324/JAPS.2016.60308

Hsieh, H.-Y., Chang, R., Huang, Y.-Y., Juan, P.-H., Tahara, H., Lee, K.-Y., et al. (2022). Continuous polymerase chain reaction microfluidics integrated with a gold-capped nanoslit sensing chip for Epstein-Barr virus detection. *Biosens. Bioelectron. X.* 195, 113672–113679. doi:10.1016/j.bios.2021.113672

Hussain, K. K., Malavia, D., Johnson, E. M., Littlechild, J., Winlove, P. C., Vollmer, F., et al. (2020). Biosensors and diagnostics for fungal detection. *J. Fungi (Basel).* 6, 349. doi:10.3390/jof6040349

Inglis, M. W., Lord, M., and Nordon, R. E. (2011). Scaling deterministic lateral displacement arrays for high throughput and dilution-free enrichment of leukocytes. *J. Micromech. Microeng.* 21, 054024–054028. doi:10.1088/0960-1317/21/5/054024

Islam, M., Keck, D., Gilmore, J., and Martinez-Duarte, R. (2020). Characterization of the dielectrophoretic response of different Candida strains using 3D carbon microelectrodes. *Micromachines (Basel)* 11, 255. doi:10.3390/mi11030255

Ji, H. M., Samper, V., Chen, Y., Heng, C. K., Lim, T. M., and Yobas, L. (2008). Silicon-based microfilters for whole blood cell separation. *Biomed. Microdevices* 10, 251–257. doi:10.1007/s10544-007-9131-x

Jung, G.-Y., Li, Z., Wu, W., Chen, Y., Olynick, D. L., Wang, S.-Y., et al. (2005). Vapor-phase self-assembled monolayer for improved mold release in nanoimprint lithography. *Langmuir* 21, 1158–1161. doi:10.1021/la0476938

Karthikeyan, K., Sujatha, L., Sundar, R., and Sharma, S. K. (2018). Dimension tolerances in fabrication of polymer microfluidic devices. *JSTS* 18, 262–269. doi:10.5573/JSTS.2018.18.2.262

Kauffman, C. A. (2014). Diagnosis and management of fungal urinary tract infection. *Infect. Dis. Clin. North Am.* 28, 61–74. doi:10.1016/j.idc.2013.09.004

Kauffman, C. A., Fisher, J. F., Sobel, J. D., and Newman, C. A. (2011). Candida urinary tract infections--diagnosis. *Clin. Infect. Dis.* 52 (6), S452–S456. doi:10.1093/cid/cir111

Kauffman, C. A., Vazquez, J. A., Sobel, J. D., Gallis, H. A., McKinsey, D. S., Karchmer, A. W., et al. (2000). Prospective multicenter surveillance study of funguria in hospitalized patients. *Clin. Infect. Dis.* 30, 14–18. doi:10.1086/313583

Kim, B., Peterson, E. T. K., and Papautsky, I. (2004). Long-term stability of plasma oxidized PDMS surfaces.

Kim, J., Erath, J., Rodriguez, A., and Yang, C. (2014). A high-efficiency microfluidic device for size-selective trapping and sorting. *Lab. Chip* 14, 2480–2490. doi:10.1039/c4lc00219a

Kim, M.-C., Isenberg, B. C., Sutin, J., Meller, A., Wong, J. Y., and Klapperich, C. M. (2011). Programmed trapping of individual bacteria using micrometre-size sieves. *Lab. Chip* 11, 1089–1095. doi:10.1039/c0lc00362j

Lee, M. S., Hyun, H., Park, I., Kim, S., Jang, D.-H., Kim, S., et al. (2022). Quantitative fluorescence *in situ* hybridization (FISH) of magnetically confined bacteria enables early detection of human bacteremia. *Small Methods* 6, e2101239. doi:10.1002/smtd.202101239

Lepowsky, E., Amin, R., and Tasoglu, S. (2018). Assessing the reusability of 3D-printed photopolymer microfluidic chips for urine processing. *Micromachines (Basel)* 9, 520. doi:10.3390/mi9100520

Luan, Q., Macaraniag, C., Zhou, J., and Papautsky, I. (2020). Microfluidic systems for hydrodynamic trapping of cells and clusters. *Biomicrofluidics* 14, 031502. doi:10.1063/5.0002866

Mach, A. J., and Di Carlo, D. (2010). Continuous scalable blood filtration device using inertial microfluidics. *Biotechnol. Bioeng.* 107, 302–311. doi:10.1002/bit.22833

Mendes, L., Rocha, R., Azevedo, A. S., Ferreira, C., Henriques, M., Pinto, M. G., et al. (2016). Novel strategy to detect and locate periodontal pathogens: The PNA-FISH technique. *Microbiol. Res.* 192, 185–191. doi:10.1016/j.micres.2016.07.002

Morshed, M. G., Lee, M.-K., Jorgensen, D., and Isaac-Renton, J. L. (2007). Molecular methods used in clinical laboratory: Prospects and pitfalls. *FEMS Immunol. Med. Microbiol.* 49, 184–191. doi:10.1111/j.1574-695X.2006.00191.x

Moter, A., and Gobel, U. B. (2000). Fluorescence *in situ* hybridization (FISH) for direct visualization of microorganisms. *J. Microbiol. Methods* 41, 85–112. doi:10.1016/s0167-7012(00)00152-4

Muller, V., Sousa, J. M., Ceylan Koydemir, H., Veli, M., Tseng, D., Cerqueira, L., et al. (2018). Identification of pathogenic bacteria in complex samples using a smartphone based fluorescence microscope. *RSC Adv.* 8, 36493–36502. doi:10.1039/c8ra06473c

Nacher-Vazquez, M., Santos, B., Azevedo, N. F., and Cerqueira, L. (2022). The role of Nucleic Acid Mimics (NAMs) on FISH-based techniques and applications for microbial detection. *Microbiol. Res.* 262, 127086. doi:10.1016/j.micres.2022.127086

Negri, M., Silva, S., Henriques, M., Azeredo, J., Svidzinski, T., and Oliveira, R. (2011). *Candida tropicalis* biofilms: artificial urine, urinary catheters and flow model. *Med. Mycol.* 49, 739–747. doi:10.3109/13693786.2011.560619

Nguyen, H. T., Trouillon, R., Matsuoka, S., Fiche, M., Leval, L. D., Bisig, B., et al. (2017). Microfluidics-assisted fluorescence *in situ* hybridization for advantageous human epidermal growth factor receptor 2 assessment in breast cancer. *Lab. Invest.* 97, 93–103. doi:10.1038/labinvest.2016.121

OECD/European Union (2018). *Healthcare-associated infections: Health at a glance: Europe 2018: State of health in the EU cycle*. Paris/European Union, Brussels: OECD Publishing.

Oliveira, I. M. de (2018). "Rapid detection of contaminant microorganisms in food containers," in *Master's Thesis. Porto: Frulact/Faculdade de Engenharia da Universidade do Porto - FEUP, Laboratório de Engenharia de Processos Ambiente - LEPABE*.

Oliveira Santos, G. C., Vasconcelos, C. C., Lopes, A. J. O., Sousa Cartagenes, M. S., Filho, A. K. D. B., et al. (2018). Candida infections and therapeutic strategies: Mechanisms of action for traditional and alternative agents. *Front. Microbiol.* 9, 1351. doi:10.3389/fmicb.2018.01351

Park, M. C., Hur, J. Y., Cho, H. S., Park, S.-H., and Suh, K. Y. (2011). High-throughput single-cell quantification using simple microwell-based cell docking and programmable time-course live-cell imaging. *Lab. Chip* 11, 79–86. doi:10.1039/c0lc00114g

Perry-O'Keefe, H., Rigby, S., Oliveira, K., Sorensen, D., Stender, H., Coull, J., et al. (2001). Identification of indicator microorganisms using a standardized PNA FISH method. *J. Microbiol. Methods* 47, 281–292. doi:10.1016/s0167-7012(01)00303-7

Pinto, E., Taboada, B., Faustino, V., Cidre, D., Rodrigues, R., Miranda, J., et al. (2013). *Blood flow in microchannels manufactured by a low cost technique: xurography*, 285–290.

Richardson, M. D. (1991). Opportunistic and pathogenic fungi. *J. Antimicrob. Chemother.* 28, 1–11. doi:10.1093/jac/28.suppl_a.1

Rocha, R., Sousa, J. M., Cerqueira, L., Vieira, M. J., Almeida, C., and Azevedo, N. F. (2019). Development and application of peptide nucleic acid fluorescence *in situ* hybridization for the specific detection of *Listeria monocytogenes*. *Food Microbiol.* 80, 1–8. doi:10.1016/j.fm.2018.12.009

Rodrigues, C. F., Rodrigues, M. E., and Henriques, M. (2019a). *Candida* sp. infections in patients with diabetes mellitus. *J. Clin. Med.* 8, 76–40. doi:10.3390/jcm8010076

Rodrigues, C. F., Vilas Boas, D., Haynes, K., and Henriques, M. (2018). The MNN2 gene knockout modulates the antifungal resistance of biofilms of *Candida glabrata*. *Biomolecules* 8, 130. doi:10.3390/biom8040130

Rodrigues, M. E., Gomes, F., and Rodrigues, C. F. (2019b). *Candida* spp./bacteria mixed biofilms. *J. Fungi (Basel).* 6, 5. doi:10.3390/jof6010005

Rohde, A., Hammerl, J. A., Appel, B., Dieckmann, R., and Al Dahouk, S. (2015). FISHing for bacteria in food--a promising tool for the reliable detection of pathogenic bacteria? *Food Microbiol.* 46, 395–407. doi:10.1016/j.fm.2014.09.002

Sampaio, D., Lopes, D., and Semiao, V. (2015). Horse and dog blood flows in PDMS rectangular microchannels: Experimental characterization of the plasma layer under different flow conditions. *Exp. Therm. Fluid Sci.* 68, 205–215. doi:10.1016/j.expthermflusci.2015.04.020

Schindelin, J., Arganda-Carreras, I., Frise, E., Kaynig, V., Longair, M., Pietzsch, T., et al. (2012). Fiji: an open-source platform for biological-image analysis. *Nat. Methods* 9, 676–682. doi:10.1038/nmeth.2019

Schrader, C., Schielke, A., Ellerbroek, L., and Johne, R. (2012). PCR inhibitors - occurrence, properties and removal. *J. Appl. Microbiol.* 113, 1014–1026. doi:10.1111/j.1365-2672.2012.05384.x

Sia, S. K., and Whitesides, G. M. (2003). Microfluidic devices fabricated in poly(dimethylsiloxane) for biological studies. *Electrophoresis* 24, 3563–3576. doi:10.1002/elps.200305584

Sohrabi, S., Kassir, N., and Moraveji, M. K. (2020). Droplet microfluidics: fundamentals and its advanced applications. *RSC Adv.* 10, 27560–27574. doi:10.1039/D0RA04566G

Spakova, I., Dubayova, K., Nagyova, V., and Marekova, M. (2020). Fluorescence biomarkers of malignant melanoma detectable in urine. *Open Chem.* 18, 898–910. doi:10.1515/chem-2020-0143

Taei, M., Chadeganipour, M., and Mohammadi, R. (2019). An alarming rise of non-albicans *Candida* species and uncommon yeasts in the clinical samples; a combination of various molecular techniques for identification of etiologic agents. *BMC Res. Notes* 12, 779. doi:10.1186/s13104-019-4811-1

Tan, S. H., Nguyen, N.-T., Chua, Y. C., and Kang, T. G. (2010). Oxygen plasma treatment for reducing hydrophobicity of a sealed polydimethylsiloxane microchannel. *Biomicrofluidics* 4, 032204. doi:10.1063/1.3466882

Torino, S., Corrado, B., Iodice, M., and Coppola, G. (2018). PDMS-based microfluidic devices for cell culture. *Inventions* 3, 65. doi:10.3390/inventions3030065

Walker, G. M., Zeringue, H. C., and Beebe, D. J. (2004). Microenvironment design considerations for cellular scale studies. *Lab. Chip* 4, 91–97. doi:10.1039/b311214d

Wang, S., Inci, F., Chaunzwa, T. L., Ramanujam, A., Vasudevan, A., Subramanian, S., et al. (2012). Portable microfluidic chip for detection of *Escherichia coli* in produce and blood. *Int. J. Nanomedicine* 7, 2591–2600. doi:10.2147/IJN.S29629

Whang, K., Lee, J.-H., Shin, Y., Lee, W., Kim, Y. W., Kim, D., et al. (2018). Plasmonic bacteria on a nanoporous mirror via hydrodynamic trapping for rapid identification of waterborne pathogens. *Light. Sci. Appl.* 7, 68. doi:10.1038/s41377-018-0071-4

Wilson, M. L., and Gaido, L. (2004). Laboratory diagnosis of urinary tract infections in adult patients. *Clin. Infect. Dis.* 38, 1150–1158. doi:10.1086/383029

Xiong, L., Chen, P., and Zhou, Q. (2014). Adhesion promotion between PDMS and glass by oxygen plasma pre-treatment. *J. Adhes. Sci. Technol.* 28, 1046–1054. doi:10.1080/01694243.2014.883774

Yamada, M., and Seki, M. (2005). Hydrodynamic filtration for on-chip particle concentration and classification utilizing microfluidics. *Lab. Chip* 5, 1233–1239. doi:10.1039/b509386d

Zhou, J., Mukherjee, P., Gao, H., Luan, Q., and Papautsky, I. (2019). Label-free microfluidic sorting of microparticles. *Apl. Bioeng.* 3, 041504. doi:10.1063/1.5120501

Frontiers in
Bioengineering and Biotechnology

Accelerates the development of therapies, devices, and technologies to improve our lives

A multidisciplinary journal that accelerates the development of biological therapies, devices, processes and technologies to improve our lives by bridging the gap between discoveries and their application.

Discover the latest Research Topics

See more →

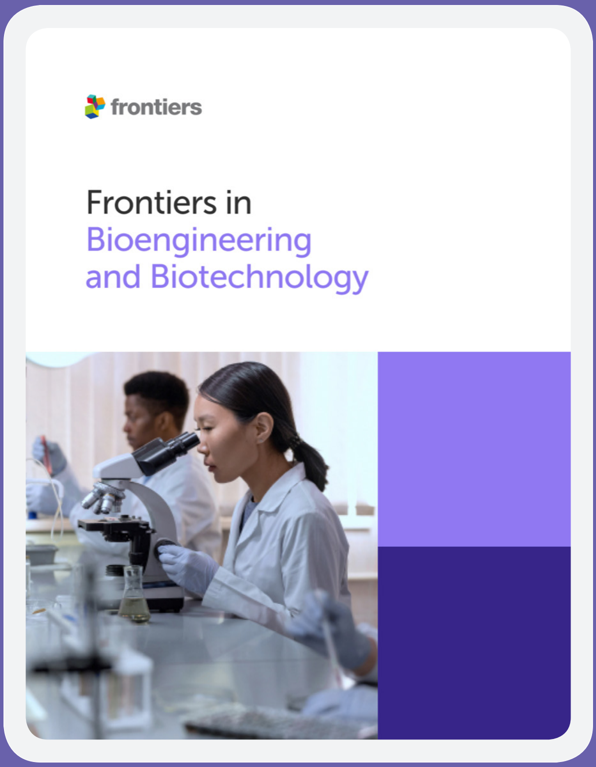

frontiers

Frontiers in
Bioengineering
and Biotechnology

Frontiers

Avenue du Tribunal-Fédéral 34
1005 Lausanne, Swizerland
frontiersin.org

Contact us

+41 (0)21 510 17 00
frontiersin.org/about/contact